New robust radar processing for model errors: the case of off-grid targets

Pierre Develter

université PARIS-SACLAY

New robust radar processing for model errors: the case of off-grid targets

Nouveaux traitements radar robustes aux erreurs de modèle : le cas des cibles hors grille

Thèse de doctorat de l'université Paris-Saclay

École doctorale n° 580 : sciences et technologies de l'information et de la communication (STIC),
Spécialité de doctorat: Traitement du signal et des images,
Graduate School : Informatique et sciences du numérique,
Référent : CentraleSupélec.

Thèse préparée dans les unités de recherche Électromagnétisme et radar (Université Paris-Saclay, ONERA) , et SONDRA (Université Paris-Saclay, CentraleSupélec, ONERA), sous la direction de **Philippe FORSTER**, Professeur des universités, la co-direction de **Jean-Philippe OVARLEZ**, Directeur de Recherche ONERA, le co-encadrement de **Jonathan BOSSE**, Chargé de Recherche ONERA et de **Olivier RABASTE**, Maître de Recherche ONERA

Thèse soutenue à Paris-Saclay, le 18 décembre 2023, par

Pierre DEVELTER

Composition du jury

Membres du jury avec voix délibérative

Sylvie MARCOS Directrice de recherche CNRS, CentraleSupélec (L2S)	Présidente
Audrey GIREMUS Professeur des Universités, Université de Bordeaux (IMS)	Rapporteur & Examinatrice
Olivier BESSON Professeur, ISAE-SUPAERO	Rapporteur & Examinateur
Guillaume GINOLHAC Professeur des Universités, Université Savoie Mont-Blanc (LISTIC)	Examinateur
Eric CHAUMETTE Professeur, ISAE-SUPAERO	Examinateur

THESE DE DOCTORAT

NNT : 2023UPASG108

université PARIS-SACLAY

ÉCOLE DOCTORALE
Sciences et technologies de l'information et de la communication (STIC)

Titre: Nouveaux traitements radar robustes aux erreurs de modèle : le cas des cibles hors grille
Mots clés: Détection, Radar, Statistiques Robustes, GLRT

Résumé: Le problème de détection d'une cible radar est classiquement représenté par un test d'hypothèse binaire. Quand tous les paramètres sont connus, pour résoudre ce test, on utilise le test du rapport de vraisemblance, optimal au sens de Neyman-Pearson. Cependant, ce cas de figure n'est pas réaliste et en contexte opérationnel, le test d'hypothèse dépendra de plusieurs paramètres inconnus. Une stratégie populaire consiste à introduire les estimateurs du maximum de vraisemblance dans le test de détection: c'est le test du rapport de vraisemblance généralisé (TRVG). Quand les paramètres inconnus sont non linéaires, il n'existe en général pas de forme analytique pour les estimateurs du maximum de vraisemblance. En détection radar, ces paramètres correspondent notamment à la distance et à l'angle de la cible ou à son effet Doppler. La stratégie retenue en pratique consiste à effectuer des tests pour des valeurs de paramètres fixées sur une grille discrète. Cela induit une désadaptation entre les vrais paramètres de cible et les paramètres sous test, qui en retour dégrade les performances de détection du test.

L'objectif de cette thèse est d'étudier l'impact des effets de grille sur la détection radar ainsi que la recherche et l'étude de stratégies à mettre en oeuvre pour le contrer. Une attention particulière est donnée à l'approximation et l'étude des TRVG hors-grille, définis comme les TRVG classiques (Filtre Adapté, Filtre Adapté Normalisé) testés en continu sur l'espace de recherche des paramètres de cibles. Ces détecteurs présentent les meilleures performances de détection connues dans la littérature en présence de cibles hors-grille mais, d'une part, leur statistique est difficile à évaluer, et, d'autre part, une implémentation précise de ces tests en pratique semble coûteuse.

Title: New robust radar processing: the case of off-grid targets
Keywords: Detection, Radar, Robust Statistics, GLRT

Abstract: The problem of detecting a radar target is classically represented by a binary hypothesis test. When all the parameters are known, to solve this test, we use the likelihood ratio test, optimal in the sense of Neyman-Pearson. However, this case is unrealistic and in an operational context, the hypothesis test will depend on several unknown parameters. A popular strategy is to introduce the maximum likelihood estimators in the detection test: this is the generalized likelihood ratio test (GLRT). When the unknown parameters are non-linear, there is no analytical form for the maximum likelihood estimators. In radar detection, these parameters correspond in particular to the distance and angle of the target or to its Doppler effect. The chosen strategy consists of performing tests for parameter values fixed on a discrete grid. This induces a mismatch between the true target parameters and the parameters under test, which in turn degrades the detection performance of the test.

The objective of this thesis is to study the impact of grid effects on radar detection, as well as to research and study strategies to counter them. Particular attention is given to the approximation and study of the off-grid GLRT, defined as the classical GLRT tests (such as the Matched Filter and the Normalized Matched Filter) computed on the continuous parameter space of the target. Those tests present the best detection performance known in the literature in the presence of off-grid targets, but, on the one hand, their statistic is difficult to evaluate, and, on the other hand, a precise implementation of those tests seems intense computationally.

Remerciements

Je tiens avant tout à remercier l'équipe qui m'a encadré pendant ces trois ans: mon directeur de thèse Philippe Forster, mon co-directeur de thèse Jean-Philippe Ovarlez et mes encadrants Jonathan Bosse et Olivier Rabaste. Merci à tous pour votre accessibilité et votre présence durant ces 3 ans ! Merci Jonathan pour les nombreux échanges que nous avons eus au quotidien, techniques ou cinéma. Merci également Olivier pour toutes les discussions que nous avons eues et ta grande disponibilité, et pour tout le coquille-proofing durant la rédaction... Merci aussi à toi Jean-Phi pour tous tes conseils scientifiques mais aussi administratifs, ce qui n'est pas à négliger pour un thésard lâché dans le monde de la recherche. J'irai à l'Initial bientôt, peut-être qu'on s'y croisera ! Et puis enfin merci à Philippe pour l'aide mathématique généreuse et absolument inestimable que tu m'as apportée tout au long de cette thèse, en particulier sur le chapitre 2. J'espère avoir l'occasion de retravailler avec vous bientôt !

Je souhaite maintenant remercier les membres du Jury pour avoir accepté d'évaluer mon travail. Merci aux rapporteurs Olivier Besson et Audrey Giremus d'avoir accepté de relire ce manuscrit légèrement technique, et merci à Sylvie Marcos, Eric Chaumette et à Guillaume Ginolhac : vos questions pertinentes lors de la soutenance ont mené à des discussions constructives.

Merci à mes collègues de MATS pour leur accueil chaleureux. Je pense en premier lieu à mes confrères de galère: les doctorants. Huy, Anthony, ça sera votre tour plus ou moins bientôt et je vous souhaite une très belle soutenance ! Merci Mariliza, Julien et Agustin pour votre mentorat ! Merci également à Abi, Dodo, Gilles, Christèle, Christian, Marc, Eugénie et David pour les bons moments passés à midi. Je tiens enfin à remercier Milan Rozel de l'unité RMES de m'avoir fourni les données HYCAM ainsi que du code pour les parser, et d'avoir eu la gentillesse de me les expliquer en détails.

Je n'oublie bien sûr pas SONDRA: j'aurais aimé pouvoir venir plus, mais chaque passage hebdomadaire était toujours très agréable grâce à la super ambiance qui règne au labo. Merci à tous pour les bons moments passés ensemble, en particulier aux doctorants de la team ICASSP/GRETSI : Cyprien, Max, Yanisse, Hugo et Antoine, et à Stéphane, Isabelle et Virginie pour leur aide administrative. Merci aussi aux membres du DSO pour leur intérêt pour mes travaux.

Merci enfin à ma famille, qui m'a encouragé dès le départ dans mon choix de faire une thèse, à mes amis, avec qui les sorties à l'imprévu m'ont aidé à tenir dans la durée, et à toi Aurore pour le soutien moral que tu m'as apporté entre Rennes, Paris et Lisbonne, en particulier lors de l'écriture du manuscrit.

Contents

List of Figures

List of Tables

List of abbreviations and notations

List of abbreviations

- ALRT: Average Likelihood Ratio Test
- CES: Complex Elliptically Symmetric
- CFAR: Constant False Alarm Rate
- DOA: Direction of Arrival
- ecdf: Empirical Cumulative Distribution Function
- FFT: Fast Fourier Transform
- FMCW: Frequency Modulated Continuous Waveform
- GLRT: Generalized Likelihood Ratio Test
- LRT: Likelihood Ratio Test
- MF: Matched Filter
- MLE: Maximum Likelihood Estimator
- NMF: Normalized Matched Filter
- ONERA: Office National d'Etudes et de Recherche Aérospatiale
- pdf: Probability Density Function
- P_D: Probability of Detection
- P_{FA}: Probability of False Alarm
- PRI: Pulse Repetition Interval
- RADAR: RAdio Detection And Ranging
- SIRV: Spherically Invariant Random Vector
- SNR: Signal to Noise Ratio
- STAP: Space-Time Adaptive Processing

List of notations

- Matrices are in bold and capital, vectors in bold. For any matrix $\mathbf{A}$ or vector, $\mathbf{A}^T$ is the transpose of $\mathbf{A}$ and $\mathbf{A}^H$ is the Hermitian transpose of $\mathbf{A}$.
- $\mathbf{I}$ is the identity matrix.
- $\mathbf{J}$ is the exchange matrix.
- $\mathcal{CN}(\boldsymbol{\mu}, \mathbf{R})$ is the circular complex Normal distribution of mean $\boldsymbol{\mu}$ and covariance matrix $\mathbf{R}$, of the form $\mathbf{R} = \sigma^2\mathbf{\Gamma}$.
- χ^2_2 is the centered chi-squared distribution.

- $\triangleq$ is a symbol used to define a quantity.
- $\odot$ is the Hadamard (element-wise) product.
- $\otimes$ is the Kronecker product.
- $\underset{\mathrm{H_0}}{\overset{\mathrm{H_1}}{\gtrless}}$ is a comparison operator used in hypothesis tests and means that if the left operand is higher than the right operand, hypothesis H_1 is chosen, and otherwise hypothesis H_0 is chosen.
- $\mathbb{R}$ is the set of real numbers.
- $\mathbb{C}$ is the set of complex numbers.
- * indicates complex conjugation.
- $\dot{f}(.)$ is used to indicate differentiation for functions of a single parameter.
- $\varphi(.)$ is the Euler characteristic of a set.
- $\mathbb{S}^{n-1}$ is the unit sphere in $\mathbb{R}^n$.
- The real and imaginary part operators of a complex number are denoted by $\mathrm{Re}(.)$ and $\mathrm{Im}(.)$.
- The operator $\angle u$ is the angle of a complex number u.
- $\Gamma(.)$ is the gamma function.
- $P(.)$ is the probability of a random event.
- $E(.)$ is the esperancy of random variables.
- $|.|$ is the absolute value of complex numbers.
- $\|.\|$ denotes the classical l_2 norm for vectors.

Introduction

Context and objectives

Since the middle of the 20th century, Radar systems have widely been used in both military and civil contexts in order to detect and track targets. The radar principle is well-known: it emits an electromagnetic wave toward a scene, and, if any target is present in the scene, the signal sent by the radar is reflected by the target. The target will then be detected by the radar, which can proceed to estimate the target parameters and track the target.

The use of signal processing is necessary in order to translate this physical principle into a working system: indeed, without any instantaneous processing, the signal returned energy is well below that of the ambient noise of the radar sensor. Detection theory intervenes in the first stage of the radar processing chain. It aims to provide detection tests that can be used to discriminate incoming echo signals from ambient noise or returns from static elements of the scene while limiting the probability of false alarms (P_{FA}) through the choice of an adequate threshold. The most common procedure is the Generalized Likelihood Ratio Test (GLRT), which consists of replacing the unknown parameters of the expected signal with their Maximum Likelihood Estimates (MLE) in the likelihood ratio. However, closed forms for the MLE of unknown parameters do not always exist. In particular, this is the case for the range, Doppler shift, and direction of arrival of radar targets. In this case, the classical solution consists of discretizing the search space of the unknown parameters as a fixed, discrete grid, often designed to have statistically independent tests. Detection tests are then run for each of the hypotheses in the grid. Under the assumption that the target parameters lie on the grid, the GLRT detectors admit closed-form solutions, making theoretical analysis easier. As a result, those "on-grid" detectors have well-known P_{FA}-threshold relationships. Of course, in practice, the true target parameters will never be exactly aligned with the tested parameters. This mismatch between the true and tested parameters will in return create a degradation of the detection performance of the classical detectors:

- The Matched Filter is the GLRT derived when supposing every parameter of the signal model is known except the amplitude of the target. The impact of off-grid targets on the Matched Filter is well-known: it creates, in the worst-case scenario, the equivalent of a 3dB loss on the Signal to Noise Ratio (SNR) per unknown parameter.
- The Normalized Matched Filter is the GLRT derived when supposing every parameter of the signal model is known except the amplitude of the target and the power level of the noise. The impact of the off-grid mismatch is much more dramatic: when a moderate (< 30) number of samples is used, the mean probability of detection of the Normalized Matched Filter does not converge to 1 with SNR when target parameters are uniformly distributed.

In order to fight off this off-grid mismatch, several solutions are considered in the literature:

- The detection problem can also be considered as a sparse reconstruction problem (where the sparsity comes from the low number of targets in the scene), for which the impact of a mismatch between the reconstruction dictionary and the true signal components is well documented [Str12; ZLG11]. Proposed solutions range from a refinement of the dictionary [FL12; SB11b] or the introduction of a linear perturbation on the dictionary to model the impact of the off-grid mismatch [ZLG11; Las+15]. However, the algorithms for sparse reconstruction make it delicate to control the Probability of a False Alarm [Ani+12], which is very important in radar applications.
- Practical radar approaches consist of the usage of an apodization window to flatten the main lobe

response of the detectors [Ric+10], at the cost of a loss in SNR and the introduction of a noise correlation at the output, or an oversampling of the grid, which increases the probability of detection but also increases the computational burden.

- In detection theory, the detection under a general mismatched signal model has been formalized to allow for the robust detection of a received signal that is mismatched with respect to the expected signal [BOR09; De 05; Bes06; De +10b; BBR07; KS95]. However, the methods introduced are not always suited for treating the case of the off-grid mismatch [BRO20]. A common approach that is more tailored for the off-grid mismatch consists of merging the detection step with the estimation of the target parameters in the radar processing chain: this procedure is commonly referred to as "joint detection and estimation" [GCL10; Aub+20; Xin+11]. The unknown parameter is estimated (not necessarily in the MLE sense), often through a first-order approximation of the radar signal, and is then injected into a detection test.

During this thesis, we focus on what we call the "off-grid" GLRT, obtained when searching for the maximum of the classical GLRT tests over the whole, continuous parameter space. It corresponds to an infinite oversampling of the GLRT tests. This solution presents the advantage of usually giving the best P_D for a given P_{FA}. While very simple in principle, the use of those detectors raises several challenges, because no closed-form are available:

- On the one hand, they are hard to analyze theoretically, and very few articles in the signal processing literature offer a theoretical study. In particular, the computation of their statistic under the null hypothesis is much more involved than when the target parameters are supposed known. As a result, their P_{FA}-threshold relationship is, to the best of our knowledge, unknown in the literature, barring some special cases [Hay03; Lei+20].
- On the other hand, a naive implementation of those detectors requires a large number of tests made on a finely oversampled grid. This greatly increases the computational load, making this solution difficult to use in operational contexts.

This thesis thus mostly focuses on addressing the aforementioned issues of the off-grid GLRT: we aim to derive the P_{FA}-threshold relationships of the considered detectors for various signal models and search low computational methods to approximate them without unduly degrading the probability of detection. Specifically, we will focus on the off-grid GLRT deriving from the Matched Filter and the Normalized Matched Filter, which are the most used radar detection tests.

Outline

The outline of the thesis is as follows:

- In chapter 1, we first review the basis of radar systems, introducing the signal models that will be used in this document. We then focus on detection theory, presenting the radar detection problem as a binary hypothesis test. The basic Matched Filter and Normalized Matched Filter GLRT detectors that are used to deal with the most common detection problems are then presented. After this, we introduce the concepts of detection under mismatched signal models. The problem of off-grid targets and how the previously introduced detectors react to them are natural developments, which leads to the presentation of the off-grid GLRT. Those detectors are the main point of focus of this thesis.
- In chapter 2, we aim to address the problem of fixing the threshold guaranteeing a given probability of false alarm when using the off-grid Normalized Matched Filter. The treatment of this problem

is mostly geometric: only the uniform distribution of the noise over the sphere is used, and the reasoning thus works when the noise follows a Gaussian or a Complex Elliptically Symmetric distribution. We first show that computing this relationship reduces to a geometrical computation. Specifically, it reduces to computing the volume of a tube around the manifold defined by the signal model in a cell embedded in the unit sphere. We thus introduce some tools from the volume of tube theory, before applying them to derive the probability of false alarm-threshold relationships for the Normalized Matched Filter with one or two unknown parameters. Those relationships are only exact as long as the tubes do not self-overlap. We then extensively discuss the condition of validity of those relationships, finding limit thresholds, before evaluating the P_{FA}-threshold relationships numerically, which shows that our theoretical relationships fit very well with what can be observed empirically.

$\rightarrow$ **Contributions:**

- An alternate new proof for the derivation of the P_{FA} of the Normalized Matched Filter in section 2.3.1 [Dev+23b].
- The derivation of a P_{FA}-threshold relationship for the off-grid Normalized Matched Filter with one unknown parameter (range, Doppler or angle using a chirp or FMCW waveform) in equation (2.33) under white noise, and in equation (2.32) under colored noise [Dev+22a; Dev+22b].
- The derivation of a P_{FA}-threshold relationship for the off-grid Normalized Matched Filter with two unknown parameters (Doppler-angle or range-Doppler using FMCW radar) over the whole domain (in equation (2.36) under white noise, or in equation (2.40) under colored noise), heuristic in the case of detection over a single cell (in equation (2.37) under white noise, or in equation (2.41) under colored noise).
- The derivation of the domain of validity of those relationships in section 2.4 [Dev+23b].

- In chapter 3, we deal with the same issue of fixing the probability of false alarm but for the off-grid Matched Filter. The treatment of this problem is this time statistical and the methods used rely on the Gaussian nature of the noise. The off-grid Matched Filter test quantity is modeled as a random field, and its P_{FA}-threshold relationship is shown to be asymptotically equal to the expected Euler characteristic of its excursion sets. We define those notions, before deriving asymptotic P_{FA}-threshold relationships under white noise. Those relationships are then given for more general contexts (with a degraded asymptotic order). We discuss the links between the method of the chapter and the volume of tubes method of chapter 2. The P_{FA}-threshold relationships are finally evaluated numerically. Again, it is shown that those asymptotic relationships fit very well with what is observed in simulations.

  $\rightarrow$ **Contributions** [Dev+23a; Dev+23c]:

  - The derivation of an asymptotic P_{FA}-threshold relationship for the off-grid Matched Filter with one unknown parameter (Doppler, Angle or range using FMCW radar) under white noise in equation (3.13), and derivation of a relationship with a higher asymptotic order for colored Gaussian noise or chirp waveform detection in equation (3.15).
  - The derivation of an asymptotic P_{FA}-threshold relationship for the off-grid Matched Filter with two unknown parameters (Doppler and Angle or range and Doppler using FMCW radar) under white noise in equation (3.14), and derivation of a relationship with a higher asymptotic order for colored Gaussian noise or chirp waveform detection in equation (3.15).

- After those theoretical developments, chapter 4 aims to approximate the off-grid detectors in practice. We start off by showing that just oversampling the grid is not an entirely satisfying solution

for the Normalized Matched Filter, because the mean P_D still does not converge to 1 with SNR for some highly correlated noise distribution. Then, we review the techniques developed in joint detection and estimation literature to propose detectors approximating the off-grid GLRT. One of them is based on the interpolation of the main Fourier transform lobe, while the other is inspired by monopulse technique. Their performance is evaluated through simulations. We show that their P_{FA}-threshold relationship is well approximated by the relationships found in chapter 2, and that their P_D is very close to that of the GLRT. Then, we finish this thesis with experimentation on real data from ONERA's HYCAM radar. We highlight the effects of off-grid targets by showing that the Normalized Matched Filter does not detect all targets even at very high SNR, and we implement the previously studied approximations of the off-grid detectors. It is shown that the interpolation-based detector as well as the monopulse-inspired one perform well, outperforming the NMF oversampled by a factor of 2.
$\rightarrow$ **Contributions**:

  - The proposition of detectors modeled by equations (4.6), (4.7) to approximate the off-grid Normalized Matched Filter with low computational cost [Dev+21].
  - The test of those detectors in simulations and against real data from ONERA's HYCAM radar.

- Finally, the conclusion reminds the developments that have been realized in the thesis and proposes some search avenues that could be investigated in the future.

Publications

The findings of this thesis have led to several publications and presentations at conferences:

- **Peer reviewed journals**

  - P. Develter, J. Bosse, O. Rabaste, P. Forster and J.-P. Ovarlez, On the False Alarm Probability of the Normalized Matched Filter for off-grid targets: A geometrical approach and its validity conditions, accepted for publication in IEEE Transactions on Signal Processing.

- **International conferences with proceedings**

  - P. Develter, J. Bosse, O. Rabaste, P. Forster and J.-P. Ovarlez, "False Alarm Regulation for Off-Grid Target Detection With The Matched Filter," ICASSP 2023 - 2023 IEEE International Conference on Acoustics, Speech and Signal Processing (ICASSP), Rhodes Island, Greece, 2023, pp. 1-5.
  - P. Develter, J. Bosse, O. Rabaste, P. Forster and J.-P. Ovarlez, "On the False Alarm Probability of the Normalized Matched Filter for Off-Grid Target Detection," ICASSP 2022 - 2022 IEEE International Conference on Acoustics, Speech and Signal Processing (ICASSP), Singapore, Singapore, 2022, pp. 5782-5786.
  - P. Develter, J. Bosse, O. Rabaste, P. Forster and J.-P. Ovarlez, "Off-Grid Radar Target Detection with the Normalized Matched Filter: A Monopulse-Based Detection Scheme," 2021 IEEE Statistical Signal Processing Workshop (SSP), Rio de Janeiro, Brazil, 2021, pp. 226-230.

- **National conferences with proceedings**

  - Pierre Develter, Jonathan Bosse, Olivier Rabaste, Philippe Forster, Jean-Philippe Ovarlez. Sur la probabilité de fausse alarme du Filtre Adapté pour la détection distance-Doppler de cibles hors-grille. GRETSI 2023, Sep 2023, Grenoble, France.

- Pierre Develter, Jonathan Bosse, Olivier Rabaste, Philippe Forster, Jean-Philippe Ovarlez. Sur la probabilité de fausse alarme du Filtre Adapté Normalisé pour la détection de cibles hors-grille. GRETSI 2022, Sep 2022, Nancy, France.

- **Workshops**
  - Presentation of the thesis work to the 4th SLSIP Workshop, Cadaquès, 2022
  - Presentation of the thesis work to the 5th SONDRA Workshop, Avignon, 2022

1 - Basic Radar Detection Theory and the problem of off-grid targets

This chapter presents the basic concepts of radar detection theory before introducing the issue of detection under mismatched signal models. Our off-grid target problem, which fits into this context, is then presented, as well as state-of-the-art solutions to it. The results and proofs therein are well-known in the signal processing literature.

In Section 1.1, we give a brief introduction to how radar systems work and of the signals encountered when dealing with radars. In Section 1.2, we present the formalization of the radar detection problem as a binary Hypothesis test. We show how to solve this composite Hypothesis test with the Generalized Likelihood Ratio Test in Section 1.3 where we also present the most common detectors. In Section 1.4, we show how to extend the detection test to take into account mismatched signal models. The off-grid mismatch is presented in Section 1.5, as well as the state-of-the-art solutions to deal with it. In Section 1.6, we present the off-grid GLRTs that are currently the detectors with the best probability of detection in the presence of off-grid targets.

1.1 . Introduction to Radar

This section is meant to give the reader all of the basic radar knowledge and models that we will reference in this document. Section 1.1.1 gives a quick overview of the radar principles and the operations it performs. Section 1.1.2 introduces the waveforms and signal models we will use in this document. Section 1.1.3 introduces the reader to the noise models of this thesis and the main ideas of statistical signal detection.

1.1.1 . Basic principles of radar systems

A Radar (RAdio Detection and Ranging) is a system that primarily aims to detect and track targets and estimate their range, velocity, and direction of arrival via the emission of electromagnetic waves.

Detection is the first step in the classical radar processing chain. It is usually followed by a refined estimation of the target parameters, and then a tracking phase, as represented in Figure 1.1. This thesis focuses on the detection step. The basic detection principle is the following: the radar emits an electromagnetic wave (a waveform with desirable properties multiplied by a carrier of frequency f_0) toward a scene, then listens if it receives any echo of the emitted signal. If this is the case, a target is present in the scene. This principle is illustrated in Figure 1.2.

This principle also enables the radar to get the distance of the target from the radar. Indeed, the distance d of the target to the radar is equal to the roundtrip delay r multiplied by the velocity of the wave c divided by 2:

$$d = \frac{c\,r}{2}\,.$$

To retrieve the radial velocity from targets and to distinguish two targets located in the same range bin or discriminate targets from the static environment, radars can take advantage of the Doppler effect to perform distance-doppler detection by measuring f_d , the frequency shift in time of the carrier frequency f_0, linked to the speed v with:

$$f_d \approx \frac{2\,v}{c}\,f_0\,, \tag{1.1}$$

Monostatic radars perform both the emission and the reception of the signal, and cannot emit and listen to the returns from the scene at the same time. In order not to leave a scene unchecked for too long, they emit several pulses toward the scene.

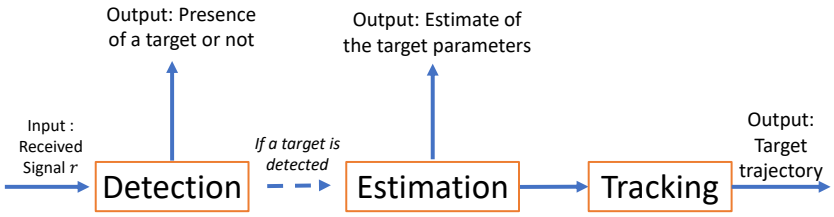

Figure 1.1: The classical Radar processing chain.

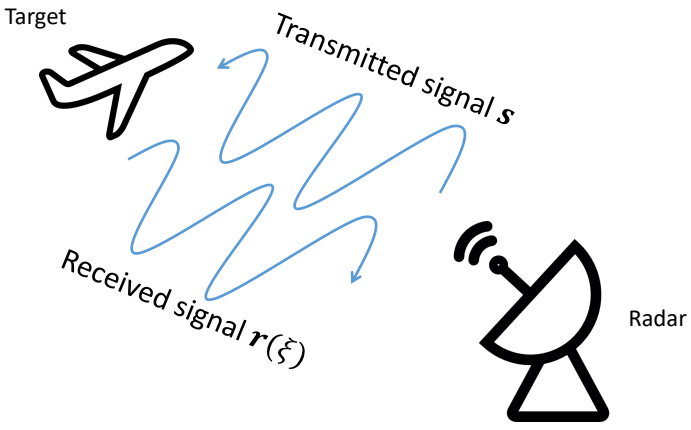

Figure 1.2: Illustration of the basic Radar mechanism

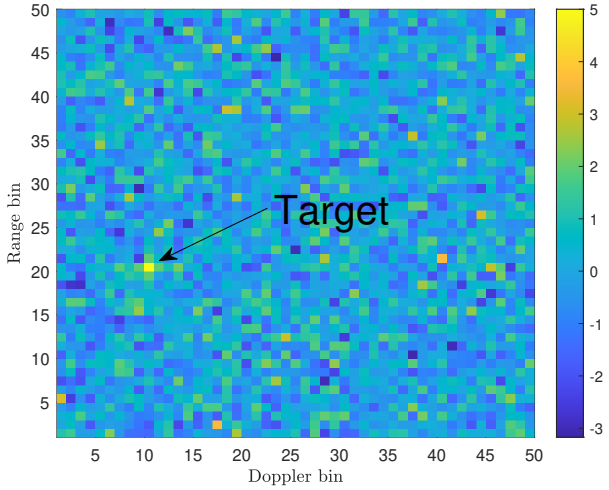

Figure 1.3: An example of a Range-Doppler map. A target has been injected in the 20th range bin, 10th Doppler bin.

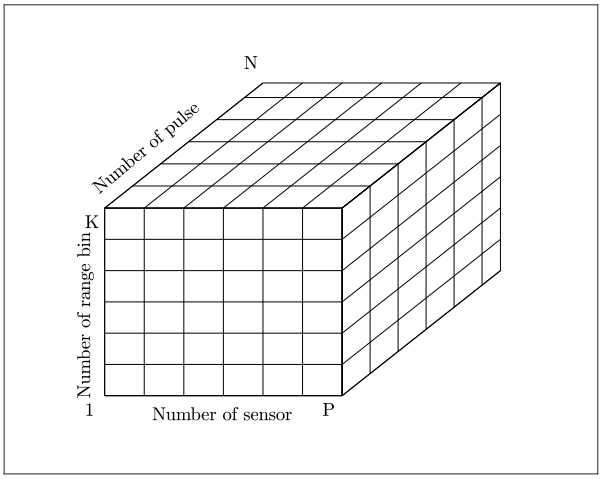

Figure 1.4: The "data cube" formed by samples of the received signal after the emission of N pulses with M sensors, and K range bins [Ric+10].

After processing, the data of a slice is often represented as a Range-Doppler map as in Figure 1.3, where the x-axis and y-axis correspond, respectively, to different Doppler and distance bins. High energy points, in yellow on the figure, will be considered as targets if their energy exceeds a certain threshold. The inputs from several sensors can also be combined to detect a target more reliably. In this case, the direction of arrival of the target can be deduced from the data. The received signal is often represented as stored in a data cube as represented in Figure 1.4, and Doppler-Angle detection, usually called Space-Time Adaptive Detection (STAP), is performed on each horizontal slice.

1.1.2 . Signal model

The signal received by the radar from a scene with L targets can be written:

$$y(t) = \sum_{i=1}^{L} \alpha_i x(t - r_i) + n(t)\,,$$

where α_i is the complex amplitude of the i-th target, r_i is its delay, x is the transmitted waveform after demodulation and $n(t)$ is a perturbation coming from thermal noise and clutter. In this section, we focus on the case $L = 1$ and we present the signal models used throughout this thesis, neglecting the noise $n(t)$ for the time being.

We note $b(t)$ the used waveform and f_0 the carrier frequency, so that

$$\begin{aligned} x(t - r) &= b(t - r)e^{2i\pi f_0(t-r)}e^{-2i\pi f_0 t} \\ &= b(t - r)e^{-2i\pi f_0 r}\,. \end{aligned}$$

If the target moves at speed v toward the receiver, the delay $r(t)$ at which the signal is received depends on the time t, according to [Le 02; Tan19]:

$$r(t) = \frac{2\,d(t - r(t)/2)}{c}\,.$$

where $d(t)$ is the distance of the target from the radar. For a target with uniform radial velocity, $d(t) = d_0 - vt$, so that:

$$r(t) = \frac{2\,d_0/c}{1 - v/c} - \frac{2vt/c}{1 - v/c}\,.$$

The received signal after demodulation is then,

$$\begin{aligned} y(t) &= \alpha\, x(t - r(t)) \\ &= \alpha\, x\left(t\left(1 + \frac{2v/c}{1 - v/c}\right) - \frac{2\, d_0/c}{1 - v/c}\right) \\ &= \alpha\, b\left(t\left(1 + \frac{2v/c}{1 - v/c}\right) - \frac{2\, d_0/c}{1 - v/c}\right) e^{2i\pi f_0\left(\frac{2vt/c}{1-v/c} - \frac{2\, d_0/c}{1-v/c}\right)} . \end{aligned} \tag{1.2}$$

Typically in a radar setting, $v << c$, so that $1 + \frac{2v/c}{1 - v/c} \approx 1$ and

$$b\left(t\left(1 + \frac{2v/c}{1 - v/c}\right) - \frac{2\, d_0/c}{1 - v/c}\right) \approx b\left(t - \frac{2d_0/c}{1 - v/c}\right) .$$

After putting the constant term $e^{-2i\pi f_0 \frac{2d_0/c}{1-v/c}}$ in the complex amplitude α, the received signal reads:

$$y(t) \approx \alpha\, b\left(t - \frac{2d_0/c}{1 - v/c}\right) e^{2i\pi f_0 t \frac{2v/c}{1-v/c}} . \tag{1.3}$$

Since $\frac{v/c}{1 - v/c} \approx \frac{v}{c}$, we can write, with f_d defined as in (1.1):

$$y(t) \approx \alpha\, b\left(t - \frac{2d_0/c}{1 - v/c}\right) e^{2i\pi t f_d} . \tag{1.4}$$

The most used radar waveform is a linear chirp taking the form:

$$b(t) = \Pi_{T_p}(t) e^{i\pi h t^2} ,$$

where $\Pi_{T_P}(.)$ is the rectangular function of length T_P and h is a constant related to the bandwidth B of the chirp through the expression:

$$B = h\, T_P .$$

Assuming that the term $e^{2i\pi t f_d}$ can be considered constant over the duration T_P of the chirp, it can be approximated as the simple phase term $e^{2i\pi f_d t_0}$ and put in the phase term α. The normalized sampled vector $\mathbf{b}(r)$ obtained at instants $t_k = \frac{k}{B}$ (Shannon criteria) to model the received signal when performing range detection is thus, noting K the number of non-zero coefficients:

$$(\mathbf{b}(r))_{0 \le k \le K-1} = \frac{1}{\sqrt{K}} \Pi_{T_p}(k/B - r) e^{i\pi h (k/B - r)^2} . \tag{1.5}$$

Remark 1.1.1. *The range resolution, i.e. the ability to separate the echoes from two distinct targets, increases with the bandwidth B, according to*

$$\Delta_{\text{range}} = \frac{c}{2B} . \tag{1.6}$$

Using a pulse of finite duration modulated by a simple cosine signal, the range resolution is inversely proportional to the duration of the signal. However, decreasing the duration of the signal decreases the transmitted energy and thus reduces the detection performance. This is why the chirp waveform, for which the bandwidth is set as needed without impacting the duration of the signal, is often preferred.

In practice, often, to better characterize the Doppler shift of a target, several pulses are sent toward the scene, regularly spaced by the *pulse repetition interval* T_{PRI}, as schematized in Figure 1.5. While the

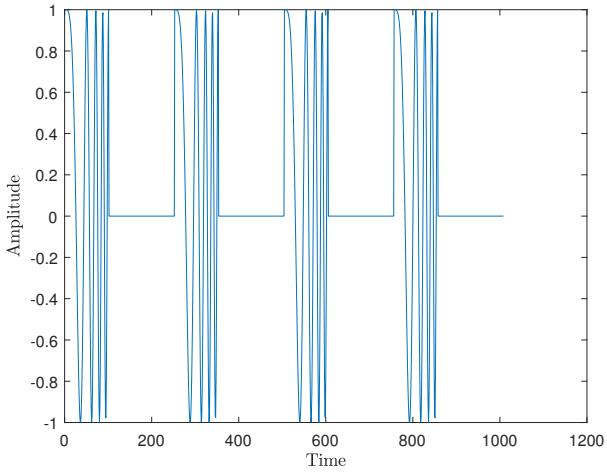

Figure 1.5: Example of a burst of 4 chirp pulses (real part).

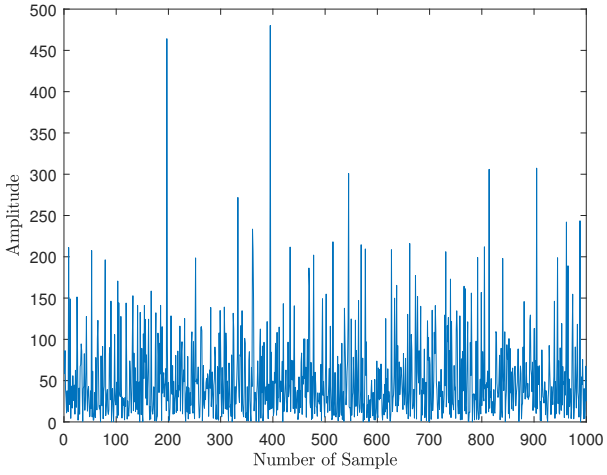

Figure 1.6: Square amplitude of a complex sinusoid embedded in noise, $SNR = -40dB$

term $e^{2i\pi t f_d}$ in (1.4) can be considered as constant over the duration of a pulse, it varies noticeably from pulse to pulse. Noting $\theta = T_{PRI} f_d$ the normalized Doppler Shift, the Fourier *steering vector* representing the change of the phase from pulse to pulse is the following:

$$(\mathbf{d}(\theta))_{0 \leq p \leq N-1} = \frac{1}{\sqrt{N}} e^{2i\pi p\theta} . \tag{1.7}$$

So that when performing distance-Doppler detection, the signal received from all pulses reshaped in a single vector is the following:

$$\mathbf{s}(r, \theta) = \mathbf{b}(r) \otimes \mathbf{d}(\theta) . \tag{1.8}$$

Remark 1.1.2. *The Doppler resolution, i.e. the minimum Doppler frequency difference to separate two targets, increases with the total emission time, given by NT_{PRI}, with:*

$$\Delta_{\text{Doppler}} = \frac{1}{NT_{PRI}} . \tag{1.9}$$

As mentioned before, it is also possible to combine the inputs from several sensors for detection, which enables the radar to retrieve the angle information of the target. This situation is represented in Figure 1.7. Sensors are aligned and separated by distance d. Furthermore, the target is supposed to be far enough so that the angle that the target-to-sensor line makes with the sensor axis can be assumed constant. Then, it can be seen that the additional distance $d\varphi$ that the emitted wave travels from and to sensor S_1 in comparison to S_2 is:

$$d\varphi = d \cos \varsigma .$$

There is thus a linear shift in the received signal phase from sensor to sensor that is proportional to $\mu = d \cos \varsigma$. The vector $\mathbf{d}(\mu)$ defined in (1.7) also accounts for those phase shifts and is a signal model that can be used to perform angle detection. When combining the angle and Doppler information, the received signal model for performing STAP detection is, considering range pulse compression has already been performed analogically:

$$\mathbf{s}'(\theta, \mu) = \mathbf{d}(\theta) \otimes \mathbf{d}(\mu) , \tag{1.10}$$

where the dimension of $\mathbf{d}(\mu)$ may differ from that of $\mathbf{d}(\theta)$. In this document, P will denote the number of sensors. Retrieving the phase shift immediately allows us to deduce the direction of arrival (DOA) ς of the target.

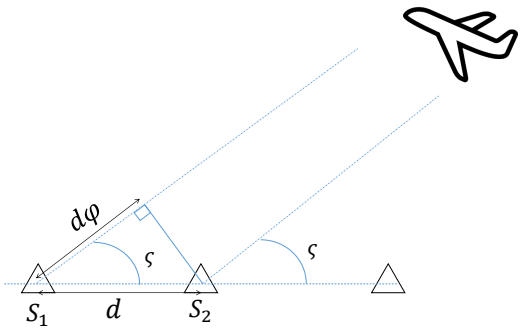

Figure 1.7: Sensor array principle

Remark 1.1.3. *In the following, we will always use the simple notation* $\mathbf{s}(\boldsymbol{\xi})$ *for the signal to be detected, where* $\boldsymbol{\xi}$ *can represent one or several parameters. When needed (e.g. for the sake of giving closed form formula), the signal model (either* (1.5) *for range detection,* (1.7) *for Doppler detection,* (1.8) *for distance-Doppler detection or* (1.10) *for STAP detection) will be specified.*

Alternatively to the chirp, during this thesis, we will also often consider the case of *Frequency Modulated Continuous Waveform* (FMCW). In this case, the transmitted waveform also has a linear instant frequency but is repeated continuously ($T_{PRI} = T_P$), so that the transmitted ($x(t)$) and received demodulated signal ($y(t)$) are, assuming here that the term $e^{2i\pi t f_d}$ is approximately constant and put in the phase α:

$$\begin{aligned} x(t) &= e^{i\pi h t^2}\,, \\ y(t) &= \alpha\, e^{i\pi h (t-r)^2}\,. \end{aligned}$$

In order to benefit from the low computational cost of the FFT algorithm (cf Remark 1.3.3) when performing FMCW detection, the received signal is usually multiplied analogically by the emitted signal before sampling, forming what is called the beat signal. The signal after this operation is, up to a constant complex factor, equal to:

$$\begin{aligned} c(t) &= x(t)^* y(t)\,, \\ &= e^{-2i\pi h t r}\,. \end{aligned}$$

When sampling at rate $\dfrac{1}{B}$, defining the normalized delay τ as

$$\tau = r\,\frac{h}{B}\,,$$

the received normalized sampled signal at instants $t_k = \dfrac{k}{B}$ reads:

$$\left(\mathbf{c}(\tau)\right)_{0<k<K-1} = \frac{1}{\sqrt{K}} e^{-2i\pi k\tau}\,, \tag{1.11}$$

which is a steering vector akin to (1.7). We can also define a distance-Doppler signal model using FMCW as:

$$\mathbf{s}(\tau,\theta) = \mathbf{c}(\tau) \otimes \mathbf{d}(\theta)\,, \tag{1.12}$$

which is akin to (1.8). The results that we will find for Doppler or distance-Doppler detection using a chirp, with signal models (1.7) and (1.8) can be extended to the FMCW signal model with only small adjustments.

1.1.3 . Noise models and statistical signal detection

In practice, detecting an echo of a target is not a trivial task as the receiving channel is always polluted by thermal noise which comes from the receptor and is unavoidable, and clutter, which is the signature of non-relevant elements in the scene (i.e. ground, trees, buildings). In order to model those random elements in the received signal, we will use the following random distributions in this thesis:

- The centered complex circular Gaussian distribution, denoted $\mathcal{CN}$. The pdf $f_{\mathcal{CN}(\mathbf{0},\mathbf{R})}$ of this distribution with a covariance matrix $\mathbf{R}$ reads:

$$f_{\mathcal{CN}(0,\mathbf{R})}(\mathbf{x}) = \frac{1}{\pi^N \det \mathbf{R}} e^{-\mathbf{x}^H \mathbf{R}^{-1} \mathbf{x}}, \tag{1.13}$$

  Note that this noise distribution is spherically invariant, meaning that random variables X following this distribution are distributed as the variables $e^{i\phi}X$, for any $\phi \in [0, 2\pi]$. Furthermore, in the case of a white noise ($\mathbf{R} = \sigma^2\mathbf{I}$), the projection on the sphere of a vector following this distribution is uniformly distributed.

- The family of Complex Elliptically Symmetric (CES) distributions (sometimes also called Spherically Invariant Random Vector (SIRV) distributions) [Oll+12]. A vector $\mathbf{n}_{CES}$ following a CES distribution can be decomposed in the following way:

$$\mathbf{n}_{CES} = \Theta \mathbf{n}_{CN},$$

  where $\mathbf{n}_{CN}$ follows a centered circular complex Gaussian noise distribution, and Θ is a scalar real random variable, which represents the texture parameter that follows some scalar distribution. Common examples of CES distributions include K-distributions when Θ follows a Gamma distribution, or Weibull distributions, for which the distribution of the texture cannot be characterized under a simple analytical form. CES distributions are covered extensively in [Jay02, Chapter 2].

Thermal noise is well represented by a centered white complex circular Gaussian distribution. Clutter is often more accurately represented by textured colored noise such as CES (complex elliptically symmetric) distributions, especially when it is impulsive (e.g. waves in marine context [WTW07]). How much an echo signal is polluted by noise is quantified by the *Signal to Noise Ratio* (SNR), which depends on the target reflectivity or distance to the radar, among other factors. Before any processing, a signal may look like the one seen in Figure 1.6. In addition to the noise, the task of detecting echoes is also made harder by the fact that the searched incoming signal is not known perfectly. This is due to many factors: for example, how the incident signal reflects on the target depends on its materials and its shape, which in return modify the incoming signal amplitude. Additionally, the distance of the target to the radar will also modify the amplitude of the signal as well as its phase.

Because of all this, even after processing the signal through detectors, statistical objects that aim to discriminate useful signal from noise, incoming echoes will not always be detected by the radar. The *Probability of Detection* (P_D) quantifies the ability of the radar system to detect targets. Having a large P_D is desirable, but increasing the P_D will tend to increase the tendency of the radar to detect echoes when the received signal is only constituted of noise. This tendency is quantified by the *Probability of False Alarm* (P_{FA}), which is ideally as low as possible. Controlling the P_{FA} is of utmost importance in radar detection in order to make decisions. Statistical detection theory is detailed in the rest of the chapter.

1.2 . Formalization of the detection problem

The detection of a single target embedded in noise described in the previous section is widespread, appears in many contexts other than radar, and is addressed by furnished literature [Kay09; SD91]. It is

		Ground Truth	
		No target	**Target**
Chosen Hypothesis	$\mathbf{H_0}$	True Negative	Missed Detection
	$\mathbf{H_1}$	False Alarm	True Detection

Table 1.1: Possible outcomes of the Hypothesis Test

classically modeled as the following binary hypothesis test:

$$\begin{cases} H_0 : \mathbf{r} = \mathbf{n}\,, \\ H_1 : \mathbf{r} = \alpha\,\mathbf{s}(\boldsymbol{\xi}) + \mathbf{n}\,, \end{cases} \tag{1.14}$$

where, in our radar context:

- $\mathbf{r} \in \mathbb{C}^N$ is the sampled received complex signal, that can be raw or preprocessed with an analogic range matched filter;
- $\mathbf{s}(\boldsymbol{\xi}) \in \mathbb{C}^N$ is the signal reflected by the target of parameters $\boldsymbol{\xi}$:
  - When $\boldsymbol{\xi}$ is equal to the scalar Doppler shift θ or to the Doppler and direction of arrival tuple (θ, μ), an analogical range matched filter may have been performed, and $\mathbf{s}$ corresponds respectilvely to signal model (1.7) or (1.10). This is less and less the case with modern numerical radars.
  - When $\boldsymbol{\xi}$ is equal to the range τ, $\mathbf{s}$ is modeled by either signal model (1.5) if a chirp waveform is used, or (1.7) in the case of FMCW detection.
  - When $\boldsymbol{\xi}$ is equal to the range and Doppler tuple (τ, θ), $\mathbf{s}$ is modeled by (1.8) when a chirp waveform is used or (1.10) for FMCW distance-Doppler detection.
- $\mathbf{n} \in \mathbb{C}^N$ models the noise and, optionally, the clutter;
- $\alpha \in \mathbb{C}$ is the complex amplitude of the target.

The dimension N of the signal is the number of collected samples: for Doppler detection, it usually corresponds to the number of transmitted pulses. For angle detection, it usually corresponds to the number of sensors. Hypothesis H_0 is called the null hypothesis, and corresponds to the case where no target is present in the scene. On the contrary, the hypothesis H_1 corresponds to the case where a target with parameters $\boldsymbol{\xi}$ is present in the scene. For a given received signal $\mathbf{r}$, the goal is to predict which hypothesis is more likely. Table 1.1 presents the different possible outcomes of the detection test, where the y-axis represents the test decision while the x-axis represents the ground truth.

Two types of errors can arise in the result of a detection test: a False Alarm (called type I error in the statistical literature) when H_1 is decided when no target is present in the scene and a Missed Detection (type II error) when H_0 is decided when a target is present in the scene. In radar context, False Alarms are very costly and the goal is to maximize the probability of true detections (P_D) (or, equivalently, minimize the probability of missed detections) under the constraint that the Probability of False Alarm (P_{FA}) should be equal to a given value. Typically in radar the fixed P_{FA} is quite low; a P_{FA} of 10^{-6} is not unusual. This probability depends on the Signal to Noise Ratio (SNR), and P_D versus SNR curves for a given P_{FA}, as well as P_D versus P_{FA} curves for a given SNR (ROC curves) are commonly drawn to showcase performance.

To solve the hypothesis test, we use a *detector* $\Lambda(\mathbf{r})$. It is a function of the received signal $\mathbf{r}$. If the test quantity $\Lambda(\mathbf{r})$ is higher than a given threshold w^2, then hypothesis H_1 is decided, and otherwise, we make the decision that we are under hypothesis H_0. This is usually noted

$$\Lambda(\mathbf{r}) \underset{\mathrm{H_0}}{\overset{\mathrm{H_1}}{\gtrless}} w^2\,.$$

Let f_{H_0} and f_{H_1} be the pdf of $\mathbf{r}$ under each hypothesis. The sets of values $\mathcal{D}_{\mathcal{A}}$ of $\mathbf{r}$ for which $\Lambda(\mathbf{r})$ is greater than w^2 is called the *domain of acceptance* of Λ. Then the P_{FA} of the detector Λ associated with the threshold w^2 is given by:

$$P_{FA} = \int_{\mathbf{r}\in\mathcal{D}_{\mathcal{A}}} f_{H_0}(\mathbf{r})\, d\mathbf{r}\,.$$

Similarly, the P_D is given by:

$$P_D = \int_{\mathbf{r}\in\mathcal{D}_{\mathcal{A}}} f_{H_1}(\mathbf{r})\, d\mathbf{r}\,.$$

For now, consider that the parameters α and $\boldsymbol{\xi}$ of the test are perfectly known and that $\mathbf{n}$ follows a probability distribution whose pdf is perfectly known. Then, the pdf f_{H_0} and f_{H_1} of $\mathbf{r}$ under each hypothesis are perfectly known. Let us define the Likelihood Ratio Test (LRT):

$$\Lambda(\mathbf{r}) = \frac{f_{H_1}(\mathbf{r})}{f_{H_0}(\mathbf{r})} \underset{\mathrm{H_0}}{\overset{\mathrm{H_1}}{\gtrless}} w^2\,, \tag{1.15}$$

where the threshold $w^2 \in \mathbb{R}$ is fixed so as to guarantee a given P_{FA}. Since fixing the P_{FA} is so important in radar detection, deriving P_{FA}-threshold relationships is critical. This will be one of the major points of focus of this thesis. The Neyman-Pearson criterion states that this test is the best in this setting in the sense that it maximizes the P_D for a given P_{FA}:

Lemma 1.2.1. *[NP33] The LRT is the uniformly most powerful test when all parameters are known, i.e. it yields the best Probability of Detection for a given Probability of False Alarm.*

1.3 . The Generalized Likelihood Ratio Test

Unfortunately, the modelization in the last section is not realistic in radar context: indeed, the target amplitude α and the target parameters $\boldsymbol{\xi}$ are unknown in practice, and often the pdf of the noise vector $\mathbf{n}$ depends on unknown parameters i.e. an unknown covariance matrix. In this case, the Neyman-Pearson lemma 1.2.1 does not hold anymore as the LRT (1.15) is then ill-defined. Another strategy has to be devised to detect targets.

When the unknown parameters are assumed deterministic, the most common strategy is to extend the LRT through the Generalized Likelihood Ratio Test (GLRT). It consists in replacing the unknown parameters in the LRT test with their Maximum Likelihood Estimates (MLE). Formally, for unknown parameters $\{\boldsymbol{\lambda}_i\}_{i\in[0,1]}$ depending on each hypothesis $\{H_i\}_{i\in[0,1]}$, the GLRT is given by:

$$\Lambda'(\mathbf{r}) = \frac{\max\limits_{\boldsymbol{\lambda}_1} f_{H_1}(\mathbf{r})}{\max\limits_{\boldsymbol{\lambda}_0} f_{H_0}(\mathbf{r})} \underset{\mathrm{H_0}}{\overset{\mathrm{H_1}}{\gtrless}} w^2\,, \tag{1.16}$$

Remark 1.3.1. *In the Bayesian context, i.e. when the unknown parameters are supposed to be random variables (in radar context when the target amplitude is distributed according to a Swerling $1, 2, 3$ or 4 fluctuation model), the test that will give the best average (over the priors for the unknown parameters) P_D for a given P_{FA} is the Average Likelihood Ratio Test (ALRT) [RB18]. The likelihood Ratio Test becomes:*

$$\Lambda'(\mathbf{r}) = \frac{\displaystyle\int f_{H_1}(\mathbf{r})\, p_{\boldsymbol{\lambda}_1}(\mathbf{z})\, d\mathbf{z}}{\displaystyle\int f_{H_0}(\mathbf{r})\, p_{\boldsymbol{\lambda}_0}(\mathbf{z})\, d\mathbf{z}} \underset{\mathrm{H_0}}{\overset{\mathrm{H_1}}{\gtrless}} w^2\,,$$

where $p_{\boldsymbol{\lambda}_0}$ and $p_{\boldsymbol{\lambda}_1}$ are the PDF of the unknown parameters under H_0 and H_1, respectively. This requires prior knowledge of the parameter distribution, which is not always simple. The Bayesian context is outside the scope of this thesis.

For now, let us suppose that the unknown target parameters $\boldsymbol{\xi}$ are still known. The complex amplitude of the target α is supposed to be deterministic unknown, and non-fluctuating (in the radar literature, such targets are said to be *Swerling* 0 [Ric+10]). Furthermore, let us assume that $\mathbf{n}$ is the thermal noise plus clutter vector, following a centered circular Gaussian distribution with covariance matrix $\mathbf{R}$ such that $\mathbf{R} = \sigma^2 \mathbf{\Gamma}$, where σ^2 represents the power level of the noise and $\mathbf{\Gamma}$ is the structure of the interference. $\mathbf{R}$ is a semi-positive definite (SPD) matrix. We write $\mathbf{n} \sim \mathcal{CN}(0, \sigma^2\mathbf{\Gamma})$, and, following (1.13), the pdf $f_{\mathbf{n}}(\mathbf{x})$ of $\mathbf{n}$ reads:

$$f_{\mathbf{n}}(\mathbf{x}) = \frac{1}{(\sigma^2\pi)^N \mathbf{\Gamma}} e^{\mathbf{x}^H (\sigma^2 \det \mathbf{\Gamma})^{-1} \mathbf{x}}.$$

$\mathbf{\Gamma}$ is often structured as a Toeplitz matrix; in particular this is the case when the noise is stationary and is sampled linearly in time and space [Fuh91]. A Toeplitz model for $\mathbf{\Gamma}$ that we will use throughout this thesis in simulations is given by the following expression:

$$\begin{aligned} \mathbf{\Gamma}(\rho) &= To\left(\begin{bmatrix} 1 & \rho & \dots \rho^{N-1} \end{bmatrix}\right), \\ &= \begin{bmatrix} 1 & \rho & \dots & \rho^{N-1} \\ \rho & 1 & \dots & \rho^{N-2} \\ \vdots & \vdots & & \vdots \\ \rho^{N-1} & \rho^{N-2} & \dots & 1 \end{bmatrix}, \end{aligned} \tag{1.17}$$

where $To(.)$ is the Toeplitz matrix operator, and ρ is a scalar in the interval $[0, 1[$ that defines the level of correlation of the noise. The higher ρ is, the more correlated the noise is. Inversely, for low values of ρ, the noise is not very correlated, and $\mathbf{\Gamma}$ is close to the identity matrix $\mathbf{I}$. When $\mathbf{\Gamma}$ is equal to $\mathbf{I}$, the noise is said to be white, and is, in this case, uncorrelated.

The GLRT then reduces to one of the well-known tests described in Table 1.2 according to which parameters are unknown. In this thesis, we will mainly focus on the non-adaptive scenario (i.e. we will assume $\mathbf{\Gamma}$ known) and the two associated detectors: the Matched Filter (MF) and the Normalized Matched Filter (NMF).

1.3.1 . The Matched Filter (MF) [SD91]

In this section, the amplitude of the target is supposed to be unknown, so that the unknown parameters sets are $\boldsymbol{\lambda}_0 = \emptyset$ and $\boldsymbol{\lambda}_1 = \{\alpha\}$.

Remark 1.3.2. *The power level of the noise σ^2 is thus known: in practice, this corresponds to contexts where the noise distribution changes slowly so that σ^2 can be reliably estimated, such as thermal noise or sky clutter.*

Under H_1, the received signal $\mathbf{r}$ is such that:

$$\mathbf{r} = \alpha\, \mathbf{s}(\boldsymbol{\xi}) + \mathbf{n}\,,$$

so that

$$\mathbf{r} \sim \mathcal{CN}\left(\alpha\, \mathbf{s}(\boldsymbol{\xi}), \mathbf{R}\right).$$

The PDF $f_{H_1}(\mathbf{x})$ of $\mathbf{r}$ under H_1 can be written as:

$$f_{H_1}(\mathbf{x}) = \frac{1}{\pi^N \det \mathbf{R}} e^{-(\mathbf{x} - \alpha\, \mathbf{s}(\boldsymbol{\xi}))^H \mathbf{R}^{-1} (\mathbf{x} - \alpha\, \mathbf{s}(\boldsymbol{\xi}))}.$$

Differentiating with respect to α^* (since α is complex and f_{H_1} is real-valued [PP+08]) gives:

$$\frac{\partial f_{H_1}}{\partial \alpha^*} = 2\left(\mathbf{s}(\boldsymbol{\xi})^H \mathbf{R}^{-1} \mathbf{x} - \alpha \mathbf{s}(\boldsymbol{\xi})^H \mathbf{R}^{-1} \mathbf{s}(\boldsymbol{\xi})\right) f_{H_1}(\mathbf{x})\,.$$

f_{H_1} attains its maximum for:

$$\hat{\alpha} = \frac{\mathbf{s}(\boldsymbol{\xi})^H \mathbf{R}^{-1} \mathbf{x}}{\mathbf{s}(\boldsymbol{\xi})^H \mathbf{R}^{-1} \mathbf{s}(\boldsymbol{\xi})}\,. \tag{1.18}$$

Injecting in (1.16), we see that in this case the GLRT reduces to the well-known Matched Filter (MF):

$$\Lambda_{\text{MF}}(\boldsymbol{\xi}) = \frac{\left|\mathbf{s}(\boldsymbol{\xi})^H \mathbf{R}^{-1}\,\mathbf{r}\right|^2}{\mathbf{s}(\boldsymbol{\xi})^H \mathbf{R}^{-1}\,\mathbf{s}(\boldsymbol{\xi})} \underset{\text{H}_0}{\overset{\text{H}_1}{\gtrless}} w^2\,. \tag{1.19}$$

Remark 1.3.3. *Under white noise, i.e. $\mathbf{R} = \sigma^2\mathbf{I}$, if the processed signal is the Fourier steering vector (1.7) (for example, when $\boldsymbol{\xi}$ is the scalar unknown Doppler shift θ or angle μ), the matched filter operation simply reduces to a Discrete Fourier Transform. A fast and efficient implementation of the matched filter, in this case, is thus the Fast Fourier Transform (FFT) algorithm [CT65]. It is also possible to enjoy the benefits of the FFT for distance detection by using FMCW or performing a technique called deramping on the received signal when using a chirp waveform. It consists in multiplying the received analog signal by the conjugate of the sent chirp so that the received signal model is expressed as a steering vector, just like in the case of FMCW. However, in order to apply this technique, the radar operator has to have a rather precise idea of the target location, so that the support of the received signal overlaps with the support of the multiplied chirp.*

The term $\mathbf{R}^{-1}$ in the products of (1.19) corresponds to a whitening of the received signal and the reference signal. The denominator corresponds to a normalization of the reference signal. Noting

$$\mathbf{s}^w(\boldsymbol{\xi}) = \frac{\mathbf{R}^{-1/2}\mathbf{s}(\boldsymbol{\xi})}{\left\|\mathbf{R}^{-1/2}\mathbf{s}(\boldsymbol{\xi})\right\|}\,, \tag{1.20}$$

the whitened and normalized version of $\mathbf{s}(\boldsymbol{\xi})$ and

$$\mathbf{r}^w = \mathbf{R}^{-1/2}\mathbf{r}\,,$$

the whitened version of $\mathbf{r}$, the MF reads:

$$\Lambda_{\text{MF}}(\boldsymbol{\xi}) = \left|\mathbf{s}^w(\boldsymbol{\xi})^H \mathbf{r}^w\right|^2 \underset{\text{H}_0}{\overset{\text{H}_1}{\gtrless}} w^2\,.$$

Under the null hypothesis H_0, it is straightforward to show that the random variable $\mathbf{s}^w(\boldsymbol{\xi})^H\mathbf{r}^w$ follows a centered normalized complex circular Gaussian distribution so that the test quantity Λ_{MF} follows a centered $\frac{1}{2}\mathcal{X}_2^2$ distribution. Its P_{FA}-threshold relationship is thus given by:

$$\begin{aligned} P_{FA} &= 1 - F_{\mathcal{X}_2^2}\left(2w^2\right)\,, \\ &= e^{\left(-w^2\right)}\,, \end{aligned} \tag{1.21}$$

where $F_{\mathcal{X}_2^2}$ is the CDF of the centered $\mathcal{X}_2^2$ distribution (which is in fact an exponential distribution).

Under the hypothesis H_1, $\left|\mathbf{s}^w(\xi)^H\mathbf{r}^w\right|^2 = \left|\alpha\mathbf{s}^w(\boldsymbol{\xi})^H\mathbf{R}^{-1/2}\mathbf{s}(\boldsymbol{\xi}) + \mathbf{s}^w(\boldsymbol{\xi})^H\mathbf{R}^{-1/2}\mathbf{n}\right|^2$. The random variable $\mathbf{s}^w(\boldsymbol{\xi})^H\mathbf{R}^{-1/2}\mathbf{n}$ follows a centered complex Gaussian distribution $\mathcal{CN}(0,1)$. The SNR *after integration* is defined as

$$SNR = |\alpha|^2\,\mathbf{s}(\boldsymbol{\xi})^H\mathbf{R}^{-1}\mathbf{s}(\boldsymbol{\xi})\,. \tag{1.22}$$

Λ_{MF} follows a non-central $\frac{1}{2}\chi_2^2$ distribution with non-centrality parameter $2SNR$. Its probability of detection is given by:

$$\begin{aligned} P_D &= 1 - F_{\chi_2^2(2SNR)}(2w^2)\,, \\ &= Q_1\left(\sqrt{2SNR}, \sqrt{2}w\right)\,, \end{aligned} \tag{1.23}$$

where Q_1 is the Marcum Q-function [Mar60].

Remark 1.3.4. *The MF works by comparing the squared norm of the projection of the received signal $\mathbf{r}$ on the subspace spanned by the reference signal $\mathbf{s}$ with a threshold. It is thus an energy detector.*

1.3.2 . The Normalized Matched Filter (NMF) [SD91]

In this section, the power level of the noise σ^2 is also assumed unknown so that $\boldsymbol{\lambda}_0 = \{\sigma^2\}$ and $\boldsymbol{\lambda}_1 = \{\sigma^2, \alpha\}$.

Remark 1.3.5. *In practice, this corresponds to contexts where the noise distribution changes rapidly from burst to burst so that σ^2 cannot be reliably estimated beforehand, such as sea clutter.*

Under H_0,

$$\mathbf{r} \sim \mathcal{CN}\left(\mathbf{0}, \sigma^2\,\boldsymbol{\Gamma}\right)\,,$$

and the PDF of $\mathbf{r}$ is given by:

$$f_{H_0}(\mathbf{x}) = \frac{1}{\left(\sigma^2\pi\right)^N \det\boldsymbol{\Gamma}} e^{-\mathbf{x}^H\left(\sigma^2\boldsymbol{\Gamma}\right)^{-1}\mathbf{x}}\,.$$

Differentiating w.r.t the σ^2 parameter, we get:

$$\frac{\partial f_{H_0}}{\partial\sigma^2} = \left(\frac{\mathbf{x}^H\boldsymbol{\Gamma}^{-1}\mathbf{x}}{\sigma^2} - N\right)\frac{f_{H_0}(\mathbf{x})}{\sigma^2}\,,$$

so that the MLE of σ^2 is

$$\hat{\sigma^2} = \frac{\mathbf{x}^H\boldsymbol{\Gamma}^{-1}\mathbf{x}}{N} \text{ under } H_0\,.$$

Under H_1,

$$\mathbf{r} \sim \mathcal{CN}\left(\alpha\,\mathbf{s}(\boldsymbol{\xi}), \sigma^2\boldsymbol{\Gamma}\right)\,,$$

so that the PDF of $\mathbf{r}$ reads

$$f_{H_1}(\mathbf{x}) = \frac{1}{\left(\sigma^2\pi\right)^N \det\boldsymbol{\Gamma}} e^{-(\mathbf{x}-\alpha\mathbf{s}(\boldsymbol{\xi}))^H\left(\sigma^2\boldsymbol{\Gamma}\right)^{-1}(\mathbf{x}-\alpha\mathbf{s}(\boldsymbol{\xi}))}\,.$$

$\hat{\alpha}$ is obtained as in Subsection 1.3.1, Equation (1.18). Differentiating once again w.r.t. σ^2 yields:

$$\frac{\partial f_{H_1}}{\partial\sigma^2} = \left(\frac{\left(\mathbf{x}-\alpha\,\mathbf{s}(\boldsymbol{\xi})\right)^H\boldsymbol{\Gamma}^{-1}\left(\mathbf{x}-\alpha\,\mathbf{s}(\boldsymbol{\xi})\right)}{\sigma^2} - N\right)\frac{f_{H_1}(\mathbf{x})}{\sigma^2}\,,$$

so that

$$\begin{aligned}\hat{\sigma^2} &= \frac{\left(\mathbf{x}-\hat{\alpha}\,\mathbf{s}(\boldsymbol{\xi})\right)^H\boldsymbol{\Gamma}^{-1}\left(\mathbf{x}-\hat{\alpha}\,\mathbf{s}(\boldsymbol{\xi})\right)}{N}\,,\\ &= \frac{1}{N}\left(\mathbf{x}^H\boldsymbol{\Gamma}^{-1}\mathbf{x} - \frac{\left|\mathbf{s}(\boldsymbol{\xi})^H\boldsymbol{\Gamma}^{-1}\mathbf{x}\right|^2}{\mathbf{s}(\boldsymbol{\xi})^H\boldsymbol{\Gamma}^{-1}\mathbf{s}(\boldsymbol{\xi})}\right) \text{ under } H_1\,.\end{aligned}$$

Injecting in (1.16), the GLRT reduces to:

$$\frac{\mathbf{x}^H\boldsymbol{\Gamma}^{-1}\mathbf{x}}{\mathbf{x}^H\boldsymbol{\Gamma}^{-1}\mathbf{x} - \dfrac{\left|\mathbf{s}(\boldsymbol{\xi})^H\boldsymbol{\Gamma}^{-1}\mathbf{x}\right|^2}{\mathbf{s}(\boldsymbol{\xi})^H\boldsymbol{\Gamma}^{-1}\mathbf{s}(\boldsymbol{\xi})}} \underset{\mathrm{H_0}}{\overset{\mathrm{H_1}}{\gtrless}} \left(w^2\right)'\,, \tag{1.24}$$

which can be written in the equivalent form, known as the Normalized Matched Filter (NMF) test:

$$\Lambda_{\mathrm{NMF}}(\boldsymbol{\xi}) = \frac{\left|\mathbf{s}(\boldsymbol{\xi})^H\boldsymbol{\Gamma}^{-1}\,\mathbf{r}\right|^2}{\left(\mathbf{s}(\boldsymbol{\xi})^H\boldsymbol{\Gamma}^{-1}\,\mathbf{s}(\boldsymbol{\xi})\right)\,\left(\mathbf{r}^H\boldsymbol{\Gamma}^{-1}\,\mathbf{r}\right)} \underset{\mathrm{H_0}}{\overset{\mathrm{H_1}}{\gtrless}} w^2\,, \tag{1.25}$$

with

$$w^2 = 1 - \frac{1}{\left(w^2\right)'}\,. \tag{1.26}$$

Equation (1.25) is the form that is generally found in the literature and used in practice.

Remark 1.3.6. *The NMF* (1.25) *is the MF* (1.19) *where the received signal* $\mathbf{r}$ *has been normalized.*

Remark 1.3.7. *Note that the NMF test quantity is the squared cosine of the angle between the received signal* $\mathbf{\Gamma}^{-1/2}\mathbf{r}$ *and the tested signal* $\mathbf{\Gamma}^{-1/2}\mathbf{s}(\boldsymbol{\xi})$*:* $\Lambda_{NMF} = \cos^2\left(\mathbf{\Gamma}^{-1/2}\mathbf{r}, \mathbf{\Gamma}^{-1/2}\mathbf{s}(\boldsymbol{\xi})\right)$*. The NMF is thus an angle detector as it only depends on the angle between the signal of reference and the received signal. This is crucial as it will allow us to translate our statistical problems into geometrical ones.*

In Appendix 1.A, we show that remarkably, the test quantity under H_0 follows a F distribution whose parameters do not depend on σ^2. The P_{FA} of the detector thus does not depend on σ^2: It is said to be a *Constant False Alarm Rate* (CFAR) detector relative to σ^2, which allows us to set an unvarying threshold w guaranteeing a given P_{FA}. Its P_{FA}-threshold relationship is given by [CLR95]:

$$P_{FA} = \left(1 - w^2\right)^{N-1} . \tag{1.27}$$

Remark 1.3.8. *Also, note that both the MF and the NMF are CFAR relative to the structure of the covariance matrix* $\mathbf{\Gamma}$ *since* $\mathbf{\Gamma}$ *does not appear in the expression of the threshold* w^2*.*

Noting

$$\mathbf{u} = \frac{\mathbf{\Gamma}^{-1/2}\mathbf{r}}{\left\|\mathbf{\Gamma}^{-1/2}\mathbf{r}\right\|} ,$$

the whitened and normalized version of $\mathbf{r}$, the NMF reads:

$$\Lambda_{\text{NMF}}(\boldsymbol{\xi}) = \left|\mathbf{s}^w(\boldsymbol{\xi})^H\mathbf{u}\right|^2 \underset{\text{H}_0}{\overset{\text{H}_1}{\gtrless}} w^2 .$$

Remark 1.3.9. *In addition to the context of Gaussian noise of unknown power level, the NMF is also widely used to deal with noise following textured distributions such as CES distributions, and it can be shown to be optimal under asymptotic conditions [CLR95; Jay+03]. This makes the NMF particularly good for detecting when the clutter is impulsive.*

1.3.3 . Adaptive detectors

In adaptive context, the covariance matrix $\mathbf{R}$ is supposed to be unknown and needs to be estimated thanks to S secondary data vectors $\mathbf{r}_1, \ldots, \mathbf{r}_S$ containing only noise. The detection problem can then be rewritten as:

$$\begin{cases} H_0 : \begin{cases} \mathbf{r} = \mathbf{n} , \\ \mathbf{r_i} = \mathbf{n}_i, 1 \leq i \leq S , \end{cases} \\ H_1 : \begin{cases} \mathbf{r} = \alpha\, \mathbf{s}(\boldsymbol{\xi}) + \mathbf{n} , \\ \mathbf{r_i} = \mathbf{n}_i, 1 \leq i \leq S . \end{cases} \end{cases} ,$$

where $\mathbf{r}_i$ are the secondary data noise sample. The most popular covariance matrix estimator is the sample covariance matrix:

$$\hat{\mathbf{R}} = \frac{1}{S}\sum_{i=1}^{S} \mathbf{r}_i\mathbf{r}_i^H .$$

It can be shown that the adaptive GLRTs reduce to Kelly's detector [Kel86] for homogeneous noise power level (i.e. the training noise data samples $\mathbf{n}_i$ follow the same distribution as $\mathbf{n}$):

$$\Lambda_{\text{Kelly}}(\boldsymbol{\xi}) = \frac{\left|\mathbf{s}(\boldsymbol{\xi})^H\hat{\mathbf{R}}^{-1}\,\mathbf{r}\right|^2}{\left(\mathbf{s}(\boldsymbol{\xi})^H\hat{\mathbf{R}}^{-1}\,\mathbf{s}(\boldsymbol{\xi})\right)\left(1 + \frac{1}{S}\mathbf{r}^H\hat{\mathbf{R}}^{-1}\,\mathbf{r}\right)} \underset{\text{H}_0}{\overset{\text{H}_1}{\gtrless}} w^2 , \tag{1.28}$$

λ_0	λ_1	GLRT
$\emptyset$	$\{\alpha\}$	Matched Filter
$\{\sigma\}$	$\{\sigma, \alpha\}$	Normalized Matched Filter
$\{\mathbf{R}\}$	$\{\mathbf{R}, \alpha\}$	Kelly's Detector [Kel86]
$\{\mathbf{R}, \sigma\}$	$\{\mathbf{R}, \sigma, \alpha\}$	Adaptive Normalized Matched Filter [KS99]

Table 1.2: Overview of the most common GLRT detectors.

and the Adaptive Normalized Matched Filter (ANMF) [KS99] for inhomogeneous noise power level (i.e. the training noise data samples $\mathbf{n}_i$ follow the same distribution as $\mathbf{n}$ up to a scale factor σ^2):

$$\Lambda_{\text{ANMF}}(\boldsymbol{\xi}) = \frac{\left|\mathbf{s}(\boldsymbol{\xi})^H \hat{\mathbf{R}}^{-1} \mathbf{r}\right|^2}{\left(\mathbf{s}(\boldsymbol{\xi})^H \hat{\mathbf{R}}^{-1} \mathbf{s}(\boldsymbol{\xi})\right)\left(\mathbf{r}^H \hat{\mathbf{R}}^{-1} \mathbf{r}\right)} \underset{\text{H}_0}{\overset{\text{H}_1}{\gtrless}} w^2 \,. \tag{1.29}$$

Remark 1.3.10. *Another popular detector, under the hypothesis of homogeneous noise power level, is the Adaptive Matched Filter (AMF) [Rob+92], which corresponds to the Matched Filter* (1.19) *where the sample covariance matrix has been injected in place of* $\mathbf{R}$ *(two-step AMF detector).*

Those detectors will not be detailed further as we mostly suppose that the noise covariance matrix structure $\boldsymbol{\Gamma}$ is known in the developments of this thesis. However, they also suffer from the off-grid mismatch of the target parameters [BRO20]. The extension of the results to the adaptive case will be considered in the perspectives.

1.4 . Detection under mismatched signal model

In the previous section, we described the most common detection strategy to detect signals following a perfectly known signal model. However, in an operational context, most of the time the incoming signal under hypothesis H_1 is not known perfectly, for example, because of small antenna steering misalignment or sampling errors. Other factors inducing mismatch that are widely studied in the literature include mismatches between the estimated covariance matrix and the true covariance matrix in the adaptive context [Wat13], as well as mismatches due to the clutter being poorly modeled by the chosen noise distribution [Bes14]. In this case, we speak about detection under a mismatched signal model (the basis of which is covered in the reference textbook [BOR09]), because the expected signal distribution under H_1 does not match with the distribution of the actual received signal. This can lead to an undesirable loss in detection probability.

Detectors are said to be **robust** or **selective** based on how they react to a mismatched received signal. Which property is more desirable depends on the application. A robust detector will tend to be more sensitive to jamming, while a selective detector will tend to miss targets. Typically, a good trade-off between selectivity and robustness has to be found.

Let us investigate the robustness of the popular radar detectors MF (1.19) and NMF (1.25) to a mismatch between the expected signal and the received signal. As previously stated, the MF is an energy detector while the NMF is an angle detector. This translates to totally different behavior regarding mismatch:

- The MF is an energy detector and its acceptance zone is the domain above a hyperplane with normal $\mathbf{s}$. When projecting a mismatched signal on the signal of reference, some energy is lost, however if the mismatched signal under test has enough energy, it will still be detected. This is illustrated in Figure 1.8a. In this figure, the incoming signal $\mathbf{s}(\xi_0 + \delta)$ is mismatched w.r.t $\mathbf{s}(\xi_0)$, and

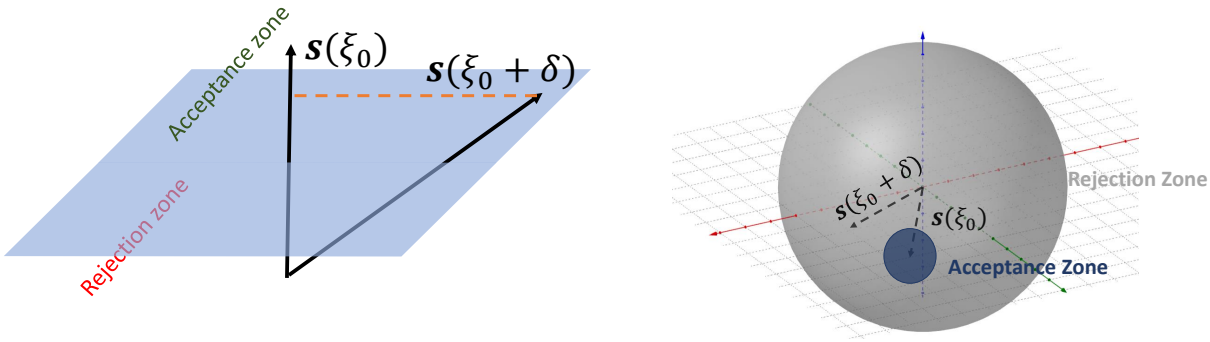

(a) MF (1.19). (b) NMF (1.25).

Figure 1.8: Illustration of the behavior of the detectors regarding mismatch.

some energy is lost after projecting. However, the incoming signal is powerful enough to still be detected by the MF. The MF can thus be said to be a robust detector: even though its detection probability is degraded when the received signals are mismatched with the expected signal, they will still be detected if the SNR is high enough.

- The NMF is an angle detector and its acceptance zone is a cone around the signal of reference, as illustrated in Figure 1.8b. In this figure, an incoming signal $\mathbf{s}(\xi + \delta)$ is mismatched w.r.t. $\mathbf{s}(\xi_0)$ with an angle δ such that $\mathbf{s}(\xi_0 + \delta)$ falls out of the detection cone. As such, it will never be detected by the NMF, regardless of its energy. The NMF is thus a selective detector.

In the literature covering this topic, typically the detectors are made more robust by extending the hypothesis H_1 in the binary test (1.3.3) to allow for more than one signal. Examples of common types of mismatch include a mismatch in a cone around the signal of reference [De 05; Bes06; Bes07; BDR07; De +08] or a mismatch constrained quadratically [De +10b]. To enhance selectivity, an approach consists of making the detectors more selective by extending the null hypothesis H_0 to contain signals orthogonal to the signal of reference [BBR07]. To obtain good robustness to selectivity tradeoff, the use of tunable detectors is proposed. They either depend on a parameter that is set according to the degree of robustness to selectivity wanted (see, for example, [Kal92]), or are expressed as the chaining of a robust detector with a selective detector such as the Adaptive Sidelobe Banker [KS95] which chains the ANMF with the AMF. In this case, the wanted degree of robustness to selectivity is obtained thanks to the setting of the thresholds of both detectors. This last scheme will detect signals if and only if they belong in the acceptance zone of both detectors.

1.5 . The off-grid issue

In this section, we investigate the off-grid issue that motivates this thesis. In Subsection 1.5.1, we describe what is the off-grid mismatch before studying its impact on the detection performance of the MF and the NMF in Subsection 1.5.2. We investigate the solutions of the literature in Subsection 1.5.3.

1.5.1 . Explaining the on-grid assumption

To derive the MF and the NMF tests, we assumed that the target parameters $\boldsymbol{\xi}$ were known. In practice, this is, of course, not true. The procedure detailed in Section 1.3 to characterize the GLRT consists of injecting the MLE of the unknown parameters in the LRT. However, no analytical form for the MLE of the target parameters $\boldsymbol{\xi}$ does exist. This is why the hypothesis that those parameters are known is commonly made to allow for the derivation and theoretical study of the MF and the NMF.

Tests are then run for values of the unknown parameters fixed on a discrete grid to explore the target parameter space. For Range detection using signal model (1.5), a common example of a grid is the following set of parameters:

$$\mathcal{G}_\tau = \left\{ \frac{k}{B}, k \in [0, 1, \dots, K-1] \right\} \text{ (range)},$$

and for Doppler detection, using signal model (1.7):

$$\mathcal{G}_\theta = \left\{ \frac{k}{N}, k \in [0, 1, \dots, N-1] \right\} \text{ (Doppler)}.$$

See that with this definition of the grid, the tested vectors for the signal model (1.7) are orthogonal. Cochran's theorem [Coc34] then states that the MF tests are independent. This enables us to easily fix the global P_{FA} when running tests on the grid as

$$P_{FA\text{global}} = 1 - (1 - P_{FA})^N \ . \tag{1.30}$$

The *cells* of the grid are then defined as the intervals of parameters centered around the values of $\mathcal{G}$. With the previous examples, the cells $\mathcal{D}_k$ for k in $[0, K-1]$ (or in $[0, N-1]$) are defined as:

$$\mathcal{D}_k = \left[\frac{k}{B} - \frac{0.5}{B}, \frac{k}{B} + \frac{0.5}{B} \right] \text{ (range)}, \tag{1.31}$$

or

$$\mathcal{D}_k = \left[\frac{k}{N} - \frac{0.5}{N}, \frac{k}{N} + \frac{0.5}{N} \right] \text{ (Doppler)}. \tag{1.32}$$

When performing distance-Doppler detection, the 2D grid $\mathcal{G}_{\tau,\theta}$ is the product $\mathcal{G}_\tau \times \mathcal{G}_\theta$, and similarly, the 2D cells are products of the above 1D cells. The fact that the true parameters of the target θ_0 may not lie on the grid creates a mismatch $\delta \triangleq \theta - \theta_0$ between the true parameters and the parameters under test.

Remark 1.5.1. *Note that the off-grid-induced mismatch is not due to any mistake during the collection of the data or poor modeling of the parameters of the detection problem as can be the case when the noise distribution or covariance matrices are mismatched. It is entirely due to the grid heuristic made to solve the hypothesis test.*

Remark 1.5.2. *Decomposing the parameter space in several cells is also a simple way to deal with the case of multiple targets, the corresponding multiple hypothesis testing being much more involved [Kay09]. It is hoped that in a single cell, only one target will be present, which is the context of the binary hypothesis test* (1.3.3) *we are trying to solve. Interferences between targets with parameters lying in different cells are neglected in this modelization.*

This mismatch lowers the output of the detectors. Under white noise, when $\mathbf{r} = \mathbf{s}(\xi+\delta)$, $\left|\mathbf{s}(\xi)^H \mathbf{s}(\xi+\delta)\right|$ in the numerator of the detectors is worth:

- In the case of range detection (signal model (1.5)):

$$\left|\mathbf{s}(\tau)^H \mathbf{s}(\tau+\delta)\right| = \frac{1}{K} \left| \frac{\sin(\pi\delta B)}{\sin(\pi\delta B/K)} \right| . \tag{1.33}$$

- In the case of Doppler (or angle) detection (signal model (1.7)):

$$\left|\mathbf{s}(\theta)^H \mathbf{s}(\theta+\delta)\right| = \frac{1}{N} \left| \frac{\sin(\pi\delta N)}{\sin(\pi\delta)} \right| . \tag{1.34}$$

The function $\left|\mathbf{s}(\xi)^H \mathbf{s}(\xi+\delta)\right|$ (autocorrelation of $\mathbf{s}$) is drawn in Figure 1.9 in the case of Doppler (or angle) detection.

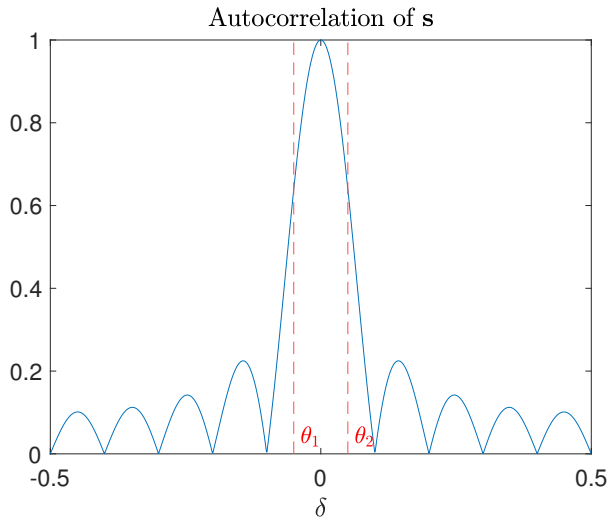

Figure 1.9: Autocorrelation of $\mathbf{s}$ under white noise (2.69) for $N = 10$. Values θ_1, θ_2 represent the limits of a cell $\mathcal{D}_k = [\theta_1, \theta_2]$.

1.5.2 . Impact of the off-grid mismatch on the detectors

As we saw in Section 1.4, the MF and the NMF do not react the same way to a mismatch. As a consequence, their mean probability of detection for targets uniformly distributed in a cell will be impacted. Formally, for a cell $[\xi_0 - \frac{\Delta}{2}, \xi_0 + \frac{\Delta}{2}]$ and given SNR a threshold w^2, this quantity is defined as:

$$P_{D_{mean}} = \frac{1}{\Delta} \int_{-\frac{\Delta}{2}}^{+\frac{\Delta}{2}} P(\Lambda_i(\xi_0 + \delta) > w^2)\, d\delta\,, \text{ for } i \in \{MF, NMF\}\,, \tag{1.35}$$

The impact of the off-grid mismatch is quantified in Figures 1.10a and 1.10b for white noise using signal model (1.7) with a P_{FA} of 10^{-6}, computed by simulating 100 targets equispaced in a cell ($P_{D_{mean}}$ being independent of the chosen cell under white noise). The mean detection probability of the detectors is compared with the mean detection probability of the oracle detectors $\Lambda_i(\boldsymbol{\xi_0})$ ($i \in \{MF, NMF\}$) that are always run at the true parameters $\boldsymbol{\xi}_0$ of the target, and the mean probability of the off-grid GLRT, to will be defined later in section 1.6.

- The off-grid mismatch degrades the average MF detection probability by a non-negligible factor compared with the oracle detector that knows the positions of the targets. However, the loss is contained: it is well-known that at worst, the off-grid loss is limited to a 3dB loss in detection probability per unknown parameter. As a result, the probability of detection of the MF converges to 1 with the SNR. This is due to the robust nature of the MF.
- In the case of the NMF for Doppler detection, the loss in average detection probability is much more concerning: indeed, see that the probability of detection does not tend to 1 with SNR anymore. This is explained by Figure 1.11a which shows the NMF response versus the mismatch in a cell. The asymptotic $P_{D_{mean}}$ is obtained as the ratio of the lobe width above the threshold over the total width of the search domain [RBO16]. It can be seen that for P_{FA} as high as 10^{-3}, the targets at the edge of a standard Fourier resolution cell fall out of the detection cone. Thus, with low P_{FA}, some targets on the edge of cells can never be detected, because of the selectivity of the NMF. This is a significant issue of this detector, hence why it has been one of the main focuses of this thesis.

  Remark 1.5.3. *This is especially true for a low number of integrated samples, for which the NMF detection cone is very narrow. As the number of samples increases, the NMF becomes more robust to off-grid*

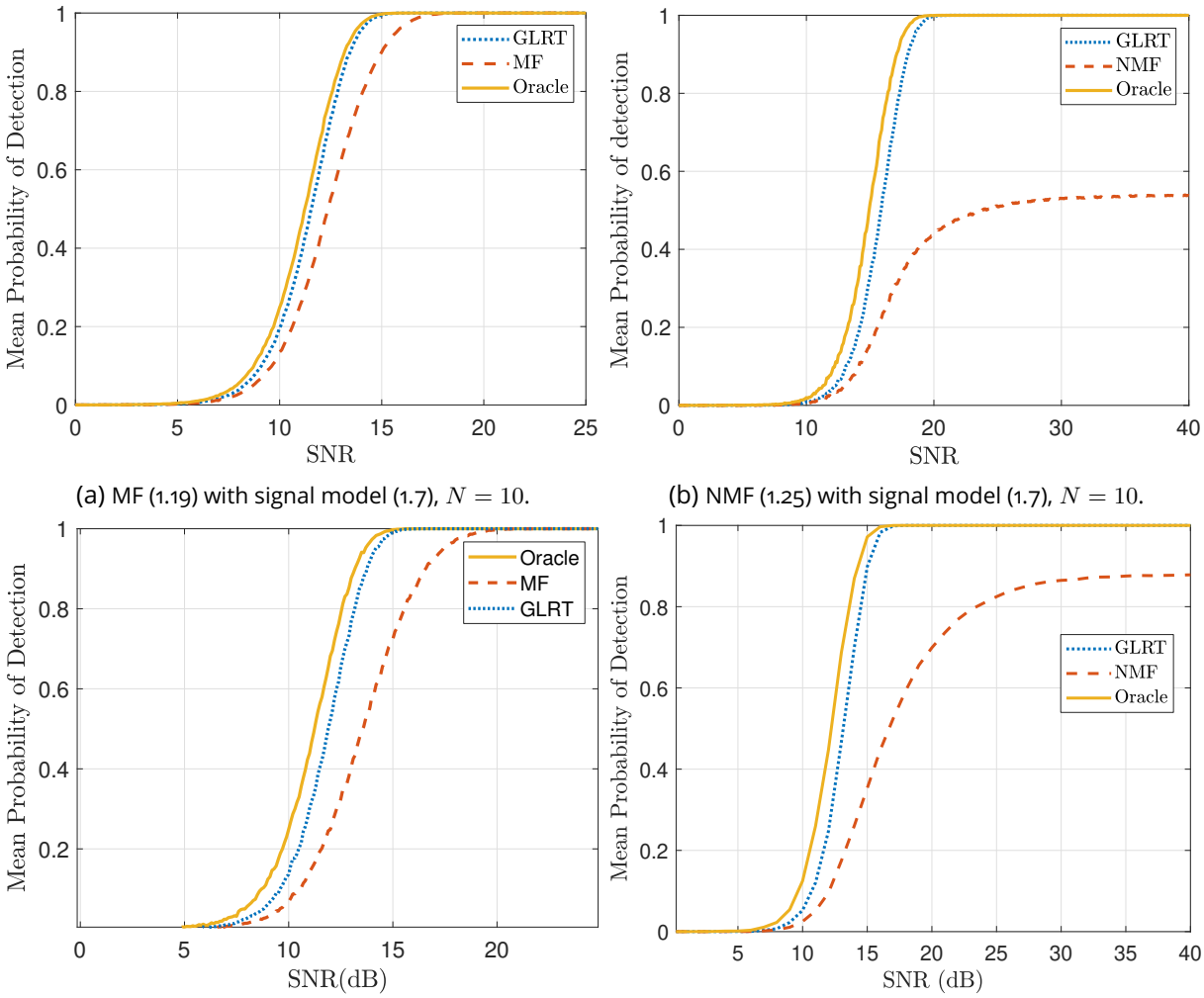

(a) MF (1.19) with signal model (1.7), $N = 10$.

(b) NMF (1.25) with signal model (1.7), $N = 10$.

(c) MF (1.19) with signal model (1.10), $N = 8$ and $P = 4$.

(d) NMF (1.25) with signal model (1.10), $N = 8$ and $P = 4$.

Figure 1.10: Plot of the P_D of the MF and the NMF against targets with parameters randomly and uniformly distributed in a Fourier resolution cell under white noise for a $P_{FA} = 10^{-6}$. The Oracle detector and the off-grid GLRT are also plotted for comparison.

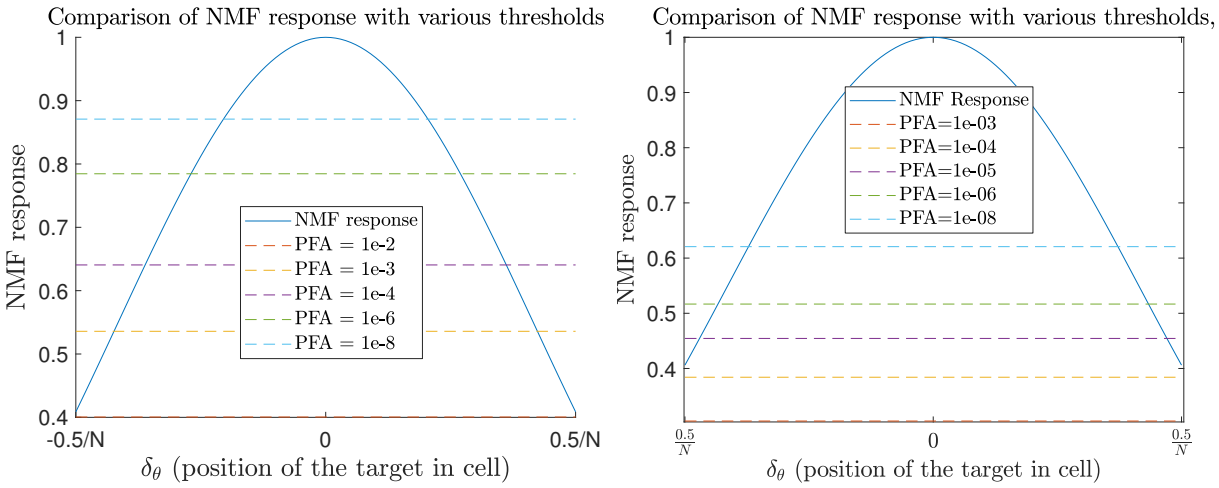

(a) $N = 10$. (b) $N = 20$.

Figure 1.11: Noiseless NMF response (1.25) to a mismatched signal $\mathbf{s}(\theta_0 + \delta)$ versus the mismatch δ. Dashed lines represent the thresholds for different P_{FA}.

mismatch because the thresholds get lower, as illustrated in Figure 1.11b where the NMF response has been redrawn as in Figure 1.11a, but this time with $N = 20$. It can be seen that this time, the NMF response is always higher than the thresholds for P_{FA}s up to 10^{-4}. As a result of this, the average probability of detection of the NMF in the presence of off-grid targets increases with the number of pulses that are used, as illustrated in Figure 1.12a where the NMF mean probability of detection for Doppler detection has been drawn in the asymptotic regime versus the number of pulses N for a P_{FA} of 10^{-6}. However, in many applications, only a low number of integrated samples is used, and using 10 samples as in Figure 1.11a is a realistic scenario.

Figures 1.10c and 1.10d show the P_D of the MF and the NMF in the STAP context. While the gap between the oracle detector and the standard MF widens, the NMF performs much better, and its probability of detection converges to a higher value with the SNR.

Remark 1.5.4. *For detection with two unknown parameters, the asymptotic deficiency of the NMF P_D is less prevailing because the detection cone is wider even when using low values for both parameters. Indeed, Figure 1.12b shows the asymptotic P_D of the NMF using signal model* (1.10) *for STAP detection and it can be seen that an asymptotic P_D of 1 is reached for $N = 8$ and $P = 10$.*

While the off-grid mismatch already has a big impact on the detection performance of the typical GLRT detectors under white noise, the situation is even worse under colored noise when $\mathbf{\Gamma} \neq \mathbf{I}$. Even though the Oracle detectors are not impacted by it, it can further degrade the P_D of the MF and the NMF. While in the white noise case, $P_{D_{mean}}$ is cell-independent for those detectors, under colored noise, it becomes cell-dependent. The P_D of those detectors under a noise highly correlated is shown in Figures 1.13 and 1.14. As expected, the P_D of the Oracle detectors, which was found to be independent of $\mathbf{\Gamma}$ in (1.23) and (1.39), does not change after correction of the SNR. However, the P_D of the MF and the NMF severely decreases in the cell $\mathcal{D}_0$, and increases in the cell $\mathcal{D}_5$. This is a consequence of the fact that for highly correlated noise, the detection cone gets thinner when testing for targets in $\mathcal{D}_0$ and widens when testing for targets in $\mathcal{D}_5$, as illustrated in Figures 1.14a and 1.14b which represent the NMF response for targets in $\mathcal{D}_0$ and $\mathcal{D}_5$

1.5.3 . The off-grid mismatch in the literature

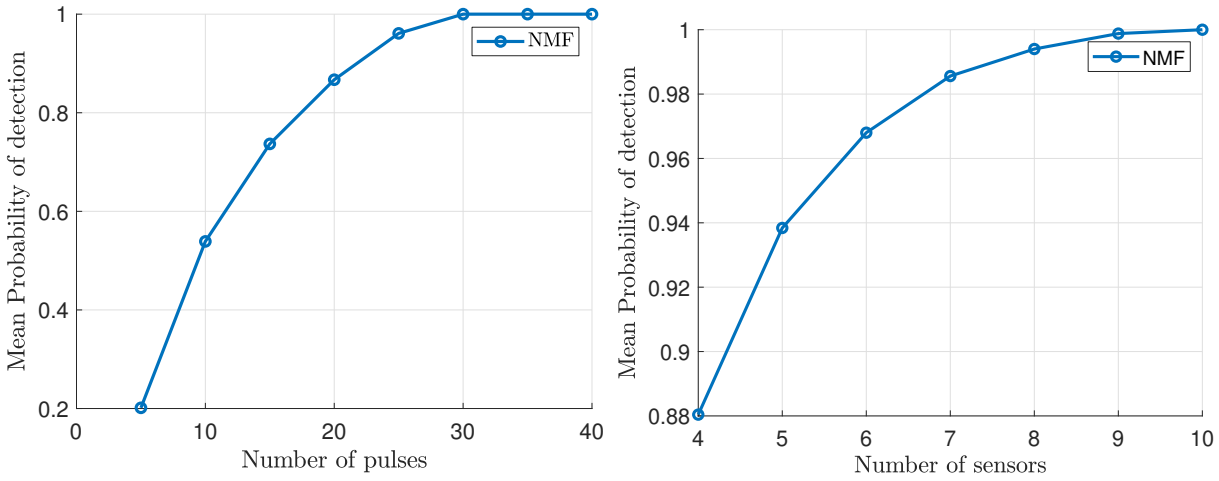

(a) Doppler detection with signal model (1.7).

(b) STAP detection with signal model (1.10), $N = 8$ is fixed.

Figure 1.12: Mean probability of detection of the NMF for off-grid targets uniformly distributed in a cell, with $SNR = 100dB$ after integration and $P_{FA} = 10^{-6}$ under white noise.

In this section, we explore the solutions given in the literature to mitigate the off-grid mismatch impact.

1.5.3.1 Litterature on the off-grid mismatch in sparse signal reconstruction

The off-grid mismatch is a topic that has been covered extensively in sparse parameter estimation or signal reconstruction.

The sparse signal reconstruction issue closely resembles our detection problem. In this application, the radar scene is modeled as

$$\mathbf{y} = \mathbf{F}\mathbf{x} + \mathbf{n}\,,$$

where $\mathbf{y}$ is the received signal, $\mathbf{F}$ is a matrix where each column corresponds to a possible received signal (in radar applications, usually $\mathbf{F}$ is taken as the oversampled Fourier dictionary (1.7)), $\mathbf{x}$ is a vector containing the target amplitudes at the target frequencies, and otherwise 0s and $\mathbf{n}$ is a noise vector. In sparse contexts, the received signal $\mathbf{x}$ contains only a few non-zero components, which is usually true in radar where only a few targets can be considered present in the scene. The goal of signal reconstruction is to estimate the vector $\mathbf{x}$, effectively detecting the targets in the scene and estimating the unknown parameters at the same time, which is made possible by the sparsity of the received vector. This is usually achieved with algorithms such as Lasso [Tib96] or Orthogonal Matching Pursuit [TG07].

When the target received vector is mismatched w.r.t. to the atoms of the dictionary matrix $\mathbf{F}$, there is an off-grid mismatch, similar to what we have described earlier in this section [SB11b; Str12]. The aforementioned classical algorithms of signal reconstruction are very sensitive to off-grid mismatch, which led to the development of several robustified algorithms. The proposed solutions include oversampling the grid [FL12] or the addition of a linear perturbation to the dictionary matrix $\mathbf{F}$ to account for off-grid mismatch, approximating the mismatched signals with a first-order Taylor approximation [ZLG11], sometimes using a Bayesian prior on the unknown parameters [Las+15] at the cost of a higher computational load. Another approach tailored for off-grid reconstruction consists of minimizing an atomic norm problem [Tan+13; BTR13], which avoids the usage of the grid.

One of the main drawbacks of sparse reconstruction algorithms compared to classical detection is that it is most of the time significantly harder to control the rate of false alarms, as most algorithms do

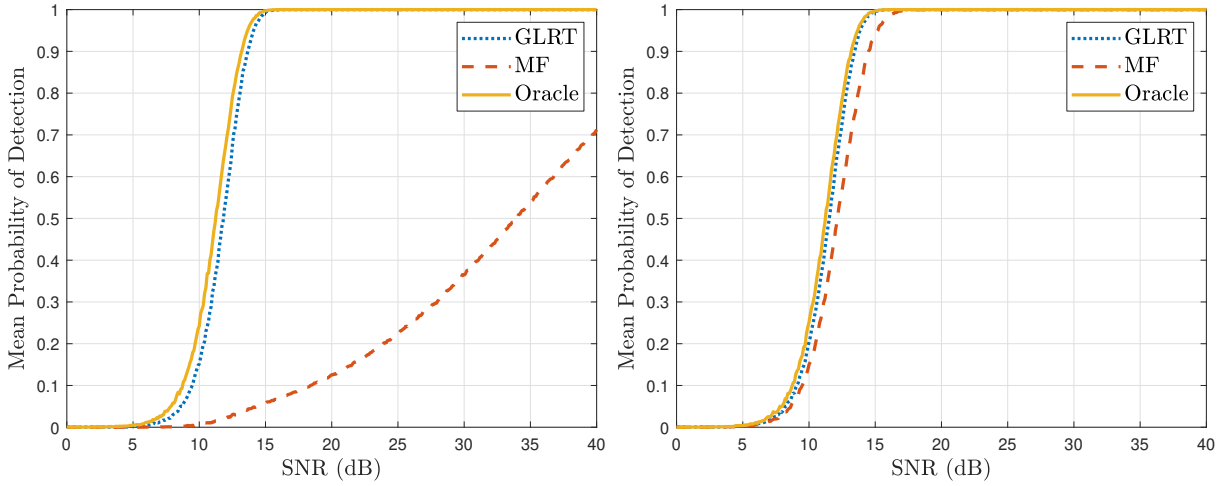

(a) MF (1.19), cell $\mathcal{D}_0$.

(b) MF (1.19), cell $\mathcal{D}_5$.

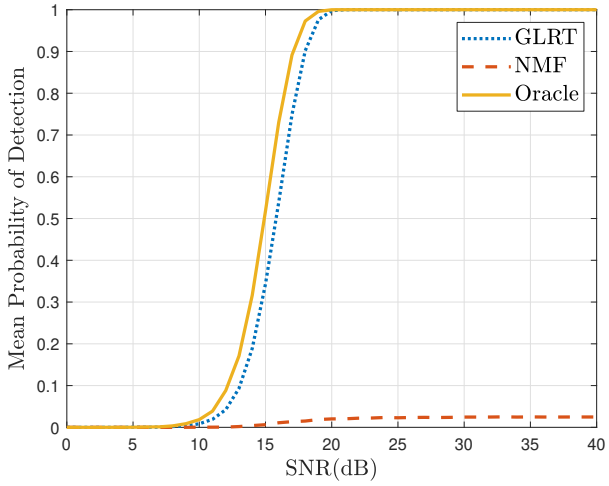

(c) NMF (1.25), cell $\mathcal{D}_0$.

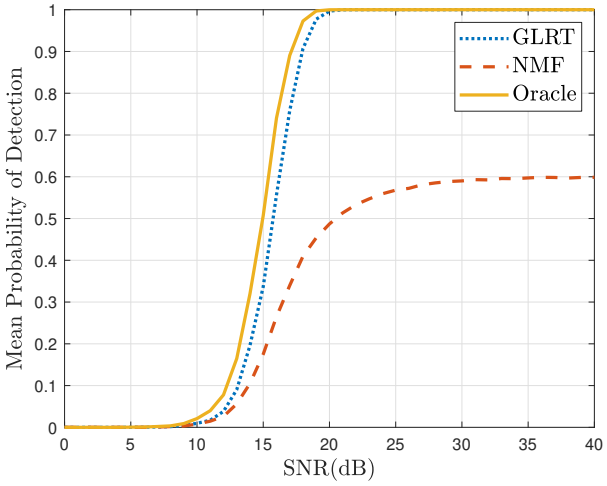

(d) NMF (1.25), cell $\mathcal{D}_5$.

Figure 1.13: P_D of the MF and NMF for Doppler detection (signal model (1.7)) under a very correlated noise model ($\rho = 0.999$ in (1.17)), with $N = 10$ and $P_{FA} = 10^{-6}$. The threshold of the GLRT is set accordingly , and SNR is defined as the maximum achievable SNR $|\alpha|^2 \mathbf{s}(\theta)^H \mathbf{\Gamma}^{-1} \mathbf{s}(\theta)$ where θ is the true parameter of the target, which is attained when the true parameter of the target coincides with the tested parameter (it is the SNR for the oracle detector).

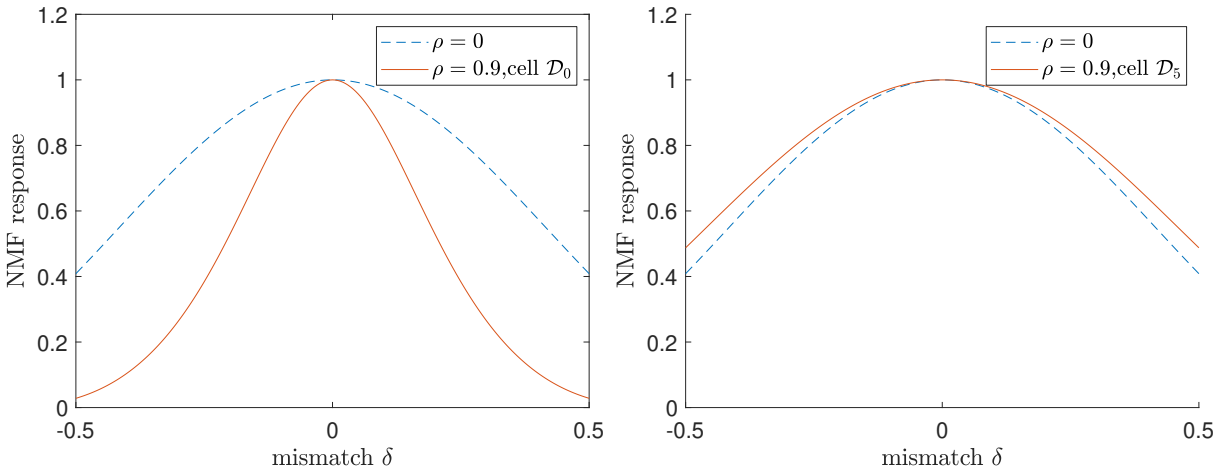

(a) Cell $\mathcal{D}_0$.

(b) Cell $\mathcal{D}_5$.

Figure 1.14: NMF response for Doppler detection (signal model (1.7)) with $N = 10$ and $\rho = 0.9$ in cells $\mathcal{D}_0$ and $\mathcal{D}_5$. The response under white noise is also drawn as a baseline.

not rely on a threshold as in detection, but rather on hyperparameters that can be hard to link with a P_{FA} [Ani+12]. It should however be noted that, as the selection rule of the pursuit algorithms (matching pursuit, orthogonal matching pursuit) reduces to a simple Fourier transform, knowing the statistics of the MF and the NMF makes it possible to set a stopping criterion enabling false alarm control for those algorithms.

1.5.3.2 Litterature on the off-grid mismatch in detection

In radar applications, the loss in detection probability due to off-grid targets is sometimes called the straddle loss [Cano2; Ric+10]. Windowing is seen as a possible way to solve this issue since it enlarges the main lobe, however, it also degrades the SNR, thus making this solution not always satisfying when the SNR is already low. Another solution widely encountered is oversampling i.e. refining the grid $\mathcal{G}$ (1.5.1) using smaller cells. This always increases the probability of detection at the cost of a higher computational load and more involved theoretical statistical characterization since the test samples are not independent anymore.

In detection theory, few authors have been interested specifically in dealing with the off-grid mismatch, and the tools developed for increasing the robustness of detectors under more general mismatch models mentioned in Section 1.4 are not suited for this application since the off-grid mismatch is very structured and is not well-encaptured by such simple models. Consider, for example, adapting the cone approach introduced in [De 05] to increase the robustness of the normalized matched filter to off-grid signals. To do this, we could center the cone of sought-for signals at the center of the cell, and define the cone extremities as the border of the cell, as represented in Figure 1.15 for real signals. However, in doing this, a large array of unwanted signals will be included in the signal model of H_1, thus dramatically decreasing the selectivity of the detector. Besides, a lower bound for the P_{FA} is imposed by the cone approach, which can be easily computed. In the real case, take the surface of a spherical cap of radius half the length of a cell on the unit sphere $\mathbb{S}^{N-1}$, representing the minimum acceptance zone of the detector to accept all signals in a cell as represented on Figure 1.15. Divide it by the surface of the sphere, representing the space of all possible incoming normalized signals. This gives the lower bound for the P_{FA}, making it impossible to reach P_{FA} as low as 10^{-6}, yet very low P_{FA} of this order are common in

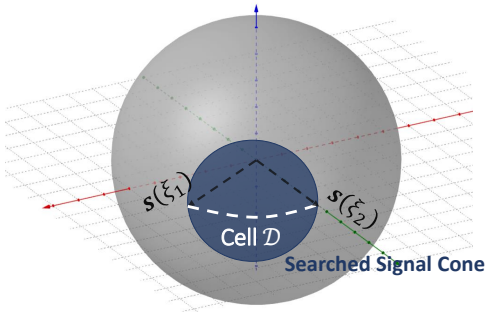

Figure 1.15: Example of a cone of sought-for signals containing a cell for detection under 'cone mismatch model.

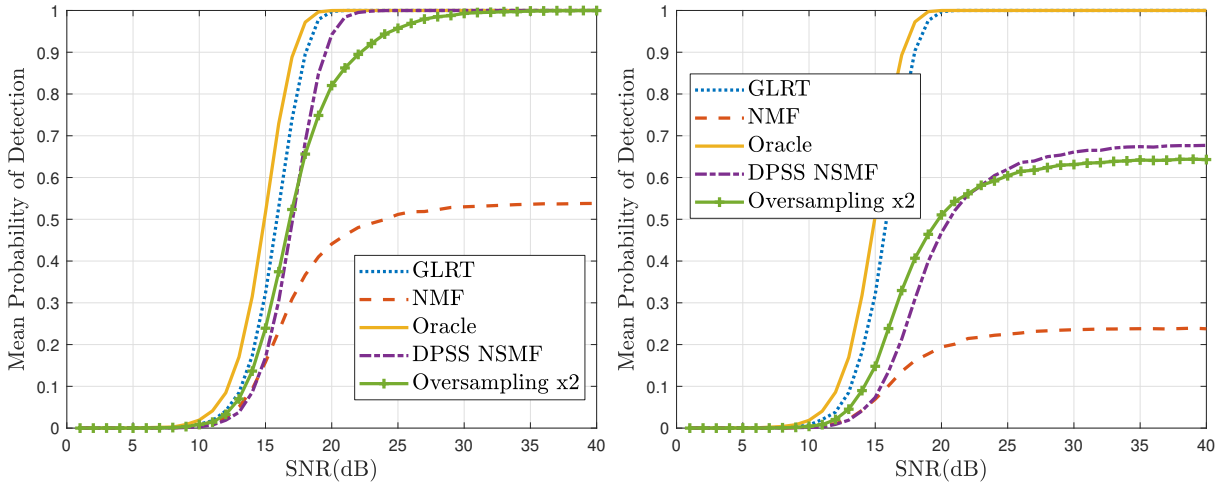

(a) In white noise.

(b) In highly correlated noise ($\rho = 0.9$ in (1.17)), cell $\mathcal{D}_0$.

Figure 1.16: P_D of the NMF, DPSS NMF (using 2 vectors to model the cell) and a x2 oversampling for Doppler detection with $N = 10$ and $P_{FA} = 10^{-6}$ under different contexts. The P_D of the GLRT described in Section 1.6 and the oracle detectors are also drawn for comparison purposes.

radar detection [BRO20].

In [RBO16] (in the case of known covariance matrix) and [BRO20] (in the adaptive case), the authors propose an approximation of the grid cells as linear subspaces thanks to Discrete Prolate Spheroidal Sequence (DPSS) to apply matched subspace detectors [SF94]. This approach increases the detection performance of the detector in the presence of off-grid targets and is, for high SNR values, better than oversampling by a factor of 2. Furthermore, statistical analysis of those detectors is rather easy to perform: in particular, analytical P_{FA}-threshold relationships can be computed. However, it does not quite reach the oracle detection probability yet, as can be seen in Figure 1.16, in which the detection probabilities of the previously described detectors are compared in white noise and highly correlated noise contexts. This is especially true under correlated noise scenarios, where the P_D of the DPSS NSMF does not converge to 1. The detection probability of the off-grid GLRT is also shown. It is introduced in the next section.

Remark 1.5.5. *Another way to deal with the off-grid mismatch that sometimes appears in the literature, which is perhaps the most powerful one, consists in performing joint detection and estimation, i.e. estimating the unknown parameters $\boldsymbol{\xi}$ during the detection process (not necessarily in the MLE sense, which differentiates*

this from the GLRT) and injecting it in the detection test. This will be described in detail in Chapter 4.

1.6 . The off-grid GLRTs

As we saw in the previous section, the solutions devised in the literature to deal with the off-grid mismatch are not entirely satisfying. Another way to tackle the loss in detection probability of the detectors which is very straightforward is simply to consider the parameters of the target $\boldsymbol{\xi}$ as unknown in the GLRT, thus performing "true" off-grid GLRT detection. In this thesis, we call those detectors *off-grid* GLRT. However, as mentioned before, no analytical form of the MLE for $\boldsymbol{\xi}$ exists, and thus no-closed form exists for the GLRT which reads as the maximum of a continuum of random variables:

$$\Lambda_{\text{off-grid MF}} = \max_{\boldsymbol{\xi}\in\mathcal{D}} \frac{\left|\mathbf{s}(\boldsymbol{\xi})^H \mathbf{R}^{-1}\,\mathbf{r}\right|^2}{\mathbf{s}(\boldsymbol{\xi})^H \mathbf{R}^{-1}\,\mathbf{s}(\boldsymbol{\xi})} \underset{\mathrm{H_0}}{\overset{\mathrm{H_1}}{\gtrless}} w^2 \quad \text{(off-grid MF)} \tag{1.36}$$

and

$$\Lambda_{\text{off-grid NMF}} = \max_{\boldsymbol{\xi}\in\mathcal{D}} \frac{\left|\mathbf{s}(\boldsymbol{\xi})^H \boldsymbol{\Gamma}^{-1}\,\mathbf{r}\right|^2}{\left(\mathbf{s}(\boldsymbol{\xi})^H \boldsymbol{\Gamma}^{-1}\,\mathbf{s}(\boldsymbol{\xi})\right)\,\left(\mathbf{r}^H \boldsymbol{\Gamma}^{-1}\,\mathbf{r}\right)} \underset{\mathrm{H_0}}{\overset{\mathrm{H_1}}{\gtrless}} w^2 \quad \text{(off-grid NMF).} \tag{1.37}$$

Their detection performance is shown in Figures 1.16a under white noise and 1.16b under correlated noise distribution. They exhibit a better P_D than their *on-grid* counterpart (1.19) and (1.25), while still being a bit lower than the oracle detector, which is explained by the fact that the threshold in (1.36) and (1.37) has to be raised to account for the increased robustness. Of course, this was to be expected since the GLRT works with less information than the oracle detector.

Remark 1.6.1. *Note that the statistics of the off-grid GLRT under the null hypothesis will a priori depend on the tested cell, so the thresholds have to be computed for each cell (this will not be the case under white noise).*

Remark 1.6.2. *Similarly, off-grid GLRT versions of the adaptive detectors presented in Section 1.3.3 can be defined, as will be shown in the perspectives. It is also possible to define off-grid ALRTs for the detection of off-grid targets in a Bayesian context when the unknown parameters $\boldsymbol{\xi}$ are assumed unknown and following a prior distribution, as shown in [Sel65] (in the case of a known nonfluctuating amplitude) or [BRS68] (in the case of a Swerling 1 target, that is with an amplitude following a Rayleigh distribution) for Doppler detection, where the unknown Doppler shift follows a uniform distribution.*

Our goal in this thesis is to answer the following questions:

- **How can we compute the P_{FA}-threshold relationship of those detectors?** Indeed, as the test quantity now depends on a continuum of non-independent variables, it is more delicate to evaluate than in the on-grid case. In Chapter 2, we find a new P_{FA}-threshold relationship for the off-grid Normalized Matched Filter, and in Chapter 3, we focus on the P_{FA}-threshold relationship for the off-grid Matched Filter.
- **How can we compute the test quantities?** In order to implement the detectors perfectly, an infinity of test quantities has to be computed. A naive approximation consists of oversampling the on-grid tests using large oversampling factors, which is not always possible in applications where computing power is limited. Chapter 4 investigates fast and efficient approximations.

1.7 . Synthesis

In this chapter, we first presented the radar detection problem and its formalization as a binary hypothesis test. We then introduced the basis of detection theory, including the Generalized Likelihood

Ratio Tests which are popular tools used to solve composite hypothesis tests. Then, we shifted our focus to the issue of robust detection under mismatched signal models, which is related to the off-grid issue that this thesis tackles. We showed that the usual GLRT detectors widely employed in radar suffer from the presence of off-grid targets and that the solutions provided in the literature are not entirely satisfying. We propose to use the off-grid GLRTs, obtained by deriving the GLRTs under the hypothesis that the target parameters are unknown. The statistical characterization and the approximation of the off-grid GLRTs are the focus of the contributions made during this thesis, which are detailed in the following chapters, starting from the derivation of the P_{FA}-threshold relationship of the off-grid NMF in the next chapter.

Appendix

1.A . On the statistic of the NMF

The goal of this section is to characterize the NMF test statistics, as was already done, for example, in [CLR95] or [Jay02]. Starting back from (1.24), see that the NMF test quantity rewrites:

$$\Lambda_{\text{NMF}} = \frac{\left\|\mathbf{\Gamma}^{-1/2}\mathbf{x}\right\|^2}{\left\|\mathbf{\Gamma}^{-1/2}\mathbf{x}\right\|^2 - \frac{\left|\mathbf{s}(\boldsymbol{\xi})^H\mathbf{\Gamma}^{-1}\mathbf{x}\right|^2}{\left\|\mathbf{\Gamma}^{-1/2}\mathbf{s}\right\|^2}} .$$

Using Pythagoras theorem, we can decompose $\left\|\mathbf{\Gamma}^{-1/2}\mathbf{x}\right\|^2$ as:

$$\left\|\mathbf{\Gamma}^{-1/2}\mathbf{x}\right\|^2 = \left\|\mathbf{x}^H\mathbf{\Gamma}^{-1/2}\mathbf{P}_s^{\perp}\right\|^2 + \left\|\mathbf{x}^H\mathbf{\Gamma}^{-1/2}\mathbf{P}_s\right\|^2 ,$$

where $\mathbf{P}_s = \mathbf{\Gamma}^{-1/2}\mathbf{s}\left(\mathbf{s}^H\mathbf{\Gamma}^{-1}\mathbf{s}\right)^{-1}\mathbf{s}^H\mathbf{\Gamma}^{-1/2}$ and $\mathbf{P}_s^{\perp} = \mathbf{I} - \mathbf{P}_\mathbf{s}$ are the projectors on $\mathbf{s}$ and its orthogonal. Note that $\left\|\mathbf{x}^H\mathbf{\Gamma}^{-1/2}\mathbf{P}_s\right\|^2 = \frac{\left|\mathbf{s}(\boldsymbol{\xi})^H\mathbf{\Gamma}^{-1}\mathbf{x}\right|^2}{\left\|\mathbf{\Gamma}^{-1/2}\mathbf{s}\right\|^2}$, so that

$$\Lambda_{\text{NMF}} = \frac{\left\|\mathbf{x}^H\mathbf{\Gamma}^{-1/2}\mathbf{P}_s^{\perp}\right\|^2 + \left\|\mathbf{x}^H\mathbf{\Gamma}^{-1/2}\mathbf{P}_s\right\|^2}{\left\|\mathbf{x}^H\mathbf{\Gamma}^{-1/2}\mathbf{P}_s^{\perp}\right\|^2} .$$

The NMF test is thus equivalent to the test:

$$\Lambda_{\text{NMF}'} = \frac{\left\|\mathbf{x}^H\mathbf{\Gamma}^{-1/2}\mathbf{P}_s\right\|^2}{\frac{\left\|\mathbf{x}^H\mathbf{\Gamma}^{-1/2}\mathbf{P}_s^{\perp}\right\|^2}{N-1}} \underset{\text{H}_0}{\overset{\text{H}_1}{\gtrless}} \left(w^2\right)'' , \tag{1.38}$$

with

$$\left(w^2\right)'' = (N-1)\left(\left(w^2\right)' - 1\right) .$$

As noted in Subsection 1.3.1, under H_0, the random variable in the numerator follows a centered $\frac{1}{2}\chi^2_2$ distribution. Similarly, the random variable in the denominator follows a centered $\frac{1}{2(N-1)}\chi^2_{2(N-1)}$ distribution. Cochran's theorem enables us to state that those variables are independent. By definition, the test ratio then follows an F-distribution with parameters $(2, 2(N-1))$. Its CDF $F_{F(2,2(N-1))}(x)$ is given by [ASR88]:

$$\begin{aligned} F_{F(2,2(N-1))}(x) &= I_{\frac{2x}{2x+2(N-1)}}(1, N-1) , \\ &= 1 - \left(1 - \frac{2x}{2x+2(N-1)}\right)^{N-1} , \end{aligned}$$

where I is the regularized incomplete Beta function. The P_{FA} of the NMF is thus given by:

$$\begin{aligned} P_{FA} &= 1 - F_{F(2,2(N-1))}\left(\left(w^2\right)''\right) , \\ &= \left(1 - \left(1 - \frac{1}{\left(w^2\right)'}\right)\right)^{N-1} , \\ &= \left(1 - w^2\right)^{N-1} . \end{aligned}$$

Under H_1, when the noise vector $\mathbf{n}$ follows a Gaussian distribution, as in Subsection 1.3.1 the upper part of (1.38) is distributed according a $\frac{1}{2}\chi^2_2$ distribution with non-centrality parameter $SNR = 2\left|\alpha\right|^2 \mathbf{s}(\boldsymbol{\xi})^H \mathbf{R}^{-1}\mathbf{s}(\boldsymbol{\xi})$. Since the signal component of $\mathbf{r}$ is projected on $\mathbf{P}_s^{\perp}$, the denominator still follows a centered $\frac{1}{2}\chi^2_{2(N-1)}$ distribution. Using Cochran's theorem, those variables are still independent. By definition, this ratio follows a noncentral F-distribution with non-centrality parameter $2\left|\alpha\right|^2 \mathbf{s}(\boldsymbol{\xi})^H \mathbf{R}^{-1}\mathbf{s}(\boldsymbol{\xi})$ where $(2, 2(N-1))$ are the degrees of freedom of the chi-squared variables. Its CDF $F(x)$ reads:

$$F(x) = \sum_{i=0}^{\infty} \left(\frac{(SNR)^i}{i!} e^{-SNR} \right) I_{\frac{2x}{2x+2(N-1)}}(1+i, N-1)\,.$$

Then,

$$P_D = 1 - F\left(\left(w^2\right)''\right)\,. \tag{1.39}$$

The P_D can also be computed in the case of a SIRV signal model, and in this case, depends on the pdf of the texture parameter Θ [OPB15].

2 - On the statistics of the off-grid Normalized Matched Filter

At the end of the previous chapter, we introduced the off-grid GLRTs as our choice of detectors to deal with the off-grid mismatch, and we observed that one question that arises is related to the computation of their P_{FA} for a given threshold. Indeed, since the statistics of the test are much more involved, so is the computation of the P_{FA}, and, as far as we know, no such P_{FA}-threshold relationship exists in the detection literature. However, applied statisticians have long been interested in the related problem of computing the probability of a random process exceeding a given threshold. The goal of this chapter is to adapt their tools to the traditional detection hypothesis test formalism to provide a new P_{FA}-threshold relationship for the off-grid Normalized Matched Filter. The approach that we will borrow in this chapter translates this statistical problem into a geometrical one, which will enable us to provide some insightful comments on the off-grid NMF. This approach is only valid under some conditions on the threshold w which will be extensively discussed.

In Section 2.1, we show how computing the P_{FA}-threshold relationship of the normalized matched filter naturally reduces to the geometrical problem of computing the volume of tubes drawn around submanifolds of the sphere $\mathbb{S}^{2N-1}$. In Section 2.2, we show how to compute the volume of such tubes thanks to [Hot39; Wey39; SW95; KS89], which enables us to compute the P_{FA}-threshold relationship of the Normalized Matched Filter, in Section 2.3, for the $1D$ signal models introduced in the previous chapter as well as exact relationships in the case of STAP signal model (1.10) when testing on the whole parameter space. The cases where the parameter space is reduced to a single cell are covered by heuristics. We discuss the domain of validity of our relationships in Section 2.4. Finally, in Section 2.5, we evaluate our relationships as well as their domain of validity through numerical simulations.

Corollary 2.3.0.1 was the subject of a publication at the conference IEEE ICASSP 2022 [Dev+22a], and GRETSI 2022 [Dev+22b]. This work was extended, including our study on overlap, in a submitted journal paper [Dev+23b].

2.1 . Motivation for a geometrical approach

In this section, we show how computing the P_{FA}-threshold relationship of the off-grid NMF naturally reduces to a geometrical problem. For that purpose, we will first start by rewriting the off-grid NMF test (1.37) with real vectors, for any of the signal models. For the sake of clarity, in this whole chapter, $\mathbf{s}$ denotes the whitened and normalized version of the received signal, noted $\mathbf{s}^w$ in the previous section (we withdraw the superscript w in (1.20)). Since we are interested in computing a P_{FA}, in this chapter the received signal $\mathbf{r}$ is only constituted of noise, either a Gaussian or SIRV distribution so that $\mathbf{u}$, the whitened and normalized version of $\mathbf{r}$, is uniformly distributed over the sphere.

Let us introduce a parameter α that will play a role related to the phase of the target. For any $\alpha \in [0, 2\pi]$, note that

$$\mathrm{Re}\left(\mathbf{s}\left(\boldsymbol{\xi}\right)^H \mathbf{u} \exp\left(-i\alpha\right)\right) \leq \left|\mathbf{s}\left(\boldsymbol{\xi}\right)^H \mathbf{u}\right|, \tag{2.1}$$

those two quantities being equal for $\alpha = \angle \mathbf{s}\left(\boldsymbol{\xi}\right)^H \mathbf{u}$. We then have, decomposing $\mathbf{s}\left(\boldsymbol{\xi}\right)$ and $\mathbf{u}$ into real and imaginary parts:

$$\mathrm{Re}\left(\mathbf{s}\left(\boldsymbol{\xi}\right)^H \mathbf{u} e^{-i\alpha}\right) = \left(\boldsymbol{\gamma}_1(\boldsymbol{\xi}) \cos\alpha + \boldsymbol{\gamma}_2(\boldsymbol{\xi}) \sin\alpha\right)^T \underline{\mathbf{u}}, \tag{2.2}$$

where

$$\boldsymbol{\gamma}_1(\boldsymbol{\xi}) = \begin{bmatrix} \mathrm{Re}(\mathbf{s}(\boldsymbol{\xi})) \\ \mathrm{Im}(\mathbf{s}(\boldsymbol{\xi})) \end{bmatrix},$$
$$\boldsymbol{\gamma}_2(\boldsymbol{\xi}) = \begin{bmatrix} -\mathrm{Im}(\mathbf{s}(\boldsymbol{\xi})) \\ \mathrm{Re}(\mathbf{s}(\boldsymbol{\xi})) \end{bmatrix},$$

and

$$\underline{\mathbf{u}} = \begin{bmatrix} \mathrm{Re}(\mathbf{u}) \\ \mathrm{Im}(\mathbf{u}) \end{bmatrix}$$

is a $2N$-real valued noise vector drawn uniformly on $\mathbb{S}^{2N-1}$. Denoting

$$\boldsymbol{\gamma}(\boldsymbol{\xi}, \alpha) = \boldsymbol{\gamma}_1(\boldsymbol{\xi}) \cos\alpha + \boldsymbol{\gamma}_2(\boldsymbol{\xi}) \sin\alpha, \tag{2.3}$$

we have, from (2.1) and (2.2):

$$\max_{\alpha\in[0,2\pi]} \boldsymbol{\gamma}(\boldsymbol{\xi}, \alpha)^T \underline{\mathbf{u}} = \left| \mathbf{s}(\boldsymbol{\xi})^H \mathbf{u} \right|. \tag{2.4}$$

All the above shows us that we can rewrite the NMF (1.25) test with real-valued vectors and that in the process we introduce a manifold $\boldsymbol{\gamma}$ depending on the unknown parameters $\boldsymbol{\xi}$ and a phase term α. The maximization of the product between $\boldsymbol{\gamma}$ and the incoming signal $\underline{\mathbf{u}}$ with respect to α yields the NMF test quantity (1.25). Now recall that the off-grid NMF is obtained by maximizing the NMF test quantity with respect to the unknown parameters $\boldsymbol{\xi}$, thus the off-grid NMF (1.37) can simply be written using real vectors with the following expression:

$$\max_{(\boldsymbol{\xi},\alpha)\in\mathcal{D}\times[0,2\pi]} \boldsymbol{\gamma}(\boldsymbol{\xi}, \alpha)^T \underline{\mathbf{u}} \underset{\mathrm{H}_0}{\overset{\mathrm{H}_1}{\gtrless}} w. \tag{2.5}$$

Remark 2.1.1. *By manifold in this thesis, we always mean a Riemannian manifold, i.e. a smooth manifold equipped with a positive-definite inner product on the tangent space for each point in the manifold [RD16, p.168]. Furthermore, we will always assume that the manifold admits a single, global chart, and we will work using such a chart.*

Remark 2.1.2. *It is important to note that, due to the parameter α that appears in (2.3), the dimension M of the manifolds $\boldsymbol{\gamma}$ is always one more than the number of parameters in the signal model. For example, when dealing with Doppler detection (one unknown parameter), $M = 2$, and when dealing with range-Doppler detection (two unknown parameters), $M = 3$.*

As explained in Section 1.4, since $\boldsymbol{\gamma}$ and $\underline{\mathbf{u}}$ are both normalized, the product $\boldsymbol{\gamma}(\boldsymbol{\xi}, \alpha)^T \underline{\mathbf{u}}$ for fixed $(\boldsymbol{\xi}, \alpha)$ reduces to the cosine of the angle between $\boldsymbol{\gamma}(\boldsymbol{\xi}, \alpha)$ and $\mathbf{u}$. Comparing $\boldsymbol{\gamma}(\boldsymbol{\xi}, \alpha)^T \underline{\mathbf{u}}$ with w thus reduces to checking whether the angle between $\boldsymbol{\gamma}(\boldsymbol{\xi}, \alpha)$ and $\underline{\mathbf{u}}$ is lower than the angle $\phi = \cos^{-1} w$, or whether $\underline{\mathbf{u}}$ belongs to the *spherical cap* $\mathcal{SC}_{\boldsymbol{\xi},\alpha}$ of radius ϕ centered around $\boldsymbol{\gamma}(\boldsymbol{\xi}, \alpha)$, defined as

$$\mathcal{SC}_{\boldsymbol{\xi},\alpha} = \left\{ \mathbf{u} \in \mathbb{S}^{n-1}, \mathbf{u}^T \boldsymbol{\gamma}(\boldsymbol{\xi}, \alpha) > \cos(\phi) \right\},$$

as was shown in Figure 1.8b.

What happens when maximizing on α and $\boldsymbol{\xi}$ when performing the off-grid GLRT? Comparing $\max_{\boldsymbol{\xi},\alpha\in\mathcal{D}\times[0,2\pi]} \boldsymbol{\gamma}(\boldsymbol{\xi}, \alpha)^T \underline{\mathbf{u}}$ with the threshold w reduces to checking whether $\underline{\mathbf{u}}$ belongs to the union of the spherical caps $\mathcal{SC}_{\boldsymbol{\xi},\alpha}$ for $(\boldsymbol{\xi}, \alpha)$ varying in $\mathcal{D} \times [0, 2\pi]$. The union of spherical caps describes a *tube* $\mathcal{T}$ of radius ϕ embedded on $\mathbb{S}^{2N-1}$ around the manifold $\boldsymbol{\gamma}$ such that

$$\mathcal{T} = \left\{ \underline{\mathbf{u}} \in \mathbb{S}^{2N-1}, \max_{(\xi,\alpha)\in\mathcal{D}\times[0,2\pi]} \boldsymbol{\gamma}(\boldsymbol{\xi}, \alpha)^T \underline{\mathbf{u}} > w \right\}.$$

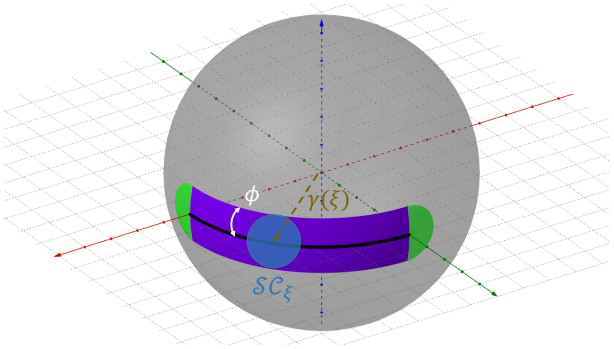

Figure 2.2.1: Example of a tube $\mathcal{T}$ on $\mathbb{S}^2$ around a curve $\boldsymbol{\gamma}(\xi)$. Since the curve is non-closed, semi-spherical caps (in green) are present at the ends of $\mathcal{T}$.

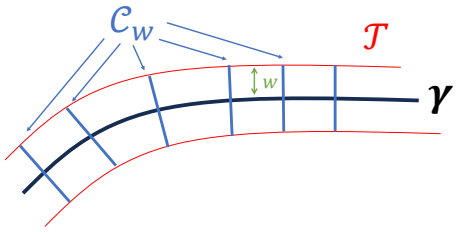

Figure 2.2.2: Example of cross-sections of $\boldsymbol{\gamma}$ embedded in $\mathbb{R}^2$.

The noise vector $\underline{\mathbf{u}}$ is distributed uniformly over the unit sphere $\mathbb{S}^{2N-1}$ due to the spherical invariance of the complex circular Gaussian distribution. A false alarm arises when a realization of $\underline{\mathbf{u}}$ falls into the tube $\mathcal{T}$. Since $\underline{\mathbf{u}}$ is uniformly distributed, the P_{FA} will simply be given by the ratio of the volume of the tube over the volume of the sphere so that the statistical problem of characterizing the P_{FA} is translated to the geometrical problem of finding the volume of the tube $\mathcal{T}$. This problem has spanned furnished literature in applied statistics since Hotelling's original paper in 1939 [Hot39; Gra03]. The next section presents the main results that we will use in order to find the volume of the tubes $\mathcal{T}$ that appear in our application.

2.2 . On the volume of tubes

In this section, we give the reader an introduction to how to derive the volume of a tube around manifolds constrained on the sphere $\mathbb{S}^{n-1}$ that we need in order to compute our P_{FA}-threshold relationships. We start with the presentation of Hotelling's original approach for computing the volume of tubes around a 1D curve drawn on the sphere, then we proceed to describe Weyl's generalization for the volume of tubes around manifolds of arbitrary dimension $M < n-1$. Weyl's approach does not take into account the borders of the manifolds: we will then see in the literature how to deal with a manifold with borders in the case $M = 2$, and then propose a heuristic in the case $M = 3$.

2.2.1 . The volume of tubes around curves: Hotelling's original formulation $(M = 1)$

In this subsection, we present Hotelling's original theorem for computing the surface of tubes on a sphere. Consider a curve $\boldsymbol{\gamma}(\xi)$ on the sphere $\mathbb{S}^{n-1}$, with $\xi \in [0, b]$. A tube $\mathcal{T}$ of geodesic radius ϕ is defined as the set of points with geodesic distance to the curve inferior to ϕ. Formally:

$$\mathcal{T} = \left\{\mathbf{u} \in \mathbb{S}^{n-1} : \exists\, \xi \in [0, b], \mathbf{u}^T \boldsymbol{\gamma}(\xi) > \cos(\phi)\right\}.$$

$\mathcal{T}$ can be seen as the union of the spherical caps $\mathcal{SC}_\xi = \left\{\mathbf{u} \in \mathbb{S}^{n-1}, \mathbf{u}^T \boldsymbol{\gamma}(\xi) > \cos(\phi)\right\}$. A graphical example of such a tube is provided in Figure 2.2.1.

Alternatively, sometimes in the literature authors prefer to define tubes as the union of *cross-sections*, defined as the set of points orthogonal to the derivative of $\boldsymbol{\gamma}$ at $\boldsymbol{\xi}$ located at a distance less than w as:

$$\mathcal{C}_w(\boldsymbol{\gamma}(\xi)) = \left\{\mathbf{u} \in \mathbb{S}^{n-1} : \mathbf{u}^T \dot{\boldsymbol{\gamma}}(\xi) = 0, \mathbf{u}^T \boldsymbol{\gamma}(\xi) > w\right\}.$$

where the notation $\dot{\boldsymbol{\gamma}}$ denotes the derivative of $\boldsymbol{\gamma}$ with respect to its scalar variable ξ. Figure 2.2.2 schematizes the cross-sections of a curve $\boldsymbol{\gamma}$ embedded in $\mathbb{R}^2$. This only leaves the purple part in Figure 2.2.1. In

this thesis, what we call a tube also contains the green semi-spherical caps at the ends.

In [Hot39], Hotelling gives a formula for computing the surface of the cross-sections of $\mathcal{T}$:

Theorem 2.2.1. [Hot39] *The surface enclosed by the cross-sections of a tube of geodesic radius ϕ around a curve on the real unit sphere $\mathbb{S}^{n-1}$ is the product of the length of the axial curve by the volume of the $n-2$ ball of radius $\sin\phi$:*

$$\frac{\pi^{(n-2)/2}}{\Gamma\left(\frac{n}{2}\right)} \sin^{n-2}(\phi)\,. \tag{2.6}$$

When dealing with a non-closed curve, one has to add the surface of the two end semi-spherical caps to Hotelling's formula in order to find the surface of $\mathcal{T}$.

Note that, in general, for Hotelling's formula to hold, it is necessary that each point in the tube belongs to a unique cross-section. Following Hotelling, this restriction will be called the non-overlap condition. Overlap phenomenons can happen when a tube draws back into itself (non-local overlap) or when its curvature becomes too large (local overlap). Non-overlap is locally guaranteed when the radius of the tube ϕ is low enough. More specifically, for a curve of constant radius of curvature ρ, Hotelling shows in [Hot39] that the condition for having no local overlap is the following:

$$\sin\phi \leq \rho\,. \tag{2.7}$$

In case of overlap, the surface given by Hotelling's theorem becomes an upper bound. An in-depth study of overlap phenomenon is given in Section 2.4.

2.2.2 . Extending Hotelling's theorem with Weyl's formula ($M > 1$)

2.2.2.1 Weyl's first formula

In [Wey39], Hotteling's approach is generalized in order to compute the surface of the "tubes" around any arbitrary M-dimensional manifold $\boldsymbol{\gamma}(\boldsymbol{\xi})$ on the sphere $\mathbb{S}^{n-1}$ for $\boldsymbol{\xi}$ in the set $\mathcal{D}$. In this case, the tube $\mathcal{T}$ of geodesic radius ϕ is defined as:

$$\mathcal{T} = \left\{ \underline{\mathbf{u}} \in \mathbb{S}^{n-1} : \max_{\boldsymbol{\xi}\in\mathcal{D}} \boldsymbol{\gamma}(\boldsymbol{\xi})^T \underline{\mathbf{u}} > \cos(\phi) \right\}. \tag{2.8}$$

Alternatively, similarly to what we noted in the previous section, tubes are sometimes defined in the literature [Gra03] as the union of cross-sections $\mathcal{C}_w(\boldsymbol{\gamma}(\boldsymbol{\xi}))$ such that:

$$\mathcal{C}_w(\boldsymbol{\gamma}(\boldsymbol{\xi})) = \left\{ \mathbf{u} \in \mathbb{S}^{n-1} : \mathbf{u}^T \frac{\partial \boldsymbol{\gamma}}{\partial \boldsymbol{\xi}^T} = \mathbf{0}, \mathbf{u}^T \boldsymbol{\gamma}(\boldsymbol{\xi}) > w \right\}. \tag{2.9}$$

This definition only coincides with (2.8) if $\boldsymbol{\gamma}$ is closed, that is to say, if $\boldsymbol{\gamma}$ does not have boundaries. As before, what we call a tube in this thesis is given by (2.8).

In the following, we present Weyl's first result. It is proven in appendix 2.A following Weyl's original proof so that readers can get more familiar with this formula and the kind of computations we will make in this chapter. Weyl's theorem is as follows:

Theorem 2.2.2. [Wey39] *Let $\boldsymbol{\gamma}(\boldsymbol{\xi})$ be a M-dimensional closed manifold embedded on the unit sphere $\mathbb{S}^{n-1}$. The volume of the cross-sections of $\mathcal{T}$ (which coincides with the volume of $\mathcal{T}$ when $\boldsymbol{\gamma}$ is closed) is, neglecting overlap effects:*

$$V = \int_{\boldsymbol{\gamma}} \left\{ \int \cdots \int_{t_1^2+\cdots+t_\nu^2 \leq \tan^2\phi} \frac{\det\left(\delta_j^i + \sum_{p=1}^{\nu} t_p\, G_i^j(p)\right)_{1\leq i,j\leq M}}{\left(1+t_1^2+\cdots+t_\nu^2\right)^{n/2}} dt_1 \ldots dt_\nu \right\} d\mathbf{s}\,, \tag{2.10}$$

where

- $d\mathbf{s} = \sqrt{\det g_{ij}}\, d\xi_1 \dots d\xi_M$ *is the surface element of* $\boldsymbol{\gamma}$*,*
- $g_{ij} = \dfrac{\partial \boldsymbol{\gamma}^T}{\partial \xi_i} \dfrac{\partial \boldsymbol{\gamma}}{\partial \xi_j}_{1 \leq i,j \leq M}$ *is called the first fundamental form of* $\boldsymbol{\gamma}$*. We note* $\left(g^{ij}\right) = \left(g_{ij}\right)^{-1}$*,*
- $\nu = n - 1 - M$ *is the codimension of the manifold,*
- $\boldsymbol{\gamma}(\boldsymbol{\xi}), \mathbf{n}_1, \dots, \mathbf{n}_\nu$ *is an arbitrary orthonormal basis for the manifold at* $\boldsymbol{\xi}$*,*
- $G_{ij}(p) = -\dfrac{\partial^2 \boldsymbol{\gamma}^T}{\partial \xi_i \partial \xi_j} \mathbf{n}_p{}_{1 \leq i,j \leq M}$ *is called the second fundamental form of* $\boldsymbol{\gamma}$ *for the normal* $\mathbf{n}(p)$*,*
- $G_i^j(p) = \sum_{k=1}^{M} g^{jk}\, G_{ik}(p)$.

Remark 2.2.1. *When* $\boldsymbol{\gamma}$ *is non-closed, in order to retrieve the volume of* $\mathcal{T}$ *as defined in* (2.8)*, some correction terms will need to be added to take into account the boundaries.*

The first and second fundamental forms are essential tools of differential geometry in order to characterize a manifold. The first fundamental form g_{ij} is the Riemannian metric induced by the standard scalar product on $\mathbb{R}^M$, and is used to compute various quantities on the manifold, such as angles or volumes, with $\sqrt{\det g_{ij}} d\xi_1 \dots d\xi_M$ being the volume element that needs to be integrated.

A case of interest is the following:

Definition 2.2.1. *Let* $\boldsymbol{\gamma}$ *be a M-dimensional manifold.* $\boldsymbol{\gamma}$ *is said to be Euclidean if there exists a parametrization such that the first fundamental form* g_{ij} *reduces to* $\mathbf{I}$*.*

In this case, the metric ds^2 is expressed as $\sum d\xi_i^2$ for every point in the manifold. We will see later that in many cases we deal with, the manifolds $\boldsymbol{\gamma}$ of interest are Euclidean, which will considerably simplify the computations.

The second fundamental form describes how the manifold curves relatively to its ambient space, and will be of lesser interest in this thesis. Readers are referred to [Gal22; RD16; SS78] for an introduction to differential geometry.

In order to use Weyl's formula (2.10) to compute the volume of a tube, one needs to find an orthonormal basis $\mathbf{n}$ to the manifold, and then compute the second fundamental form. But Weyl shows that (2.10) can be expressed in terms of the first fundamental form g_{ij} only (V is then called an *intrisic* quantity). In our applications, the coefficients g_{ij} can easily be found from the expression of the considered signals, making it possible to obtain the volume of the tube of interest in a more direct and easy fashion. In the next sections, we will first check that (2.10) reduces to the volume given by Hotelling's theorem 2.2.1 when $M = 1$. We will then develop the determinant in (2.10) and see how this formula simplifies for $M = 2$ and $M = 3$, only expressing it with quantities that are derived from the g_{ij}.

2.2.2.2 The case $M = 1$

In this section, we will check that (2.10) reduces to Hotelling's formula (2.6) when $M = 1$. In this case, the codimension is $\nu = n - 2$, and

$$\det\left(\delta_j^i + \sum_{p=1}^{\nu} t_p\, G_i^j(p)\right)_{1 \leq i,j \leq M} = 1 + \sum_{p=1}^{n-2} t_p\, G_1^1(p)\,.$$

Per imparity of t_p, the integral of the factors $\frac{t_p}{\left(1+t_1^2+\cdots+t_{n-2}^2\right)^{n/2}}$ over the $n-2$-dimensional ball of radius $\tan^2\phi$ is zero. After some technical computations, done in [Wey39, section 3], it is shown that the integral of the factor $\frac{1}{\left(1+t_1^2+\cdots+t_{n-2}^2\right)^{n/2}}$ is given by $w_{n-3}J_0$ where w_{n-3} is the surface of $\mathbb{S}^{n-3}$, obtained thanks to following formula giving the surface of $\mathbb{S}^{\nu-1}$:

$$w_{\nu-1} = \frac{2\pi^{\nu/2}}{\Gamma(\nu/2)}\,, \tag{2.11}$$

so that $w_{n-3} = \frac{2\pi^{(n-2)/2}}{\Gamma((n-2)/2)}$, and the term J_0 is defined thanks to:

$$J_0 \triangleq \int_0^{\phi} \sin^{\nu-1}\rho\,\cos^M\rho\;d\rho\,. \tag{2.12}$$

In our case $J_0 = \int_0^{\phi}\sin^{n-3}\rho\,\cos\rho\;d\rho$ is shown to be equal to $\frac{\sin^{n-2}(\phi)}{n-2}$ by integrating by part, and the volume V is thus expressed as

$$\begin{aligned} V &= w_{n-3}J_0\int_{\mathcal{D}} d\mathbf{s} \\ &= \frac{\pi^{\frac{n-2}{2}}}{\Gamma(\frac{n}{2})}\sin^{n-2}(\phi)\int_{\mathcal{D}} d\mathbf{s}\,. \end{aligned}$$

Since $\int_{\mathcal{D}} d\mathbf{s}$ is the length of $\boldsymbol{\gamma}$, the volume V is what was given by Hotelling's theorem 2.2.1.

2.2.2.3 The case $M = 2$

In this section, we will see how to express (2.10) in a simple form depending only on the first fundamental form g_{ij} for $M = 2$. In this case, the codimension is $\nu = n-3$, and

$$\begin{aligned} \det\left(\delta_j^i + \sum_{p=1}^{\nu} t_p\,G_i^j(p)\right)_{1\le i,j\le M} &= \det\begin{pmatrix} 1+\sum_{p=1}^{n-3} t_pG_1^1(p) & \sum_{p=1}^{n-3} t_pG_1^2(p) \\ \sum_{p=1}^{n-3} t_pG_2^1(p) & 1+\sum_{p=1}^{n-3} t_pG_2^2(p)\end{pmatrix} \\ &= 1+\sum_{p=1}^{n-3}(G_1^1(p)G_2^2(p)-G_2^1(p)G_1^2(p))t_p^2 + \sum_{p=1}^{n-3}\sum_{q=1,q\neq p}^{n-3}\ldots t_pt_q + \sum_{p=1}^{n-3}\ldots t_p\,. \end{aligned}$$

where the dotted factors are of no interest to us since the integral of the terms $\frac{t_pt_q}{\left(1+t_1^2+\cdots+t_{n-3}^2\right)^{n/2}}$ for $p\neq q$ and $\frac{t_p}{\left(1+t_1^2+\cdots+t_{n-3}^2\right)^{n/2}}$ over the $n-3$-dimensional ball of radius $\tan^2\phi$ is zero per imparity.

Again referring to [Wey39, section 3], it can be shown that the integrals of the factors $\frac{t_p^2}{\left(1+t_1^2+\cdots+t_{n-3}^2\right)^{n/2}}$ for any p over the $n-3$-dimensional ball of radius $\tan^2\phi$ are given by $w_{n-4}J_2$ where the term J_2 is defined with:

$$J_2 \triangleq \frac{1}{\nu}\int_0^{\phi}\sin^{\nu+1}\rho\,\cos^{M-2}\rho\;d\rho \tag{2.13}$$

Integrating the term $\frac{1}{\left(1+t_1^2+\cdots+t_{n-3}^2\right)^{n/2}}$ gives $w_{n-4}J_0$. This brings us to the following intermediate result:

$$V = w_{n-4}\left(J_0\int_{\mathcal{D}} d\mathbf{s} + J_2\int_{\mathcal{D}}\sum_{p=1}^{n-3} G_1^1(p)G_2^2(p) - G_2^1(p)G_1^2(p)d\mathbf{s}\right), \tag{2.14}$$

The integrand $\sum_{p=1}^{n-3} G_1^1(p)G_2^2(p) - G_2^1(p)G_1^2(p)$ in (2.14) can be expressed only in terms of the g_{ij} through the Riemannian tensor, that we set out to define in the following. For that purpose, we will need to define the Christofel symbols of the second kind $\mathbf{\Gamma}^{\kappa}_{\alpha\beta}$. For a manifold of arbitrary dimension M, those symbols are expressed in a coordinate system $(u^1,\ldots,u^M)$ as [SS78, p.76]:

$$\mathbf{\Gamma}_{\kappa\alpha\beta} = \frac{1}{2}\left(\frac{\partial g_{\alpha\kappa}}{\partial u^\beta} + \frac{\partial g_{\beta\kappa}}{\partial u^\alpha} - \frac{\partial g_{\alpha\beta}}{\partial u^\kappa}\right), \tag{2.15}$$

$$\mathbf{\Gamma}^{\kappa}_{\alpha\beta} = \sum_{\lambda} g^{\lambda\kappa}\,\mathbf{\Gamma}_{\lambda\alpha\beta}\,. \tag{2.16}$$

Then the Riemannian tensor reads [Wey39, section 4]:

$$R^{\kappa}_{\lambda\alpha\beta} = \left(\frac{\partial \mathbf{\Gamma}^{\kappa}_{\lambda\beta}}{\partial u^\alpha} - \frac{\partial \mathbf{\Gamma}^{\kappa}_{\lambda\alpha}}{\partial u^\beta}\right) + \sum_{\rho}\left(\mathbf{\Gamma}^{\kappa}_{\rho\alpha}\mathbf{\Gamma}^{\rho}_{\lambda\beta} - \mathbf{\Gamma}^{\kappa}_{\rho\beta}\mathbf{\Gamma}^{\rho}_{\lambda\alpha}\right). \tag{2.17}$$

Remark 2.2.2. *Notice how the Riemannian tensor is entirely characterized by the first fundamental form (g_{ij}) through the Christoffel symbols.*

"Raising the index λ" [SS78], we note

$$R^{\kappa\lambda}_{\alpha\beta} = \sum_{\mu} g^{\lambda\mu}\,R^{\kappa}_{\mu\alpha\beta}\,. \tag{2.18}$$

From the Gauss equations [Gra03, p.65], Weyl shows that for manifolds embedded on $\mathbb{S}^{n-1}$

$$R^{\kappa\lambda}_{\alpha\beta} - \left(\delta^\kappa_\alpha\delta^\lambda_\beta - \delta^\kappa_\beta\delta^\lambda_\alpha\right) = \sum_{p=1}^{\nu}\left(G^\kappa_\alpha(p)G^\lambda_\beta(p) - G^\kappa_\beta(p)G^\lambda_\alpha(p)\right), \tag{2.19}$$

where the δ^κ_α are the kronecker symbols which equal 1 if $\alpha=\kappa$ and 0 otherwise.

Thus, the term $\sum_{p=1}^{n-3} G_1^1(p)G_2^2(p) - G_2^1(p)G_1^2(p)$ in (2.14) is linked to the Riemannian tensor with $R^{12}_{12} - 1 = \sum_{p=1}^{n-3} G_1^1(p)G_2^2(p) - G_2^1(p)G_1^2(p)$. Taking all of this into account results in the following proposition for the volume V:

Corollary 2.2.2.1. *Consider a 2-dimensional manifold γ embedded on $\mathbb{S}^{n-1}$. The volume of the tube $\mathcal{T}$ of geodesic radius $\phi = \cos^{-1} w$ about γ (defined in (2.8)) is given by:*

$$V = w_{n-4}\left(J_0\int_{\mathcal{D}} d\mathbf{s} + J_2\int_{\mathcal{D}}\left(R^{12}_{12} - 1\right)d\mathbf{s}\right). \tag{2.20}$$

This expression of the volume only depends on the first fundamental form g_{ij}: indeed, the terms w_{n-4} and J_0, J_2 are constant, while the Riemannian tensor depends on the Christoffel symbols of the second kind, which in turn are determined by the first fundamental form.

An easy case arises when the manifold γ of interest is Euclidean. Indeed, in this case, the following property holds:

Corollary 2.2.2.2. *If γ is defined as in Corollary 2.2.2.1 is Euclidean, the volume V further reduces to:*

$$V = w_{n-4}\left(J_0|\mathcal{D}'| - J_2|\mathcal{D}'|\right)\,, \tag{2.21}$$

where $|\mathcal{D}'|$ is the surface measure of the parameter space $\mathcal{D}'$ for the parametrization ψ such that $g_{ij} = \mathbf{I}$.

Proof. The proof relies on the fact that the Riemannian tensor $R^{\kappa}_{\lambda\alpha\beta}$ equals zero for Euclidean manifolds. Indeed, since there exists a parametrization such that the first fundamental form is constant, the Christoffel symbols expressed in this parametrization equal zero (2.15), and thus so does the Riemannian tensor. Thus, (2.20) reduces to:

$$V = w_{n-4}\left(J_0\int_{\mathcal{D}'} d\mathbf{s} - J_2\int_{\mathcal{D}'} d\mathbf{s}\right). \tag{2.22}$$

For the parametrization ψ for which $g_{ij} = \mathbf{I}$, the volume element simply reduces to $d\mathbf{s} = d\psi_1 \dots d\psi_M$. In this case, the integrals $\int_{\mathcal{D}'} d\mathbf{s}$ simply reduce to:

$$\int_{\mathcal{D}'} d\mathbf{s} = |\mathcal{D}'|\,,$$

Injecting this expression in 2.22 yields the final result. □

2.2.2.4 The case $M = 3$

When $M = 3$, ν reduces to $n-4$, and:

$$\det\left(\delta^i_j + \sum_{p=1}^{\nu} t_p\, G^j_i(p)\right) = \det\begin{pmatrix} 1+\sum_{p=1}^{n-4} t_p G^1_1(p) & \sum_{p=1}^{n-4} t_p G^2_1(p) & \sum_{p=1}^{n-4} t_p G^3_1(p) \\ \sum_{p=1}^{n-4} t_p G^1_2(p) & 1+\sum_{p=1}^{n-4} t_p G^2_2(p) & \sum_{p=1}^{n-4} t_p G^3_2(p) \\ \sum_{p=1}^{n-4} t_p G^1_3(p) & \sum_{p=1}^{n-4} t_p G^2_3(p) & 1+\sum_{p=1}^{n-4} t_p G^3_3(p) \end{pmatrix},$$

$$= 1 + \sum_{p=1}^{n-4}(G^1_1(p)G^2_2(p) - G^1_2(p)G^2_1(p))t_p^2 + \sum_{p=1}^{n-4}(G^1_1(p)G^3_3(p) - G^1_3(p)G^3_1(p))t_p^2\,,$$

$$+ \sum_{p=1}^{n-4}(G^3_3(p)G^2_2(p) - G^3_2(p)G^2_3(p))t_p^2 + \dots\,.$$

where dotted factors are odd and so their integral over the ball of radius $\tan^2\phi$ cancels. The integrals of $\frac{1}{\left(1+t_1^2+\dots+t_{n-3}^2\right)^{n/2}}$ and $\frac{t_p^2}{\left(1+t_1^2+\dots+t_{n-3}^2\right)^{n/2}}$ over the $n-4$ dimensional ball are equal to $w_{n-5}J_0$ and $w_{n-5}J_2$, respectively. From (2.19), the terms $\sum_{p=1}^{n-4} G^1_1(p)G^2_2(p) - G^1_2(p)G^2_1(p) = R^{12}_{12} - 1$, $\sum_{p=1}^{n-4} G^1_1(p)G^3_3(p) - G^1_3(p)G^3_1(p) = R^{13}_{13} - 1$ and $\sum_{p=1}^{n-4} G^3_3(p)G^2_2(p) - G^3_2(p)G^2_3(p) = R^{23}_{23} - 1$. In the end, the above computations enable us to give the following corollary to Weyl's formula:

Corollary 2.2.2.3. *For a 3-dimensional manifold γ embedded on $\mathbb{S}^{n-1}$, the volume of the tube $\mathcal{T}$ of geodesic radius $\phi = \cos^{-1} w$ about γ (defined in (2.8)) is given by:*

$$V = w_{n-5}\left(J_0\int_{\mathcal{D}} d\mathbf{s} + J_2\int_{\mathcal{D}}(R^{12}_{12} + R^{23}_{23} + R^{13}_{13} - 3)\,d\mathbf{s}\right). \tag{2.23}$$

Similarly to the case $M = 2$, when $\boldsymbol{\gamma}$ is Euclidean, (2.23) *reduces to the simple form:*

$$V = w_{n-5}\left(J_0|\mathcal{D}'| - 3J_2|\mathcal{D}'|\right) , \tag{2.24}$$

where $\mathcal{D}'$ is the parameter space for the parametrization of $\boldsymbol{\gamma}$ such that $g_{ij} = \mathbf{I}$.

And here again, this volume only depends on the first fundamental form g_{ij} through the Riemannian tensor. The determinant computations that we did in the cases $M = 2$ and $M = 3$ are generalized for any dimension M in [Wey39, Section 4]. In the next section, we present Weyl's final formula.

2.2.2.5 Weyl's general formula $(M > 3)$

This section presents Weyl's generalization of the formula (2.20) and (2.23) obtained in the previous section. In this manuscript, we will limit our studies to a number of unknown parameters equal to $M = 2$ or $M = 3$, thus we will not need this general formulation in our developments : we will rather use the formula developed by hand in the previous sections since the general formulation is much more involved. It should, however, be useful to readers interested in extending our approach when the number of unknown parameters exceeds 3, when considering a range-Doppler-angle signal model for example.

For $\alpha, \beta, \kappa, \lambda \in [1, M]$, define $H\begin{pmatrix}\kappa\lambda\\ \alpha\beta\end{pmatrix}$ as:

$$H\begin{pmatrix}\kappa\lambda\\ \alpha\beta\end{pmatrix} \triangleq R^{\kappa\lambda}_{\alpha\beta} - \left(\delta^\kappa_\alpha\delta^\lambda_\beta - \delta^\kappa_\beta\delta^\lambda_\alpha\right) = \sum_{p=1}^{\nu}\left(G^\kappa_\alpha(p)G^\lambda_\beta(p) - G^\kappa_\beta(p)G^\lambda_\alpha(p)\right) . \tag{2.25}$$

Then, for even k with $2 \leq k \leq M$, define the following quantities H_k that appear when developing the determinant in (2.10):

$$H_k = \sum_{[\boldsymbol{\alpha},\boldsymbol{\beta}]} P\begin{pmatrix}\boldsymbol{\beta}\\ \boldsymbol{\alpha}\end{pmatrix} H\begin{pmatrix}\beta_1\beta_2\\ \alpha_1\alpha_2\end{pmatrix} H\begin{pmatrix}\beta_3\beta_4\\ \alpha_3\alpha_4\end{pmatrix} \dots H\begin{pmatrix}\beta_{k-1}\beta_k\\ \alpha_{k-1}\alpha_k\end{pmatrix} , \tag{2.26}$$

where $\boldsymbol{\alpha}$ and $\boldsymbol{\beta}$ are any k-terms ordered arrangements of the numbers $1, \dots M$, with $\boldsymbol{\alpha}$ and $\boldsymbol{\beta}$ featuring the same k-terms, excluding the redundant arrangements from the sum. In order to define what we mean by redundant, decompose $\boldsymbol{\alpha}$ and $\boldsymbol{\beta}$ as blocks of pairs as $\left(\begin{pmatrix}\alpha_1 & \alpha_2\\ \beta_1 & \beta_2\end{pmatrix}, \begin{pmatrix}\alpha_3 & \alpha_4\\ \beta_3 & \beta_4\end{pmatrix}, \dots, \begin{pmatrix}\alpha_{k-1} & \alpha_k\\ \beta_{k-1} & \beta_k\end{pmatrix}\right)$. Two arrangements are said to be redundant if we can switch from one to the other by inverting any pair $\alpha_{2e-1}, \alpha_{2e}$ (or β_{2e-1}, β_{2e}) or by permuting blocks of pairs. For example, in the case $M = 5$, in order to compute the term H_4, only one of the pairs of arrangements $\begin{pmatrix}1 & 2 & 3 & 5\\ 1 & 2 & 3 & 5\end{pmatrix}$, $\begin{pmatrix}1 & 2 & 3 & 5\\ 2 & 1 & 3 & 5\end{pmatrix}$ and $\begin{pmatrix}3 & 5 & 1 & 2\\ 3 & 5 & 1 & 2\end{pmatrix}$ will be kept in the sum: $\begin{pmatrix}1 & 2 & 3 & 5\\ 2 & 1 & 3 & 5\end{pmatrix}$ is obtained by inverting 1 and 2 in the first $\boldsymbol{\beta}$-pair of terms in $\begin{pmatrix}1 & 2 & 3 & 5\\ 1 & 2 & 3 & 5\end{pmatrix}$, while $\begin{pmatrix}3 & 5 & 1 & 2\\ 3 & 5 & 1 & 2\end{pmatrix}$ is obtained by inverting the two blocks of $\boldsymbol{\alpha}$ and $\boldsymbol{\beta}$ pairs in $\begin{pmatrix}1 & 2 & 3 & 5\\ 1 & 2 & 3 & 5\end{pmatrix}$. However, the arrangement $\begin{pmatrix}1 & 3 & 2 & 5\\ 1 & 2 & 3 & 5\end{pmatrix}$ is not redundant with any of those arrangements. $P\begin{pmatrix}\boldsymbol{\beta}\\ \boldsymbol{\alpha}\end{pmatrix}$ is defined as the parity of the permutation from $\boldsymbol{\alpha}$ to $\boldsymbol{\beta}$. Furthermore, set:

$$H_0 = 1 .$$

Weyl finally proves that the volume (2.10) reads:

$$V = w_{\nu-1} \sum_{k=0, k \text{ even}}^{M} J_k \int_{\mathcal{D}} H_k \, ds , \tag{2.27}$$

where w_ν is the surface of the unit sphere $\mathbb{S}^{\nu-1}$, obtained thanks to (2.11) and, for $k \geq 2$,

$$J_k = \frac{1}{\nu(\nu+2)\dots(\nu+k-2)} \int_0^\phi \sin^{\nu+k-1}\rho \, \cos^{M-k}\rho \; d\rho \,, \tag{2.28}$$

with J_0 defined as in (2.98)

In the next section, we see how to deal with non-closed manifolds, with borders.

2.2.3 . Dealing with the borders

2.2.3.1 Theorems in the case $M = 2$

Weyl's result gives the volume of the cross-sections of a manifold: as such, it will not exactly give the volume of a tube defined as in (2.8) around a manifold with boundaries. In [JS89] and [KS89], the result of Weyl is extended for manifolds of dimensions $M = 2$ with boundaries. Below is the version given in [JS89] in the special case where the manifold γ can be expressed as a linear combination of two orthogonal curves γ_1 and γ_2, thus reducing the number of non-linear parameters to only one:

Theorem 2.2.3. [JS89] *For $i \in [1,2]$, let $\gamma_i : [\theta_1, \theta_2] \to \mathbb{S}^{n-1}$ be regular curves. Assume $\gamma_1(\theta)^T \gamma_2(\theta) = 0$ for all θ. Let $Z(\theta) = \left[\left(\gamma_1(\theta)^T \mathbf{u}\right)^2 + \left(\gamma_2(\theta)^T \mathbf{u}\right)^2 \right]^{1/2}$ where $\mathbf{u}$ is uniformly distributed on $\mathbb{S}^{n-1}$. Then for $0 < w < 1$, we have:*

$$P\left(\max_{\theta_1 \leq \theta \leq \theta_2} Z(\theta) > w \right) \leq (1-w^2)^{(n-2)/2} + \frac{\Gamma\left(\frac{n}{2}\right) w (1-w^2)^{(n-3)/2}}{2\pi^{3/2}\,\Gamma\left(\frac{n-1}{2}\right)} \int_{\theta_1}^{\theta_2} \int_0^{2\pi} \left[\left\| \dot\gamma_1(\theta)\cos\Omega + \dot\gamma_2(\theta)\sin\Omega \right\|^2 - \left(\dot\gamma_1(\theta)^T \gamma_2(\theta) \right)^2 \right]^{1/2} d\Omega \, d\theta \,, \tag{2.29}$$

where $\dot\gamma_i(\theta)$ is the derivative of $\gamma_i(\theta)$ with respect to θ. When there is no overlap (see Section 2.4 for a detailed study), this inequality becomes equality.

Remark 2.2.3. *If we write $\gamma = \cos\Omega\gamma_1(\theta) + \sin\Omega\gamma_2(\theta)$, making use of the fact that $-\dot\gamma_1(\theta)^T\gamma_2(\theta) = \gamma_1(\theta)^T\dot\gamma_2(\theta)$ and $-\dot\gamma_1(\theta)^T\gamma_1(\theta) = 0$ (obtained by differentiating $\gamma_1(\theta)^T\gamma_1(\theta) = 1$ and $\gamma_1(\theta)^T\gamma_2(\theta) = 0$), we have that*

$$g_{ij} = \begin{bmatrix} \left\| \dot\gamma_1(\theta)\cos\Omega + \dot\gamma_2(\theta)\sin\Omega \right\|^2 & \dot\gamma_1(\theta)^T\gamma_2(\theta) \\ \dot\gamma_1(\theta)^T\gamma_2(\theta) & 1 \end{bmatrix}$$

so that $d\mathbf{s} = \sqrt{\det g_{ij}}\, d\Omega d\theta$ is the integrand in (2.29), as well as the integrand $\int_{\mathcal{D}} d\mathbf{s}$ in (2.20) derived from Weyl's formula (2.10) to get the volume of cross-sections.

The result provided in [KS89] is more general and does not rely on this assumption on γ. It makes use of the Gauss-Bonnet theorem, which links the *Gaussian curvature* of γ with its *Euler characteristic*, a quantity that will be the focus of Chapter 3. We will not need the volume expression developed in [KS89] as, as we will see, the manifolds γ we will consider for $M = 2$ meet the hypotheses of theorem 2.2.3. However, following the authors' approach, we will use the Gauss-Bonnet theorem later in this Chapter to prove a result on the P_{FA}-threshold relationship of the NMF for STAP detection under colored noise.

2.2.3.2 An heuristic to treat the case $M = 3$

While the articles that treat the borders rigorously mostly investigate the case $M = 2$, we propose the following heuristic to deal with the case $M = 3$ in the case of an Euclidean manifold. In this case, the representation of the manifold γ in $\mathbb{R}^3$ is that of its parameter space for the parametrization ψ such that $g_{ij} = \mathbf{I}$.

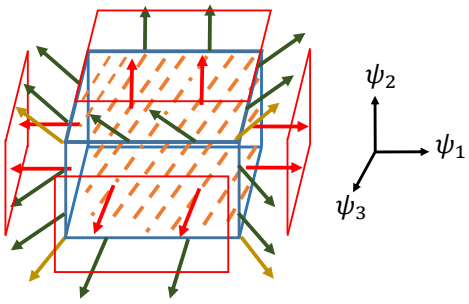

Figure 2.2.3: Illustration of γ when defined on a regular cuboid of dimensions $\Delta\psi_1, \Delta\psi_2, \Delta\psi_3$.

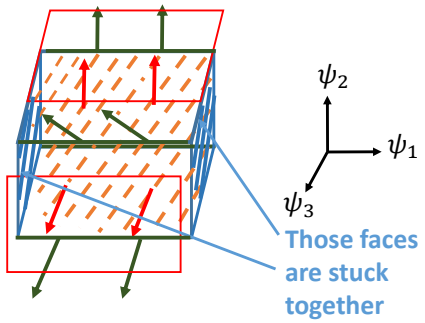

Figure 2.2.4: Illustration of γ when defined on a cuboid with two of its faces stuck together.

- If the parameter space is a regular rectangular cuboid of dimensions $\Delta\psi_1, \Delta\psi_2, \Delta\psi_3$, as represented schematically in Figure 2.2.3, the heuristic consists of adding up
  - the volume of the cross-sections of γ given by (2.24) with $|\gamma| = \Delta\psi_1\Delta\psi_2\Delta\psi_3$ (dotted, in orange on the figure),
  - the volume of the outer cross-sections of the borders $\partial\gamma$, which is, under the no overlap regime, equal to half the volume of the cross-sections of the borders $\partial\gamma$. This volume is given by (2.21) with $|\partial\gamma| = \Delta\psi_1\Delta\psi_2 + \Delta\psi_2\Delta\psi_3 + \Delta\psi_1\Delta\psi_3$ (in red on the figure).
  - the volume of the cross-sections of the edges of the border $\partial\gamma_E$ not enclosed in the border cross-sections (represented by green arrows on the figure). It can be obtained through Hotelling's formula (2.6), using $\Delta\psi_1 + \Delta\psi_2 + \Delta\psi_3$ as the length of the edges.
  - the volume of a single spherical cap (to take into account the 8 corners of the parameter space, represented by yellow arrows on the figure).
- Sometimes the parameter space will be a rectangular cuboid but with two of its faces stuck together, as will happen when the manifold is closed along one of its dimensions when testing for a Doppler shift in $[0, 1]$ for example. This case is represented in Figure 2.2.4 where the previous cuboid has its faces along dimension ψ_1 stuck together, and the heuristic is this time obtained by adding up:
  - the volume of the cross-sections of γ given by (2.24) where this time $|\gamma| = \Delta\psi_1\Delta\psi_2\Delta\psi_3$,
  - the volume of the outer cross-sections of the borders $\partial\gamma$, given by (2.21) with $|\partial\gamma| = \Delta\psi_1\Delta\psi_2 + \Delta\psi_1\Delta\psi_3$.
  - the volume of the cross-sections of the edges of the border $\partial\gamma_E$ not enclosed in the border cross-sections obtained through Hotelling's formula (2.6) using $\Delta\psi_1$ as the length of the edges.

  Note that in this case, there are no corners to take into account.

Now that we have presented all the theoretical tools that we will need, we can finally begin applying them to the off-grid NMF in the next section.

2.3 . Application to the P_{FA}-threshold relationship of the off-grid NMF

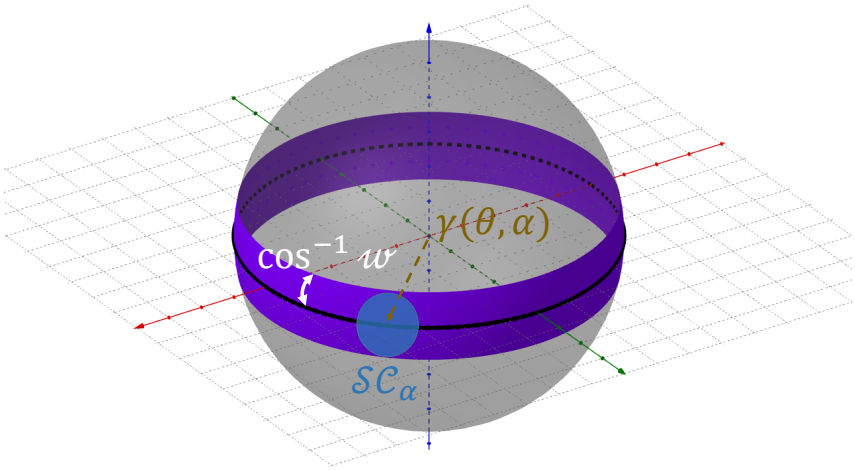

Figure 2.3.1: $\mathcal{T}$ (in violet) embedded on the unit sphere $\mathbb{S}^2$ in $\mathbb{R}^3$. $\mathcal{SC}_\alpha$ is drawn in blue. [Hoh02]

We start this section with an easy application of Subsection 2.2.1 in order to find an original alternative derivation of the P_{FA}-threshold relationship of the NMF. Then we apply the results of Subsection 2.2.3.1 on manifolds with borders in order to find new P_{FA}-threshold relationships of the NMF with one unknown parameter in Subsection 2.3.2. Finally, the particularization of Weyl's formula for $M = 3$, along with the heuristic detailed in 2.2.3.2, are used in order to find the P_{FA}-threshold relationship with two unknown parameters in Subsection 2.3.3.

Remark 2.3.1. *Most results of this section can more or less be obtained as corollaries of the most general result given in Subsection 2.3.3.2 by using Weyl's general formula* (2.27)*. We follow a more didactic approach, extending the results little by little using more and more tools from the tube theory introduced in Section 2.2.*

2.3.1 . An alternative derivation for the P_{FA}-threshold relationship of the on-grid NMF

In this section, we provide a simple alternative derivation to the classical method [Jay02; SF94] for the on-grid P_{FA} of the NMF (1.25). In this simple case, $\boldsymbol{\xi}$ is fixed and the maximization is only performed on α.

A false alarm occurs when $\underline{\mathbf{u}} \in \mathcal{T}$, where $\mathcal{T}$ is a tube drawn around the curve $\boldsymbol{\gamma}(\boldsymbol{\xi}, \alpha)$ parameterized by α for fixed $\boldsymbol{\xi}$:

$$\mathcal{T} = \left\{ \underline{\mathbf{u}} \in \mathbb{S}^{2N-1}, \max_{\alpha \in [0,2\pi]} \boldsymbol{\gamma}(\boldsymbol{\xi}, \alpha)^T \underline{\mathbf{u}} > w \right\}. \tag{2.30}$$

The tube $\mathcal{T}$ we deal with here is represented in Figure 2.3.1 in $\mathbb{R}^3$. Note that $\mathcal{T}$ is drawn around a closed curve: indeed $\boldsymbol{\gamma}(\boldsymbol{\xi}, 0) = \boldsymbol{\gamma}(\boldsymbol{\xi}, 2\pi)$, so that we will not have to add the volume of two semi-spherical caps at its ends in order to retrieve its volume.

We can apply Theorem 2.2.1 to the tube $\mathcal{T}$ (2.30) to find the P_{FA} of the NMF (1.27). The length of the axial curve is equal to 2π. We prove that $\mathcal{T}$ does not overlap in Appendix 2.B.1 so that the surface given by Hotelling's formula is thus exact in this case. Applying Theorem 2.2.1 with $n = 2N$, $\phi = \cos^{-1} w$ gives:

$$\begin{aligned} V &= 2\pi \frac{\pi^{N-1}}{\Gamma(N)} \sin^{2(N-1)}(\phi) \\ &= \frac{2\,\pi^N}{\Gamma(N)} \left(1 - w^2\right)^{N-1}. \end{aligned} \tag{2.31}$$

Dividing (2.31) by the surface $\frac{2\,\pi^N}{\Gamma(N)}$ of $\mathbb{S}^{2N-1}$ leads to the well-known expected result (1.27). This geometrical approach provides an alternative to the traditional one based on statistical tools [SF94].

2.3.2 . The P_{FA}-threshold relationship of the off-grid NMF with one unknown parameter

In this section, the unknown parameter vector $\boldsymbol{\xi}$ is a scalar ξ representing an unknown Doppler shift, angle, or delay in radar. Unfortunately, Hotelling's result is not immediately applicable to the considered GLRT (2.5): since a maximization on the parameter ξ is introduced, the acceptance region, in this case, is a new tube $\mathcal{T}$ around the two-dimensional manifold $\boldsymbol{\gamma}(\xi, \alpha)$:

$$\mathcal{T} = \left\{ \underline{\mathbf{u}} \in \mathbb{S}^{2N-1}, \max_{(\xi,\alpha)\in\mathcal{D}\times[0,2\pi]} \boldsymbol{\gamma}(\xi,\alpha)^T \underline{\mathbf{u}} > w \right\}.$$

Note that in this case, $\mathcal{T}$ follows a manifold that is often not closed since, writing $\mathcal{D} = [\xi_1, \xi_2]$, $\boldsymbol{\gamma}(\xi_1, \alpha) \neq \boldsymbol{\gamma}(\xi_2, \alpha)$ in general. This is the case for a radar Doppler resolution cell $\mathcal{D}_k$ (1.32), for example. Unlike previously, when computing the surface of the tube, a term accounting for its boundaries will appear.

Hotelling's result does not cover this multi-dimensional manifold case as it gives the surface of a tube around a curve. However, as we mentioned in Subsection 2.3.3, there exist extensions of Hotelling's formula for the computation of the volume of tubes around 2D manifolds. Specifically, it turns out that we can reformulate our problem in order to fulfill the assumptions of Theorem 2.2.3 with $n = 2N$. Indeed, using (2.3) and (2.4), we can check that $\boldsymbol{\gamma}_1(\xi)$ and $\boldsymbol{\gamma}_2(\xi)$ are orthogonal, and that:

$$\left| \mathbf{s}\left(\xi\right)^H \mathbf{u} \right|^2 = \left| \boldsymbol{\gamma}_1(\xi)^T \underline{\mathbf{u}} \right|^2 + \left| \boldsymbol{\gamma}_2(\xi)^T \underline{\mathbf{u}} \right|^2 ,$$

so that Theorem 2.2.3 gives us the desired P_{FA} (when equality holds in (2.29)). Follows the first original result of the thesis:

Corollary 2.3.0.1. *In the absence of overlap (low P_{FA} regimes), for one unknown parameter using signal models* (1.7) *for Doppler (or angle) detection and* (1.5) *for range detection with a chirp (swapping N with K in this case), the P_{FA} for the GLRT* (1.37) *is given by:*

$$P_{FA} = (1-w^2)^{N-1} + \frac{\Gamma(N)\, w\, (1-w^2)^{N-\frac{3}{2}}}{\pi^{1/2}\, \Gamma\left(N-\frac{1}{2}\right)} \int_{\xi_1}^{\xi_2} \left\| \dot{\boldsymbol{\gamma}}_1(\xi)^T \mathbf{P}^{\perp}_{\boldsymbol{\gamma}_2(\xi)} \right\| d\xi \,, \tag{2.32}$$

where $\mathbf{P}^{\perp}_{\boldsymbol{\gamma}_2(\xi)} = \mathbf{I} - \boldsymbol{\gamma}_2(\xi)\boldsymbol{\gamma}_2(\xi)^T$ is the orthogonal projector on $\boldsymbol{\gamma}_2(\xi)$. Under white noise ($\boldsymbol{\Gamma} = \sigma^2\, \mathbf{I}$), this result simplifies to:

$$P_{FA} = (1-w^2)^{N-1} + \sqrt{\frac{\pi}{3}}\, \frac{\Gamma(N)\, w\, (1-w^2)^{N-\frac{3}{2}}}{\Gamma\left(N-\frac{1}{2}\right)}\, \sqrt{(N^2-1)}\, (\xi_2 - \xi_1) \,. \tag{2.33}$$

When $\mathcal{D} = [0, 1]$, i.e. when the whole spectral domain is under test for Doppler detection using signal model (1.7)*, the first term has to be removed from the equations.*

In the colored noise case, the integral in (2.32) can be easily evaluated numerically, using the following expression of $\dot{\boldsymbol{\gamma}}_1(\xi)$:

$$\dot{\boldsymbol{\gamma}}_1(\xi) = \left(\mathbf{I} - \boldsymbol{\gamma}_1(\xi)\boldsymbol{\gamma}_1(\xi)^T\right) \mathbf{B}^{-1} \left(\left(\mathbf{B}\boldsymbol{\gamma}_2(\xi)\right) \odot \begin{bmatrix} \mathbf{x} \\ \mathbf{x} \end{bmatrix} \right) ,$$

where $\mathbf{B} = \begin{bmatrix} \mathrm{Re}(\boldsymbol{\Gamma}^{-1/2}) & -\mathrm{Im}(\boldsymbol{\Gamma}^{-1/2}) \\ \mathrm{Im}(\boldsymbol{\Gamma}^{-1/2}) & \mathrm{Re}(\boldsymbol{\Gamma}^{-1/2}) \end{bmatrix}^{-1}$ is designed to unwhiten $\boldsymbol{\gamma}_1$ and $\boldsymbol{\gamma}_2$ (and $\mathbf{B}^{-1}$ whitens them), with $\mathbf{x}$ as in (2.78) in the case of Doppler detection using signal model (1.7) or (2.84) in case of range detection using a chirp waveform with signal model (1.5).

Proof. The proof is provided in Appendix 2.B.2. It is a straight application of Theorem 2.2.3 to our manifolds γ_1, γ_2. □

Remark 2.3.2. *Note that the white noise relationship obtained for range detection using a chirp waveform (signal model* (1.5) *is the same as the one obtained when using an FMCW (signal model* (1.7)*) waveform.*

Note that the first term $(1-w^2)^{N-1}$ in the expression (2.33) can be seen as the surface of two semi-spherical caps at the extremities of a tube (to be exact, they must be seen as two semi-"strips" as can be seen in figure 2.3.1, bordering the surface described by $\boldsymbol{\gamma}$, but visualizing the tube around $\boldsymbol{\gamma}$ as simple tube such as the one on 2.2.1 essentially allows for the same interpretations and is easier to represent). The surface of the semi-spherical caps is equal to the P_{FA} of the on-grid NMF expressed in (1.27). For detection on the whole spectral domain (i.e. $\mathcal{D} = [0,1]$), this term disappears since the manifold is closed in this case and the semi-spherical caps thus do not appear. The second term shows the influence of the manifold induced by the off-grid nature of the problem. Here, the term $\int_{\xi_1}^{\xi_2} \left\| \dot{\boldsymbol{\gamma}}_1(\xi)^T \mathbf{P}^{\perp}_{\boldsymbol{\gamma}_2(\xi)} \right\| d\xi$, which reduces to $\pi \frac{\sqrt{N^2-1}}{3} (\xi_2 - \xi_1)$ under white noise, plays a role akin to the manifold length, and the rest of the rightmost term is the surface of a cross-section divided by the area of $\mathbb{S}^{2N-1}$.

The relationships given in Corollary 2.3.0.1 are upper bounds in the presence of overlap. In this case, they still hold interest in the radar context where controlling the P_{FA} is fundamental. Besides, simulations of Subsection 2.5.1 show that even in the presence of overlap, the relationship quickly becomes a very precise approximation of the true P_{FA}-threshold relationship. Section 2.4 investigates the conditions under which no overlap happens.

2.3.3 . The P_{FA}-threshold relationship of the NMF with two unknown parameter

When dealing with two unknown parameters, for example for range-Doppler or STAP detection, $\boldsymbol{\xi}$ becomes a vector of two parameters, and as such the manifold $\boldsymbol{\gamma}(\boldsymbol{\xi}, \alpha)$ is defined on $M = 3$ parameters. The theorems presented in Subsection 2.2.3.1 to deal with manifolds with borders and that we used to find the P_{FA}-threshold relationships in the cases of one unknown parameter are not enough to deal with those contexts, and we have to start back from Weyl's formula for $M = 3$ (2.23) in order to find the P_{FA}-threshold relationships of the off-grid GLRT. First, we tackle the case of white noise, in which we will see that the considered manifolds are Euclidean. Then, we will consider the more involved case of detection under colored noise.

2.3.3.1 Under white noise

In this section, we consider the noise to be white, that is to say, $\boldsymbol{\Gamma} = \mathbf{I}$. Our first step is to show that the manifolds described by $\boldsymbol{\gamma}$ for STAP detection (signal model (1.10)) is Euclidean under this noise context, which motivates the following lemma.

Lemma 2.3.1. *The manifold described by* $\boldsymbol{\gamma}$ (2.3) *defined by* $\mathbf{s}$ *with signal model* (1.10) *is Euclidean under white noise.*

Proof. To prove the lemma, we have to exhibit a new parametrization $\boldsymbol{\psi} = (\alpha, \boldsymbol{\zeta})$ such that the first fundamental form of the manifold $(g_{ij}) = \left(\frac{\partial \boldsymbol{\gamma}}{\partial \psi_i}^T \frac{\partial \boldsymbol{\gamma}}{\partial \psi_j} \right)$ is equal to the identity, for the STAP signal model (1.10).

Noting $\boldsymbol{\psi}' = (\alpha, \theta, \mu)$ the original parametrization, the first fundamental form $\left(\frac{\partial \boldsymbol{\gamma}}{\partial \psi'_i}^T \frac{\partial \boldsymbol{\gamma}}{\partial \psi'_j} \right)$ is not identity. Actually, it is not even diagonal since the derivatives $\frac{\partial \boldsymbol{\gamma}}{\partial \alpha}$, $\frac{\partial \boldsymbol{\gamma}}{\partial \theta}$ and $\frac{\partial \boldsymbol{\gamma}}{\partial \mu}$ are not, in general, orthogonal. We redefine the steering vectors $\mathbf{d}(\theta)$ and $\mathbf{d}(\mu)$ (signal model Doppler or Angle (1.7)) that appear in $\mathbf{s}$ (1.10). We take the following vector $\mathbf{d}'(v)$ and $\mathbf{d}'(u)$ instead of $\mathbf{d}(\theta)$ and $\mathbf{d}(\mu)$ in the derivations, changing the origin of phases and rescaling the Doppler and angle parameters, the new set of variables under consideration being $\boldsymbol{\psi} = (\alpha, v, u)$:

$$(\mathbf{d}'(v))_k = \frac{1}{\sqrt{N}} \exp\left(2i\pi \left(k - \frac{N-1}{2} \right) l_\theta^{-1} v \right), \tag{2.34}$$

$$(\mathbf{d}'(u))_k = \frac{1}{\sqrt{P}} \exp\left(2i\pi \left(k - \frac{P-1}{2} \right) l_\mu^{-1} u \right), \tag{2.35}$$

for $0 \leq n \leq N-1$, $0 \leq k \leq P-1$ and where

$$l_\theta = \pi \sqrt{\frac{N^2-1}{3}} \quad , \quad v = l_\theta \, \theta \, ,$$
$$l_\mu = \pi \sqrt{\frac{P^2-1}{3}} \quad , \quad u = l_\mu \, \mu \, .$$

Since $\mathbf{d}'^* = \mathbf{J}_N \mathbf{d}'$ with $\mathbf{J}_N$ defined in Appendix 2.C, $\mathbf{d}'$ is centrosymetric. Thus the vector $\mathbf{d}'$ is said to be the centrosymmetric version of $\mathbf{s}$. As the passage from $\mathbf{s}$ to $\mathbf{d}'$ just introduces a constant phase term $e^{-2i\pi \frac{N-1}{2}\theta}$ that can be put in the unknown complex amplitude α, it is equivalent to taking one or the other. The passage from $\mathbf{d}'(\theta)$ to $\mathbf{d}'(v)$ or $\mathbf{d}'(\mu)$ to $\mathbf{d}'(u)$ is then just a reparametrization.

Remark 2.3.3. *We will often make reference to this centrosymmetric parametrization in the rest of this thesis. The vector of unknown parameters (v, u) will be noted $\boldsymbol{\zeta}$, and takes values in $\mathcal{D}' = \left[\pi\sqrt{\frac{N^2-1}{3}}\theta_1, \pi\sqrt{\frac{N^2-1}{3}}\theta_2 \right] \times \left[\pi\sqrt{\frac{P^2-1}{3}}\mu_1, \pi\sqrt{\frac{P^2-1}{3}}\mu_2 \right]$.*

After some tedious computations, relegated in the appendix 2.B.3, we show that

$$\frac{\partial \boldsymbol{\gamma}}{\partial \alpha}^T \frac{\partial \boldsymbol{\gamma}}{\partial \alpha} = \frac{\partial \boldsymbol{\gamma}}{\partial v}^T \frac{\partial \boldsymbol{\gamma}}{\partial v} = \frac{\partial \boldsymbol{\gamma}}{\partial u}^T \frac{\partial \boldsymbol{\gamma}}{\partial u} = 1 \, ,$$
$$\frac{\partial \boldsymbol{\gamma}}{\partial u}^T \frac{\partial \boldsymbol{\gamma}}{\partial v} = \frac{\partial \boldsymbol{\gamma}}{\partial u}^T \frac{\partial \boldsymbol{\gamma}}{\partial \alpha} = \frac{\partial \boldsymbol{\gamma}}{\partial v}^T \frac{\partial \boldsymbol{\gamma}}{\partial \alpha} = 0.$$

This proves that the first fundamental form $\left(\frac{\partial \boldsymbol{\gamma}^T}{\partial \psi_i} \frac{\partial \boldsymbol{\gamma}}{\partial \psi_j} \right)_{1 \leq i,j \leq 3}$ is equal to the identity matrix, and thus that $\boldsymbol{\gamma}$ is Euclidean (the centrosymmetry makes it so that the first fundamental form $\left(\frac{\partial \boldsymbol{\gamma}^T}{\partial \psi_i} \frac{\partial \boldsymbol{\gamma}}{\partial \psi_j} \right)_{1 \leq i,j \leq 3}$ is diagonal, while the rescaling of the variables normalizes the diagonal terms so that the first fundamental form is equal to identity).

□

The previous lemma enables us to express the P_{FA} easily by using Weyl's formula (2.27) when the manifold $\boldsymbol{\gamma}$ is closed. $\boldsymbol{\gamma}$ is closed when performing detection on the whole Doppler and angle domains i.e. when $\mathcal{D} = [0,1]^2$.

Corollary 2.3.0.2. *Using signal model (1.10) for STAP detection on the whole domain, i.e. $\mathcal{D} = [0,1]^2$, when w is chosen big enough so that no overlap phenomena happens, the PFA of the off-grid GLRT under white noise is given by:*

$$PFA = \frac{\pi}{6} \left(1 - w^2\right)^{NP-2} \left((2NP-1)\, w^2 - 1 \right) \sqrt{N^2-1} \sqrt{P^2-1} \, . \tag{2.36}$$

A detailed study of the non-overlap conditions is provided in Section 2.4.

Proof. This is a straight application of Weyl's formula (2.24) for an Euclidean manifold. The detailed proof is given in Appendix 2.B.4. □

This is a nice result, however, we would like to extend it to the STAP cases where the search domain is not the whole domain, for example when $\mathcal{D}$ is restricted to a single cell $\mathcal{D}_k$, in order to detect multiple targets in a scene. However in this case, the manifold γ is not closed anymore in this case, and Weyl's formula will only give the exact volume of $\mathcal{T}$ for closed manifolds. Extending Weyl results rigorously to non-closed manifolds is not a trivial task: in fact, this appears to be an open problem in arbitrary dimension [Adloo].

We propose here to treat the case of detection over an arbitrary domain through the heuristic described in Subsection 2.2.3.2, which consists of adding corrections terms to the formula (2.36) which takes into account the boundaries. Using the centrosymmetric parametrization $\psi = (\alpha, v, u)$, we are here in the case of the rectangular cuboid of dimensions $\Delta\alpha, \Delta v, \Delta u$ with two of its faces stuck together along the α axis. Applying the method detailed here yields a heuristic for the volume of the tube $\mathcal{T}$, and dividing it by the surface of $\mathbb{S}^{2N-1}$ gives the following heuristic for the P_{FA}-threshold relationship:

Heuristic 2.3.1. *For STAP detection, when testing on a search domain $\mathcal{D} = [\theta_1, \theta_2] \times [\mu_1, \mu_2]$, the P_{FA}-threshold relationship of the off-grid GLRT is given by:*

$$\begin{aligned} P_{FA} = {} & \frac{\pi}{6}\left(1-w^2\right)^{NP-2}\left((2NP-1)\,w^2-1\right)\sqrt{N^2-1}\,\sqrt{P^2-1}(\theta_2-\theta_1)\left(\mu_2-\mu_1\right) \\ & + \left((\theta_2-\theta_1)\sqrt{N^2-1}+(\mu_2-\mu_1)\sqrt{P^2-1}\right)\sqrt{\frac{\pi}{3}}\,\frac{\Gamma(NP)\,w\left(1-w^2\right)^{NP-\frac{3}{2}}}{\Gamma\left(NP-\frac{1}{2}\right)} \\ & + \left(1-w^2\right)^{NP-1}. \end{aligned} \tag{2.37}$$

Remark 2.3.4. *We saw in Subsection 2.3.2 that the volume of tubes around a manifold γ with one unknown parameter with borders could be expressed as a constant term, corresponding to the volume of a "strip" on the sphere, represented in* (2.3.1) *plus another term, equal to the volume of the cross-section of γ. While an accurate representation of the tube around γ is only possible when depicting γ as a surface on the sphere, closed along one of its dimensions, looking at Figure 2.2.1 is a good way to make sense of what happens. Similarly, the heuristic that we use here can be visualized by representing γ as a surface on the sphere in Figure 2.3.2, losing a dimension in the process, in a way that is perhaps easier to understand than Figure 2.2.4*

- *the cross-sections of γ are represented in orange,*
- *the outer cross-sections around the borders $\partial\gamma$ are represented in red,*
- *the volume represented in green corresponds to the green volume in Figure 2.2.1, i.e. the volume of the strip in the phase α, and the volume around the edges of the borders $\partial\gamma_E$ in the heuristic of Subsection 2.2.3.2.*

Numerical simulations in Section 2.5 suggest that this seems to be the right way to address the problem of testing on a single cell for STAP detection.

Unfortunately, the distance-Doppler signal model (1.8) using a chirp does not seem to be Euclidean: this is due to the fact that its derivates $\dfrac{\partial \mathbf{s}}{\partial r}$ depend on r. As a consequence, it cannot be treated as above. However, note that the STAP "result" (2.37) can be extended for radar FMCW range-Doppler detection since it shares the same signal model. We will see in simulations that the P_{FA}-threshold relationship obtained this way fits very well with the empirical relationship obtained when using a chirp and may be used in order to set the P_{FA} in this case. We suspect that as in the case of range detection using a chirp waveform, the P_{FA}-threshold relationship for range-Doppler detection using a chirp waveform is the same as when using a FMCW waveform.

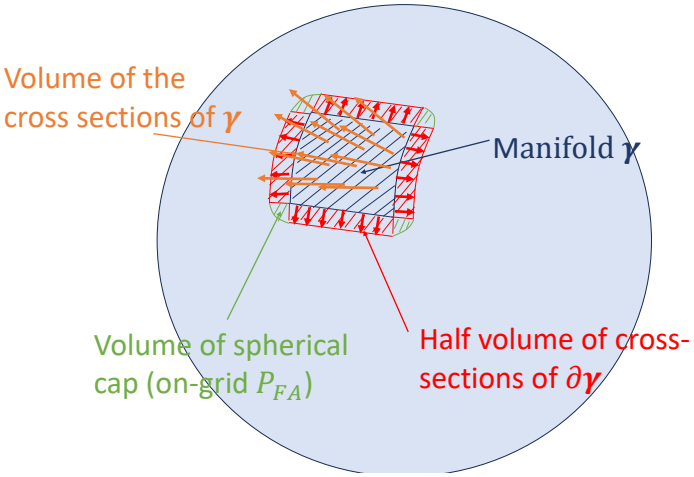

Figure 2.3.2: Representation of the heuristic method for the volume of tubes around a manifold with two unknown parameters, represented on $\mathbb{S}^2$ (bear in mind that this representation serves as a conceptual aid for the reader, while the actual manifold is three-dimensional).

2.3.3.2 Under colored noise

A white Gaussian noise model is sometimes unrealistic, especially for STAP detection: STAP detection is precisely made in order to mitigate clutter which is not white Gaussian. It would thus be useful to extend the previous results to colored noise distributions. Under colored noise, the considered manifold associated with $\mathbf{s}$ is not Euclidean anymore: see that in the proof of Lemma 2.3.1, the step from the set of equations (2.90),(2.91) to (2.94),(2.93),(2.95) is not possible when $\mathbf{\Gamma} \neq \mathbf{I}$ since the norm of each component of $\mathbf{s}$ is not constant anymore. This makes the computations less tractable. Indeed, in the general case, $R^{\kappa\lambda}_{\alpha\beta}$ is not zero everywhere anymore. The terms R^{12}_{12}, R^{23}_{23} and R^{13}_{13} have to be computed from (2.15), (2.17) and (2.18) for each $\boldsymbol{\xi}$ in the search domain in order to apply Weyl's formula (2.23) as is. While this is possible once the first fundamental form g_{ij} has been obtained, this can be highly unpractical to use: an analytical expression seems hard to reach. In the following, we show how we can make use of the Gauss-Bonnet Theorem 2.B.1 to simplify the expression greatly when testing on the whole domain.

Our first step is to find a useful expression for the first fundamental form (g_{ij}). In order to do that, we will have to consider some additional assumptions on the covariance matrix $\mathbf{R}$ (recall that $\mathbf{R} = \sigma^2\mathbf{I}$): we will no longer consider any SPD matrix. Instead, let us make the hypothesis that $\mathbf{R}$ can be written as:

$$\mathbf{R} = \int_{\boldsymbol{\zeta}} p(\boldsymbol{\zeta})\, \mathbf{s}^u(\boldsymbol{\zeta})\mathbf{s}^u(\boldsymbol{\zeta})^H \, d\boldsymbol{\zeta} + \sigma^2\, \mathbf{I}\,, \tag{2.38}$$

where $\boldsymbol{\zeta} = (v, u)$ is the centrosymmetric parametrization for (θ, μ) in the proof of Lemma (2.3.1), p is a real function on $\mathcal{D}$ such that $p(\zeta_1, \zeta_2)$ represents the power density backscattered from the clutter in the interval $[\zeta_1, \zeta_1 + d\zeta_1] \times [\zeta_2, \zeta_2 + d\zeta_2]$, and $\mathbf{s}^u$ is the unwhitened version of $\mathbf{s}$. The term $\sigma^2\mathbf{I}$ models the thermal receiver noise. While we lose some generality, for radar applications this hypothesis is realistic.

Let us establish the following result on the first fundamental form of the manifold γ:

Proposition 2.3.1. *The first fundamental form $g_{ij}, 1 \leq i, j \leq 3$ of $\boldsymbol{\gamma}$ when using signal model* (1.10) *with a covariance matrix of the form* (2.38) *can be written as:*

$$(g_{ij}) = \begin{pmatrix} 1 & \mathbf{0} \\ \mathbf{0} & \left(\dfrac{\partial \mathbf{s}^H}{\partial \zeta_i} \dfrac{\partial \mathbf{s}}{\partial \zeta_j} \right) \end{pmatrix}. \tag{2.39}$$

Proof. The proof is given in the Appendix 2.B.5. The matrix $\frac{\partial \mathbf{s}^H}{\partial \zeta_i}\frac{\partial \mathbf{s}}{\partial \zeta_j}$ is shown to be real, so that g_{ij} is well defined. □

This proposition shows that, in the metric, the phase is decoupled with the remaining unknown target parameters $\boldsymbol{\zeta}$. This allows us to derive the following result, giving the probability of false alarm under an easy-to-evaluate integral form in the following new corollary:

Corollary 2.3.0.3. *Using signal model* (1.10) *for STAP detection on the whole domain, i.e.* $\mathcal{D} = [0,1]^2$*, when* w *is chosen big enough so that no overlap phenomena happens, the* P_{FA} *of the off-grid GLRT with a covariance matrix of the form* (2.38) *is given by (using the parametrization* $\boldsymbol{\psi} = (\alpha, \boldsymbol{\zeta})$ *from the proof of Lemma 2.3.1):*

$$P_{FA} = \frac{\pi}{2}\,\sin^{2NP-4}\left((2NP-1)\,w^2-1\right)\int_{\boldsymbol{\zeta}\in\mathcal{D}'}\sqrt{\det a_{ij}}\,d\zeta_1 d\zeta_2\,, \tag{2.40}$$

where

$$a_{ij} = \frac{\partial \mathbf{s}(\boldsymbol{\zeta})^H}{\partial \zeta_i}\frac{\partial \mathbf{s}(\boldsymbol{\zeta})}{\partial \zeta_j}\,.$$

The integral has to be evaluated numerically, with the derivates of $\mathbf{s}$ *that are given by:*

$$\begin{aligned}
\frac{\partial \mathbf{s}(\boldsymbol{\zeta})}{\partial v} &= \left(\mathbf{I}-\mathbf{s}(\boldsymbol{\zeta})\mathbf{s}(\boldsymbol{\zeta})^H\right)\boldsymbol{\Gamma}^{-1/2}\left(\left(\boldsymbol{\Gamma}^{1/2}\mathbf{s}(\boldsymbol{\zeta})\right)\odot\left(2i\pi\, l_\theta^{-1}\mathbf{x}_N\otimes\mathbf{1}_P\right)\right)\,,\\
\frac{\partial \mathbf{s}(\boldsymbol{\zeta})}{\partial u} &= \left(\mathbf{I}-\mathbf{s}(\boldsymbol{\zeta})\mathbf{s}(\boldsymbol{\zeta})^H\right)\boldsymbol{\Gamma}^{-1/2}\left(\left(\boldsymbol{\Gamma}^{1/2}\mathbf{s}(\boldsymbol{\zeta})\right)\odot\left(\mathbf{1}_N\otimes 2i\pi\, l_\mu^{-1}\mathbf{x}_P\right)\right)\,.
\end{aligned}$$

where $\mathbf{x}_N, \mathbf{x}_P$ *are defined in* (2.89) *and* $\mathbf{1}_N$*,* $\mathbf{1}_P$ *are the column vectors of size* N *and* P *composed of ones.*

Proof. The proof is given in Appendix 2.B.6 and makes use of the shape of the metric found in the previous corollary as well as the Gauss-Bonnet theorem. □

Note that this result covers the white noise result over the whole domain given in Subsection 2.3.3.1 (in this case, the determinant under the integral is equal to one). The integral term corresponds to the surface described by $\boldsymbol{\gamma}$.

In the case where the manifold $\boldsymbol{\gamma}$ is not closed, (for a search domain $\mathcal{D} \neq [0,1]^2$), even though it makes less sense than in the Euclidean case, we still decide to apply the heuristic described in section 2.2.3.2, as we will see that it still gives very good results numerically in section 2.5.1. Thus, we express the P_{FA} as the sum of (2.40), with the integral limited to $\mathcal{D}$, plus some terms accounting for the outer cross-sections around the border surface that can be computed using (2.32) injecting the STAP values of $\boldsymbol{\gamma}_1$ and $\boldsymbol{\gamma}_2$, plus the on-grid term $(1-w^2)^{NP-1}$ that accounts for the integral of the cross-sections around the curve borders of the border surfaces. This leads to the following heuristic:

Heuristic 2.3.2. *Using STAP signal model* (1.10)*, the* P_{FA} *for the NMF under colored noise with a search domain* $\mathcal{D} = [\theta_1,\theta_2]\times[\mu_1,\mu_2] \neq [0,1]^2$ *is given by (using the parametrization* $\boldsymbol{\psi} = (\alpha, u, v)$ *from the proof of Lemma 2.3.1):*

$$\begin{aligned}
P_{FA} \;=\; & \frac{\pi}{2}\,(1-w^2)^{NP-2}\left((2NP-1)\,w^2-1\right)\int_{\boldsymbol{\zeta}\in\mathcal{D}'}\sqrt{\det a_{ij}}\,d\boldsymbol{\zeta}\\
&+\frac{1}{2}\frac{\Gamma(NP)\,w\,(1-w^2)^{NP-\frac{3}{2}}}{\pi^{1/2}\Gamma\left(NP-\frac{1}{2}\right)}\left(\int_{v_1}^{v_2}\left\|\frac{\partial\boldsymbol{\gamma}_1}{\partial v}(v,u_1)^T\mathbf{P}^{\perp}_{\boldsymbol{\gamma}_2(v,u_1)}\right\|dv+\int_{v_1}^{v_2}\left\|\frac{\partial\boldsymbol{\gamma}_1}{\partial v}(v,u_2)^T\mathbf{P}^{\perp}_{\boldsymbol{\gamma}_2(v,u_2)}\right\|dv\right.\\
&\left.+\int_{u_1}^{u_2}\left\|\frac{\partial\boldsymbol{\gamma}_1}{\partial u}(v_1,u)^T\mathbf{P}^{\perp}_{\boldsymbol{\gamma}_2(v_1,u)}\right\|du+\int_{u_1}^{u_2}\left\|\frac{\partial\boldsymbol{\gamma}_1}{\partial u}(v_2,u)^T\mathbf{P}^{\perp}_{\boldsymbol{\gamma}_2(v_2,u)}\right\|du\right)+\left(1-w^2\right)^{NP-1}\,.
\end{aligned} \tag{2.41}$$

The derivatives of $\boldsymbol{\gamma}_1$ to be used in the integrals are:

$$\frac{\partial \boldsymbol{\gamma}_1(\boldsymbol{\psi})}{\partial v} = \left(\mathbf{I} - \boldsymbol{\gamma}_1(\boldsymbol{\psi})\boldsymbol{\gamma}_1(\boldsymbol{\psi})^T\right)\mathbf{B}^{-1}\left(\left(\mathbf{B}\boldsymbol{\gamma}_2(\boldsymbol{\psi})\right) \odot \begin{pmatrix} 2\pi\, l_\theta^{-1}\, \mathbf{x}_N \otimes \mathbf{1}_P \\ 2\pi\, l_\theta^{-1}\, \mathbf{x}_N \otimes \mathbf{1}_P \end{pmatrix}\right),$$

$$\frac{\partial \boldsymbol{\gamma}_1(\boldsymbol{\psi})}{\partial u} = \left(\mathbf{I} - \boldsymbol{\gamma}_1(\boldsymbol{\psi})\boldsymbol{\gamma}_1(\boldsymbol{\psi})^T\right)\mathbf{B}^{-1}\left(\left(\mathbf{B}\boldsymbol{\gamma}_2(\boldsymbol{\psi})\right) \odot \begin{pmatrix} \mathbf{1}_N \otimes 2\pi\, l_\theta^{-1}\mathbf{x}_P \\ \mathbf{1}_N \otimes 2\pi\, l_\theta^{-1}\mathbf{x}_P \end{pmatrix}\right).$$

Again, we will see in Subsection 2.5.1 that this heuristic seems to be working very well in practice, and that the relationship obtained for FMCW-distance detection is a good approximate of the distance-Doppler relationship using a chirp, which enables one to set the thresholds when using signal model (1.8).

2.4 . Derivation of the domain of validity of the previous P_{FA}-threshold relationships

The goal of this section is to determine for which thresholds the P_{FA}-threshold relationships derived in the previous section holds equality. This requires us to investigate the conditions under which overlap occurs. We will start by exhibiting general results on arbitrary M-dimensional manifolds from [JJ90; KT01] as well as some original results on shift-invariant manifolds before delving into our specific problem where we consider the manifold $\boldsymbol{\gamma}$ defined in (2.3) with $M = 2$ or $M = 3$.

Let us consider an M-dimensional manifold $\mathcal{M} = \{\boldsymbol{\gamma}(\boldsymbol{\xi}), \boldsymbol{\xi} = (\xi_1, \ldots, \xi_M) \in \mathcal{D}\}$ defined on the search domain $\mathcal{D}$ over $\mathbb{S}^{n-1}$ and let us consider the tube $\mathcal{T}$ over $\mathbb{S}^{n-1}$ around $\mathcal{M}$ consisting of the points $\mathbf{u}$ satisfying $\mathbf{u}^T\boldsymbol{\gamma}(\boldsymbol{\xi}) > w$ for some $\boldsymbol{\xi}$ in $\mathcal{D}$. $\mathcal{M}$ can be seen, loosely speaking, as the axis of $\mathcal{T}$. Recall that the cross-section $\mathcal{C}_w(\boldsymbol{\gamma}(\boldsymbol{\xi}))$ defined in (2.9) is the set of points of $\mathcal{T}$ orthogonal to the derivatives of $\boldsymbol{\gamma}$ in $\boldsymbol{\xi}$ at a distance less than w. Formally:

$$\mathcal{C}_w(\boldsymbol{\gamma}(\boldsymbol{\xi})) = \left\{\mathbf{u} \in \mathcal{T}, \mathbf{u}^T \frac{\partial \boldsymbol{\gamma}}{\partial \boldsymbol{\xi}^T} = \mathbf{0}, \mathbf{u}^T\boldsymbol{\gamma}(\boldsymbol{\xi}) > w\right\}. \tag{2.42}$$

Excluding the edge effects defined later in this section, the tube defined as the union of cross-sections overlaps if and only if a point $\mathbf{u}$ of $\mathcal{T}$ belongs to more than one cross-section: in this case, Hotelling's geometrical approach and its extensions lead to an overestimation of the Probability of False Alarm. Otherwise, the equality holds true in (2.29). There are two types of overlap defined in [Hot39]: local overlap, which derives from local differential properties of the manifold generating the tube, and non-local overlap, which depends on the overall shape of the tube. Global overlap encompasses both types of overlap. It is linked to a limit overlap threshold w_{lim} and there is no overlap if

$$w \geq w_{\text{lim}}\,. \tag{2.43}$$

The limit threshold can be equivalently seen as an angle ϕ_{lim} such that

$$\cos\phi_{\text{lim}} = w_{\text{lim}}\,,$$

and there is no overlap if

$$\phi = \cos^{-1} w \leq \phi_{\text{lim}}\,.$$

In the sequel, the conditions are expressed in terms of ϕ_{lim}.

In addition to those phenomena, edge effects also have to be considered. They can appear when dealing with non-closed manifold and cause the same problems as overlap i.e. an overestimation of the P_{FA}. In the 1D case illustrated in Figure 2.2.1, edge effects would occur when the green semi-spherical caps at the end overlap each other. A manifold is said to be closed along dimension k if its k-th variable ξ_k belongs to an interval $[\xi_{k_1}, \xi_{k_2}]$ such that $\boldsymbol{\gamma}(\xi_1, \ldots, \xi_{k_1}, \ldots, \xi_M) = \boldsymbol{\gamma}(\xi_1, \ldots, \xi_{k_2}, \ldots, \xi_M)$ for all $\xi_i, i \neq k$. A manifold is said to be closed if it is closed along all its dimensions.

Figure 2.4.1 summarizes all the phenomena that can arise.

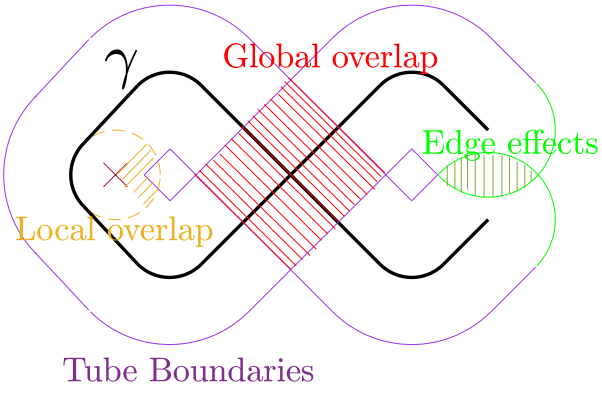

Figure 2.4.1: Illustration of all the phenomena leading to an overestimation of the P_{FA} when using the P_{FA}-threshold relationships of the previous chapter.

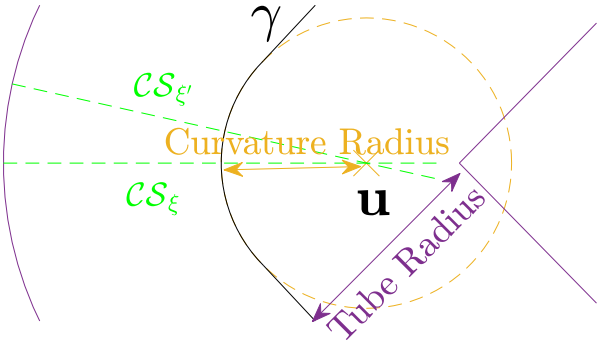

Figure 2.4.2: Illustration of local overlap in 1D in the Euclidean case. Here, the radius of the tube (in purple) is greater than the radius of curvature. This causes overlap: see, for example, that the point $\mathbf{u}$ belongs to both cross-sections $\mathcal{C}_w(\boldsymbol{\gamma}(\boldsymbol{\xi}))$ and $\mathcal{C}_w(\boldsymbol{\gamma}(\boldsymbol{\xi}'))$.

2.4.1 . The general case

In this section, we give the conditions under which no overlap happens under general conditions for any M-dimensional manifold $\boldsymbol{\gamma}(\xi_1, \ldots, \xi_M)$ embedded in $\mathbb{S}^{n-1}$.

In [JJ90], a criterion for characterizing the overlap of a tube embedded on a sphere around a curve is introduced that is a direct consequence of the fact that the union of the cross-section needs to be disjoint. It turns out that the arguments used by the authors can be generalized in order to find overlap criteria for tubes around any M-dimensional manifolds, as suggested in [KT01].

Theorem 2.4.1. *[JJ90; KT01] Let $\boldsymbol{\gamma}(\boldsymbol{\xi})$ be a C^2 M-dimensional manifold parameterized by $\boldsymbol{\xi} = (\xi_1, \ldots, \xi_M) \in \mathcal{D}$. Let ϕ_{lim} be the limit angle for which no overlap occurs, related to w_{lim} (2.43) by $\cos(\phi_{lim}) = w_{lim}$. Let $\mathbf{Q}_{\boldsymbol{\xi}'}$ be the projection onto the subspace spanned by $\boldsymbol{\gamma}(\boldsymbol{\xi}')$ and its derivatives $\dfrac{\partial \boldsymbol{\gamma}}{\partial \boldsymbol{\xi}'}$. ϕ_{lim} is given by:*

$$\begin{aligned} \cot^2 \phi_{lim} &= \sup_{\boldsymbol{\xi}, \boldsymbol{\xi}' \in \mathcal{D}^2} \frac{1 - \boldsymbol{\gamma}(\boldsymbol{\xi})^T \mathbf{Q}_{\boldsymbol{\xi}'} \boldsymbol{\gamma}(\boldsymbol{\xi})}{\left(1 - \boldsymbol{\gamma}(\boldsymbol{\xi})^T \boldsymbol{\gamma}(\boldsymbol{\xi}')\right)^2} \\ &\triangleq \sup_{\boldsymbol{\xi}, \boldsymbol{\xi}' \in \mathcal{D}^2} h(\boldsymbol{\xi}, \boldsymbol{\xi}') \,. \end{aligned} \tag{2.44}$$

Remark 2.4.1. *To clarify, this theorem gives the limit geodesic radius (angle) of the tube $\mathcal{T}$ around γ so that all points in $\mathcal{T}$ belong to a single cross-section.*

The criterion (2.44) encompasses both local and non-local overlap:

$$\phi_{\text{lim}} = \min\{\phi_{\text{local}}, \phi_{\text{non-local}}\} \,, \tag{2.45}$$

where ϕ_{local} and $\phi_{\text{non-local}}$ are the limit angles such that local and non-local overlaps occur. Local overlap occurs when $\boldsymbol{\xi}'$ tends to $\boldsymbol{\xi}$, and non-local overlap arises when the $\sup$ of h in (2.44) is attained for $\boldsymbol{\xi} \neq \boldsymbol{\xi}'$.

Remark 2.4.2. *Note that* (2.44) *does not take into account edge effects.*

It can be simplified in the case of a shift-invariant manifold, a notion that we define as an analogy to the shift-invariant curves introduced in [JJ90]:

Definition 2.4.1. *A real manifold $\boldsymbol{\gamma}(\boldsymbol{\xi})$ is said to be shift-invariant when, for any $\boldsymbol{\xi}, \boldsymbol{\xi}'$, the scalar product $\boldsymbol{\gamma}(\boldsymbol{\xi})^T \boldsymbol{\gamma}(\boldsymbol{\xi}')$ depends only on $\boldsymbol{\xi} - \boldsymbol{\xi}'$:*

$$\boldsymbol{\gamma}(\boldsymbol{\xi})^T \boldsymbol{\gamma}(\boldsymbol{\xi}') = f(\boldsymbol{\xi} - \boldsymbol{\xi}'), \tag{2.46}$$

where f is an even function.

Remark 2.4.3. *Note that shift-invariant manifolds are a subset of Euclidean manifolds: indeed, see that the first fundamental form coefficients of the manifold are constants:*

$$\begin{aligned} g_{ij} &= \frac{\partial \boldsymbol{\gamma}(\boldsymbol{\xi})^T}{\partial \xi_i} \frac{\partial \boldsymbol{\gamma}(\boldsymbol{\xi})}{\partial \xi_j}, \\ &= -\frac{\partial^2 f}{\partial \xi_i \partial \xi_j}\bigg|_0. \end{aligned}$$

where the second equality is obtained by derivating (2.46) w.r.t. ξ_i and ξ'_j, then evaluating in $\boldsymbol{\xi} = \boldsymbol{\xi}'$. g_{ij} is thus constant: it is then easy to reparametrize to have a first fundamental form equal to identity.

Then, similarly to the case of a single parameter, we have the following property:

Proposition 2.4.1. *For a shift-invariant manifold $\boldsymbol{\gamma}(\boldsymbol{\xi})$, h as defined in (2.44) is a function of $\boldsymbol{\xi} - \boldsymbol{\xi}'$: $h(\boldsymbol{\xi}, \boldsymbol{\xi}') = g(\boldsymbol{\xi} - \boldsymbol{\xi}')$. Consequently,*

$$\cot^2 \phi_{lim} = \sup_{\mathbf{x} \in \mathcal{E}} g(\mathbf{x}), \tag{2.47}$$

where $\mathcal{E}$ is the image of $\mathcal{D} \times \mathcal{D}$ by the function $(\boldsymbol{\xi}, \boldsymbol{\xi}') \to \boldsymbol{\xi} - \boldsymbol{\xi}'$.

Proof. The proof is given in Appendix 2.B.7. □

The implications of this result are detailed in the following sections.

2.4.1.1 On local overlap

In this section, we discuss the occurrence of local overlap around a M-dimensional manifold. The results of this section are particularized to our complex signal models (1.5), (1.7), (1.8) and (1.10) in Subsection 2.4.2.1.

Local overlap is linked to the curvature of the manifold. To illustrate this, consider the case of a tube around a curve in Euclidean space drawn in Figure 2.4.2: there is local overlap whenever the tube radius is greater than the radius of curvature of the curve.

In [KT01], a local overlap criterion is developed extending Hotelling's result to higher dimensions. We recall that it corresponds to the case where $\boldsymbol{\xi}'$ tends to $\boldsymbol{\xi}$.

We define the local overlap angle ϕ_{local} in $\boldsymbol{\xi}$ similarly in the multi-dimensional case as:

Corollary 2.4.1.1. [KT01] *In the case of a tube around an M-dimensional manifold $\boldsymbol{\gamma}$, using the same notations as before with $\boldsymbol{\beta}$ representing the directions of convergence from $\boldsymbol{\xi}'$ to $\boldsymbol{\xi}$, the limit local overlap angle is given by:*

$$\begin{aligned} \cot^2 \phi_{local} &= \sup_{\boldsymbol{\xi} \in \mathcal{D}} \sup_{\boldsymbol{\beta} \in \mathbb{S}^{M-1}} \lim_{\epsilon \to 0} h(\boldsymbol{\xi}, \boldsymbol{\xi} + \epsilon \boldsymbol{\beta}) \\ &= \sup_{\boldsymbol{\xi} \in \mathcal{D}} \sup_{\boldsymbol{\beta} \in \mathbb{S}^{M-1}} \frac{\left\| (\mathbf{I} - \mathbf{Q}_{\boldsymbol{\xi}}) \sum_{i,j} \beta_i \beta_j \frac{\partial^2 \boldsymbol{\gamma}}{\partial \xi_i \partial \xi_j} \right\|^2}{\left(\sum_{i,j} \beta_i \beta_j \frac{\partial \boldsymbol{\gamma}^T}{\partial \xi_i} \frac{\partial \boldsymbol{\gamma}}{\partial \xi_j} \right)^2}. \end{aligned} \tag{2.48}$$

It coincides with the principal curvature of γ at ξ having the largest absolute value.

Proof. The proof is given in [KT01]. □

Formula (2.48) can be simplified in the case of an Euclidean manifold:

Corollary 2.4.1.2. *Let $\gamma(\xi)$ be a M-dimensional shift-invariant manifold, with ψ being a parameterization such that $g_{ij} = \mathbf{I}$. Then* (2.48) *reduces to:*

$$\cot \phi_{\textit{local}}^2 = \sup_{\beta \in \mathbb{S}^{M-1}} \left\| \sum_{i,j} \beta_i \beta_j \left(\frac{\partial^2 \gamma}{\partial \psi_i \partial \psi_j} \right) \right\|^2 - 1 \,. \tag{2.49}$$

Proof. The proof is given in the Appendix 2.B.8. □

2.4.1.2 On non-local overlap

Non-local overlap arises when the tube draws back into itself, as shown in red in Figure 2.4.1 for a tube spanned by a curve. In [JJ90], it is shown in the case $M = 1$ that the limit angle around a closed manifold $\gamma(\xi)$ linked to this type of overlap can be characterized entirely by looking at the pairs of points (ξ, ξ') that minimize locally the distance $\|\gamma(\xi) - \gamma(\xi')\|$, with $\xi \neq \xi'$. In such case, (2.44) reduces to an intuitive geodesic distance criteria when $\xi \neq \xi'$. In the general case, M is arbitrary, and the following holds:

Proposition 2.4.2. *Consider a tube around the M-dimensional manifold γ lying on the sphere. The set of pairs (ξ, ξ') that characterizes non-local overlap is:*

$$\Xi = \left\{ (\xi, \xi') \,, \xi \neq \xi', \left(\gamma(\xi) - \gamma(\xi')\right)^T \frac{\partial \gamma}{\partial \xi_k} = 0 \text{ and } \left(\gamma(\xi) - \gamma(\xi')\right)^T \frac{\partial \gamma}{\partial \xi'_k} = 0, \ \forall k \in [1, M] \right\} . \tag{2.50}$$

Then, if the manifold is closed:

$$\phi_{\textit{non-local}} = \min_{(\xi, \xi') \in \Xi} \frac{1}{2} \cos^{-1} \left(\gamma(\xi)^T \gamma(\xi') \right) \,. \tag{2.51}$$

For a non-closed manifold, a term accounting for the boundaries must be taken into account:

$$\phi_{\textit{non-local}} = \min \left\{ \min_{(\xi, \xi') \in \Xi} \frac{1}{2} \cos^{-1} \left(\gamma(\xi)^T \gamma(\xi') \right), E \right\} \,, \tag{2.52}$$

where

$$E = \inf_{(\xi, \xi') \in \mathcal{B} \times \mathcal{D}} \cot^{-1} \sqrt{h\left(\xi, \xi'\right)} \,. \tag{2.53}$$

Remark 2.4.4. *In our case where the vectors $\gamma(\xi)$ and $\gamma(\xi')$ lie on $\mathbb{S}^{M-1}$, the geometrical criteria $\left(\gamma(\xi) - \gamma(\xi')\right)^T \frac{\partial \gamma(\xi)}{\partial \xi_k} = 0$ and $\left(\gamma(\xi) - \gamma(\xi')\right)^T \frac{\partial \gamma(\xi')}{\partial \xi_k} = 0$ simply read $\gamma(\xi')^T \frac{\partial \gamma(\xi)}{\partial \xi_k} = 0$ and $\gamma(\xi)^T \frac{\partial \gamma(\xi')}{\partial \xi_k} = 0$ since $\gamma(\xi)^T \frac{\partial \gamma(\xi)}{\partial \xi} = 0$ and $\gamma(\xi')^T \frac{\partial \gamma(\xi')}{\partial \xi} = 0$.*

The meaning of this criteria is illustrated in Figure 2.4.3 on a curve embedded in Euclidean space. A pair of points is in Ξ if the tangent planes of γ at ξ, ξ' are orthogonal to the vectors going from $\gamma(\xi)$ to $\gamma(\xi')$. See that in the 1D case of the figure, the pair of points (ξ_1, ξ_2) belongs to Ξ since the tangents to the curve at ξ_1, ξ_2 are parallel. Here, it is intuitive that a condition for non-overlap is that the cross-sections at ξ_1 and ξ_2 do not intersect.

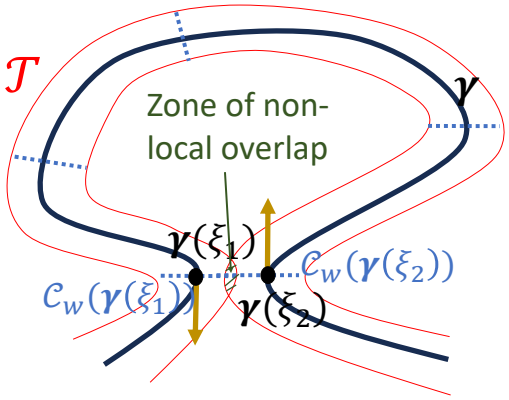

Figure 2.4.3: Illustration of the non-local overlap criteria (2.51) for a curve γ embedded in Euclidean space. The yellow arrows represent the derivatives of γ.

Proof. In Appendix 2.B.9, we adapt the proof of of [JJ90, Proposition 4.2] for an M-dimensional manifold. □

In the non-closed case, the limit angle $\phi_{\text{non-local}}$ also encompasses instances of local overlap when ξ' tends to $\xi \in \mathcal{B}$. Plugging it in (2.45) still yields the right exact limit angle ϕ_{lim}.

As noted in [JJ90], this formulation is not necessarily simpler to use than (2.44) since it can be as involved to find the set of pairs Ξ as to compute (2.44). However, in Subsection 2.4.2.2, we show that in our specific case, it enables us to reduce the computational complexity of the search.

2.4.1.3 On edge effects

The formula (2.44) does not take into account edge effects that can arise when dealing with non-closed manifolds: indeed, in [JJ90], (2.44) is derived (for $M = 1$) by checking what is the minimal tube radius so that a point in cross-sections $\mathcal{C}_w(\gamma(\boldsymbol{\xi}))$ does not belong to spherical caps $\mathcal{CS}_{\boldsymbol{\xi}'}$. This leaves out the overlapping of the end semi-spherical caps. Edge effects appear when a point $\mathbf{u}$ is such that there exist two distinct points $\boldsymbol{\xi}_1$, $\boldsymbol{\xi}_2$ in $\mathcal{B}$ such that $\mathbf{u}^T\boldsymbol{\gamma}(\boldsymbol{\xi}_1) > w$ and $\mathbf{u}^T\boldsymbol{\gamma}(\boldsymbol{\xi}_2) > w$, and $\mathbf{u}$ does not belong to any cross-section. It is illustrated in Figure 2.4.1 in the case $M = 1$. One has to check that the limit angle ϕ_{lim} is large enough so that edge effects do not appear.

2.4.2 . Application to the complex radar signal models

We apply here the general results of the previous section to our case of interest where γ is given by (2.3) using signal model (1.5), (1.7), (1.8) or (1.10). This first result gives the limit global overlap threshold for our application:

Corollary 2.4.1.3. *With γ defined as in* (2.3)*, the limit angle for no global overlap is:*

$$\cot^2 \phi_{lim} = \sup_{\substack{\boldsymbol{\xi}, \alpha \in \mathcal{D} \times [0, 2\pi] \\ \boldsymbol{\xi}', \alpha' \in \mathcal{D} \times [0, 2\pi]}} \frac{1 - \boldsymbol{\gamma}(\boldsymbol{\xi}, \alpha)^T \mathbf{Q}_{\boldsymbol{\xi}', \alpha'} \boldsymbol{\gamma}(\boldsymbol{\xi}, \alpha)}{\left(1 - \boldsymbol{\gamma}(\boldsymbol{\xi}, \alpha)^T \boldsymbol{\gamma}(\boldsymbol{\xi}', \alpha')\right)^2}, \tag{2.54}$$

where

$$\mathbf{Q}_{\boldsymbol{\xi}, \alpha} = \mathbf{M}_{\boldsymbol{\xi}, \alpha} \left(\mathbf{M}_{\boldsymbol{\xi}, \alpha}^T \mathbf{M}_{\boldsymbol{\xi}, \alpha}\right)^{-1} \mathbf{M}_{\boldsymbol{\xi}, \alpha}^T, \tag{2.55}$$

with $\mathbf{M}_{\xi,\alpha} = \left[\boldsymbol{\gamma}(\xi,\alpha), \dfrac{\partial\boldsymbol{\gamma}(\xi,\alpha)}{\partial\alpha}, \dfrac{\partial\boldsymbol{\gamma}(\xi,\alpha)}{\partial\xi}\right]$ *for* $M=2$ *and* $\mathbf{M}_{\boldsymbol{\xi},\alpha} = \left[\boldsymbol{\gamma}(\boldsymbol{\xi},\alpha), \dfrac{\partial\boldsymbol{\gamma}(\boldsymbol{\xi},\alpha)}{\partial\alpha}, \dfrac{\partial\boldsymbol{\gamma}(\boldsymbol{\xi},\alpha)}{\partial\xi_1}, \dfrac{\partial\boldsymbol{\gamma}(\boldsymbol{\xi},\alpha)}{\partial\xi_2}\right]$ *for* $M=3$.

Proof. We simply inject (2.3) in (2.44). □

The derivatives of $\boldsymbol{\gamma}$ to be injected in this expression are given in Appendix 2.D.1.

Under white noise, for Doppler detection over one cell $\mathcal{D}_k$, one can quickly check numerically that the corresponding limit P_{FA} is equal to (a more thorough test will be run in Subsection 2.5.2):

$$P_{FA\text{lim}} \approx 10^{-2.52}\,, \tag{2.56}$$

Fortunately, this P_{FA} is well above the common P_{FA} encountered in radar applications.

The search domain in (2.54) is $2M$-dimensional and so the criterion can be heavy to evaluate. We can simplify the search of the global limit angle by first finding the local and non-local overlap angle ϕ_{local} and $\phi_{\text{non-local}}$ through (2.48) and (2.51) then combining them using (2.45). In the following sections, we then set out to find the limit angles ϕ_{local} and $\phi_{\text{non-local}}$ through the aforementioned equations.

2.4.2.1 On local overlap

The following corollary gives ϕ_{local} in our case:

Corollary 2.4.1.4. *For our manifold* $\boldsymbol{\gamma}$ *defined in* (2.3)*, defining* $\mathbf{Q}^{\perp}_{\boldsymbol{\xi},\alpha} = \mathbf{I} - \mathbf{Q}_{\boldsymbol{\xi},\alpha}$ *we have,*

- *when* $M=2$ *for one unknown parameter* ξ *(signal model* (1.5) *or* (1.7)*):*

$$\cot^2\phi_{\textit{local}} = \sup_{\xi,\alpha\in\mathcal{D}\times[0,2\pi]} \sup_{\varphi\in[0,2\pi]} J_2(\xi,\alpha,\varphi)\,, \tag{2.57}$$

where

$$J_2(\xi,\alpha,\varphi) = \frac{\left\|\mathbf{Q}^{\perp}_{\xi,\alpha}\left(\cos^2\varphi\dfrac{\partial^2\boldsymbol{\gamma}}{\partial\xi^2} + \sin 2\varphi\dfrac{\partial^2\boldsymbol{\gamma}}{\partial\xi\partial\alpha} + \sin^2\varphi\dfrac{\partial^2\boldsymbol{\gamma}}{\partial\alpha^2}\right)\right\|}{\cos^2\varphi\left\|\dfrac{\partial\boldsymbol{\gamma}}{\partial\xi}\right\|^2 \sin 2\varphi\dfrac{\partial\boldsymbol{\gamma}^T}{\partial\xi}\dfrac{\partial\boldsymbol{\gamma}}{\partial\alpha} + \sin^2\varphi\left\|\dfrac{\partial\boldsymbol{\gamma}}{\partial\alpha}\right\|^2}\,,$$

- *when* $M=3$ *for two unknown parameters* $\boldsymbol{\xi}=(\xi_1,\xi_2)$ *(signal model* (1.10)*,* (1.8)*):*

$$\cot^2\phi_{\textit{local}} = \sup_{\boldsymbol{\xi},\alpha\in\mathcal{D}\times[0,2\pi]} \sup_{\boldsymbol{\beta}\in\mathbb{S}^2} J_3(\boldsymbol{\xi},\alpha,\boldsymbol{\beta})\,, \tag{2.58}$$

where

$$J_3(\boldsymbol{\xi},\alpha,\boldsymbol{\beta}) = \frac{\left\|\mathbf{Q}^{\perp}_{\boldsymbol{\xi},\alpha}\left(\beta_1^2\frac{\partial^2\boldsymbol{\gamma}}{\partial\alpha^2} + \beta_2^2\frac{\partial^2\boldsymbol{\gamma}}{\partial\xi_1^2} + \beta_3^2\frac{\partial^2\boldsymbol{\gamma}}{\partial\xi_2^2} + 2\beta_1\beta_2\frac{\partial^2\boldsymbol{\gamma}}{\partial\alpha\xi_1} + 2\beta_2\beta_3\frac{\partial^2\boldsymbol{\gamma}}{\partial\xi_1\xi_2} + 2\beta_1\beta_3\frac{\partial^2\boldsymbol{\gamma}}{\partial\alpha\xi_2}\right)\right\|}{\beta_1^2\left\|\frac{\partial\boldsymbol{\gamma}}{\partial\alpha}\right\|^2 + \beta_2^2\left\|\frac{\partial\boldsymbol{\gamma}}{\partial\xi_1}\right\|^2 + \beta_3^2\left\|\frac{\partial\boldsymbol{\gamma}}{\partial\xi_2}\right\|^2 + 2\beta_1\beta_2\frac{\partial\boldsymbol{\gamma}^T}{\partial\alpha}\frac{\partial\boldsymbol{\gamma}}{\partial\xi_1} + 2\beta_2\beta_3\frac{\partial\boldsymbol{\gamma}^T}{\partial\xi_1}\frac{\partial\boldsymbol{\gamma}}{\partial\xi_2} + 2\beta_1\beta_3\frac{\partial\boldsymbol{\gamma}^T}{\partial\alpha}\frac{\partial\boldsymbol{\gamma}}{\partial\xi_2}}.$$

This expression is easily evaluated numerically by setting $\beta_1 = \cos\varphi_1\cos\varphi_2, \beta_2 = \sin\varphi_1\cos\varphi_2, \beta_3 = \sin\varphi_2$ *and maximizing for* $\varphi_1,\varphi_2\in[0,2\pi]^2$*.*

Proof. We simply inject (2.3) in (2.48), with $M=2$ and $M=3$. □

In order to use this expression, one should inject the expressions for the second derivatives of $\boldsymbol{\gamma}$ that are given in Appendix 2.D.2.

It is then possible to find the analytical limit threshold for local overlap under white noise for Doppler and STAP detection (signal models (1.7) and (1.10)) by observing that in those cases, the manifold $\boldsymbol{\gamma}$ is shift-invariant. Indeed, with $\mathbf{s}$ following the signal model (1.7) ($\boldsymbol{\xi} = \theta$), remark that:

$$\begin{aligned}\mathbf{s}(\theta)^H \mathbf{s}(\theta') &= \frac{1}{\sqrt{N}} \sum_{k=0}^{N-1} e^{2i\pi\, k(\theta'-\theta)} \\ &= f_N(\theta - \theta') \\ &= \mathrm{Re}\left(f_N(\theta-\theta')\right) + i\,\mathrm{Im}\left(f_N(\theta-\theta')\right)\,. \end{aligned} \tag{2.59}$$

where $f_N(\theta-\theta') = e^{i\pi(N-1)(\theta'-\theta)} \dfrac{\sin(\pi N(\theta'-\theta))}{\sin(\pi(\theta'-\theta))}$, and with $\mathbf{s}$ following signal model (1.10) ($\boldsymbol{\xi} = (\theta, \mu)$), using the mixed product property of the Kronecker product:

$$\begin{aligned}\mathbf{s}(\theta,\mu)^H \mathbf{s}(\theta',\mu') &= \frac{1}{\sqrt{NM}} \sum_{k=0}^{N-1} e^{2i\pi\, k(\theta'-\theta)} \sum_{k=0}^{P-1} e^{2i\pi\, k(\mu'-\mu)} \\ &= f_N(\theta-\theta') f_P(\mu-\mu') \\ &= \mathrm{Re}\left(f_N(\theta-\theta') f_P(\mu-\mu')\right) + i\,\mathrm{Im}\left(f_N(\theta-\theta') f_P(\mu-\mu')\right)\,. \end{aligned} \tag{2.60}$$

Then, recall that (for any signal model):

$$\boldsymbol{\gamma}(\boldsymbol{\xi},\alpha)^T \boldsymbol{\gamma}(\boldsymbol{\xi}',\alpha') = \cos\left(\alpha-\alpha'\right) \mathrm{Re}\left(\mathbf{s}(\boldsymbol{\xi})^H \mathbf{s}(\boldsymbol{\xi})\right) + \sin(\alpha-\alpha') \mathrm{Im}\left(\mathbf{s}(\boldsymbol{\xi})^H \mathbf{s}(\boldsymbol{\xi})\right).$$

Thus one finds, for Doppler detection:

$$\boldsymbol{\gamma}(\theta,\alpha)^T \boldsymbol{\gamma}(\theta',\alpha') = \cos(\alpha-\alpha') \,\mathrm{Re}\left(f(\theta-\theta')\right) + \sin(\alpha-\alpha')\,\mathrm{Im}\left(f(\theta-\theta')\right)\,,$$

and for STAP detection:

$$\boldsymbol{\gamma}(\theta,\mu,\alpha)^T \boldsymbol{\gamma}(\theta',\mu',\alpha') = \cos(\alpha-\alpha')\,\mathrm{Re}\left(f_N(\theta-\theta') f_P(\mu-\mu')\right) + \sin(\alpha-\alpha')\,\mathrm{Im}\left(f_N(\theta-\theta') f_P(\mu-\mu')\right)\,.$$

We then propose the following corollary to compute analytically the limit local overlap threshold under white noise:

Corollary 2.4.1.5. *Under white noise with one unknown parameter (signal model* (1.7)*), the limit local angle* (2.57) *is:*

$$\phi_{\mathit{local}} = \tan^{-1}\left(\frac{\sqrt{5-C_N}}{2}\right)\,,$$

and the limit local threshold is

$$w^2_{\mathit{local}} = \cos^2\left(\tan^{-1}\left(\frac{\sqrt{5-C_N}}{2}\right)\right)\,, \tag{2.61}$$

where in the case of Doppler detection (signal model (1.7)*)*

$$C_N = \frac{3}{5}\frac{3N^2-7}{(N-1)^2}\,. \tag{2.62}$$

In the case of signal model (1.10) *for STAP detection, the limit local overlap angle is found by maximizing the following expression:*

$$\begin{aligned}\cot^2\phi_{\mathit{local}} = \max_{\varphi,\psi\in[0,2\pi]} & \cos(\varphi)^4\cos(\psi)^4 C_N + \sin(\varphi)^4\cos(\psi)^4 C_P + \sin(\psi)^4 & (2.63)\\ & + 3\left(\cos(\varphi)^2\sin(\varphi)^2\cos(\psi))^4 + \cos(\varphi)^2\cos(\psi)^2\sin(\psi)^2 + \sin(\varphi)^2\cos(\psi)^2\sin(\psi)^2\right) - 1 & (2.64)\end{aligned}$$

Proof. The proof is given in Appendix 2.B.10. □

Note that for Doppler detection, $\lim_{N\to\infty} C_N = \frac{9}{5}$: for N large enough,

$$w_{\text{local}}^2 \approx \cos^2\left(\tan^{-1}\left(\frac{2}{\sqrt{5}}\right)\right). \tag{2.65}$$

For $N = 10$, according to (2.33) this corresponds to the limit:

$$P_{FA\text{local}} \approx 10^{-2.52} = P_{FA\text{lim}}.$$

Thus local overlap is the limiting factor for this noise setting.

2.4.2.2 On non-local overlap

First, consider the case where the target is searched over the whole spectral domain, i.e. $\mathcal{D} = [0,1]$ for Doppler detection or $\mathcal{D} = [0,1]^2$ for STAP detection. This corresponds to the operational context where a single target is searched in the scene. In this case, the manifold γ in (2.3) is closed. In order to compute the non-local limit angle $\phi_{\text{non-local}}$, one should evaluate criterion (2.51). For the case of a non-closed manifold, i.e. $\mathcal{D}$ is partitioned when several targets are expected or when one of the unknown parameters is the range of the target (in which case the manifold cannot be closed), one should instead evaluate criterion (2.52). The following corollary simplifies the criteria.

Corollary 2.4.1.6. *Consider a tube lying on the sphere around the manifold γ defined in* (2.3)*. Define Ξ' as:*

$$\Xi' = \left\{ \left(\boldsymbol{\xi}, \boldsymbol{\xi}'\right), \boldsymbol{\xi} \neq \boldsymbol{\xi}', \frac{\partial}{\partial \boldsymbol{\xi}} \left|\mathbf{s}(\boldsymbol{\xi})^H \mathbf{s}(\boldsymbol{\xi}')\right| = 0 \right\}. \tag{2.66}$$

Then when $\mathcal{D} = [0,1]$, $\phi_{\text{non-local}}$ in (2.51) *reduces to:*

$$\phi_{\text{non-local}} = \min_{(\boldsymbol{\xi},\boldsymbol{\xi}')\in\Xi'} \frac{1}{2}\cos^{-1}\left|\mathbf{s}(\boldsymbol{\xi})^H \mathbf{s}(\boldsymbol{\xi}')\right|, \tag{2.67}$$

and otherwise, $\phi_{\text{non-local}}$ in (2.52) *reduces to*

$$\phi_{\text{non-local}} = \min\left\{ \min_{(\boldsymbol{\xi},\boldsymbol{\xi}')\in\Xi'} \frac{1}{2}\cos^{-1}\left|\mathbf{s}(\boldsymbol{\xi})^H \mathbf{s}(\boldsymbol{\xi}')\right|, E \right\}, \tag{2.68}$$

where E has been defined in (2.53)*.*

Proof. The proof is provided in Appendix 2.B.11. □

This simplification allows us to simply investigate the critical points with $(\boldsymbol{\xi} \neq \boldsymbol{\xi}')$ of ambiguity maps $\left|\mathbf{s}(\boldsymbol{\xi})^H \mathbf{s}(\boldsymbol{\xi}')\right|$ such as the two-dimensional one drawn in Figure 2.4.4 for Doppler detection (signal model (1.7)). In the case of a closed manifold the search (2.67) becomes two-dimensional for Doppler detection, and four-dimensional for STAP detection (signal model (1.10)). When the manifold is non-closed, one has to also evaluate E in (2.53) in order to compute (2.68). Since the boundaries are of dimension $M-1$, the evaluation of E requires an $M(M-1)$ dimensional search. The search (2.68) is thus three-dimensional in the case of one unknown parameter or five-dimensional in the case of two unknown parameters.

When considering Doppler or STAP detection under white noise (signal models (1.7) or (1.10)), the search space can be further simplified. Indeed, we have shown in the previous section that in those cases the products $\left|\mathbf{s}(\boldsymbol{\xi})^H \mathbf{s}(\boldsymbol{\xi}')\right|$ depend only on the difference $\boldsymbol{\delta} = \boldsymbol{\xi}' - \boldsymbol{\xi}$. Finding the local maxima of $\left|\mathbf{s}(\boldsymbol{\xi})^H \mathbf{s}(\boldsymbol{\xi}')\right|$ simply reduces in finding the local maxima of $\left|\mathbf{s}(\boldsymbol{\xi})^H \mathbf{s}(\boldsymbol{\xi}+\boldsymbol{\delta})\right|$ for any fixed $\boldsymbol{\xi}$.

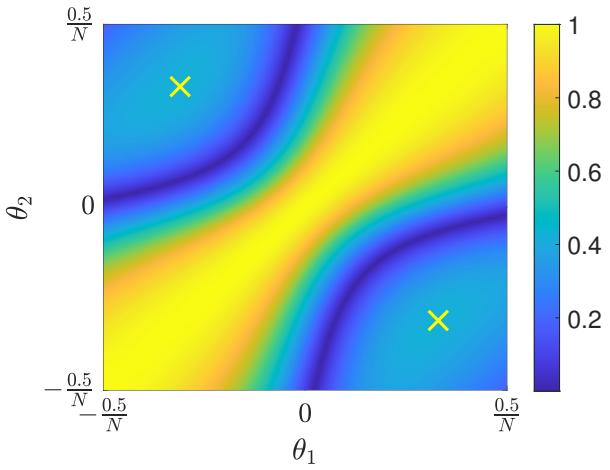

Figure 2.4.4: Ambiguity map $\left|\mathbf{s}(\theta)^H\mathbf{s}(\theta')\right|$ drawn for $\theta, \theta' \in \mathcal{D}_0 = [-0.5/N, 0.5/N]$ for highly correlated noise ($\rho = 0.9$, see Eq. (1.17)), with $N = 10$, with $\mathbf{s}$ following signal model (1.7) ($\boldsymbol{\xi} = \theta$). Yellow crosses represent local maxima with $\theta \neq \theta'$.

In particular, for Doppler detection, the search space is one-dimensional, and $\left|\mathbf{s}(\theta)^H\mathbf{s}(\theta+\delta)\right|$ represents the autocorrelation of $\mathbf{s}$, and it is well known that:

$$\left|\mathbf{s}(\theta)^H\mathbf{s}(\theta+\delta)\right| = \frac{1}{N}\left|\frac{\sin(\pi\delta N)}{\sin(\pi\delta)}\right| . \tag{2.69}$$

The autocorrelation of $\mathbf{s}$ is represented in Figure 1.9. In this case, in a single cell $\mathcal{D}_k$ the set Ξ is empty since the derivative of $\left|\mathbf{s}(\theta)^H\mathbf{s}(\theta+\delta)\right|$ only vanishes for $\delta = 0$. If $\mathcal{D} = [0,1]$, ϕ_{local} can be readily obtained from the first secondary lobe level, i.e. for $\delta = \dfrac{3}{2N}$ (see figure 1.9).

2.4.3 . On edge effects

If detection is not performed over the whole parameter domain ($\mathcal{D} = [\theta_1, \theta_2] \subsetneq [0,1]$ for signal model (1.7) or $\mathcal{D} = [\theta_1, \theta_2] \times [\mu_1, \mu_2] \subsetneq [0,1]^2$ for signal model (1.10), the manifold always having boundaries for range detection), then $\mathcal{B} = \{\boldsymbol{\xi}_1, \boldsymbol{\xi}_2\} \times [0, 2\pi]$ and one has to take into account edge effects. In order to ensure no edge effects arise, two criteria should be checked:

- The borders do not self-overlap.
- The borders do not overlap each other.

2.4.3.1 The case of one unknown parameter $(M = 2)$

Let us first treat the single parameter case, using signal model (1.7) ($\boldsymbol{\xi} = \theta$). The boundaries of the manifold $\boldsymbol{\gamma}$ are tubes around the sub-manifolds $\{\boldsymbol{\gamma}(\theta_1, \alpha), \alpha \in [0, 2\pi]\}$ and $\{\boldsymbol{\gamma}(\theta_2, \alpha), \alpha \in [0, 2\pi]\}$, and the result in Subsection 2.B.1 in appendix shows those tubes do not self-overlap. We then simply need to check that those tubes do not overlap with each other:

Proposition 2.4.3. *Consider the tube around the manifold $\boldsymbol{\gamma}$ defined in* (2.3) *on a cell $\mathcal{D} = [\theta_1, \theta_2] \subsetneq [0,1]$. No edge effects appear if*

$$\phi < \phi_{edge} \triangleq \frac{1}{2}\cos^{-1}\left(\left|\mathbf{s}(\theta_1)^H\mathbf{s}(\theta_2)\right|\right) . \tag{2.70}$$

In particular, under white noise, if $[\theta_1, \theta_2]$ is a cell $\mathcal{D}_k$ as defined in (1.32)*, $\mathbf{s}(\theta_1)^H\mathbf{s}(\theta_2) = 0$, so that $\phi_{edge} = \pi/4$, which corresponds to a limit threshold $w_{edge} = \sqrt{2}/2$.*

Proof. No edge effect occurs if:

$$\phi < \min_{\alpha,\alpha'} \frac{1}{2} \cos^{-1}\left(\boldsymbol{\gamma}(\theta_1,\alpha)^T \boldsymbol{\gamma}(\theta_2,\alpha')\right). \tag{2.71}$$

With (2.112), the minimum (2.71) is reached for $\alpha - \alpha' = \angle \mathbf{s}(\theta_1)^H \mathbf{s}(\theta_2)$. In this case, $\boldsymbol{\gamma}(\theta_1,\alpha)^T \boldsymbol{\gamma}(\theta_2,\alpha') = \left|\mathbf{s}(\theta_1)^H \mathbf{s}(\theta_2)\right|$, and the rightmost term of (2.71) reduces to ϕ_{edge} in (2.70). □

Note that this is only a sufficient condition that checks whether the whole tubes at the ends of the manifold overlap, while we are only interested in knowing whether the outer semi-tubes overlap. If the length of the manifold for fixed α is very small, then the distance between $\mathbf{s}(\theta_1)$ and $\mathbf{s}(\theta_2)$ is very small but overlap does not necessarily arise. Formula (2.70) is thus only meaningful if the length $\int_{\theta_1}^{\theta_2} \left\| \dot{\boldsymbol{\gamma}}_1(\theta)^T \mathbf{P}^{\perp}_{\boldsymbol{\gamma}_2(\theta)} \right\| d\theta$ (which reduces to $\frac{\pi}{\sqrt{3}}\sqrt{N^2-1}(\theta_2-\theta_1)$ under white noise) is greater than the threshold w, which should be the case for any reasonable cell length.

2.4.3.2 The case of two unknown parameters $(M = 3)$

For STAP detection using signal model (1.10), with two unknown parameters ($\boldsymbol{\xi} = (\theta, \mu)$), the P_{FA}-threshold relationships have only been properly established in the case where there are no boundaries so that there are no edge effects as well.

The situation is more involved than in the case $M = 2$ if one were to try to find the limit overlap angle for the heuristic relationships. Using a search domain $[\theta_1, \theta_2] \times [\mu_1, \mu_2]$ where neither of the intervals is $[0, 1]$ the boundary is a manifold formed of the surfaces $\{\boldsymbol{\gamma}(\theta_1, \mu, \alpha) : (\mu, \alpha) \in [\mu_1, \mu_2] \times [0, 2\pi]\}$, $\{\boldsymbol{\gamma}(\theta_2, \mu, \alpha) : (\mu, \alpha) \in [\mu_1, \mu_2] \times [0, 2\pi]\}$, $\{\boldsymbol{\gamma}(\theta, \mu_1, \alpha) : (\theta, \alpha) \in [\theta_1, \theta_2] \times [0, 2\pi]\}$ and $\{\boldsymbol{\gamma}(\theta, \mu_2, \alpha) : (\theta, \alpha) \in [\theta_1, \theta_2] \times [0, 2\pi]\}$, and one should check that the outer half cross-sections around those borders do not overlap. Unfortunately, the border of the manifold is not necessarily smooth: indeed, discontinuities appear at the junctions of the surfaces (one can look at the green edges in figure 2.2.4 to understand what we mean by junctions). As a consequence, the results of this chapter should not be applied to the boundary in its entirety. Instead, each of the 4 surfaces can be treated independently with the results of Subsections 2.4.2.1 and 2.4.2.2 and the results at the start of this section for $M = 2$ to check that the tubes around them do not self-overlap. However, one should also check that the outer cross-sections of each surface do not overlap with the outer cross-sections of the other surfaces, and this seems difficult, as just relying on a distance criterion will not work, since the distance between the surfaces is always equal to zero (thus, the distance criterion is non-informative). We do not have a clear-cut solution to provide here.

The situation seems a bit easier if one of the two domains $[\theta_1, \theta_2]$ or $[\mu_1, \mu_2]$ is equal to $[0, 1]$: in this case, the boundary of $\boldsymbol{\gamma}$ will consist of two disjoint surfaces that can be treated independently with the results of section 2.4 to compute a limit angle ϕ_{self} so that each surface do not self-overlap. Then a distance criterion will yield a limit angle ϕ_{other} that gives a sufficient condition so that both surfaces do not overlap each other as (assuming here that the domain $[\theta_1, \theta_2]$ is equal to $[0, 1]$):

$$\phi_{\text{other}} = \min_{\mu,\mu',\alpha,\alpha'} \frac{1}{2} \cos^{-1}\left(\boldsymbol{\gamma}(\theta_1,\mu,\alpha)^T \boldsymbol{\gamma}(\theta_2,\mu',\alpha')\right),$$

and a sufficient condition so that no edge effect arises is

$$\phi < \min\left(\phi_{\text{other}}, \phi_{\text{self}}\right).$$

Needless to say, this seems to be a lot of work to check whether edge effects happen for a relationship that is already a heuristic!

2.5 . Numerical results

The goal of this section is to verify the relationships we derived in Sections 2.3 and 2.4 through numerical simulations, respectively in Subsections 2.5.1 and 2.5.2.

2.5.1 . Goodness of fit of the P_{FA}-threshold relationship

First, we will check the validity of the relationships obtained in Section 2.3. Figure 2.5.1a presents the P_{FA}-threshold relationship for one unknown parameter given by (2.33) using signal model (1.7) in Subsection 2.3.2 and empirically computed thresholds. The empirical relationship is obtained by computing the empirical cumulative distribution (ecdf) of off-grid GLRT test quantities (1.37) using 10^8 complex circular white Gaussian noise samples for a steering vector size of $N = 10$ (we obtain all simulated empirical P_{FA}-threshold relationships this way in the rest of this thesis). The continuous research over the domain $\mathcal{D}$ is replaced by a discrete search using 30 tests in the cell, where $\mathcal{D} = \mathcal{D}_0$. As expected, this simulation shows that the formula is not valid for P_{FA} close to 1 because of overlap (they even exceed 1: a more precise approximation can be obtained simply by capping the relationships to 1). However, such high P_{FA} have no practical interest for standard applications in radar. Furthermore, the theoretical relationship still seems to fit very well before reaching the limit threshold w_{lim} for which no overlap happens.

We have also compared this formula with empirical thresholds for colored noise ($\mathbf{\Gamma} \neq \mathbf{I}$). We define the covariance matrix $\mathbf{\Gamma}$ using the Toeplitz covariance matrix model defined in (1.17) with $\rho = 0.9$. Results can be observed in Figure 2.5.1b for the edge cell $\mathcal{D}_0$ where average detection performance has been shown to be lower in Figure 1.13c. Zooming on the leftmost part of the curves, it can be seen that the overlapping phenomenon for low P_{FA} values tends to increase slightly with ρ: the gap between the curves widens slightly and spans higher threshold values as noise becomes more correlated. This is not surprising, as correlated noise bends the manifold, increasing the likeliness of both local and non-local global overlap. However, the relationship still fits very well before attaining w_{lim}.

In Figures $2.5.2$, we compare the empirical relationships obtained when using a chirp waveform (signal model (1.5)) for the cases $\rho = 0$ (Figure 2.5.2a) and $\rho = 0.9$ (Figure 2.5.2b). Remark that the relationships still seem to fit pretty well.

The P_{FA}-threshold relationship for two unknown parameters under white noise found in subsection 2.3.3.1 is compared with the empirical relationship, with the GLRT approximated with 15×15 test points per cell on Figure 2.5.3a in the case of STAP detection over the whole domain (using relationship (2.36)) and Figure 2.5.5a when not testing on the whole domain, and using the relationship (2.37) obtained through our heuristic. Once again, the theoretical relationships seem to fit very well with what is observed, even in the case of the relationship obtained through the heuristic. The empirical P_{FA}-threshold relationship of the distance-Doppler signal model using a chirp waveform (signal model (1.8)) is then compared with the FMCW distance-Doppler relationship adapted from the STAP heuristic relationship (2.37) by replacing P with K and $\mu_2 - \mu_1$ by $\tau_2 - \tau_1$ in Figure 2.5.5b. It can be seen that both relationships fit pretty well.

The relationship (2.40) found in Subsection 2.3.3.2 for STAP detection over the whole search domain with colored Gaussian noise is tested in Figure 2.5.3b, still using the covariance matrix model (1.17) with $\rho = 0.9$ (the matrix so defined is centrosymmetric so that the theorem applies). In order to obtain a satisfying approximation of the off-grid GLRT when testing on the whole parameter space under colored noise, a very large number of samples is needed when sampling uniformly: as such, we compute 250×250 (!) samples per test in order to obtain the empirical relationship on this figure. This is explained by the fact that some of the lobes become very thin when using correlated noise, as was observed in figure 1.14a. Those computational challenges highlight the practical interest of the developed P_{FA}-threshold relationships in this thesis, as obtaining the thresholds for very low P_{FA}s with the developed relationships is practically instantaneous. In figure 2.5.3b, both relationships fit very well, which tends to validate

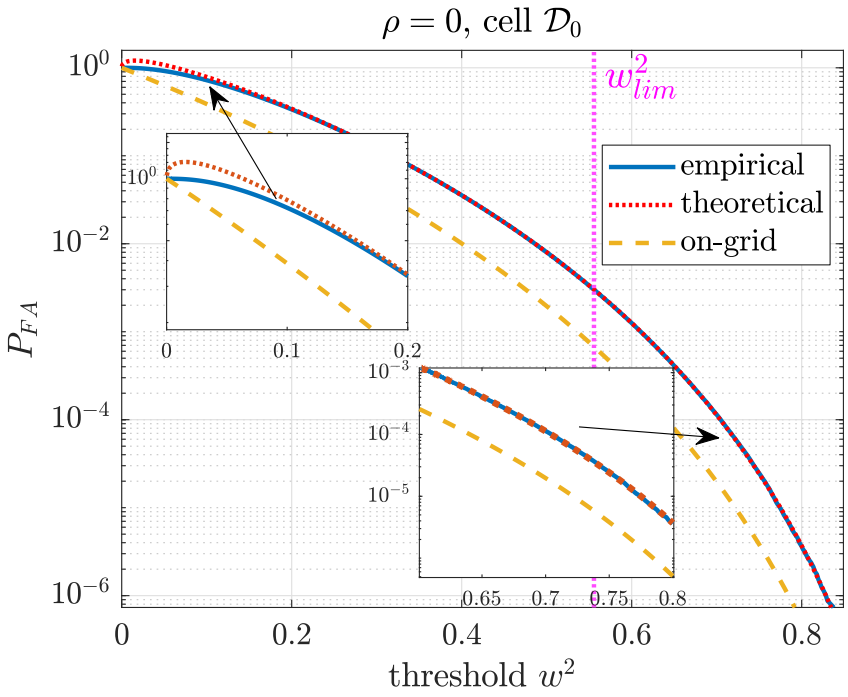

(a) Uncorrelated noise : $\rho = 0$.

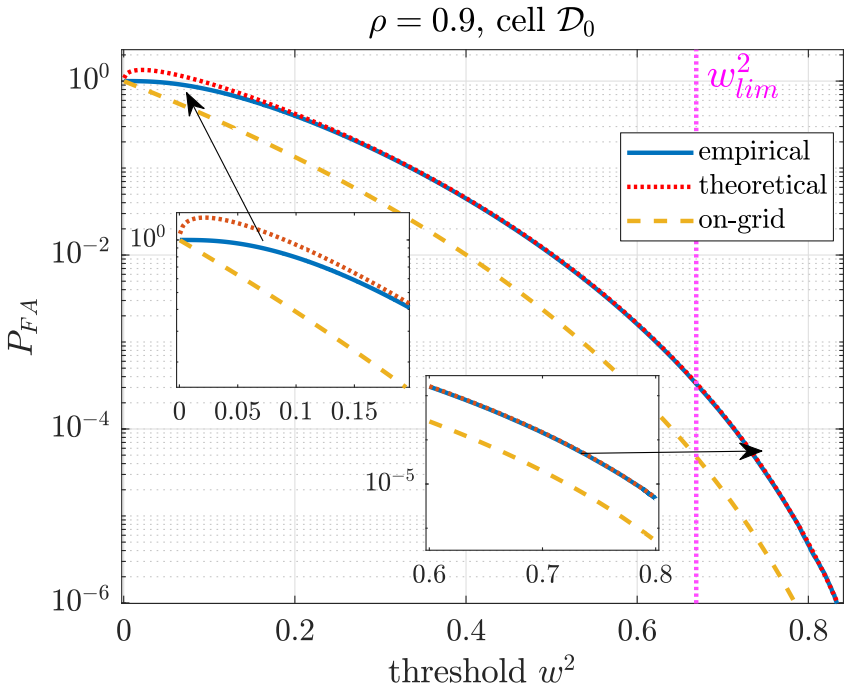

(b) Highly correlated noise : $\rho = 0.9$.

Figure 2.5.1: Comparison between the theoretical P_{FA}-threshold given in (2.33) for (a) and (2.32) for (b) and the empirical Monte Carlo P_{FA}-threshold relationships for $N = 10$ and for several values of ρ (1.17) for Doppler (or angle) detection. The relationship is drawn for the search domain $\mathcal{D}_0$. The on-grid relation (1.27) is also drawn for comparison purposes. The limit overlap threshold w_{lim} proposed in (2.43) is in purple.

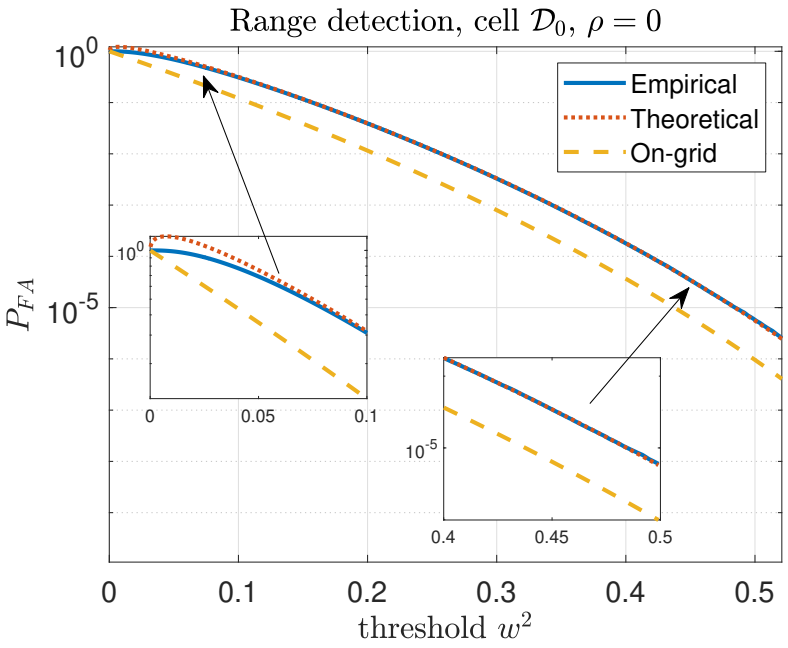

(a) Uncorrelated noise : $\rho = 0$.

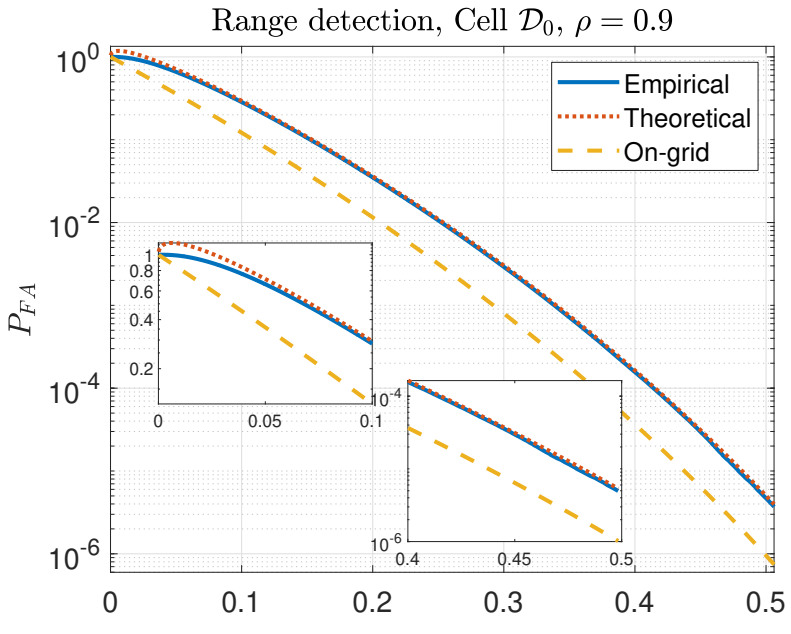

(b) Highly correlated noise : $\rho = 0.9$.

Figure 2.5.2: Comparison between the theoretical P_{FA}-threshold given in (2.33) for (a) and (2.32) for (b) and the empirical Monte Carlo P_{FA}-threshold relationships for $K = 20$ and for several values of ρ (1.17) in range detection context using a chirp waveform (signal model (1.5)). The relationship is drawn for the search domain $\mathcal{D}_0$, with the on-grid relationship (1.27) in yellow.

corollary 2.3.0.3. It can be observed that the obtained P_{FA}-threshold relationship is close to the white noise case but not exactly the same.

Remark 2.5.1. *It is remarkable that a non-white covariance matrix changes the P_{FA}: we initially thought that the covariance matrix induced a distortion of the signal manifold locally in each cell but that the overall*

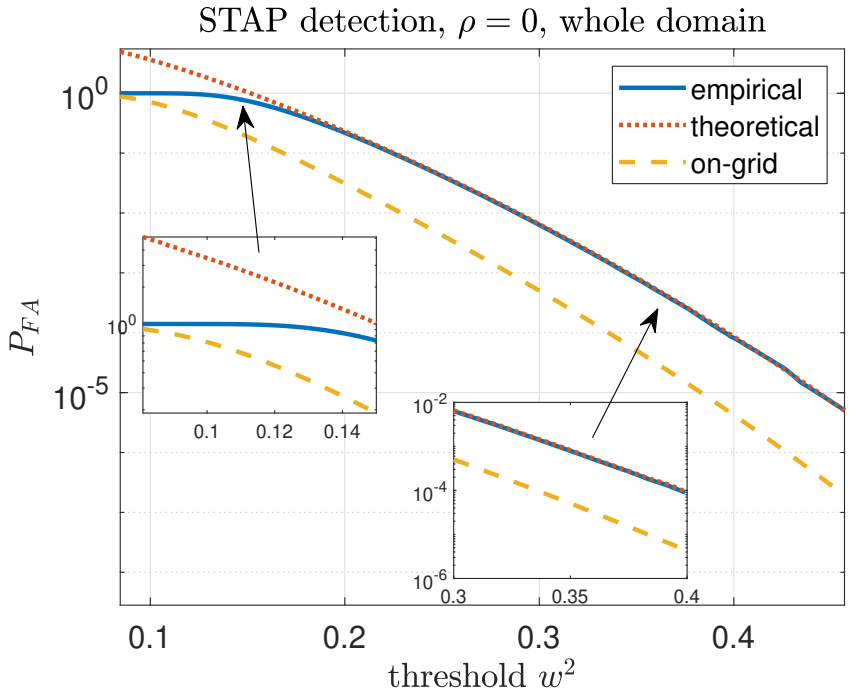

(a) White noise.

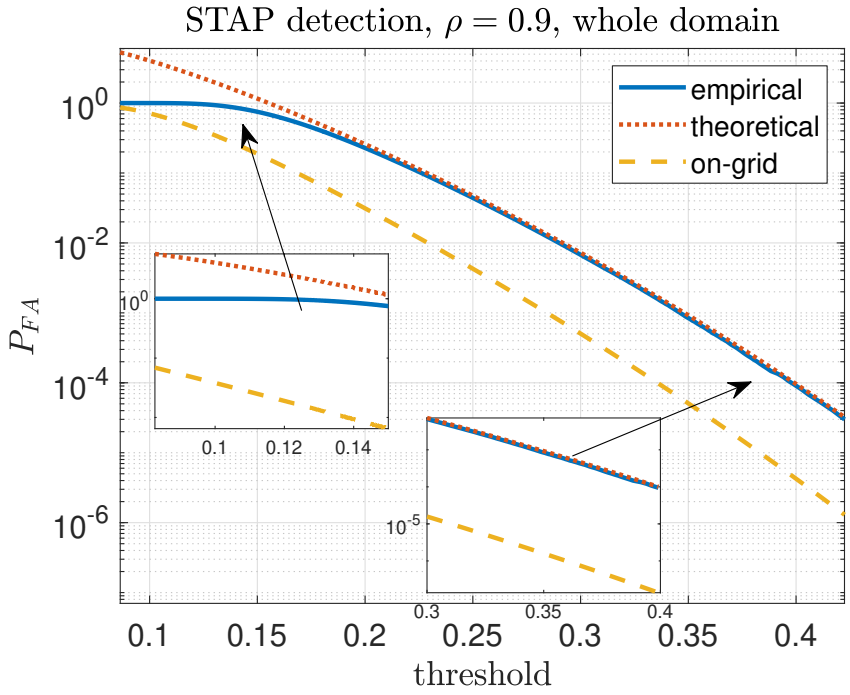

(b) $\rho = 0.9$.

Figure 2.5.3: Comparison between the theoretical P_{FA}-threshold for a search on the whole domain given in (2.36) for the case of white noise (2.5.3a) and (2.40) for a the case of colored noise (2.5.5a), and the empirical Monte Carlo P_{FA}-threshold relationships for STAP detection with $N = 8, P = 4$. The on-grid global relation (1.30) is also drawn.

surface stayed the same. Since a greater P_{FA} means a greater surface, figure 2.5.4 shows that there is a global distortion of the manifold surface under the presence of a non-white covariance matrix. This is true for all tested threshold values so this is not due to overlap.

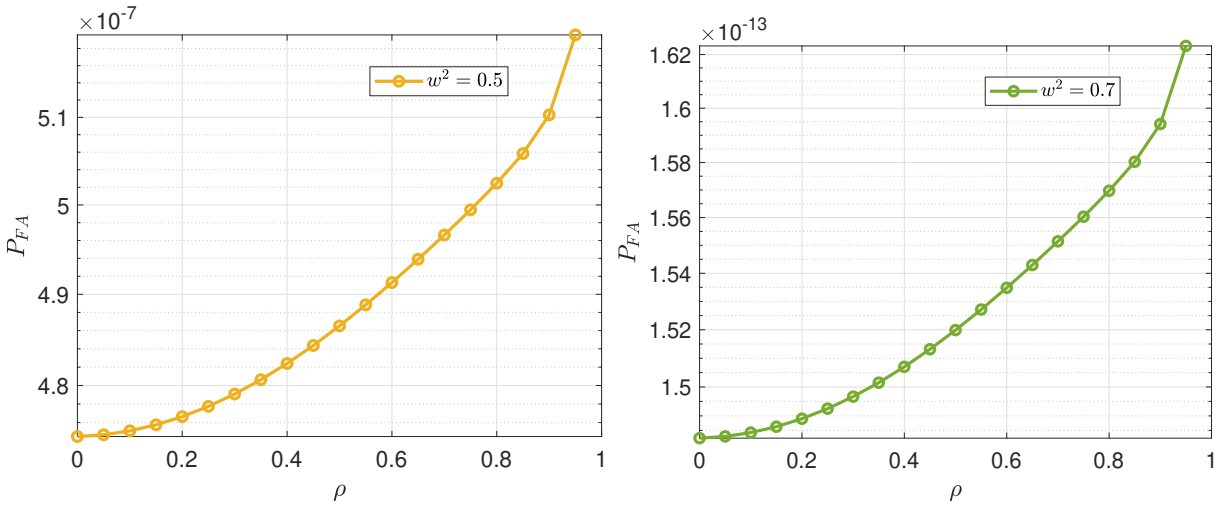

(a) $w^2 = 0.5$ (b) $w^2 = 0.7$.

Figure 2.5.4: Evolution of the global P_{FA} ($\mathcal{D} = [0,1]^2$) for STAP detection with $N = 8, P = 4$, and predefined thresholds. The P_{FA} values are computed thanks to (2.40).

Finally, we compared the heuristic formula (2.40) for detection over $\mathcal{D} \neq [0,1]^2$ under colored noise, in the case of STAP signal model. We take $\rho = 0.9$ in (1.17), and run tests in cell $\mathcal{D}_0$, using 90×90 samples per test. Again, this heuristic seems to be a perfectly appropriate way of estimating the P_{FA} in this case. In all the above cases, the derived formula are good approximation of the P_{FA}-threshold relationship well before the limit threshold for no overlap w_{lim}.

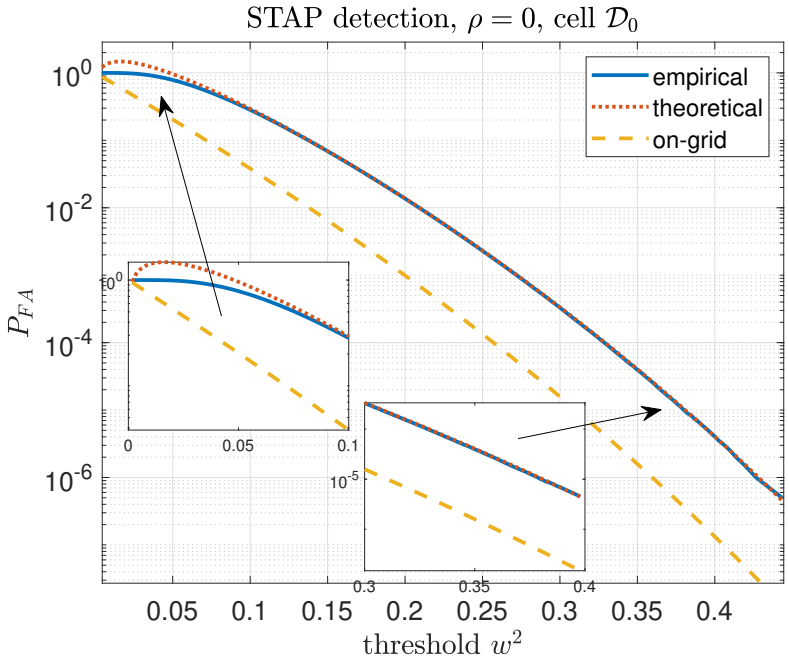

(a) STAP tests in the cell $\mathcal{D}_0$.

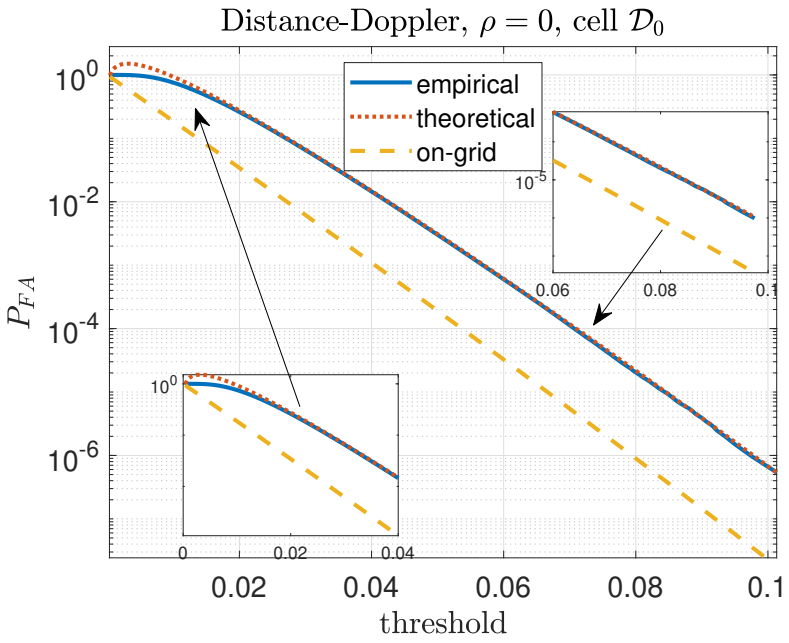

(b) Range-Doppler test in the cell $\mathcal{D}_0$.

Figure 2.5.5: Comparison between the heuristic P_{FA}-threshold given in (2.37) for a search in a single cell and the empirical Monte Carlo P_{FA}-threshold relationships under white noise in the case of STAP detection with $N = 8, P = 4$ and range-Doppler detection with $K = 20, N = 10$ using a chirp (in which case the theoretical relationship of the FMCW is used), under white noise. The on-grid relationship (1.27) is also drawn.

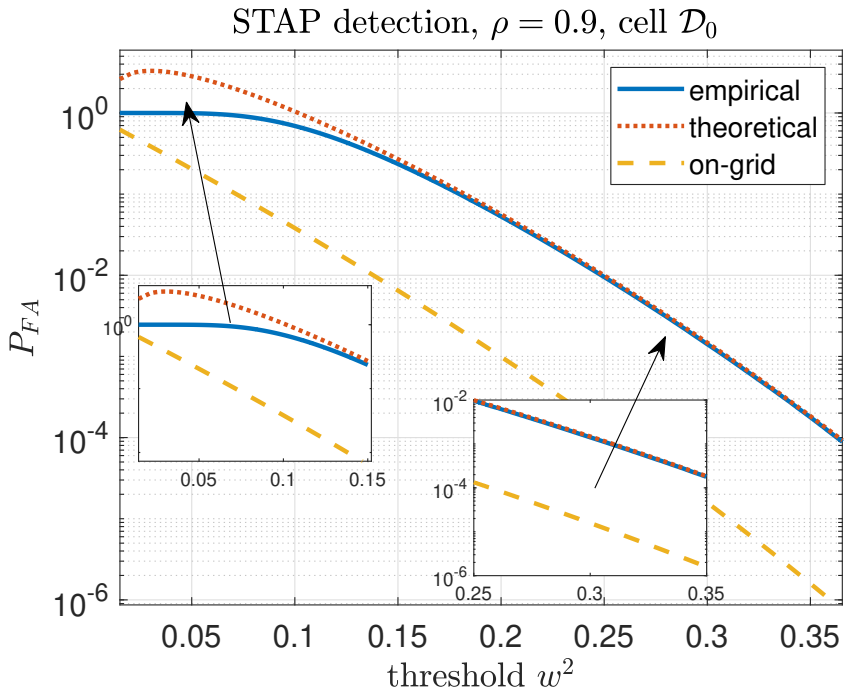

Figure 2.5.6: Comparison of the heuristic P_{FA}-threshold relationship (2.40) with the empirical relationship for STAP detection with $N = 8, P = 4$, over the search domain $\mathcal{D}_0$ with $\rho = 0.9$.

2.5.2 . Numerical investigation of overlap

As we just noted, the simulations seem to fit well for threshold values below limit overlap angle values (2.54) so it is not trivial to verify them simply by looking at the figures: overlap seems to stop having a significant impact on the relationship well before attaining w_{lim}. In particular, we numerically check our value of w_{lim} under white noise for Doppler detection. The idea is to consider a point located on the frontier of the tube in the direction where the curvature of $\boldsymbol{\gamma}$ is the strongest: this represents the worst-case scenario for local overlap. We show that this point belongs to a single cross-section for a threshold w very close below w_{lim} but belongs to several cross-sections as soon as w crosses w_{lim}. For that purpose, consider the following point (for any $v, \alpha \in \mathcal{D} \times [0, 2\pi]$ since $\boldsymbol{\gamma}$ is shift invariant):

$$\underline{\mathbf{u}} = \cos(\phi)\, \boldsymbol{\gamma}(v, \alpha) + \sin(\phi)\, \mathbf{n}\,, \tag{2.72}$$

with $\cos\phi = w$ and $\mathbf{n}$ is the unit norm vector such that:

$$\mathbf{n} \propto \boldsymbol{\gamma}(v, \alpha) + \sum_{i,j \in [1,2]} \beta_i \beta_j \left(\frac{\partial^2 \boldsymbol{\gamma}}{\partial \psi_i \partial \psi_j} \right) ,$$

where $\boldsymbol{\psi} = (\alpha, v)$ is the centrosymmetric parametrization of $\boldsymbol{\gamma}$, and

$$(\beta_1, \beta_2) = \underset{(\beta_1,\beta_2)\in\mathbb{S}^1}{\arg\max} \left\| \sum_{i,j} \beta_i \beta_j \left(\frac{\partial^2 \boldsymbol{\gamma}}{\partial \psi_i \partial \psi_j} \right) \right\|^2 ,$$

where the right quantity has to be maximized numerically with $\beta_1 = \sin(\varphi)$, $\beta_2 = \cos(\varphi)$. Note that, using (2.107), $\mathbf{n}$ is orthogonal to $\boldsymbol{\gamma}(v, \alpha)$:

$$\begin{aligned} \boldsymbol{\gamma}(v, \alpha)^T \mathbf{n} &\propto 1 + \beta_1^2 \boldsymbol{\gamma}(v, \alpha)^T \frac{\partial^2 \boldsymbol{\gamma}}{\partial \psi_1^2} + \beta_2^2 \boldsymbol{\gamma}(v, \alpha)^T \frac{\partial^2 \boldsymbol{\gamma}}{\partial \psi_2^2} \\ &\propto 1 - \beta_1^2 - \beta_2^2 \\ &= 0\,. \end{aligned}$$

$\underline{\mathbf{u}}$ is then indeed a point of the tube since $\underline{\mathbf{u}}^T \boldsymbol{\gamma}(v, \alpha) = \cos\phi = w$ and $\|\underline{\mathbf{u}}\| = 1$. Figure 2.5.7 shows that $\mathbf{u}$ belongs to only one cross-section when $\phi < \phi_{\text{lim}}$ and to three cross-sections when $\phi > \phi_{\text{lim}}$. To see that, define the complex vector $\mathbf{u}$ by $\underline{\mathbf{u}} = \begin{bmatrix} \text{Re}(\mathbf{u}) \\ \text{Im}(\mathbf{u}) \end{bmatrix}$, and see that the derivative of the product $\left|\mathbf{u}^H \mathbf{s}(v + \delta)\right|^2$ w.r.t. δ vanishes to 0 above the threshold once in the first case, and three times in the second, at values $\delta_1, 0, \delta_2$. Using (2.4), $\boldsymbol{\gamma}(\boldsymbol{v} + \delta_i, \angle \mathbf{u}^H \mathbf{s}(v + \delta_i))^T \underline{\mathbf{u}} = \left| \mathbf{s}\,(v + \delta_i)^H\, \mathbf{u} \right|$ is a local maxima w.r.t. α. Thus $\underline{\mathbf{u}}^T \dfrac{\partial \boldsymbol{\gamma}}{\partial v} = \underline{\mathbf{u}}^T \dfrac{\partial \boldsymbol{\gamma}}{\partial \alpha} = 0$ for 3 values $\psi_i = \left(v + \delta_i, \angle \mathbf{u}^H \mathbf{s}(v + \delta_i)\right)$ so that $\underline{\mathbf{u}}$ belongs to 3 cross-sections $\mathcal{C}_w(\boldsymbol{\gamma}(\psi_{\mathbf{i}}))$ according to the definition (2.9). Even though it is hard to detect visually in Figure 2.5.1a, overlap occurs right before the limit threshold value w_{lim} found in (2.61): the limit threshold is very conservative and formula (2.33) can be used as a good approximate of the true P_{FA} threshold relationship for thresholds well below that.

In Figure 2.5.8, we plot the relationship between ρ and the minimum threshold for which there is no overlap w_{lim} computed thanks to (2.45) for Doppler detection. The components w_{local} and $w_{\text{non-local}}$ are obtained thanks to (2.57) and (2.52). As we suspected, w_{lim} tends to increase with ρ. The arising of non-local overlap can be explained by looking at Figure 2.4.4: when ρ increases, a side-lobe enters cell $\mathcal{D}_0$, and the distance between the pair of points maximizing the ambiguity function decreases, making the manifold $\boldsymbol{\gamma}$ more prone to self-overlap.

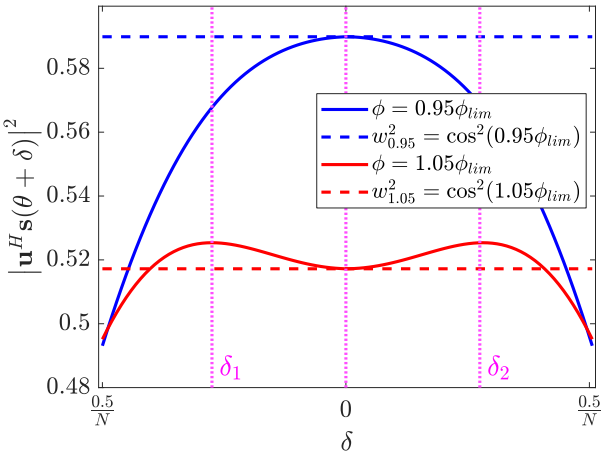

Figure 2.5.7: Illustration of the overlap phenomenon: squared projection of $\mathbf{u}$ defined in (2.72) on $\mathbf{s}(\theta+\delta)$ for $\theta+\delta \in \mathcal{D}_0$ for two values of ϕ: $\phi = 0.95\phi_{\text{lim}}$ and $\phi = 1.05\phi_{\text{lim}}$. The values of δ highlighted in purple correspond to the critical points of this quantity.

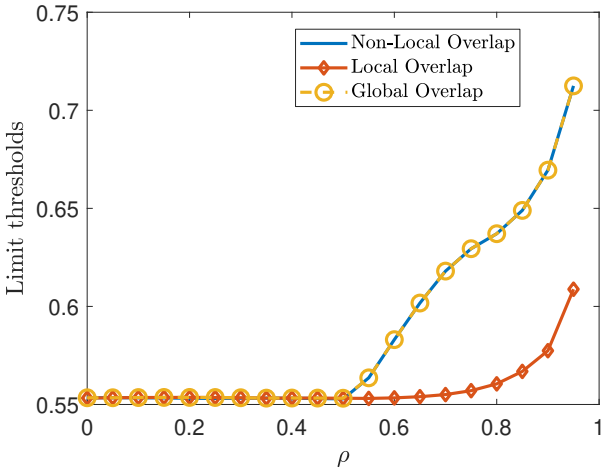

Figure 2.5.8: Comparison of the limit global overlap thresholds w_{lim} (yellow), w_{local} (blue) and $w_{\text{non-local}}$ (red) versus ρ obtained with (2.45), (2.57) and (2.52) for Doppler detection with $N = 10$, in the cell $\mathcal{D}_0$.

	Borderless ($\mathcal{D} = [0,1]$)	With borders ($\mathcal{D} \subsetneq [0,1]$)
Doppler (Angle)	Yes (2.32), (2.33)	Yes (2.32), (2.33)
Range	N/A	Yes (2.32), (2.33)
STAP	Yes (2.36),(2.40)	Heuristic 2.3.1, 2.3.2
Doppler-Range	N/A	Heuristic 2.3.2

Table 2.6.1: Recap of the P_{FA}-threshold relationship obtained for the off-grid NMF

2.6 . Synthesis

In this chapter, we derived new P_{FA}-threshold relationships for the off-grid Normalized Matched Filter thanks to a geometrical approach based on finding the volume of tubes around the manifolds linked to the signals of reference in a cell. In particular, closed-form expressions are derived for signal model (1.7) and (1.10) under white noise. All expressions are exact when the P_{FA} is low enough, which seem of great interest for radar applications. We derived precisely their domain of validity thanks to a thorough study of the overlap phenomena that can appear when dealing with tubes. We verified numerically that both the relationships and the limit thresholds w_{lim} we computed seem correct thanks to numerical simulations. Table 2.6.1 sums up the contexts in which we achieved the derivation of P_{FA}-thresholds relationships. In the following chapter, we have a similar objective: we want to compute the P_{FA}-threshold relationship of the off-grid Matched Filter. In order to do so, we will use a different but closely related approach, based on the expected Euler characteristic of excursion sets.

Appendix

2.A . On Weyl's formula for the volume of tubes

Our goal in this section is to establish Weyl's formula (2.10) following his proof in [Wey39], filling some intermediate steps not provided in the original paper, making its reading quite difficult.

Consider an M-dimensional manifold $\boldsymbol{\gamma}(\boldsymbol{\xi})$ embedded on $\mathbb{S}^{n-1}$, where $\boldsymbol{\xi}$ runs in a search domain $\mathcal{D}$. Our goal is to compute the volume V of the cross-sections spanned by $\boldsymbol{\gamma}$, defined in (2.9), with a geodesic radius $w = \cos\phi$.

Defining the codimension as $\nu = n - 1 - M$, let us introduce an orthonormal basis $\mathbf{n}_1(\boldsymbol{\xi}), \dots, \mathbf{n}_\nu(\boldsymbol{\xi})$ to the orthogonal of $\boldsymbol{\gamma}$ and its tangent plane generated by $\left(\frac{\partial \boldsymbol{\gamma}}{\partial \xi_1}, \dots, \frac{\partial \boldsymbol{\gamma}}{\partial \xi_M}\right)$, so that:

$$\begin{aligned}\mathbf{n}_i(\boldsymbol{\xi})^T \boldsymbol{\gamma}(\boldsymbol{\xi}) &= 0 \text{ for } i \in [1, \nu]\,,\\ \mathbf{n}_i(\boldsymbol{\xi})^T \frac{\partial \boldsymbol{\gamma}}{\partial \xi_j}(\boldsymbol{\xi}) &= 0 \text{ for } i \in [1, \nu], j \in [1, M]\,.\end{aligned}$$

Following definition (2.9), the points $\mathbf{u}$ in a cross-section $\mathcal{C}_w(\boldsymbol{\gamma}(\boldsymbol{\xi}))$ can be expressed as:

$$\begin{aligned}\tilde{\mathbf{r}} &= \frac{\boldsymbol{\gamma}(\boldsymbol{\xi}) + t_1\mathbf{n}_1(\boldsymbol{\xi}) + \dots + t_\nu \mathbf{n}_\nu(\boldsymbol{\xi})}{\|\boldsymbol{\gamma}(\boldsymbol{\xi}) + t_1\mathbf{n}_1(\boldsymbol{\xi}) + \dots + t_\nu \mathbf{n}_\nu(\boldsymbol{\xi})\|}\\ &= \frac{\boldsymbol{\gamma}(\boldsymbol{\xi}) + t_1\mathbf{n}_1(\boldsymbol{\xi}) + \dots + t_\nu \mathbf{n}_\nu(\boldsymbol{\xi})}{\sqrt{1 + t_1^2 + \dots + t_\nu^2}}\,,\end{aligned}$$

where $\tilde{\mathbf{r}}^T\boldsymbol{\gamma}(\boldsymbol{\xi}) < w \triangleq \cos\phi$ so that $\frac{1}{\sqrt{1 + t_1^2 + \dots + t_\nu^2}} < \cos\phi$, i.e. $\frac{1}{\cos^2\phi} = 1 + \tan^2\phi > 1 + t_1^2 + \dots + t_\nu^2$, and finally $t_1^2 + \dots + t_\nu^2 < \tan^2\phi$. The manifold described by the union of the cross-sections can then be parametrized by $\xi_1, \dots, \xi_M, t_1, \dots, t_\nu$. Direct computation of the surface of this manifold can be obtained with:

$$V = \int_{\mathcal{D}} \int_{t_1^2 + \dots + t_\nu^2 < \tan^2\phi} \sqrt{\det\left(\left(\frac{\partial \tilde{\mathbf{r}}}{\partial \xi_1}, \dots, \frac{\partial \tilde{\mathbf{r}}}{\partial \xi_M}, \frac{\partial \tilde{\mathbf{r}}}{\partial t_1}, \dots, \frac{\partial \tilde{\mathbf{r}}}{\partial t_\nu}\right)^T \left(\frac{\partial \tilde{\mathbf{r}}}{\partial \xi_1}, \dots, \frac{\partial \tilde{\mathbf{r}}}{\partial \xi_M}, \frac{\partial \tilde{\mathbf{r}}}{\partial t_1}, \dots, \frac{\partial \tilde{\mathbf{r}}}{\partial t_\nu}\right)\right)} d\boldsymbol{\xi} dt_1 \dots dt_\nu\,.$$

In the following, we note $\mathbf{u} = \boldsymbol{\gamma}(\boldsymbol{\xi}) + t_1\mathbf{n}_1(\boldsymbol{\xi}) + \dots + t_\nu\mathbf{n}_\nu(\boldsymbol{\xi})$ and $U = \|\boldsymbol{\gamma}(\boldsymbol{\xi}) + t_1\mathbf{n}_1(\boldsymbol{\xi}) + \dots + t_\nu\mathbf{n}_\nu(\boldsymbol{\xi})\|$, such that $\tilde{\mathbf{r}} = \frac{\mathbf{u}}{U}$. Uee how

$$\begin{aligned}\det\left(\mathbf{u}, \frac{\partial \mathbf{u}}{\partial \xi_1}, \dots, \frac{\partial \mathbf{u}}{\partial \xi_M}, \frac{\partial \mathbf{u}}{\partial t_1}, \dots, \frac{\partial \mathbf{u}}{\partial t_\nu}\right) &= \det\left(U\tilde{\mathbf{r}}, U\frac{\partial \tilde{\mathbf{r}}}{\partial \xi_1} + \frac{\partial U}{\partial \xi_1}\tilde{\mathbf{r}}, \dots, U\frac{\partial \tilde{\mathbf{r}}}{\partial \xi_M} + \frac{\partial U}{\partial \xi_M}\tilde{\mathbf{r}}, U\frac{\partial \tilde{\mathbf{r}}}{\partial t_1} + \frac{\partial U}{\partial t_1}\tilde{\mathbf{r}}, \dots, U\frac{\partial \tilde{\mathbf{r}}}{\partial t_\nu} + \frac{\partial U}{\partial t_\nu}\tilde{\mathbf{r}}\right)\\ &= \det\left(U\tilde{\mathbf{r}}, U\frac{\partial \tilde{\mathbf{r}}}{\partial \xi_1}, \dots, U\frac{\partial \tilde{\mathbf{r}}}{\partial \xi_M}, U\frac{\partial \tilde{\mathbf{r}}}{\partial t_1}, \dots, U\frac{\partial \tilde{\mathbf{r}}}{\partial t_\nu}\right)\\ &= U^n \det\left(\tilde{\mathbf{r}}, \frac{\partial \tilde{\mathbf{r}}}{\partial \xi_1}, \dots, \frac{\partial \tilde{\mathbf{r}}}{\partial \xi_M}, \frac{\partial \tilde{\mathbf{r}}}{\partial t_1}, \dots, \frac{\partial \tilde{\mathbf{r}}}{\partial t_\nu}\right)\\ &= U^n \sqrt{\det\left(\left(\tilde{\mathbf{r}}, \frac{\partial \tilde{\mathbf{r}}}{\partial \xi_1}, \dots, \frac{\partial \tilde{\mathbf{r}}}{\partial \xi_M}, \frac{\partial \tilde{\mathbf{r}}}{\partial t_1}, \dots, \frac{\partial \tilde{\mathbf{r}}}{\partial t_\nu}\right)^T \left(\tilde{\mathbf{r}}, \frac{\partial \tilde{\mathbf{r}}}{\partial \xi_1}, \dots, \frac{\partial \tilde{\mathbf{r}}}{\partial \xi_M}, \frac{\partial \tilde{\mathbf{r}}}{\partial t_1}, \dots, \frac{\partial \tilde{\mathbf{r}}}{\partial t_\nu}\right)\right)}\\ &= U^n \sqrt{\det\begin{pmatrix}1 & \mathbf{0}\\ \mathbf{0} & \left(\frac{\partial \tilde{\mathbf{r}}}{\partial \xi_1}, \dots, \frac{\partial \tilde{\mathbf{r}}}{\partial \xi_M}, \frac{\partial \tilde{\mathbf{r}}}{\partial t_1}, \dots, \frac{\partial \tilde{\mathbf{r}}}{\partial t_\nu}\right)^T \left(\frac{\partial \tilde{\mathbf{r}}}{\partial \xi_1}, \dots, \frac{\partial \tilde{\mathbf{r}}}{\partial \xi_M}, \frac{\partial \tilde{\mathbf{r}}}{\partial t_1}, \dots, \frac{\partial \tilde{\mathbf{r}}}{\partial t_\nu}\right)\end{pmatrix}}\\ &= U^n \sqrt{\det\left(\left(\frac{\partial \tilde{\mathbf{r}}}{\partial \xi_1}, \dots, \frac{\partial \tilde{\mathbf{r}}}{\partial \xi_M}, \frac{\partial \tilde{\mathbf{r}}}{\partial t_1}, \dots, \frac{\partial \tilde{\mathbf{r}}}{\partial t_\nu}\right)^T \left(\frac{\partial \tilde{\mathbf{r}}}{\partial \xi_1}, \dots, \frac{\partial \tilde{\mathbf{r}}}{\partial \xi_M}, \frac{\partial \tilde{\mathbf{r}}}{\partial t_1}, \dots, \frac{\partial \tilde{\mathbf{r}}}{\partial t_\nu}\right)\right)},\end{aligned}$$

where the passage from the first to the second line results from the multilinearity of the determinant, noting that $\frac{\partial U}{\partial \xi_i}\tilde{\mathbf{r}}$ is colinear to the first column $U\tilde{\mathbf{r}}$. Thus,

$$\begin{aligned} V &= \int_{\mathcal{D}} \int_{t_1^2+\cdots+t_\nu^2<\tan^2\phi} \frac{\det\left(\mathbf{u}, \frac{\partial \mathbf{u}}{\partial \xi_1}, \ldots, \frac{\partial \mathbf{u}}{\partial \xi_M}, \frac{\partial \mathbf{u}}{\partial t_1}, \ldots, \frac{\partial \mathbf{u}}{\partial t_\nu}\right)}{U^n} d\boldsymbol{\xi} dt_1 \ldots dt_\nu \\ &= \int_{\mathcal{D}} \int_{t_1^2+\cdots+t_\nu^2<\tan^2\phi} \frac{\det\left(\mathbf{u}, \frac{\partial \mathbf{u}}{\partial \xi_1}, \ldots, \frac{\partial \mathbf{u}}{\partial \xi_M}, \mathbf{n}_1, \ldots, \mathbf{n}_\nu\right)}{(1+t_1^2+\cdots+t_\nu^2)^{n/2}} d\boldsymbol{\xi} dt_1 \ldots dt_\nu \,. \end{aligned} \tag{2.73}$$

In the following, let $g_{ij} = \frac{\partial \boldsymbol{\gamma}}{\partial \xi_i}^T \frac{\partial \boldsymbol{\gamma}}{\partial \xi_j}$ and $G_{ij}(p) = -\frac{\partial^2 \boldsymbol{\gamma}^T}{\partial \xi_i \partial \xi_j}\mathbf{n}_p = \frac{\partial \boldsymbol{\gamma}}{\partial \xi_i}^T \frac{\partial \mathbf{n}_p}{\partial \xi_j}$. g_{ij} is the first fundamental form of $\boldsymbol{\gamma}$, and $G_{ij}(p)$ is the second fundamental form of $\boldsymbol{\gamma}$ for the normal $\mathbf{n}_p$. In order to evaluate the terms $\frac{\partial \mathbf{u}}{\partial \xi_i}$ in (2.73), let us express the derivatives of the normals $\frac{\partial \mathbf{n}_i}{\partial \xi_j}$ for $i \in [1, \nu]$ and $j \in [1, M]$ in the basis $\left(\boldsymbol{\gamma}, \frac{\partial \boldsymbol{\gamma}}{\partial \xi_1}, \ldots, \frac{\partial \boldsymbol{\gamma}}{\partial \xi_M}, \mathbf{n}_1, \ldots, \mathbf{n}_\nu\right)$ of $\mathbb{R}^n$:

$$\frac{\partial \mathbf{n}_i}{\partial \xi_j} = e_1 \boldsymbol{\gamma} + e_2 \frac{\partial \boldsymbol{\gamma}}{\partial \xi_1} + \cdots + e_{M+1} \frac{\partial \boldsymbol{\gamma}}{\partial \xi_M} + e_{M+2}\mathbf{n}_1 + \cdots + e_n \mathbf{n}_\nu \,.$$

Scalar multiplying by $\frac{\partial \boldsymbol{\gamma}}{\partial \xi_k}$ yields:

$$G_{jk}(i) = e_2 g_{1k} + \cdots + e_{M+1} g_{Mk} \,.$$

Thus, the coefficients $e_2, \ldots, e_{M+1}$ will be noted $G_j^1(i), \ldots, G_j^M(i)$ in the following, as the operation $G_j^1(i)g_{1k} + \cdots + G_j^M(i)g_{Mk}$ "lowers the indice" in tensor notation [SS78], thus giving $G_{jk}(i)$. The vectors $\frac{\partial \mathbf{u}}{\partial \xi_i}$ can then be expressed as:

$$\begin{aligned} \frac{\partial \mathbf{u}}{\partial \xi_i} &= \frac{\partial \boldsymbol{\gamma}}{\partial \xi_i} + \sum_{j=1}^{\nu} t_j \frac{\partial \mathbf{n}_j}{\partial \xi_i} \\ &= \frac{\partial \boldsymbol{\gamma}}{\partial \xi_i} + \sum_{j=1}^{\nu} t_j \sum_{k=1}^{M} G_i^k(j) \frac{\partial \boldsymbol{\gamma}}{\partial \xi_k} + e_1 \boldsymbol{\gamma} + \sum_{l=1}^{\nu} e_{M+1+l} \mathbf{n}_l \\ &= \sum_{k=1}^{M} \left(\delta_i^k + \sum_{j=1}^{\nu} t_j G_i^k(j)\right) \frac{\partial \boldsymbol{\gamma}}{\partial \xi_k} + \ldots \end{aligned}$$

where δ_i^k is the Kronecker symbol. Exploiting the multilinearity property of the determinant, the dotted terms are not involved in the determinant in (2.73). Noting $\mathbf{G}$ the matrix $\left(\delta_i^k + \sum_{j=1}^{\nu} t_j G_i^k(j)\right)_{k,i \in [1,M]^2}$:

$$\begin{aligned} \det\left(\mathbf{u}, \frac{\partial \mathbf{u}}{\partial \xi_1}, \ldots, \frac{\partial \mathbf{u}}{\partial \xi_M}, \mathbf{n}_1, \ldots, \mathbf{n}_\nu\right) &= \det\left(\left(\mathbf{u}, \frac{\partial \boldsymbol{\gamma}}{\partial \xi_1}, \ldots, \frac{\partial \boldsymbol{\gamma}}{\partial \xi_M}, \mathbf{n}_1, \ldots, \mathbf{n}_\nu\right) \begin{pmatrix} 1 & \mathbf{0} & \mathbf{0} \\ \mathbf{0} & \mathbf{G} & \mathbf{0} \\ \mathbf{0} & \mathbf{0} & \mathbf{I} \end{pmatrix}\right) \\ &= \det \mathbf{G} \det\left(\mathbf{u}, \frac{\partial \boldsymbol{\gamma}}{\partial \xi_1}, \ldots, \frac{\partial \boldsymbol{\gamma}}{\partial \xi_M}, \mathbf{n}_1, \ldots, \mathbf{n}_\nu\right) \,. \end{aligned} \tag{2.74}$$

Note that:

$$\det\left(\mathbf{u}, \frac{\partial \boldsymbol{\gamma}}{\partial \xi_1}, \ldots, \frac{\partial \boldsymbol{\gamma}}{\partial \xi_M}, \mathbf{n}_1, \ldots, \mathbf{n}_\nu\right) = \det\left(\boldsymbol{\gamma}, \frac{\partial \boldsymbol{\gamma}}{\partial \xi_1}, \ldots, \frac{\partial \boldsymbol{\gamma}}{\partial \xi_M}, \mathbf{n}_1, \ldots, \mathbf{n}_\nu\right) \tag{2.75}$$

$$= \sqrt{\det\left(\left(\boldsymbol{\gamma}, \frac{\partial \boldsymbol{\gamma}}{\partial \xi_1}, \ldots, \frac{\partial \boldsymbol{\gamma}}{\partial \xi_M}, \mathbf{n}_1, \ldots, \mathbf{n}_\nu\right)^T \left(\boldsymbol{\gamma}, \frac{\partial \boldsymbol{\gamma}}{\partial \xi_1}, \ldots, \frac{\partial \boldsymbol{\gamma}}{\partial \xi_M}, \mathbf{n}_1, \ldots, \mathbf{n}_\nu\right)\right)}$$

$$= \sqrt{\det\begin{pmatrix} 1 & \mathbf{0} & \mathbf{0} \\ \mathbf{0} & \left(\frac{\partial \boldsymbol{\gamma}^T}{\partial \xi_i}\frac{\partial \boldsymbol{\gamma}}{\partial \xi_j}\right)_{1\le i,j\le M} & \mathbf{0} \\ \mathbf{0} & \mathbf{0} & \mathbf{I} \end{pmatrix}}$$

$$= \sqrt{\det g_{ij}}\,. \tag{2.76}$$

$\sqrt{\det g_{ij}}d\xi_1 \ldots d\xi_M$ is the manifold surface element, noted $d\mathbf{u}$ in the following. Finally, injecting (2.76) in (2.74) we obtain from (2.73):

$$V = \int_\gamma \left\{ \int \cdots \int_{t_1^2+\cdots+t_\nu^2 \le \tan^2\phi} \frac{\det\left(\delta_j^i + \sum_{p=1}^{\nu} t_p\, G_i^j(p)\right)}{\left(1+t_1^2+\cdots+t_\nu^2\right)^{n/2}} dt_1 \ldots dt_\nu \right\} d\mathbf{u}\,,$$

This is Weyl's result that was given in (2.10).

2.B . Proofs of the chapter

In the first section of the appendix, we prove that the tube $\mathcal{T}$, defined in (2.30) for fixed $\boldsymbol{\xi}$, does not overlap. Then, we provide the proof of the results of the chapter.

2.B.1 . On the absence of overlap of the tube $\mathcal{T}$ (2.30) for fixed ξ

Since $\left\|\frac{\partial \boldsymbol{\gamma}(\boldsymbol{\xi},\alpha)}{\partial \alpha}\right\| = 1$, $\boldsymbol{\gamma}(\boldsymbol{\xi},.)$ is parameterized by arc length. The radius of first curvature is then defined as $\rho = \left\|\frac{\partial^2 \boldsymbol{\gamma}(\boldsymbol{\xi},\alpha)}{\partial \alpha^2}\right\|^{-1} = 1$. Then, since $\sin(\cos^{-1} w) < 1$ for all w, there is no local overlap according to (2.7): the tube radius is indeed always smaller than the radius of curvature of the manifold.

Let us prove there is no non-local overlap either by searching the pairs of points of interest (α, α') in Ξ, that verify (cf. Remark 2.4.4):

$$\boldsymbol{\gamma}(\boldsymbol{\xi},\alpha')^T \dot{\boldsymbol{\gamma}}(\boldsymbol{\xi},\alpha) = \boldsymbol{\gamma}(\boldsymbol{\xi},\alpha)^T \dot{\boldsymbol{\gamma}}(\boldsymbol{\xi},\alpha') = 0\,.$$

Those conditions imply that:

$$(\cos\alpha' \boldsymbol{\gamma}_1(\boldsymbol{\xi}) + \sin\alpha' \boldsymbol{\gamma}_2(\boldsymbol{\xi}))^T (\cos\alpha \boldsymbol{\gamma}_2(\boldsymbol{\xi}) - \sin\alpha \boldsymbol{\gamma}_1(\boldsymbol{\xi})) = 0\,,$$

that can be rewritten as:

$$-\cos\alpha' \sin\alpha \|\gamma_1(\boldsymbol{\xi})\|^2 + \sin\alpha' \cos\alpha \|\gamma_2(\boldsymbol{\xi})\|^2 = 0\,,$$

which is equivalent to:

$$\sin(\alpha - \alpha') = 0\,.$$

Thus, the set Ξ is defined as:

$$\begin{aligned}\Xi &= \{(\alpha, \alpha') : \alpha \neq \alpha', \sin(\alpha - \alpha') = 0\} \,, \\ &= \{(\alpha, \alpha + \pi), \alpha \in [0, \pi]\} \,.\end{aligned}$$

Remark 2.B.1. *The critical points of the ambiguity function are thus opposed on the sphere: since the manifold we are dealing with is a great circle of the sphere, this seems logical.*

For any $\alpha \in [0, \pi]$, we have $\boldsymbol{\gamma}(\alpha, \boldsymbol{\xi})^T \boldsymbol{\gamma}(\alpha + \pi, \boldsymbol{\xi}) = -1$, so that $\phi_{\text{non-local}} = \frac{1}{2} \arccos(-1) = \frac{\pi}{2}$ according to (2.52): there is no non-local overlap for $\mathcal{T}$. Thus, $w_{\text{lim}} = \cos \phi_{\text{lim}} = 0$ and the surface given by (2.31) is exact for any threshold w.

2.B.2 . Proof of Corollary 2.3.0.1

We showed in the development that we were under the conditions of application of 3.2.3: all that remains to do is to compute the integral in 2.29. We first calculate this integral for Doppler detection, using signal model (1.7) with $\xi = \theta$. First, notice that the derivatives $\dot{\boldsymbol{\gamma}}_1(\theta)$ and $\dot{\boldsymbol{\gamma}}_2(\theta)$ are orthogonal, and that $\|\dot{\boldsymbol{\gamma}}_1(\theta)\| = \|\dot{\boldsymbol{\gamma}}_2(\theta)\|$. Thus, for all $\Omega \in [0, 2\pi]$, we have that

$$\|\dot{\boldsymbol{\gamma}}_1(\theta) \cos \Omega + \dot{\boldsymbol{\gamma}}_2(\theta) \sin \Omega\|^2 = \|\dot{\boldsymbol{\gamma}}_1(\theta)\|^2 \,,$$

which does not depend on Ω. The double integral simplifies:

$$\begin{aligned}\int_{\theta_1}^{\theta_2} \int_0^{2\pi} \left[\|\dot{\boldsymbol{\gamma}}_1(\theta) \cos \Omega + \dot{\boldsymbol{\gamma}}_2(\theta) \sin \Omega\|^2 - \left(\dot{\boldsymbol{\gamma}}_1(\theta)^T \boldsymbol{\gamma}_2(\theta)\right)^2\right]^{1/2} d\Omega \, d\theta \; &= 2\pi \int_{\theta_2}^{\theta_1} \left(\|\dot{\boldsymbol{\gamma}}_1(\theta)\|^2 - \left(\dot{\boldsymbol{\gamma}}_1(\theta)^T \boldsymbol{\gamma}_2(\theta)\right)^2\right)^{1/2} d\theta, \\ &= 2\pi \int_{\theta_1}^{\theta_2} \left\|\dot{\boldsymbol{\gamma}}_1(\theta)^T \mathbf{P}^{\perp}_{\boldsymbol{\gamma}_2(\theta)}\right\| d\theta, \qquad (2.77)\end{aligned}$$

In the case of white noise, this integral can be computed analytically. Let $\mathbf{x}$ be the following vector:

$$\mathbf{x} = 2\pi \, [0, 1, \ldots, N-1]^T \,, \qquad (2.78)$$

so that

$$\dot{\boldsymbol{\gamma}}_1(\theta) = \begin{bmatrix}\mathbf{x} \\ \mathbf{x}\end{bmatrix} \odot \boldsymbol{\gamma}_2(\theta) \,, \qquad (2.79)$$

$$\dot{\boldsymbol{\gamma}}_2(\theta) = -\begin{bmatrix}\mathbf{x} \\ \mathbf{x}\end{bmatrix} \odot \boldsymbol{\gamma}_1(\theta) \,. \qquad (2.80)$$

Then:

$$\|\dot{\boldsymbol{\gamma}}_1(\theta)\| = \|\dot{\boldsymbol{\gamma}}_2(\theta)\| \; = 2\pi \sqrt{\frac{(N-1)(2N-1)}{6}} \,. \qquad (2.81)$$

and

$$\begin{aligned}\dot{\boldsymbol{\gamma}}_1(\theta)^T \boldsymbol{\gamma}_2(\theta) &= \left(\begin{bmatrix}\mathbf{x} \\ \mathbf{x}\end{bmatrix} \odot \boldsymbol{\gamma}_2(\theta)\right)^T \boldsymbol{\gamma}_2(\theta) \\ &= \frac{2\pi}{N} \sum_{k=0}^{N-1} k = \pi \, (N-1) \,. \qquad (2.82)\end{aligned}$$

Then, injecting (2.81) and (2.82) into (2.77):

$$2\pi \int_{\theta_1}^{\theta_2} \left\|\dot{\boldsymbol{\gamma}}_1(\theta)^T \mathbf{P}^{\perp}_{\boldsymbol{\gamma}_2(\theta)}\right\|^2 d\theta = 2(\theta_2 - \theta_1)\pi^2 \sqrt{\frac{(N^2-1)}{3}} \,. \qquad (2.83)$$

Replacing the double integral in (2.29) with (2.83) gives the expected result.

In the case of range detection ($\xi = r$), using signal model (1.5), the derivates of $\boldsymbol{\gamma}_1$, $\boldsymbol{\gamma}_2$ depend on r. Noting

$$(\mathbf{x}')_k = 2\pi h(t_k - r)\,, \tag{2.84}$$

where $t_k = \dfrac{k}{B}$ for $k \in [0, K-1]$, we have

$$\dot{\boldsymbol{\gamma}}_1(r) \;=\; \begin{bmatrix}\mathbf{x}'\\ \mathbf{x}'\end{bmatrix} \odot \boldsymbol{\gamma}_2(r)\,, \tag{2.85}$$

$$\dot{\boldsymbol{\gamma}}_2(r) \;=\; -\begin{bmatrix}\mathbf{x}'\\ \mathbf{x}'\end{bmatrix} \odot \boldsymbol{\gamma}_1(r)\,, \tag{2.86}$$

It follows that:

$$\begin{aligned}\|\dot{\boldsymbol{\gamma}}_1(r)\|^2 \;&=\; \frac{4\pi^2 h^2}{K}\left(\frac{K(2K-1)(K-1)}{6B^2} - \frac{K(K-1)r}{B} + Kr^2\right)\,,\\ \dot{\boldsymbol{\gamma}}_1(r)^T\boldsymbol{\gamma}_2(r) \;&=\; \frac{2\pi h}{K}\left(\frac{K(K-1)}{2B} - Kr\right)\,.\end{aligned}$$

so that:

$$\left(\|\dot{\boldsymbol{\gamma}}_1(r)\|^2 - \left(\dot{\boldsymbol{\gamma}}_1(r)^T\boldsymbol{\gamma}_2(r)\right)^2\right)^{1/2} = \frac{\pi h}{B}\sqrt{\frac{K^2-1}{3}}.$$

The integrand in (2.77) does not depend on r anymore. Evaluating (2.77) gives (recall that τ is the normalized version of the delay r):

$$2\pi\int_{\tau_1}^{\tau_2}\left\|\dot{\boldsymbol{\gamma}}_1(\tau)^T\mathbf{P}^{\perp}_{\boldsymbol{\gamma}_2(\tau)}\right\|^2 d\tau = 2(\tau_2-\tau_1)\pi^2\sqrt{\frac{(K^2-1)}{3}}\,,$$

which is basically the result that was obtained for the steering vector signal model (1.7).

2.B.3 . Extra computations for the proof of Lemma 2.3.1

In this section, we give the extra tedious computations of Lemma 2.3.1 not included in the proof.

Remark 2.B.2. *We recall the mixed product property of the Kronecker product over the Hadamard product: for any matrices $\mathbf{A}, \mathbf{B}, \mathbf{C}, \mathbf{D}$ where, respectively, $\mathbf{A}$ and $\mathbf{B}$ share the same size that $\mathbf{C}$ and $\mathbf{D}$:*

$$(\mathbf{A}\otimes\mathbf{B})\odot(\mathbf{C}\otimes\mathbf{D}) = (\mathbf{A}\odot\mathbf{C})\otimes(\mathbf{B}\odot\mathbf{D}).$$

Using the mixed product property of the Kronecker product over the Hadamard product, see that the derivatives of $\mathbf{s}$ are worth:

$$\frac{\partial\mathbf{s}(\boldsymbol{\zeta})}{\partial v} \;=\; \mathbf{s}(\boldsymbol{\zeta})\odot\left(2i\pi\, l_\theta^{-1}\mathbf{x}_N\otimes\mathbf{1}_P\right)\,, \tag{2.87}$$

$$\frac{\partial\mathbf{s}(\boldsymbol{\zeta})}{\partial u} \;=\; \mathbf{s}(\boldsymbol{\zeta})\odot\left(\mathbf{1}_N\otimes 2i\pi\, l_\mu^{-1}\mathbf{x}_P\right)\,, \tag{2.88}$$

where

$$\mathbf{x}_A = \left[0-\frac{A-1}{2}, 1-\frac{A-1}{2}, \ldots, \frac{A-1}{2}\right]^T \tag{2.89}$$

and $\mathbf{1}_A$ is the column vector of size A composed of ones. Note that $\mathbf{x}_A$ is constructed such that

$$\begin{aligned}\sum_{k=1}^{A}(\mathbf{x}_A)_k \;&=\; 0\,,\\ \sum_{k=1}^{A}(\mathbf{x}_A)_k^2 \;&=\; \frac{A(A^2-1)}{12}\,.\end{aligned}$$

The partial derivatives of $\boldsymbol{\gamma}$ are then:

$$\frac{\partial \boldsymbol{\gamma}(\boldsymbol{\psi})}{\partial v} = (\cos\alpha\boldsymbol{\gamma}_2(\boldsymbol{\zeta}) - \sin\alpha\boldsymbol{\gamma}_1(\boldsymbol{\zeta})) \odot \begin{pmatrix} 2\pi\, l_\theta^{-1}\mathbf{x}_N \otimes \mathbf{1}_P \\ 2\pi\, l_\theta^{-1}\mathbf{x}_N \otimes \mathbf{1}_P \end{pmatrix}, \tag{2.90}$$

$$\frac{\partial \boldsymbol{\gamma}(\boldsymbol{\psi})}{\partial u} = (\cos\alpha\boldsymbol{\gamma}_2(\boldsymbol{\zeta}) - \sin\alpha\boldsymbol{\gamma}_1(\boldsymbol{\zeta})) \odot \begin{pmatrix} \mathbf{1}_N \otimes 2\pi\, l_\mu^{-1}\mathbf{x}_P \\ \mathbf{1}_N \otimes 2\pi\, l_\mu^{-1}\mathbf{x}_P \end{pmatrix}. \tag{2.91}$$

Notice how the products $\boldsymbol{\gamma}_1(\boldsymbol{\zeta})^T \left(\boldsymbol{\gamma}_2(\boldsymbol{\zeta}) \odot \begin{pmatrix} 2\pi\, l_\theta^{-1}\mathbf{x}_N \otimes \mathbf{1}_P \\ 2\pi\, l_\theta^{-1}\mathbf{x}_N \otimes \mathbf{1}_P \end{pmatrix}\right), \boldsymbol{\gamma}_2(\boldsymbol{\zeta})^T \left(\boldsymbol{\gamma}_1(\boldsymbol{\zeta}) \odot \begin{pmatrix} 2\pi\, l_\theta^{-1}\mathbf{x}_N \otimes \mathbf{1}_P \\ 2\pi\, l_\theta^{-1}\mathbf{x}_N \otimes \mathbf{1}_P \end{pmatrix}\right)$ are still zero since

$$\begin{aligned}
\boldsymbol{\gamma}_1(\boldsymbol{\zeta})^T \left(\boldsymbol{\gamma}_2(\boldsymbol{\zeta}) \odot \begin{pmatrix} 2\pi\, l_\theta^{-1}\mathbf{x}_N \otimes \mathbf{1}_P \\ 2\pi\, l_\theta^{-1}\mathbf{x}_N \otimes \mathbf{1}_P \end{pmatrix}\right) &= -\left(\operatorname{Im}(\mathbf{s}) \odot \left(2\pi\, l_\theta^{-1}\mathbf{x}_N \otimes \mathbf{1}_P\right)\right)^T \operatorname{Re}(\mathbf{s}) + \left(\operatorname{Re}(\mathbf{s}) \odot \left(2\pi\, l_\theta^{-1}\mathbf{x}_N \otimes \mathbf{1}_P\right)\right)^T \operatorname{Im}(\mathbf{s}) \\
&= -\sum_{k=1}^{NP} \left(\operatorname{Im}(\mathbf{s})\right)_k \left(2\pi\, l_\theta^{-1}\mathbf{x}_N \otimes \mathbf{1}_P\right)_k \left(\operatorname{Re}(\mathbf{s})\right)_k \\
&\quad + \sum_{k=1}^{NP} \left(\operatorname{Im}(\mathbf{s})\right)_k \left(2\pi\, l_\theta^{-1}\mathbf{x}_N \otimes \mathbf{1}_P\right)_k \left(\operatorname{Re}(\mathbf{s})\right)_k \\
&= 0\,.
\end{aligned} \tag{2.92}$$

Remark 2.B.3. *This could also be noticed simply by differentiating $\boldsymbol{\gamma}_1(\boldsymbol{\zeta})^T\boldsymbol{\gamma}_1(\boldsymbol{\zeta}) = 1$ and $\boldsymbol{\gamma}_2(\boldsymbol{\zeta})^T\boldsymbol{\gamma}_2(\boldsymbol{\zeta}) = 1$ with respect to v.*

Similar reasoning yields that the products $\boldsymbol{\gamma}(\boldsymbol{\zeta})_1^T \left(\boldsymbol{\gamma}_2(\boldsymbol{\zeta}) \odot \begin{pmatrix} \mathbf{1}_N \otimes 2\pi\, l_\mu^{-1}\mathbf{x}_P \\ \mathbf{1}_N \otimes 2\pi\, l_\mu^{-1}\mathbf{x}_P \end{pmatrix}\right), \boldsymbol{\gamma}_2(\boldsymbol{\zeta})^T \left(\boldsymbol{\gamma}_1(\boldsymbol{\zeta}) \odot \begin{pmatrix} \mathbf{1}_N \otimes 2\pi\, l_\mu^{-1}\mathbf{x}_P \\ \mathbf{1}_N \otimes 2\pi\, l_\mu^{-1}\mathbf{x}_P \end{pmatrix}\right)$ are zero. Also, note that:

$$\begin{aligned}
\boldsymbol{\gamma}_1(\boldsymbol{\zeta})^T \left(\boldsymbol{\gamma}_1(\boldsymbol{\zeta}) \odot \begin{pmatrix} 2\pi\, l_\theta^{-1}\mathbf{x}_N \otimes \mathbf{1}_P \\ 2\pi\, l_\theta^{-1}\mathbf{x}_N \otimes \mathbf{1}_P \end{pmatrix}\right) &= \boldsymbol{\gamma}_2(\boldsymbol{\zeta})^T \left(\boldsymbol{\gamma}_2(\boldsymbol{\zeta}) \odot \begin{pmatrix} 2\pi\, l_\theta^{-1}\mathbf{x}_N \otimes \mathbf{1}_P \\ 2\pi\, l_\theta^{-1}\mathbf{x}_N \otimes \mathbf{1}_P \end{pmatrix}\right) \\
&= \left(\operatorname{Re}(\mathbf{s}) \odot \left(2\pi\, l_\theta^{-1}\mathbf{x}_N \otimes \mathbf{1}_P\right)\right)^T \operatorname{Re}(\mathbf{s}) + \left(\operatorname{Im}(\mathbf{s}) \odot \left(2\pi\, l_\theta^{-1}\mathbf{x}_N \otimes \mathbf{1}_P\right)\right)^T \operatorname{Im}(\mathbf{s}) \\
&= \sum_{k=1}^{NP} \left(\operatorname{Re}(\mathbf{s})\right)_k^2 \left(2\pi\, l_\theta^{-1}\mathbf{x}_N \otimes \mathbf{1}_P\right)_k + \sum_{k=1}^{NP} \left(\operatorname{Im}(\mathbf{s})\right)_k^2 \left(2\pi\, l_\theta^{-1}\mathbf{x}_N \otimes \mathbf{1}_P\right)_k \\
&= \frac{1}{NP} \sum_{k=1}^{NP} \left(2\pi\, l_\theta^{-1}\mathbf{x}_N \otimes \mathbf{1}_P\right)_k \\
&= \frac{2\pi\, l_\theta^{-1}}{N} \sum_{k=1}^{N} \left(\mathbf{x}_N\right)_k \\
&= 0\,.
\end{aligned}$$

Again, this is also true of $\boldsymbol{\gamma}_1(\boldsymbol{\zeta})^T \left(\boldsymbol{\gamma}_1(\boldsymbol{\zeta}) \odot \begin{pmatrix} \mathbf{1}_N \otimes 2\pi\, l_\mu^{-1}\mathbf{x}_P \\ \mathbf{1}_N \otimes 2\pi\, l_\mu^{-1}\mathbf{x}_P \end{pmatrix}\right)$ and $\boldsymbol{\gamma}_2(\boldsymbol{\zeta})^T \left(\boldsymbol{\gamma}_2(\boldsymbol{\zeta}) \odot \begin{pmatrix} \mathbf{1}_N \otimes 2\pi\, l_\mu^{-1}\mathbf{x}_P \\ \mathbf{1}_N \otimes 2\pi\, l_\mu^{-1}\mathbf{x}_P \end{pmatrix}\right)$.
Using these facts, we get that:

$$\frac{\partial \boldsymbol{\gamma}(\boldsymbol{\psi})^T}{\partial \alpha} \frac{\partial \boldsymbol{\gamma}(\boldsymbol{\psi})}{\partial v} = \frac{1}{NP} \sum_{k=1}^{PN} 2\pi\, l_\theta^{-1} \left(\mathbf{x}_N \otimes \mathbf{1}_P\right)_k = 0\,, \tag{2.93}$$

$$\frac{\partial \boldsymbol{\gamma}(\boldsymbol{\psi})^T}{\partial \alpha} \frac{\partial \boldsymbol{\gamma}(\boldsymbol{\psi})}{\partial u} = \frac{1}{NP} \sum_{k=1}^{PN} 2\pi\, l_\mu^{-1} \left(\mathbf{1}_N \otimes \mathbf{x}_P\right)_k = 0\,. \tag{2.94}$$

Similar computations to (2.92) give us that:

$$\begin{aligned}
\left(\boldsymbol{\gamma}_1(\boldsymbol{\zeta}) \odot \begin{pmatrix} 2\pi\, l_\theta^{-1}\mathbf{x}_N \otimes \mathbf{1}_P \\ 2\pi\, l_\theta^{-1}\mathbf{x}_N \otimes \mathbf{1}_P \end{pmatrix}\right)^T \left(\boldsymbol{\gamma}_2(\boldsymbol{\zeta}) \odot \begin{pmatrix} \mathbf{1}_N \otimes 2\pi\, l_\mu^{-1}\mathbf{x}_P \\ \mathbf{1}_N \otimes 2\pi\, l_\mu^{-1}\mathbf{x}_P \end{pmatrix}\right) &= \left(\boldsymbol{\gamma}_2(\boldsymbol{\zeta}) \odot \begin{pmatrix} 2\pi\, l_\theta^{-1}\mathbf{x}_N \otimes \mathbf{1}_P \\ 2\pi\, l_\theta^{-1}\mathbf{x}_N \otimes \mathbf{1}_P \end{pmatrix}\right)^T \left(\boldsymbol{\gamma}_1(\boldsymbol{\zeta}) \odot \begin{pmatrix} \mathbf{1}_N \otimes 2\pi\, l_\mu^{-1}\mathbf{x}_P \\ \mathbf{1}_N \otimes 2\pi\, l_\mu^{-1}\mathbf{x}_P \end{pmatrix}\right), \\
&= 0\,.
\end{aligned}$$

Then, note that

$$\begin{aligned}\left(\boldsymbol{\gamma}_1(\boldsymbol{\zeta}) \odot \begin{pmatrix} 2\pi\, l_\theta^{-1}\mathbf{x}_N \otimes \mathbf{1}_P \\ 2\pi\, l_\theta^{-1}\mathbf{x}_N \otimes \mathbf{1}_P \end{pmatrix}\right)^T \left(\boldsymbol{\gamma}_1(\boldsymbol{\zeta}) \odot \begin{pmatrix} \mathbf{1}_N \otimes 2\pi\, l_\mu^{-1}\mathbf{x}_P \\ \mathbf{1}_N \otimes 2\pi\, l_\mu^{-1}\mathbf{x}_P \end{pmatrix}\right) &= \left(\boldsymbol{\gamma}_2(\boldsymbol{\zeta}) \odot \begin{pmatrix} 2\pi\, l_\theta^{-1}\mathbf{x}_N \otimes \mathbf{1}_P \\ 2\pi\, l_\theta^{-1}\mathbf{x}_N \otimes \mathbf{1}_P \end{pmatrix}\right)^T \left(\boldsymbol{\gamma}_2(\boldsymbol{\zeta}) \odot \begin{pmatrix} \mathbf{1}_N \otimes 2\pi\, l_\mu^{-1}\mathbf{x}_P \\ \mathbf{1}_N \otimes 2\pi\, l_\mu^{-1}\mathbf{x}_P \end{pmatrix}\right) \\ &= \frac{1}{NP}\sum_{k=1}^{PN} 4\pi^2 l_\mu^{-1} l_\theta^{-1} \left((\mathbf{1}_N \otimes \mathbf{x}_P) \odot (\mathbf{x}_N \otimes \mathbf{1}_P)\right)_k , \\ &= \frac{4\pi^2 l_\mu^{-1} l_\theta^{-1}}{NP} \sum_{k=1}^{P} (\mathbf{x}_P)_k \sum_{l=1}^{N} (\mathbf{x}_N)_l \\ &= 0 .\end{aligned}$$

Thus

$$\frac{\partial \boldsymbol{\gamma}(\boldsymbol{\psi})^T}{\partial v}\frac{\partial \boldsymbol{\gamma}(\boldsymbol{\psi})}{\partial u} = \frac{1}{NP}\sum_{k=1}^{PN} -4\pi^2 l_\mu^{-1} l_\theta^{-1} \left((\mathbf{1}_N \otimes \mathbf{x}_P) \odot (\mathbf{x}_N \otimes \mathbf{1}_P)\right)_k = 0 . \tag{2.95}$$

Finally,

$$\begin{aligned}\left(\boldsymbol{\gamma}_1(\boldsymbol{\zeta}) \odot \begin{pmatrix} 2\pi\, l_\theta^{-1}\mathbf{x}_N \otimes \mathbf{1}_P \\ 2\pi\, l_\theta^{-1}\mathbf{x}_N \otimes \mathbf{1}_P \end{pmatrix}\right)^T \left(\boldsymbol{\gamma}_1(\boldsymbol{\zeta}) \odot \begin{pmatrix} 2\pi\, l_\theta^{-1}\mathbf{x}_N \otimes \mathbf{1}_P \\ 2\pi\, l_\theta^{-1}\mathbf{x}_N \otimes \mathbf{1}_P \end{pmatrix}\right) &= \left(\boldsymbol{\gamma}_1(\boldsymbol{\zeta}) \odot \begin{pmatrix} \mathbf{1}_N \otimes 2\pi\, l_\mu^{-1}\mathbf{x}_P \\ \mathbf{1}_N \otimes 2\pi\, l_\mu^{-1}\mathbf{x}_P \end{pmatrix}\right)^T \left(\boldsymbol{\gamma}_1(\boldsymbol{\zeta}) \odot \begin{pmatrix} \mathbf{1}_N \otimes 2\pi\, l_\mu^{-1}\mathbf{x}_P \\ \mathbf{1}_N \otimes 2\pi\, l_\mu^{-1}\mathbf{x}_P \end{pmatrix}\right) \\ &= \frac{1}{NP}\sum_{k=1}^{PN} 4\pi^2 l_\mu^{-2} \left((\mathbf{1}_N \otimes \mathbf{x}_P) \odot (\mathbf{1}_N \otimes \mathbf{x}_P)\right)_k \\ &= \frac{N}{NP}\sum_{k=1}^{P} 4\pi^2 l_\mu^{-2} \left((\mathbf{x}_P) \odot (\mathbf{x}_P)\right)_k \\ &= \frac{1}{P} 4\pi^2 \frac{3}{\pi^2(P^2-1)} \frac{P(P^2-1)}{12} \\ &= 1 .\end{aligned}$$

and this also holds true replacing $\boldsymbol{\gamma}_1(\boldsymbol{\zeta})$ with $\boldsymbol{\gamma}_2(\boldsymbol{\zeta})$. In the end,

$$\begin{aligned}\frac{\partial \boldsymbol{\gamma}(\boldsymbol{\psi})^T}{\partial v}\frac{\partial \boldsymbol{\gamma}(\boldsymbol{\psi})}{\partial v} &= \frac{\partial \boldsymbol{\gamma}(\boldsymbol{\psi})^T}{\partial u}\frac{\partial \boldsymbol{\gamma}(\boldsymbol{\psi})}{\partial u} \\ &= 1 .\end{aligned}$$

2.B.4 . Proof of Corollary 2.3.0.2

Proof. In Lemma 2.3.1, we proved that under white noise, for STAP detection (signal model (1.10)), $\boldsymbol{\gamma}$ is Euclidean, meaning $ds = d\alpha du dv$ when integrated on the new parameter space $[0, 2\pi] \times \mathcal{D}'$ after the change of variables $\boldsymbol{\psi}$ from the proof of Lemma (2.3.1). Then, from (2.24):

$$V = 2\pi w_{2NP-5} \left|\mathcal{D}'\right| (J_0 - 3J_2) , \tag{2.96}$$

where $|\mathcal{D}'|$ is the volume of the parameter space $\mathcal{D}'$. Since v and u range respectively from 0 to $\pi\sqrt{\frac{N^2-1}{3}}$ and from 0 to $\pi\sqrt{\frac{P^2-1}{3}}$ when testing on the whole domain, the volume $|\mathcal{D}'|$ is given by:

$$|\mathcal{D}'| = \frac{\pi^2}{3}\sqrt{N^2-1}\,\sqrt{P^2-1}\,, \tag{2.97}$$

the terms J_0 and J_2 are easily computed from (2.28):

$$\begin{aligned} J_0 &= \int_0^\phi \sin^{2NP-5}\rho\,\cos^3\rho\,d\rho\,, \\ &= \frac{1}{2(NP-2)}\sin^{2(NP-2)}\phi\,\cos^2\phi + \frac{1}{NP-2}\int_0^\phi \sin^{2NP-3}\rho\,\cos\rho\,d\rho\,, \\ &= \frac{1}{2(NP-2)}\sin^{2(NP-2)}\phi\,\cos^2\phi + \frac{1}{2(NP-2)}\frac{1}{NP-1}\sin^{2(NP-1)}\phi\,, \end{aligned} \tag{2.98}$$

$$\begin{aligned} J_2 &= \frac{1}{2(NP-2)}\int_0^\phi \sin^{2NP-3}\rho\,\cos\rho\,d\rho\,, \\ &= \frac{1}{2(NP-2)}\frac{1}{2(NP-1)}\sin^{2(NP-1)}\phi\,, \end{aligned} \tag{2.99}$$

so that

$$J_0 - 3J_2 = \frac{\sin^{2(NP-2)}\phi\left((2NP-1)\cos^2\phi - 1\right)}{2(NP-2)2(NP-1)}\,. \tag{2.100}$$

and

$$w_{2NP-5} = 2\frac{\pi^{NP-2}}{\Gamma(NP-2)}\,. \tag{2.101}$$

Plugging (2.97), (2.100), and (2.101) in (2.96) yields the volume of the cross-sections, assuming ϕ is low enough so that there isn't any overlap:

$$V = \frac{\pi^{NP+1}}{3\,\Gamma(NP-2)}\frac{\sin^{2(NP-2)}\phi\left((2NP-1)\cos^2\phi - 1\right)}{(NP-2)(NP-1)}\sqrt{N^2-1}\sqrt{P^2-1}\,. \tag{2.102}$$

Dividing (2.102) by $w_{2NP-1} = \dfrac{2\pi^{NP}}{\Gamma(NP)}$, the surface of the sphere $\mathbb{S}^{2NP-1}$, gives the expected result, replacing $\cos^2\phi$ with w^2 and $\sin^{2(NP-2)}\phi$ with $(1-w^2)^{NP-2}$. □

2.B.5 . Proof of Proposition 2.3.1

In this section, we will need some definitions and results about complex centrosymmetric matrices. Readers are referred to Appendix 2.C. Before proving the proposition, we need the following result on the covariance matrix $\mathbf{R}$ as defined in (2.38).

Lemma 2.B.1. *The matrix $\mathbf{R}$ as defined in* (2.38) *is centrosymmetric.*

Proof. This is proved with a direct computation:

$$\begin{aligned} \mathbf{J}_N\,\mathbf{R}\,\mathbf{J}_N &= \mathbf{J}_N\left(\int_{\boldsymbol{\zeta}} p(\boldsymbol{\zeta})\,\mathbf{s}^u(\boldsymbol{\zeta})\mathbf{s}^u(\boldsymbol{\zeta})^H\,d\boldsymbol{\zeta} + \sigma^2\,\mathbf{I}\right)\mathbf{J}_N\,, \\ &= \int_{\boldsymbol{\zeta}} p(\boldsymbol{\zeta})\,\mathbf{J}_N\,\mathbf{s}^u(\boldsymbol{\zeta})\mathbf{s}^u(\boldsymbol{\zeta})^H\,\mathbf{J}_N\,d\boldsymbol{\zeta} + \sigma^2\,\mathbf{J}_N\,\mathbf{I}\,\mathbf{J}_N\,. \end{aligned}$$

Since $\mathbf{s}^u$ and $\mathbf{I}$ are centrosymmetric:

$$\begin{aligned} \mathbf{J}_N\,\mathbf{R}\,\mathbf{J}_N &= \int_{\boldsymbol{\zeta}} p(\boldsymbol{\zeta})\,\mathbf{s}^u(\boldsymbol{\zeta})^*\mathbf{s}^u(\boldsymbol{\zeta})^{H^*}\,d\boldsymbol{\zeta} + \sigma^2\,\mathbf{I}\,, \\ &= \mathbf{R}^*\,. \end{aligned}$$

□

We can now prove proposition 2.3.1:

Proof. We note $f(\boldsymbol{\zeta}, \boldsymbol{\zeta}')$ the ambiguity function of $\mathbf{s}$

$$f(\boldsymbol{\zeta}, \boldsymbol{\zeta}') = \mathbf{s}(\boldsymbol{\zeta})^H \mathbf{s}(\boldsymbol{\zeta}') \ = \mathbf{s}^u(\boldsymbol{\zeta})^H \mathbf{R}^{-1} \mathbf{s}^u(\boldsymbol{\zeta}') \, .$$

Using some trigonometry, it is easy to show that:

$$\boldsymbol{\gamma}(\alpha, \boldsymbol{\zeta})^T \boldsymbol{\gamma}(\alpha', \boldsymbol{\zeta}') = \cos(\alpha - \alpha') \operatorname{Re}(f(\boldsymbol{\zeta}, \boldsymbol{\zeta}')) + \sin(\alpha - \alpha') \operatorname{Im}(f(\boldsymbol{\zeta}, \boldsymbol{\zeta}')) \, .$$

But the ambiguity function of $\mathbf{s}$ is real. Indeed, since $\mathbf{s}^u$ and $\mathbf{R}$ are centrosymmetric, according to Proposition 2.C.1, f is real. Thus:

$$\boldsymbol{\gamma}(\alpha, \boldsymbol{\zeta})^T \boldsymbol{\gamma}(\alpha', \boldsymbol{\zeta}') = \cos(\alpha - \alpha') f(\boldsymbol{\zeta}, \boldsymbol{\zeta}) \, .$$

Thus:

$$\begin{aligned}
\frac{\partial \boldsymbol{\gamma}(\alpha, \boldsymbol{\zeta})^T}{\partial \alpha} \frac{\partial \boldsymbol{\gamma}(\alpha', \boldsymbol{\zeta}')}{\partial \alpha} &= \cos(\alpha - \alpha') f(\boldsymbol{\zeta}, \boldsymbol{\zeta}') \, , \\
\frac{\partial \boldsymbol{\gamma}(\alpha, \boldsymbol{\zeta})^T}{\partial \alpha} \frac{\partial \boldsymbol{\gamma}(\alpha', \boldsymbol{\zeta}')}{\partial \zeta_i} &= -\sin(\alpha - \alpha') \frac{\partial f(\boldsymbol{\zeta}, \boldsymbol{\zeta}')}{\partial \zeta_i'} \ \text{ for } i \neq 1 \, , \\
\frac{\partial \boldsymbol{\gamma}(\alpha, \boldsymbol{\zeta})^T}{\partial \zeta_i} \frac{\partial \boldsymbol{\gamma}(\alpha', \boldsymbol{\zeta}')}{\partial \zeta_j} &= \cos(\alpha - \alpha') \frac{\partial^2 f(\boldsymbol{\zeta}, \boldsymbol{\zeta}')}{\partial \zeta_i \partial \zeta_j'} \ \text{ for } i, j \neq 1 \, .
\end{aligned}$$

Evaluating for $(\alpha, \boldsymbol{\zeta}) = (\alpha', \boldsymbol{\zeta}')$ gives the first fundamental form g_{ij}:

$$\begin{aligned}
g_{11} &= 1 \, , \\
g_{1i} &= g_{i1} = 0 \ \text{ for } i \neq 1 \, , \\
g_{ij} &= \frac{\partial \mathbf{s}(\boldsymbol{\zeta})^H}{\partial \zeta_i} \frac{\partial \mathbf{s}(\boldsymbol{\zeta})}{\partial \zeta_j} \ \text{ for } i, j \neq 1 \, ,
\end{aligned} \tag{2.103}$$

which achieves the proof of the proposition. □

2.B.6 . Proof of Corollary 2.3.0.3

Proof. In this proof, we use the centrosymmetric parametrization $\boldsymbol{\psi} = (\alpha, \boldsymbol{\zeta})$ from the proof of lemma 2.3.3.1, for which we proved that the first fundamental form g_{ij} is expressed as in (2.39). In the general case ($\boldsymbol{\Gamma} \neq \mathbf{I}$), the Riemannian tensor components are a priori, not zero anymore, so we have to start the computation of the volume V of the tube from (2.23):

$$V = w_{2NP-5} \left(J_0 \int_{\mathcal{D}'} d\mathbf{s} + J_2 \int_{\mathcal{D}'} (R_{12}^{12} + R_{23}^{23} + R_{13}^{13} - 3) \, d\mathbf{s} \right) . \tag{2.104}$$

But R_{12}^{12} and R_{13}^{13} are, as we will see, in fact, equal to zero. See that the Christoffel symbols of the first kind $\boldsymbol{\Gamma}_{\kappa\alpha\beta}$ are zero as soon as one of the indices α, β, κ is equal to 1: indeed, in this case, 1 appears in all of the terms in (2.15), either as $\dfrac{\partial g_{1i}}{\partial \psi_j}$ or $\dfrac{\partial g_{ij}}{\partial \alpha}$. The terms g_{1i} are either equal to 0 or 1 and are constant either way so that $\dfrac{\partial g_{1i}}{\partial \psi_j} = 0$, and the terms $\dfrac{\partial g_{ij}}{\partial \alpha}$ are also zero since g_{ij} does not depend on α as can be seen in (2.103). From (2.16), it follows that the Christoffel symbols of the second kind $\boldsymbol{\Gamma}_{\alpha\beta}^{\kappa}$ are also zero when α or β is equal to 1. Noting that

$$\begin{aligned}
g^{ij} &= (g_{ij})^{-1} \\
&= \begin{pmatrix} 1 & \mathbf{0} \\ \mathbf{0} & \left(\dfrac{\partial \mathbf{s}^H}{\partial \zeta_i} \dfrac{\partial \mathbf{s}}{\partial \zeta_j} \right)^{-1} \end{pmatrix} ,
\end{aligned}$$

$\mathbf{\Gamma}^1_{\alpha\beta} = g^{11}\mathbf{\Gamma}_{1\alpha\beta} + g^{21}\mathbf{\Gamma}_{2\alpha\beta} + g^{31}\mathbf{\Gamma}_{3\alpha\beta}$ is also equal to zero since $g^{21} = g^{31} = 0$. Now, see that $R^{12}_{12} = g^{21}R^1_{112} + g^{22}R^1_{212} + g^{23}R^1_{312}$. From (2.17), all the $R^1_{\mu 12}$ involved in this addition are zero, so that R^{12}_{12} is also zero. Similarly, R^{13}_{13} is zero. Thus,

$$V = w_{2NP-5}\left(J_0\int_{\mathcal{D}'} d\mathbf{s} + J_2\int_{\mathcal{D}'}(R^{23}_{23} - 3)\, d\mathbf{s}\right). \tag{2.105}$$

In order to further simplify this result, we will need some more definitions. The Ricci curvature tensor R_{ij} for $1 \leq i, j \leq 3$ is defined as [SS78, p. 88]:

$$R_{ij} \triangleq \sum_{k=1}^{M} R^k_{ijk}.$$

The scalar curvature R is then defined as [SS78, p. 89]:

$$R \triangleq \sum_{1\leq i,j\leq M} g^{ij}R_{ij}.$$

Then,

$$\begin{aligned} R &= \sum_{1\leq i,j,k\leq M} g^{ij}R^k_{ijk} \\ &= \sum_{1\leq j,k\leq M}\sum_{1\leq i\leq M} g^{ij}R^k_{ijk} \\ &= \sum_{1\leq j,k\leq M} R^{kj}_{jk} \end{aligned}$$

From (2.19), noting that $G^j_i(p) = G^i_j(p)$, we have that $R^{kj}_{jk} = -R^{jk}_{jk}$ and $R^{jk}_{jk} = R^{kj}_{kj}$. This leads to:

$$R = -2\sum_{1\leq k<j\leq M} R^{kj}_{kj}$$

R^{23}_{23} in (2.105) is thus linked to the curvature scalar R of the surface $S_\alpha(\zeta_1, \zeta_2)$ obtained from $\boldsymbol{\gamma}(\alpha, \boldsymbol{\zeta})$ when ζ_1, ζ_2 vary for fixed α (which metric is equal to $(a_{ij}) = \begin{pmatrix} g_{22} & g_{23} \\ g_{32} & g_{33}\end{pmatrix}$ and does not depend on α from (2.103)) with $R^{23}_{23} = -\dfrac{R}{2}$. The scalar curvature is in turn linked to the Gaussian curvature K of this surface with $R = 2K$ [GHL+90, p.136], so that $R^{23}_{23} = -K$. Then,

$$\int_{\alpha,\boldsymbol{\zeta}\in[0,2\pi]\times\mathcal{D}'} (R^{23}_{23} - 3)\sqrt{\det g_{ij}}\, d\alpha\, d\zeta_1\, d\zeta_2 = 2\pi\int_{\boldsymbol{\zeta}\in\mathcal{D}'} (-K - 3)\ \sqrt{\det a_{ij}}\, d\zeta_1\, d\zeta_2\,.$$

We will need the Gauss-Bonnet theorem to get our final result:

Theorem 2.B.1. [KS89] *(Gauss-Bonnet) Let $\boldsymbol{\gamma}$ be a compact $2D$ manifold with boundary $\partial\boldsymbol{\gamma}$. Let K be the Gaussian curvature of $\boldsymbol{\gamma}$ and k_g be the geodesic curvature of $\partial\boldsymbol{\gamma}$. Finally, let $\varphi(\boldsymbol{\gamma})$ be its Euler characteristic. Then:*

$$2\pi\varphi(\boldsymbol{\gamma}) = \int_{\boldsymbol{\gamma}} K ds + \int_{\partial\boldsymbol{\gamma}} k_g dl\,,$$

where ds is the surface element of the surface $\boldsymbol{\gamma}$, and dl is the line element of the curve $\partial\boldsymbol{\gamma}$.

Since by hypothesis $\mathcal{D} = [0, 1]^2$, the surface S_α is closed and thus has no boundaries ($\partial\boldsymbol{\gamma} = \emptyset$). Applying Gauss-Bonnet:

$$\int_{\boldsymbol{\zeta}\in\mathcal{D}'} K\sqrt{\det a_{ij}}\, d\zeta_1\, d\zeta_2 = \chi(S_\alpha)\,,$$

where $\chi(S_\alpha)$ is the Euler characteristic of the surface S_α. As S_α is homeomorphic to the cartesian product of two circles that the parameters ζ_1 and ζ_2 describe, it is a torus, thus its Euler characteristic is zero. This finally gives us

$$\int_{\alpha,\boldsymbol{\zeta}\in[0,2\pi]\times\mathcal{D}'} (R^{23}_{23}-3)\sqrt{\det g_{ij}}\,d\alpha\,d\zeta_1\,d\zeta_2 = -6\pi\int_{\zeta\in\mathcal{D}'}\sqrt{\det a_{ij}}\,d\zeta_1\,d\zeta_2\,.$$

The values of the terms J_0, J_2, and w_{2NP-5} do not change from the case of the Euclidean manifold treated in proof 2.B.4. Plugging (2.98), (2.99), (2.101) into (2.27) gives the final result. □

2.B.7 . Proof of Proposition 2.4.1

Proof. Let $\boldsymbol{\gamma}(\boldsymbol{\xi})^T\boldsymbol{\gamma}(\boldsymbol{\xi}') = f(\boldsymbol{\xi}-\boldsymbol{\xi}')$. The quantity $h(\boldsymbol{\xi},\boldsymbol{\xi}')$ depends on $\boldsymbol{\xi}$ and $\boldsymbol{\xi}'$ through $f(\boldsymbol{\xi}-\boldsymbol{\xi}')$ in the denominator, and, by the way of $\mathbf{Q}_{\boldsymbol{\xi}'}$ in the numerator, $\boldsymbol{\gamma}(\boldsymbol{\xi})^T\dfrac{\partial\boldsymbol{\gamma}(\boldsymbol{\xi}')}{\partial\xi_k}$ and $\dfrac{\partial\boldsymbol{\gamma}(\boldsymbol{\xi})^T}{\partial\xi_i}\dfrac{\partial\boldsymbol{\gamma}(\boldsymbol{\xi}')}{\partial\xi_j}$ for $k\in[1,M]$ and $(i,j)\in[1,M]^2$. Notice how

$$\begin{aligned}\boldsymbol{\gamma}(\boldsymbol{\xi})^T\frac{\partial\boldsymbol{\gamma}(\boldsymbol{\xi}')}{\partial\xi_k} &= -\frac{\partial f}{\partial\xi_k}\bigg|_{\boldsymbol{\xi}-\boldsymbol{\xi}'},\\ \frac{\partial\boldsymbol{\gamma}(\boldsymbol{\xi})^T}{\partial\xi_i}\frac{\partial\boldsymbol{\gamma}(\boldsymbol{\xi}')}{\partial\xi_j} &= -\frac{\partial^2 f}{\partial\xi_i\partial\xi_j}\bigg|_{\boldsymbol{\xi}-\boldsymbol{\xi}'},\end{aligned} \tag{2.106}$$

so that in the end, h depends only on the difference $\boldsymbol{\xi}-\boldsymbol{\xi}'$. □

2.B.8 . Proof of Corollary 2.4.1.2

Proof. First, note that a parametrization $\boldsymbol{\psi}$ such that $g_{ij}=\mathbf{I}$ exists since, as noted in remark 2.4.3, shift-invariant manifolds are Euclidean. Note that differentiating $\boldsymbol{\gamma}(\boldsymbol{\psi})^T\boldsymbol{\gamma}(\boldsymbol{\psi})=1$ twice yields:

$$\boldsymbol{\gamma}(\boldsymbol{\psi})^T\frac{\partial^2\boldsymbol{\gamma}(\boldsymbol{\psi})}{\partial\psi_i\partial\psi_j} = -\frac{\partial\boldsymbol{\gamma}(\boldsymbol{\psi})^T}{\partial\psi_i}\frac{\partial\boldsymbol{\gamma}(\boldsymbol{\psi})}{\partial\psi_j} = -\delta_{ij}\,. \tag{2.107}$$

It can be easily verified that the expression of the Christoffel symbols of the first kind in (2.15) is equivalent to:

$$\Gamma_{ijk} = \frac{\partial^2\boldsymbol{\gamma}(\boldsymbol{\psi})^T}{\partial\psi_j\partial\psi_k}\frac{\partial\boldsymbol{\gamma}(\boldsymbol{\psi})}{\partial\psi_i}\,. \tag{2.108}$$

Since $g_{ij}=\mathbf{I}$, (2.15) gives

$$\Gamma_{ijk}=0\,. \tag{2.109}$$

The denominator in (2.48) reduces to 1:

$$\sum_{i,j}\beta_i\beta_j\,\frac{\partial\boldsymbol{\gamma}(\boldsymbol{\psi})^T}{\partial\psi_i}\frac{\partial\boldsymbol{\gamma}(\boldsymbol{\psi})}{\partial\psi_j} = \sum_{i,j}\beta_i\beta_j\,\delta_{i,j} = \sum_i\beta_i^2 = 1\,.$$

We thus have:

$$\begin{aligned}\cot^2\phi_{\text{local}} &= \sup_{\beta\in\mathbb{S}^{M-1}}\left\|\sum_{i,j}\beta_i\beta_j\,(\mathbf{I}-\mathbf{Q}_\psi)\,\frac{\partial^2\boldsymbol{\gamma}(\boldsymbol{\psi})}{\partial\psi_i\partial\psi_j}\right\|^2,\\ &= \sup_{\beta\in\mathbb{S}^{M-1}}\left(\left\|\sum_{i,j}\beta_i\beta_j\frac{\partial^2\boldsymbol{\gamma}(\boldsymbol{\psi})}{\partial\psi_i\partial\psi_j}\right\|^2 - \left\|\mathbf{Q}_\psi\sum_{i,j}\beta_i\beta_j\frac{\partial^2\boldsymbol{\gamma}(\boldsymbol{\psi})}{\partial\psi_i\partial\psi_j}\right\|^2\right),\end{aligned} \tag{2.110}$$

where the maximization on ψ has been omitted using proposition 2.4.1.
$\left(\boldsymbol{\gamma}(\boldsymbol{\psi}),\dfrac{\partial\boldsymbol{\gamma}(\boldsymbol{\psi})}{\partial\psi_1},\ldots,\dfrac{\partial\boldsymbol{\gamma}(\boldsymbol{\psi})}{\partial\psi_M}\right)$ forms an orthonormal family so that the second term of (2.110) is, with

Pythagoras's theorem:

$$\begin{aligned}\left\|\mathbf{Q}_{\psi}\sum_{i,j}\beta_i\beta_j\frac{\partial^2\boldsymbol{\gamma}(\boldsymbol{\psi})}{\partial\psi_i\partial\psi_j}\right\|^2 &= \left|\sum_{i,j}\beta_i\beta_j\boldsymbol{\gamma}(\boldsymbol{\psi})^T\frac{\partial^2\boldsymbol{\gamma}(\boldsymbol{\psi})}{\partial\psi_i\partial\psi_j}\right|^2+\sum_k\left|\sum_{i,j}\beta_i\beta_j\frac{\partial\boldsymbol{\gamma}(\boldsymbol{\psi})^T}{\partial\psi_k}\frac{\partial^2\boldsymbol{\gamma}(\boldsymbol{\psi})}{\partial\psi_i\partial\psi_j}\right|^2,\\ &= \left|\sum_{i,j}\beta_i\beta_j\delta_{i,j}\right|^2+\sum_k\left|\sum_{i,j}\beta_i\beta_j\Gamma_{kij}\right|^2,\\ &= 1\,,\end{aligned}$$

using (2.107), (2.108) and (2.109). □

2.B.9 . Proof of Proposition 2.4.2

Proof. We adapt Johansen and Johnstone's proof of Proposition 4.2 in [JJ90] to the case of an M-dimensional manifold. Following the authors, we consider the case of a manifold embedded in $\mathbb{R}^n$. The result can then be extended to a manifold embedded in $\mathbb{S}^{n-1}$.

The start of the proof is the same: suppose that the limiting angle ϕ_{global} is lower than the local limit angle ϕ_{local}. Following the autors, we can find $\mathbf{x}\in\mathbb{R}^n$, $\boldsymbol{\xi}$ and $\boldsymbol{\xi}'$ in $\mathcal{D}$ such that $\boldsymbol{\xi}\neq\boldsymbol{\xi}'$, $\mathbf{x}\in\mathcal{C}_{\phi_{\text{global}}}(\boldsymbol{\gamma}(\boldsymbol{\xi}))$ and $\mathbf{x}\in\mathcal{C}_{\phi_{\text{global}}}(\boldsymbol{\gamma}(\boldsymbol{\xi}'))$. Define $\phi_{\boldsymbol{\xi}}$ and $\phi_{\boldsymbol{\xi}'}$ as the the distances from $\boldsymbol{\gamma}(\boldsymbol{\xi})$ and $\boldsymbol{\gamma}(\boldsymbol{\xi}')$ to $\mathbf{x}$. $\max\{\phi_{\boldsymbol{\xi}},\phi_{\boldsymbol{\xi}'}\}=\phi_{\text{global}}$, otherwise there would be overlap for a radius $\phi<\phi_{\text{global}}$, which contradicts the definition of ϕ_{global}.

Since $\mathbf{x}$ belongs to the cross sections $\mathcal{C}_{\phi_{\text{global}}}(\boldsymbol{\gamma}(\boldsymbol{\xi}))$ and $\mathcal{C}_{\phi_{\text{global}}}(\boldsymbol{\gamma}(\boldsymbol{\xi}'))$, the points $\boldsymbol{\xi}$, $\boldsymbol{\xi}'$ are strict local minima of the function $\mathbf{v}\to|\mathbf{x}-\boldsymbol{\gamma}(\mathbf{v})|$. The strictness comes from the fact that by hypothesis, $|\mathbf{x}-\boldsymbol{\gamma}(\xi)|<\phi_{\text{local}}$ and $|\mathbf{x}-\boldsymbol{\gamma}(\xi')|<\phi_{\text{local}}$: in the one-dimensional case, the distance between $\boldsymbol{\gamma}(\mathbf{s})$ and $\boldsymbol{\gamma}(\mathbf{t})$ to $\mathbf{x}$ is less than the curvature radius of $\boldsymbol{\gamma}$ at $\mathbf{s}$ and $\mathbf{t}$, so that $\mathbf{x}$ moves away from $\boldsymbol{\gamma}(\mathbf{s})$ and $\boldsymbol{\gamma}(\mathbf{t})$ when moving infinitesimally. Similar reasoning holds in the general case, making use of the fact that ϕ_{local} in (2.48) is the maximum of the principal curvatures of $\boldsymbol{\gamma}$ [KT01] (the maximum curvature of the curves obtained when intersecting $\boldsymbol{\gamma}$ with plans containing the normal). We can then define frontiers $\mathcal{F}_{\boldsymbol{\xi}}$ and $\mathcal{F}_{\boldsymbol{\xi}'}$ around $\boldsymbol{\xi}$ and $\boldsymbol{\xi}'$ such that for all $\mathbf{v}\in\mathcal{F}_{\boldsymbol{\xi}}$, $|\mathbf{x}-\boldsymbol{\gamma}(\mathbf{v})|>\phi_{\boldsymbol{\xi}}$ and for all $\mathbf{v}\in\mathcal{F}_{\boldsymbol{\xi}'}$, $|\mathbf{x}-\boldsymbol{\gamma}(\mathbf{v})|>\phi_{\boldsymbol{\xi}'}$. Furthermore, we require the domains delimited by the frontiers to be disjoint. By contradiction, if $(\boldsymbol{\xi},\boldsymbol{\xi}')\notin\Xi$, there exists $k\in[1,M]$ such that $(\boldsymbol{\gamma}(\boldsymbol{\xi})-\boldsymbol{\gamma}(\boldsymbol{\xi}'))^T\dfrac{\partial\boldsymbol{\gamma}}{\partial\xi_k}\neq 0$ and we can then proceed as Johansen to construct a point $\tilde{\mathbf{x}}\in\mathbb{S}^{n-1}$ such that $|\tilde{\mathbf{x}}-\boldsymbol{\gamma}(\boldsymbol{\xi})|<\phi_{\boldsymbol{\xi}}$, $|\tilde{\mathbf{x}}-\gamma(\boldsymbol{\xi}')|<\phi_{\boldsymbol{\xi}'}$ and with $|\mathbf{x}-\tilde{\mathbf{x}}|$ small enough so that $\forall\mathbf{v}\in\mathcal{F}_{\boldsymbol{\xi}},|\tilde{\mathbf{x}}-\boldsymbol{\gamma}(\mathbf{v})|>\phi_{\boldsymbol{\xi}}$ and $\forall\mathbf{v}\in\mathcal{F}_{\boldsymbol{\xi}'},|\tilde{\mathbf{x}}-\boldsymbol{\gamma}(\mathbf{v})|>\phi_{\boldsymbol{\xi}'}$. By the extreme value theorem, there are two local minima $\tilde{\boldsymbol{\xi}},\tilde{\boldsymbol{\xi}}'$ of the function $\mathbf{v}\to|\tilde{\mathbf{x}}-\boldsymbol{\gamma}(\mathbf{v})|$ in the (compact) domains encompassed by $\mathcal{F}_{\boldsymbol{\xi}}$ and $\mathcal{F}_{\boldsymbol{\xi}'}$, such that $\left|\tilde{\mathbf{x}}-\boldsymbol{\gamma}\left(\tilde{\boldsymbol{\xi}}\right)\right|<\phi_{\boldsymbol{\xi}}$ and $\left|\tilde{\mathbf{x}}-\boldsymbol{\gamma}\left(\tilde{\boldsymbol{\xi}}'\right)\right|<\phi_{\boldsymbol{\xi}'}$. Since the domains delimited by $\mathcal{F}_{\boldsymbol{\xi}}$ and $\mathcal{F}_{\boldsymbol{\xi}'}$ are disjoint, $\tilde{\boldsymbol{\xi}}$ and $\tilde{\boldsymbol{\xi}}'$ are distinct. Thus $\tilde{\mathbf{x}}$ belongs to two cross-sections with a distance less than ϕ_{global} since $\phi_{\xi}\leq\phi_{\text{global}}$ and $\phi_{\xi'}\leq\phi_{\text{global}}$. This is impossible, and thus $(\boldsymbol{\xi},\boldsymbol{\xi}')\in\Xi$.

For a non-closed manifold, if the limit pair $(\boldsymbol{\xi},\boldsymbol{\xi}')$ is in $(\mathcal{D}\setminus\mathcal{B})^2$, then nothing changes in the proof above. $\phi_{\text{non-local}}$ given in Equation (2.52) is thus a lower bound for the appearance of non-local overlap in this case. □

2.B.10 . Proof of Corollary 2.4.1.5

Proof. The manifolds corresponding to the signal models under consideration ((1.7), (1.10)) have been showed to be shift-invariant under white noise so that we can apply the result of Corollary 2.4.1.2 in order to find ϕ_{local}. Vectors $\mathbf{s}$ are taken under their centrosymmetric forms, and we use the parametrization $\boldsymbol{\psi}=(\alpha,v)$ from the proof of Lemma 2.3.1. We need the expressions of the second derivatives of $\boldsymbol{\gamma}$ under each signal model. Let us compute the value of $\dfrac{\partial^2\boldsymbol{\gamma}^T}{\partial v^2}\dfrac{\partial^2\boldsymbol{\gamma}}{\partial v^2}$, where the superscript $^{\odot 2}$ denotes the

Hadarmad product of a vector with itself:

$$\begin{aligned}\frac{\partial^2\boldsymbol{\gamma}^T}{\partial v^2}\frac{\partial^2\boldsymbol{\gamma}}{\partial v^2} &= \left\|(\cos(\alpha)\boldsymbol{\gamma}_1(v)+\sin(\alpha)\boldsymbol{\gamma}_2(v))\odot\begin{pmatrix}2\pi\, l_\theta^{-1}\mathbf{x}_N\\ 2\pi\, l_\theta^{-1}\mathbf{x}_N\end{pmatrix}^{\odot 2}\right\|^2\\ &= \frac{\left(2\pi l_\theta^{-1}\right)^4}{N}\sum_{n=0}^{N-1}\left(n-\frac{N-1}{2}\right)^4\\ &= \frac{144\pi^4}{N(N^2-1)\pi^4}\frac{N(N^2-1)}{60}\left(3\frac{N-1}{4}^2+3\frac{N-1}{2}-1\right)\\ &= \frac{3}{5}\frac{3N^2-7}{(N-1)^2}\,,\end{aligned}$$

which is the constant C_N (2.62). In the end, we find that:

$$\begin{aligned}\frac{\partial^2\boldsymbol{\gamma}^T}{\partial v^2}\frac{\partial^2\boldsymbol{\gamma}}{\partial v^2} &= C_N\,,\\ \frac{\partial^2\boldsymbol{\gamma}^T}{\partial v\,\partial\alpha}\frac{\partial^2\boldsymbol{\gamma}}{\partial v^2} &= \frac{\partial^2\boldsymbol{\gamma}^T}{\partial v\,\partial\alpha}\frac{\partial^2\boldsymbol{\gamma}}{\partial\alpha^2} = 0\,,\\ \frac{\partial^2\boldsymbol{\gamma}^T}{\partial^2 v}\frac{\partial^2\boldsymbol{\gamma}}{\partial\alpha^2} &= \frac{\partial^2\boldsymbol{\gamma}^T}{\partial v\,\partial\alpha}\frac{\partial^2\boldsymbol{\gamma}}{\partial v\,\partial\alpha} = \frac{\partial^2\boldsymbol{\gamma}^T}{\partial\alpha^2}\frac{\partial^2\boldsymbol{\gamma}}{\partial\alpha^2} = 1\,,\end{aligned}$$

Injecting the second derivative products into (2.49), with $\beta_1=\cos\varphi$, $\beta_2=\sin\varphi$ and maximizing on φ, we get:

$$\begin{aligned}\cot^2\phi_{\text{local}} &= \max_{\varphi}\; C_N\cos^4\varphi+6\cos^2\varphi\sin^2\varphi+\sin^4\varphi-1\,,\\ &= \max_{\varphi}\;(C_N-5)\cos^4\varphi+4\cos^2\varphi\,.\end{aligned}\tag{2.111}$$

The maximum is obtained for $\cos^2\varphi=\dfrac{2}{5-C_N}$. Then, injecting this value in (2.111) and simplifying, we obtain:

$$\cot^2\phi_{\text{local}}=\frac{4}{5-C_N}\,.$$

Since $w_{\text{local}}^2=\cos^2\left(\tan^{-1}\dfrac{1}{\sqrt{\cot^2\phi_{\text{local}}}}\right)$, result (2.61) holds.

For STAP detection, it is useful to note that when the total number of ∂v or ∂u in a second derivative product is odd, this product equals zero, and it is equal to one when 2 or 0 such terms appear. The only remaining products to compute are $\dfrac{\partial^2\boldsymbol{\gamma}^T}{\partial v^2}\dfrac{\partial^2\boldsymbol{\gamma}}{\partial v^2}$ and $\dfrac{\partial^2\boldsymbol{\gamma}^T}{\partial u^2}\dfrac{\partial^2\boldsymbol{\gamma}}{\partial u^2}$, which are shown to be equal to C_N and C_P (2.62). In the end, injecting in (2.49), with $\boldsymbol{\beta}=(\cos\varphi\cos\psi,\sin\varphi\cos\psi,\sin\psi)$ for $\varphi,\psi\in[0,2\pi]$ yields expression (2.58). □

2.B.11 . Proof of Corollary 2.4.1.6

Proof. First, see that:

$$\begin{aligned}\boldsymbol{\gamma}(\boldsymbol{\xi},\alpha)^T\boldsymbol{\gamma}(\boldsymbol{\xi}',\alpha') &= \cos(\alpha-\alpha')\,\mathrm{Re}\left(\mathbf{s}(\boldsymbol{\xi})^H\mathbf{s}(\boldsymbol{\xi}')\right)+\sin(\alpha-\alpha')\,\mathrm{Im}\left(\mathbf{s}(\boldsymbol{\xi})^H\mathbf{s}(\boldsymbol{\xi}')\right)\,,\\ &= \mathrm{Re}\left(e^{-i\,(\alpha-\alpha')}\,\mathbf{s}(\boldsymbol{\xi})^H\mathbf{s}(\boldsymbol{\xi}')\right)\,,\\ &\leq \left|\mathbf{s}(\boldsymbol{\xi})^H\,\mathbf{s}(\boldsymbol{\xi}')\right|\,,\end{aligned}\tag{2.112}$$

with the equality attained for $\alpha-\alpha'=\angle\mathbf{s}(\boldsymbol{\xi})^H\mathbf{s}(\boldsymbol{\xi}')$.

Inequality (2.112) implies that the pairs of points $(\boldsymbol{\xi}, \alpha), (\boldsymbol{\xi}', \alpha')$ with $(\boldsymbol{\xi}, \boldsymbol{\xi}') \in \Xi'$ and (α, α') chosen arbitrarily so that $\alpha - \alpha' = \angle \mathbf{s}(\boldsymbol{\xi})^H \mathbf{s}(\boldsymbol{\xi}')$ belong to Ξ. Since the $\min$ of (2.52) is attained at the maximum of $\boldsymbol{\gamma}(\boldsymbol{\xi}, \alpha)^T \boldsymbol{\gamma}(\boldsymbol{\xi}', \alpha')$ for $\big((\boldsymbol{\xi}, \alpha), (\boldsymbol{\xi}', \alpha')\big) \in \Xi$, and that this product is lower than the maximum of $\left|\mathbf{s}(\boldsymbol{\xi})^H \mathbf{s}(\boldsymbol{\xi}')\right|$, attained in Ξ for $(\boldsymbol{\xi}, \boldsymbol{\xi}') \in \Xi'$, the only subset of points of Ξ worth investigating are the points in Ξ'. □

2.C . On complex centrosymmetric vectors

This short section formalizes the concept of complex centrosymmetric vectors and introduces some properties used in Subsection 2.3.3.2. We will note $\mathbf{J}_N$ the antidiagonal matrix of size N:

$$\mathbf{J}_N = \begin{pmatrix} 0 & 0 & \dots & 0 & 1 \\ 0 & 0 & \dots & 1 & 0 \\ \vdots & \vdots & \iddots & \vdots & \vdots \\ 1 & 0 & \dots & 0 & 0 \end{pmatrix}.$$

Definition 2.C.1.

- *A complex vector $\mathbf{a} \in \mathbb{C}^N$ is said to be complex centrosymmetric if:*

$$\mathbf{a}^* = \mathbf{J}_N \, \mathbf{a} \, .$$

- *A complex square matrix $\mathbf{A} \in \mathbb{C}^{N,N}$ is said to be complex centrosymmetric if:*

$$\mathbf{A}^* = \mathbf{J}_N \, \mathbf{A} \, \mathbf{J}_N \, .$$

As an example, the vector $\mathbf{d}'(.)$ introduced in (2.34) is complex centrosymmetric. Let us introduce some properties for this class of objects that we will need in the development of the section:

Proposition 2.C.1. *Let $\mathbf{A} \in \mathbb{C}^{N,N}$ be a centrosymmetric matrix, and $\mathbf{a} \in \mathbb{C}^N$, $\mathbf{b} \in \mathbb{C}^N$ be complex centrosymmetric vectors. Then the following holds:*

- *If $\mathbf{A}$ is invertible, then $\mathbf{A}^{-1}$ is centrosymmetric.*
- *$\mathbf{a}^H \mathbf{A} \mathbf{b} \in \mathbb{R}$.*
- *If $\mathbf{A}$ is invertible, then $\mathbf{a}^H \mathbf{A}^{-1} \mathbf{b} \in \mathbb{R}$*

Proof.

- Note that $\mathbf{J}_N$ is invertible, with $\mathbf{J}_N^{-1} = \mathbf{J}_N$.

$$\begin{aligned} (\mathbf{A}^{-1})^* = (\mathbf{A}^*)^{-1} &= (\mathbf{J}_N \, \mathbf{A} \, \mathbf{J}_N)^{-1} \, , \\ &= \mathbf{J}_N \, \mathbf{A}^{-1} \, \mathbf{J}_N \, . \end{aligned}$$

- $\mathbf{a}^H \, \mathbf{A} \, \mathbf{b} \in \mathbb{R}$ if $\left(\mathbf{a}^H \, \mathbf{A} \, \mathbf{b}\right)^* = \mathbf{a}^H \mathbf{A} \mathbf{b}$. See that

$$\begin{aligned} \left(\mathbf{a}^H \, \mathbf{A} \, \mathbf{b}\right)^* &= (\mathbf{a}^*)^H \, \mathbf{A}^* \, \mathbf{b}^* \, , \\ &= \mathbf{a}^H \, \mathbf{J}_N \, (\mathbf{J}_N \, \mathbf{A} \, \mathbf{J}_N) \, \mathbf{J}_N \, \mathbf{b} \, , \\ &= \mathbf{a}^H \, \mathbf{A} \, \mathbf{b} \, . \end{aligned}$$

- The last property is obtained by combining the other two.

□

2.D . Derivatives of γ

This section is an inventory of the derivatives of γ for the signal model considered under the general case ($\mathbf{\Gamma} \neq \mathbf{I}$), to be used in formulas (2.54), (2.57), (2.58) to determine the limit overlap angles.

2.D.1 . First order derivatives

For $M = 2$, under signal model (1.7) ($\boldsymbol{\xi} = \theta$), the derivatives are given by, with $\mathbf{B} = \begin{bmatrix} \mathrm{Re}(\mathbf{\Gamma}^{-1/2}) & -\mathrm{Im}(\mathbf{\Gamma}^{-1/2}) \\ \mathrm{Im}(\mathbf{\Gamma}^{-1/2}) & \mathrm{Re}(\mathbf{\Gamma}^{-1/2}) \end{bmatrix}^{-1}$:

$$\frac{\partial \boldsymbol{\gamma}}{\partial \theta} = \left(\mathbf{I} - \boldsymbol{\gamma}(\theta,\alpha)\boldsymbol{\gamma}(\theta,\alpha)^T\right)\mathbf{B}^{-1}\left(\mathbf{B}\left(\cos\alpha\,\boldsymbol{\gamma}_2(\theta) - \sin\alpha\,\boldsymbol{\gamma}_1(\theta)\right) \odot \begin{bmatrix}\mathbf{x}\\ \mathbf{x}\end{bmatrix}\right), \tag{2.113}$$

$$\frac{\partial \boldsymbol{\gamma}}{\partial \alpha} = -\sin\alpha\,\boldsymbol{\gamma}_1(\xi) + \cos\alpha\,\boldsymbol{\gamma}_2(\xi)\,. \tag{2.114}$$

with $\mathbf{x}$ defined as in (2.78). When using signal model (1.5) instead ($\boldsymbol{\xi} = r$):

$$\frac{\partial \boldsymbol{\gamma}}{\partial r} = \left(\mathbf{I} - \boldsymbol{\gamma}(r,\alpha)\boldsymbol{\gamma}(r,\alpha)^T\right)\mathbf{B}^{-1}\left(\mathbf{B}\left(\cos\alpha\,\boldsymbol{\gamma}_2(r) - \sin\alpha\,\boldsymbol{\gamma}_1(r)\right) \odot \begin{bmatrix}\mathbf{x}'(r)\\ \mathbf{x}'(r)\end{bmatrix}\right),$$

$$\frac{\partial \boldsymbol{\gamma}}{\partial \alpha} = -\sin\alpha\,\boldsymbol{\gamma}_1(\xi) + \cos\alpha\,\boldsymbol{\gamma}_2(\xi)\,.$$

with $\mathbf{x}'$ defined as in (2.84).

In the case of $M = 3$, with parameters (α, v, u) for STAP detection with the centrosymmetric signal model defined in the proof of Lemma 2.3.1

$$\frac{\partial \boldsymbol{\gamma}}{\partial v} = (\mathbf{I} - \boldsymbol{\gamma}\boldsymbol{\gamma}^T)\mathbf{B}^{-1}\left(\mathbf{B}\left(\cos\alpha\boldsymbol{\gamma}_2 - \sin\alpha\boldsymbol{\gamma}_1\right) \odot \begin{pmatrix} 2\pi\, l_\theta^{-1}\,\mathbf{x}_N \otimes \mathbf{1}_P \\ 2\pi\, l_\theta^{-1}\,\mathbf{x}_N \otimes \mathbf{1}_P \end{pmatrix}\right),$$

$$\frac{\partial \boldsymbol{\gamma}}{\partial u} = (\mathbf{I} - \boldsymbol{\gamma}\boldsymbol{\gamma}^T)\mathbf{B}^{-1}\left(\mathbf{B}\left(\cos\alpha\boldsymbol{\gamma}_2 - \sin\alpha\boldsymbol{\gamma}_1\right) \odot \begin{pmatrix} \mathbf{1}_N \otimes 2\pi\, l_\mu^{-1}\,\mathbf{x}_P \\ \mathbf{1}_N \otimes 2\pi\, l_\mu^{-1}\,\mathbf{x}_P \end{pmatrix}\right),$$

$$\frac{\partial \boldsymbol{\gamma}}{\partial \alpha} = -\sin\alpha\,\boldsymbol{\gamma}_1(\boldsymbol{\xi}) + \cos\alpha\,\boldsymbol{\gamma}_2(\boldsymbol{\xi})\,.$$

or (α, r, v) for distance-Doppler detection using a chirp (1.8) with a centrosymmetric steering vector:

$$\frac{\partial \boldsymbol{\gamma}}{\partial r} = (\mathbf{I} - \boldsymbol{\gamma}\boldsymbol{\gamma}^T)\mathbf{B}^{-1}\left(\mathbf{B}\left(\cos\alpha\boldsymbol{\gamma}_2 - \sin\alpha\boldsymbol{\gamma}_1\right) \odot \begin{pmatrix} \mathbf{x}' \otimes \mathbf{1}_N \\ \mathbf{x}' \otimes \mathbf{1}_N \end{pmatrix}\right),$$

$$\frac{\partial \boldsymbol{\gamma}}{\partial v} = (\mathbf{I} - \boldsymbol{\gamma}\boldsymbol{\gamma}^T)\mathbf{B}^{-1}\left(\mathbf{B}\left(\cos\alpha\boldsymbol{\gamma}_2 - \sin\alpha\boldsymbol{\gamma}_1\right) \odot \begin{pmatrix} \mathbf{1}_K \otimes 2\pi\, l_\theta^{-1}\,\mathbf{x}_N \\ \mathbf{1}_K \otimes 2\pi\, l_\theta^{-1}\,\mathbf{x}_N \end{pmatrix}\right),$$

$$\frac{\partial \boldsymbol{\gamma}}{\partial \alpha} = -\sin\alpha\,\boldsymbol{\gamma}_1(\boldsymbol{\xi}) + \cos\alpha\,\boldsymbol{\gamma}_2(\boldsymbol{\xi})\,,$$

2.D.2 . Second order derivatives

In this section, squared vectors indicate the Hadamard product of the vector with itself: $\mathbf{x}^{\odot 2} = \mathbf{x} \odot \mathbf{x}$. With $M = 2$, using signal model (1.7) for Doppler detection ($\boldsymbol{\xi} = \theta$), noting $\mathring{\boldsymbol{\gamma}}_{\text{Doppler}} = \mathbf{B}^{-1}\left(\mathbf{B}\left(\cos\alpha\,\boldsymbol{\gamma}_2(\theta) - \sin\alpha\,\boldsymbol{\gamma}_1(\theta)\right) \odot \begin{bmatrix}\mathbf{x}\\ \mathbf{x}\end{bmatrix}\right)$, the second order derivatives are given by

$$\frac{\partial^2 \boldsymbol{\gamma}}{\partial \theta^2} = -\left(\frac{\partial \boldsymbol{\gamma}}{\partial \theta}\boldsymbol{\gamma}^T + \boldsymbol{\gamma}\frac{\partial \boldsymbol{\gamma}^T}{\partial \theta}\right)\mathring{\boldsymbol{\gamma}}_{\text{Doppler}} + \left(\mathbf{I} - \boldsymbol{\gamma}\boldsymbol{\gamma}^T\right)\left(-\mathbf{B}^{-1}\left(\mathbf{B}\boldsymbol{\gamma} \odot \begin{bmatrix}\mathbf{x}\\ \mathbf{x}\end{bmatrix}^{\odot 2}\right) - \mathring{\boldsymbol{\gamma}}_{\text{Doppler}}\boldsymbol{\gamma}^T\mathring{\boldsymbol{\gamma}}_{\text{Doppler}}\right),$$

$$\frac{\partial^2 \boldsymbol{\gamma}}{\partial \theta \partial \alpha} = -\left(\frac{\partial \boldsymbol{\gamma}}{\partial \alpha}\boldsymbol{\gamma}^T + \boldsymbol{\gamma}\frac{\partial \boldsymbol{\gamma}^T}{\partial \alpha}\right)\mathring{\boldsymbol{\gamma}}_{\text{Doppler}} + \left(\mathbf{I} - \boldsymbol{\gamma}\boldsymbol{\gamma}^T\right)\left(-\mathbf{B}^{-1}\left(\mathbf{B}\boldsymbol{\gamma} \odot \begin{bmatrix}\mathbf{x}\\ \mathbf{x}\end{bmatrix}\right)\right),$$

$$\frac{\partial^2 \boldsymbol{\gamma}}{\partial \alpha^2} = -\boldsymbol{\gamma}$$

In the range case, using signal model (1.5) and noting $\mathring{\boldsymbol{\gamma}}_{\mathsf{Range}} = \mathbf{B}^{-1}\left(\mathbf{B}\left(\cos\alpha\,\boldsymbol{\gamma}_2(r) - \sin\alpha\,\boldsymbol{\gamma}_1(r)\right) \odot \begin{bmatrix}\mathbf{x}'(r)\\ \mathbf{x}'(r)\end{bmatrix}\right)$:

$$
\begin{aligned}
\frac{\partial^2\boldsymbol{\gamma}}{\partial r^2} &= -\left(\frac{\partial\boldsymbol{\gamma}}{\partial r}\boldsymbol{\gamma}^T + \boldsymbol{\gamma}\frac{\partial\boldsymbol{\gamma}^T}{\partial r}\right)\mathring{\boldsymbol{\gamma}}_{\mathsf{Range}} + \left(\mathbf{I} - \boldsymbol{\gamma}\boldsymbol{\gamma}^T\right)\left(-\mathbf{B}^{-1}\left(\mathbf{B}\boldsymbol{\gamma} \odot \begin{bmatrix}\mathbf{x}'(r)\\ \mathbf{x}'(r)\end{bmatrix}^{\odot 2}\right)\right.\\
&\quad \left. - 2\pi h\left(\cos\alpha\,\boldsymbol{\gamma}_2(r) - \sin\alpha\,\boldsymbol{\gamma}_1(r)\right) - \mathring{\boldsymbol{\gamma}}_{\mathsf{Range}}\boldsymbol{\gamma}^T\mathring{\boldsymbol{\gamma}}_{\mathsf{Range}}\right),\\
\frac{\partial^2\boldsymbol{\gamma}}{\partial r\partial\alpha} &= -\left(\frac{\partial\boldsymbol{\gamma}}{\partial\alpha}\boldsymbol{\gamma}^T + \boldsymbol{\gamma}\frac{\partial\boldsymbol{\gamma}^T}{\partial\alpha}\right)\mathring{\boldsymbol{\gamma}}_{\mathsf{Range}} + \left(\mathbf{I} - \boldsymbol{\gamma}\boldsymbol{\gamma}^T\right)\left(-\mathbf{B}^{-1}\left(\mathbf{B}\boldsymbol{\gamma} \odot \begin{bmatrix}\mathbf{x}'(r)\\ \mathbf{x}'(r)\end{bmatrix}\right)\right),\\
\frac{\partial^2\boldsymbol{\gamma}}{\partial\alpha^2} &= -\boldsymbol{\gamma}\,.
\end{aligned}
$$

With $M = 3$ in the case of STAP detection using the centrosymmetric signal model and parametrization (α, v, u) introduced in the proof of Lemma 2.3.1, noting $\mathring{\boldsymbol{\gamma}}_{\mathsf{STAP},\theta} = \mathbf{B}^{-1}\left(\mathbf{B}\left(\cos\alpha\boldsymbol{\gamma}_2 - \sin\alpha\boldsymbol{\gamma}_1\right) \odot \begin{pmatrix}2\pi\, l_\theta^{-1}\mathbf{x}_N \otimes \mathbf{1}_P\\ 2\pi\, l_\theta^{-1}\mathbf{x}_N \otimes \mathbf{1}_P\end{pmatrix}\right)$ and $\mathring{\boldsymbol{\gamma}}_{\mathsf{STAP},\mu} = \mathbf{B}^{-1}\left(\mathbf{B}\left(\cos\alpha\boldsymbol{\gamma}_2 - \sin\alpha\boldsymbol{\gamma}_1\right) \odot \begin{pmatrix}\mathbf{1}_N \otimes 2\pi\, l_\mu^{-1}\mathbf{x}_P\\ \mathbf{1}_N \otimes 2\pi\, l_\mu^{-1}\mathbf{x}_P\end{pmatrix}\right)$:

$$
\begin{aligned}
\frac{\partial^2\boldsymbol{\gamma}}{\partial v^2} &= -\left(\frac{\partial\boldsymbol{\gamma}}{\partial v}\boldsymbol{\gamma}^T + \boldsymbol{\gamma}\frac{\partial\boldsymbol{\gamma}^T}{\partial v}\right)\mathring{\boldsymbol{\gamma}}_{\mathsf{STAP},\theta} + \left(\mathbf{I} - \boldsymbol{\gamma}\boldsymbol{\gamma}^T\right)\left(-\mathbf{B}^{-1}\left(\mathbf{B}\boldsymbol{\gamma} \odot \begin{pmatrix}2\pi\, l_\theta^{-1}\mathbf{x}_N \otimes \mathbf{1}_P\\ 2\pi\, l_\theta^{-1}\mathbf{x}_N \otimes \mathbf{1}_P\end{pmatrix}^{\odot 2}\right) - \mathring{\boldsymbol{\gamma}}_{\mathsf{STAP},\theta}\boldsymbol{\gamma}^T\mathring{\boldsymbol{\gamma}}_{\mathsf{STAP},\theta}\right),\\
\frac{\partial^2\boldsymbol{\gamma}}{\partial u^2} &= -\left(\frac{\partial\boldsymbol{\gamma}}{\partial u}\boldsymbol{\gamma}^T + \boldsymbol{\gamma}\frac{\partial\boldsymbol{\gamma}^T}{\partial u}\right)\mathring{\boldsymbol{\gamma}}_{\mathsf{STAP},\mu} + \left(\mathbf{I} - \boldsymbol{\gamma}\boldsymbol{\gamma}^T\right)\left(-\mathbf{B}^{-1}\left(\mathbf{B}\boldsymbol{\gamma} \odot \begin{pmatrix}\mathbf{1}_N \otimes 2\pi\, l_\mu^{-1}\mathbf{x}_P\\ \mathbf{1}_N \otimes 2\pi\, l_\mu^{-1}\mathbf{x}_P\end{pmatrix}^{\odot 2}\right) - \mathring{\boldsymbol{\gamma}}_{\mathsf{STAP},\mu}\boldsymbol{\gamma}^T\mathring{\boldsymbol{\gamma}}_{\mathsf{STAP},\mu}\right),\\
\frac{\partial^2\boldsymbol{\gamma}}{\partial v\partial u} &= -\left(\frac{\partial\boldsymbol{\gamma}}{\partial u}\boldsymbol{\gamma}^T + \boldsymbol{\gamma}\frac{\partial\boldsymbol{\gamma}^T}{\partial u}\right)\mathring{\boldsymbol{\gamma}}_{\mathsf{STAP},\theta}\\
&\quad + \left(\mathbf{I} - \boldsymbol{\gamma}\boldsymbol{\gamma}^T\right)\left(-\mathbf{B}^{-1}\left(\mathbf{B}\boldsymbol{\gamma} \odot \begin{pmatrix}2\pi\, l_\theta^{-1}\mathbf{x}_N \otimes \mathbf{1}_P\\ 2\pi\, l_\theta^{-1}\mathbf{x}_N \otimes \mathbf{1}_P\end{pmatrix} \odot \begin{pmatrix}\mathbf{1}_N \otimes 2\pi\, l_\mu^{-1}\mathbf{x}_P\\ \mathbf{1}_N \otimes 2\pi\, l_\mu^{-1}\mathbf{x}_P\end{pmatrix}\right) - \mathring{\boldsymbol{\gamma}}_{\mathsf{STAP},\theta}\boldsymbol{\gamma}^T\mathring{\boldsymbol{\gamma}}_{\mathsf{STAP},\mu}\right),\\
\frac{\partial^2\boldsymbol{\gamma}}{\partial v\partial\alpha} &= -\left(\frac{\partial\boldsymbol{\gamma}}{\partial\alpha}\boldsymbol{\gamma}^T + \boldsymbol{\gamma}\frac{\partial\boldsymbol{\gamma}^T}{\partial\alpha}\right)\mathring{\boldsymbol{\gamma}}_{\mathsf{STAP},\theta} + \left(\mathbf{I} - \boldsymbol{\gamma}\boldsymbol{\gamma}^T\right)\left(-\mathbf{B}^{-1}\left(\mathbf{B}\boldsymbol{\gamma} \odot \begin{pmatrix}2\pi\, l_\theta^{-1}\mathbf{x}_N \otimes \mathbf{1}_P\\ 2\pi\, l_\theta^{-1}\mathbf{x}_N \otimes \mathbf{1}_P\end{pmatrix}\right)\right),\\
\frac{\partial^2\boldsymbol{\gamma}}{\partial u\partial\alpha} &= -\left(\frac{\partial\boldsymbol{\gamma}}{\partial\alpha}\boldsymbol{\gamma}^T + \boldsymbol{\gamma}\frac{\partial\boldsymbol{\gamma}^T}{\partial\alpha}\right)\mathring{\boldsymbol{\gamma}}_{\mathsf{STAP},\mu} + \left(\mathbf{I} - \boldsymbol{\gamma}\boldsymbol{\gamma}^T\right)\left(-\mathbf{B}^{-1}\left(\mathbf{B}\boldsymbol{\gamma} \odot \begin{pmatrix}\mathbf{1}_N \otimes 2\pi\, l_\mu^{-1}\mathbf{x}_P\\ \mathbf{1}_N \otimes 2\pi\, l_\mu^{-1}\mathbf{x}_P\end{pmatrix}\right)\right),\\
\frac{\partial^2\boldsymbol{\gamma}}{\partial\alpha^2} &= -\boldsymbol{\gamma}\,.
\end{aligned}
$$

3 - On the statistics of the off-grid Matched Filter

In the previous section, we computed the P_{FA}-threshold relationship of the Normalized Matched Filter by computing the volume of tubes on the sphere. While the NMF detector suffers the most from the presence of off-grid targets, there is also a gain when using the off-grid MF instead of the regular MF, and we would like to find its P_{FA}-threshold relationship. This is the aim of this chapter: we will find a P_{FA}-threshold relationship for the off-grid MF asymptotic in the threshold w^2.

Unfortunately, the geometrical approach used in the previous chapter does not apply to the Matched Filter detector as is, since the noise is not uniformly distributed on the unit sphere anymore. We use a different approach in this chapter: we study the geometry of the *parameter space* associated with the test vectors manifold. The tools we use are the expected Euler characteristics of excursion sets. This method is deeply related to the volume of tubes approach, but is, in the case of the MF, easier to apply.

This chapter heavily draws from [Adl00] which introduces the expected Euler characteristic and links them to the volume of tubes method. While the tools detailed here have been used for the detection of a signal depending on unknown parameters [SW95; Wor01], as far as we know, it has rarely been used with the signal processing detection GLRT formalism that we use, with complex signals. [Hay03] applies them for Doppler detection, [Lei+20] for MIMO target detection, and [HTW00; HTW01] mix up results about the distribution of the maxima of random fields with order statistics for determining P_{FA}-threshold relationships for the matched filter in a general context, but all those studies neglect border effects and as such are more suited when trying to detect a target globally rather than when the search space is decomposed into several cells, which is useful for detecting several targets in a given scene.

In Section 3.1, we model the Matched Filter test quantity as a random field. We show *the expected Euler characteristics* of the associated excursion sets are good estimates of the P_{FA}: those notions are presented in Section 3.2. This enables us to compute the P_{FA}-threshold relationships for the Matched Filter in Section 3.3 under white noise, before obtaining more general (but less precise) relationships in Section 3.4. We show the links between the tube method and the Euler characteristic in 3.5, before evaluating in simulations the obtained P_{FA}-threshold relationships in Section 3.6.

The results of this chapter were the subject of publications at the conferences ICASSP 2023 [Dev+23a] and GRETSI 2023 [Dev+23c].

3.1 . Motivation for the use of Expected Euler characteristics

In section 3.1.1, we start by recasting the off-grid Matched Filter as a random field, a notion that is formalized in 3.1.2 along with the definition of stationarity for random fields, which will be a crucial hypothesis for the main theorems used in this chapter. In section 3.1.3, we explain how we will evaluate the P_{FA} of the off-grid MF using the random field formalism.

3.1.1 . Modelling the off-grid matched filter as a random field

Our goal in this chapter is to evaluate the off-grid MF P_{FA}. By hypothesis, under H_0, the received signal $\mathbf{r}$ follows a complex circular white Gaussian distribution. The white noise assumption will be mandatory in the first proposed results. In this chapter as well, $\mathbf{s}$ will denote the normalized and whitened version of the searched signal. We note $Y(\boldsymbol{\xi})$ the expression of the MF test quantity in (1.19) tested for a parameter $\boldsymbol{\xi}$:

$$Y(\boldsymbol{\xi}) = \left| s(\boldsymbol{\xi})^H \mathbf{r} \right|^2 . \tag{3.1}$$

Recall how in the previous chapter, we showed that the product $\left|\mathbf{s}(\boldsymbol{\xi})^H \mathbf{r}\right|$ can be rewritten as

$$\left|\mathbf{s}(\boldsymbol{\xi})^H \mathbf{r}\right| = \max_{\alpha\in[0,2\pi]} \boldsymbol{\gamma}(\alpha,\boldsymbol{\xi})^T \, \underline{\mathbf{r}}\,,$$

where, as we defined previously in (2.3):

$$\boldsymbol{\gamma}(\boldsymbol{\xi},\alpha) = \boldsymbol{\gamma}_1(\boldsymbol{\xi}) \cos\alpha + \boldsymbol{\gamma}_2(\boldsymbol{\xi}) \sin\alpha\,,$$

with

$$\boldsymbol{\gamma}_1(\boldsymbol{\xi}) = \begin{bmatrix} \mathrm{Re}(\mathbf{s}(\boldsymbol{\xi})) \\ \mathrm{Im}(\mathbf{s}(\boldsymbol{\xi})) \end{bmatrix},$$
$$\boldsymbol{\gamma}_2(\boldsymbol{\xi}) = \begin{bmatrix} -\mathrm{Im}(\mathbf{s}(\boldsymbol{\xi})) \\ \mathrm{Re}(\mathbf{s}(\boldsymbol{\xi})) \end{bmatrix}.$$

$\underline{\mathbf{r}} = \begin{bmatrix} \mathrm{Re}(\mathbf{r}) \\ \mathrm{Im}(\mathbf{r}) \end{bmatrix}$ is a $2N$-real-valued noise vector following a centered Gaussian distribution of covariance $\mathbf{I}_{2N}/2$. Recall that α is a phase scalar, such that $\boldsymbol{\gamma}(\alpha,\boldsymbol{\xi})^T \, \underline{\mathbf{r}}$ attains its maximum for $\alpha = \angle \mathbf{s}(\boldsymbol{\xi})^H \underline{\mathbf{r}}$. We note

$$X(\alpha,\boldsymbol{\xi}) = \boldsymbol{\gamma}(\alpha,\boldsymbol{\xi})^T \, \mathbf{r}\,. \tag{3.2}$$

Notice how

$$\max_{\alpha\in[0,2\pi]} X(\alpha,\boldsymbol{\xi}) = \sqrt{Y(\boldsymbol{\xi})}\,.$$

The P_{FA} to characterize in this chapter can be linked to X. Indeed:

$$P_{FA} = P\left(\max_{\boldsymbol{\xi}\in\mathcal{D}} Y(\boldsymbol{\xi}) > w^2\right) = P\left(\max_{\alpha,\boldsymbol{\xi}\in[0,2\pi]\times\mathcal{D}} X(\alpha,\boldsymbol{\xi}) > w\right). \tag{3.3}$$

Our object X is a real-valued *random field*, a generalization of a stochastic process defined on a multi-dimensional space. The problem of knowing when a random process exceeds a given threshold is well-known in the statistical literature and has long been studied (see [Ric44], for example). Since then, it has also been generalized to random fields [Adl00; Wor94]. In the sequel, we seek to apply the results from this theory to our random field X in order to find the desired P_{FA}-threshold relationship. Before doing so, we will introduce some basic definitions on random fields and will then study the stationarity of X and its gradient covariance matrix: we will use this throughout the chapter.

3.1.2 . Some definitions on random fields and basic results on X

Formally, a real-valued random field is a collection of real-valued random variables indexed by elements in its parameter space T. As for stochastic processes, a real-valued random field $Z(\mathbf{t})$ is said to be Gaussian if and only if, for any $\mathbf{t_1},\ldots,\mathbf{t_k} \in T$, $(Z(\mathbf{t_1}),\ldots Z(\mathbf{t_k}))$ follows a multivariate normal distribution. Autocovariance and stationarity are defined similarly to stochastic processes:

Definition 3.1.1. *The autocovariance of a real-valued random field $Z(\mathbf{t})$ is defined as the following function f:*

$$f(\mathbf{t},\mathbf{t}') = E\left[\left(Z(\mathbf{t}) - E[Z(\mathbf{t})]\right)\left(Z(\mathbf{t}') - E[Z(\mathbf{t}')]\right)\right],$$

Z is said to be stationary i.i.f. f only depends on the difference $\mathbf{t}-\mathbf{t}'$.

The quantities Y and X defined in (3.1) and (3.2) are random fields. For Doppler or range detection when $\boldsymbol{\xi}$ is a scalar ($\boldsymbol{\xi} = \theta$ or $\boldsymbol{\xi} = r$ in signal models (1.7) or (1.5)), Y is a $1D$ χ^2_2 random field, while X is a $2D$ Gaussian random field. For range-Doppler or STAP detection (signal model (1.8) or (1.10)), Y is a $2D$ χ^2_2 random field and X is a $3D$ Gaussian random field.

Remark 3.1.1. *Some of the results of this chapter can be obtained by applying results on χ^2_2 random fields to Y (such as the DT characteristic computed in [Wor94]). However, there are more results regarding the Gaussian random fields in the literature, notably in Adler's articles [Adl00; ATW07; ATW15], which motivates the introduction of X, on which we will focus from now on.*

Under white noise, X is easily shown to be stationary for Doppler or STAP contexts (signal models (1.7), (1.10)): indeed X is centered and:

$$\begin{aligned} E\left[X(\alpha,\boldsymbol{\xi})^T X(\alpha',\boldsymbol{\xi}')\right] &= \boldsymbol{\gamma}(\alpha,\boldsymbol{\xi})^T E[\underline{\mathbf{r}}\underline{\mathbf{r}}^T]\boldsymbol{\gamma}(\alpha',\boldsymbol{\xi}') \\ &= \frac{1}{2}\boldsymbol{\gamma}(\alpha,\boldsymbol{\xi})^T \mathbf{I}\boldsymbol{\gamma}(\alpha',\boldsymbol{\xi}') \\ &= \frac{1}{2}\boldsymbol{\gamma}(\alpha,\boldsymbol{\xi})^T \boldsymbol{\gamma}(\alpha',\boldsymbol{\xi}') \end{aligned}$$

and we have shown in (2.59), (2.60) that $\boldsymbol{\gamma}$ was shift-invariant in those contexts, i.e. the product $\boldsymbol{\gamma}(\alpha,\boldsymbol{\xi})^T\boldsymbol{\gamma}(\alpha',\boldsymbol{\xi}')$ depends only on the differences $\alpha'-\alpha$, $\boldsymbol{\xi}'-\boldsymbol{\xi}$. The stationarity of X is thus equivalent to the shift-invariancy of $\boldsymbol{\gamma}$ defined in (2.46). The function f that was defined as $f\left((\alpha,\boldsymbol{\xi})^T-(\alpha',\boldsymbol{\xi}')^T\right) = \boldsymbol{\gamma}(\alpha,\boldsymbol{\xi})^T\boldsymbol{\gamma}(\alpha',\boldsymbol{\xi}')$ is also the autocorrelation function of X, up to a factor $1/2$.

The expectancy of the product of the derivatives of X is constant: indeed,

$$\begin{aligned} E\left[\frac{\partial X^T}{\partial\alpha}\frac{\partial X}{\partial\alpha}\right] &= \frac{1}{2}\frac{\partial\boldsymbol{\gamma}(\boldsymbol{\xi})^T}{\partial\alpha}\frac{\partial\boldsymbol{\gamma}(\boldsymbol{\xi})}{\partial\alpha}\,, \\ &= \frac{1}{2}\,, \\ E\left[\frac{\partial X^T}{\partial\xi_i}\frac{\partial X}{\partial\alpha}\right] &= \frac{1}{2}\frac{\partial\boldsymbol{\gamma}(\boldsymbol{\xi})^T}{\partial\xi_i}\frac{\partial\boldsymbol{\gamma}(\boldsymbol{\xi})}{\partial\alpha}\,, \\ &= 0\,, \\ E\left[\frac{\partial X^T}{\partial\xi_i}\frac{\partial X}{\partial\xi_j}\right] &= \frac{1}{2}\frac{\partial\boldsymbol{\gamma}(\boldsymbol{\xi})^T}{\partial\xi_i}\frac{\partial\boldsymbol{\gamma}(\boldsymbol{\xi})}{\partial\xi_j}\,, \\ &= -\frac{1}{2}\frac{\partial^2 f}{\partial\xi_i\partial\xi_j}\bigg|_{\mathbf{0}}\,. \end{aligned}$$

Thus, the covariance matrix of its gradient, which we denote by $\boldsymbol{\Lambda}$, is constant:

$$\begin{aligned} \boldsymbol{\Lambda} &= E\left[\begin{pmatrix} \frac{\partial X^T}{\partial\alpha}\frac{\partial X}{\partial\alpha} & \frac{\partial X^T}{\partial\boldsymbol{\xi}}\frac{\partial X}{\partial\alpha} \\ \frac{\partial X^T}{\partial\boldsymbol{\xi}}\frac{\partial X}{\partial\alpha} & \frac{\partial X^T}{\partial\boldsymbol{\xi}}\frac{\partial X}{\partial\boldsymbol{\xi}} \end{pmatrix}\right]\,, \\ &= \frac{1}{2}g_{ij} \end{aligned}$$

It is half the first fundamental form g_{ij} of the manifold $\boldsymbol{\gamma}$. In particular, for the centrosymmetric version of the signal model (2.34), using parametrization $\boldsymbol{\psi}=(\alpha,v,u)$, for which $g_{ij}=\mathbf{I}$:

$$\boldsymbol{\Lambda} = \frac{1}{2}\mathbf{I}\,.$$

3.1.3 . A result to establish the P_{FA} of the off-grid matched filter

Now that we have established those basic results on X, we are ready to introduce the result that we will use in this chapter to compute our asymptotic P_{FA}-threshold relationships. It relies on the *excursion set* $A_w(X)$ associated with a realization of X for a threshold w, defined as the set of parameters such that the realization $X(\alpha,\boldsymbol{\xi})$ exceeds w [Adl00]:

$$A_w(X) = \{(\alpha,\boldsymbol{\xi}), X(\alpha,\boldsymbol{\xi}) > w\}\,. \tag{3.4}$$

Examples of excursion sets can be seen in figures 3.2.1 and 3.2.2. In [ATW07], it is shown that $E(\varphi(A_w(X)))$, the expected *Euler characteristic* of $A_w(X)$, that is defined in the next section, is a precise estimation of the probability of $X(\alpha, \boldsymbol{\xi})$ exceeding w and so the desired P_{FA}:

$$|P_{FA} - E\left[\varphi(A_w(X))\right]| < O\left(\exp\left(-c\,w^2\right)\right)\,, \tag{3.5}$$

for some $c > 1$.

Remark 3.1.2. *This is actually only true for non-periodic random fields, i.e. random fields of autocorrelation function f such that [ATW07, Eq. (14.1.12), p.361]:*

$$f(s,t) = 1 \iff t = s\,, \tag{3.6}$$

We will need to make some adjustments later since the process X we defined is periodic in α.

Computing the expected Euler characteristic of the excursion set of our process X will then be the focus of this chapter. In the next section, we define what is this Euler characteristic and introduce the basic tools to calculate it.

3.2 . Expected Euler characteristics: a brief introduction

At the end of the previous section, we showed how the computation of P_{FA}s approximately reduces to the calculation of the expected Euler characteristic of the excursion set of the random field X associated with the manifold γ. This section aims to briefly explain what is the expected Euler characteristic of the excursion set of a random field and give some intuition as to why it is a good estimate of the probability of an excursion, and then give the closed-form results we will use to compute the expected Euler characteristic. This section is written based on Adler's works [Adl00; ATW15], to which readers are referred for a more thorough introduction.

Remark 3.2.1. *For this explanation to be quick and simple, we will neglect border effects in the discussion of Subsections 3.2.1 and 3.2.2, however the influence of the border is well taken into account in the formula of Theorems 3.2.3 and 3.2.4.*

3.2.1 . Some words on the expected Euler characteristic of excursion sets and why it approximates the P_{FA}

We introduced the excursion set of a realization of X in (3.4) as the set $A_w(X)$ of parameters for which the realization of X is higher than the threshold w. To see how the expected Euler characteristic of this set relates to the P_{FA}, we begin by studying the simple case where the dimension of the parameter space is $M = 1$. The random field X is a stochastic process, and $A_w(X)$ is related to the number of upcrossings N_w above w, a well-known quantity in probability theory. Indeed, counting the number of disjoint intervals in $A_w(X)$ gives the number of upcrossings (maybe one more if X is already above the threshold at the start of its definition interval). An example of an excursion set $A_w(X)$ is given in Figure 3.2.1. The expectation of the number of upcrossings is then linked to the probability $P(\max_{t\in[0,T]} X(t) > w)$ for a stationary stochastic process X defined on $[0,T]$ [Adl00, p.3]:

$$\begin{aligned} P(\max_{t\in[0,T]} X(t) > w) &= P(N_w \geq 1 \text{ or } X(0) > w) \\ &\leq P(N_w \geq 1) + P(X(0) > w) \\ &\leq E[N_w] + P(X(0) > w) \end{aligned} \tag{3.7}$$

And it can be shown that (3.7) can turn into:

$$P(\max_{t\in[0,T]} X(t) > w) = E[N_w] + P(X(0) > w) + O\left(\exp\left(-\frac{w}{2\sigma^2}\right)\right)$$

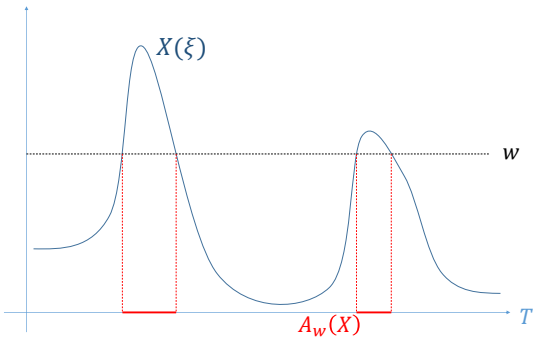

Figure 3.2.1: Excursion set $A_w(X)$ of a 1D random field, in red.

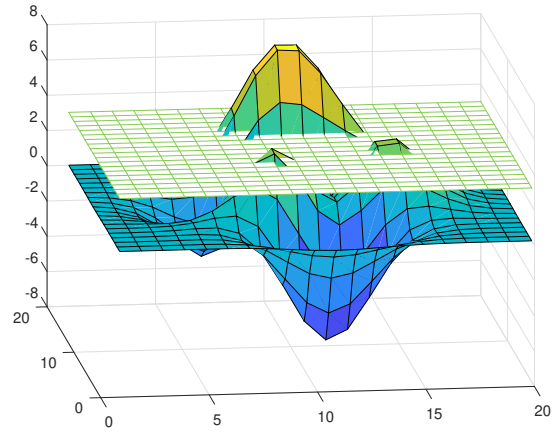

(a) Realisation of a 2D random field Z, with an hyperplane $z = w$ at threshold w level.

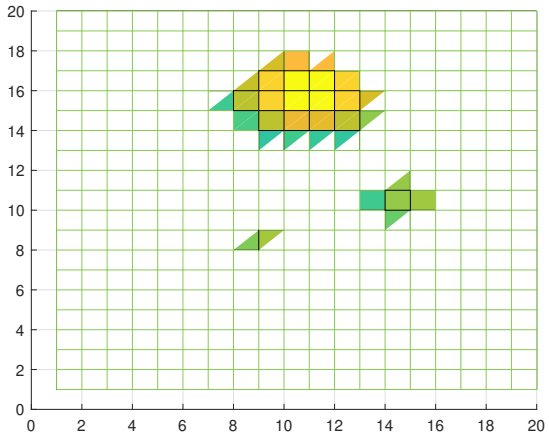

(b) Associated excursion set $A_w(Z)$.

Figure 3.2.2: Realisation of a random field Z and associated excursion set.

It turns out that, for white Gaussian noise, the expectancy of the number of upcrossings was derived in [Ric44], enabling to get expressions of the P_{FA} in this case.

For $M > 1$, we deal with multi-dimensional random fields, and the number of upcrossing is not defined anymore. Instead, we need to consider a generalization of this quantity. Figure 3.2.2 represents an example of a realization of a random field and the associated excursion set. In order to extend the approach of the case $M = 1$, we should find a quantity that counts the number of non-connected components above the threshold. The Euler characteristic of excursion sets will allow us to achieve this. It is however more involved than the number of upcrossings, so a little explanation is required.

The Euler characteristic $\varphi(A)$ is a function associating an integer to a set A of $\mathbb{R}^M$. Let us give some classical global characterizations for $M = 1$, $M = 2$ and $M = 3$:

- When $M = 1$, the Euler characteristic counts the number of disjoint intervals so that the expected Euler characteristic of the excursion sets $A_w(X)$ reduces to the number of upcrossings.
- When $M = 2$, the Euler characteristic is the sum of connected components of A minus the number of holes.
- When $M = 3$, it is the sum of the number of connected components plus the number of holes minus the number of handles (think of a teacup handle). For example, the Euler characteristic of a solid ball is 1, while that of a sphere is 2.

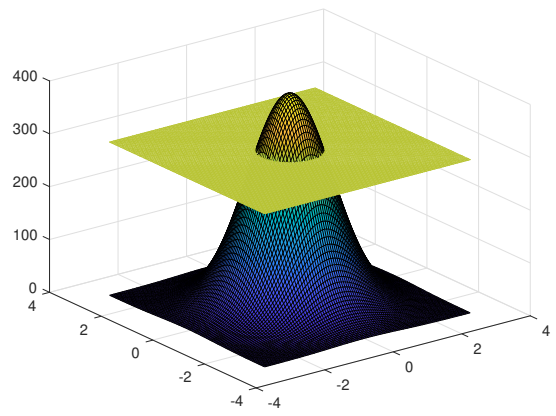

(a) Appearance of a random field around its local maxima above w for high threshold w level.

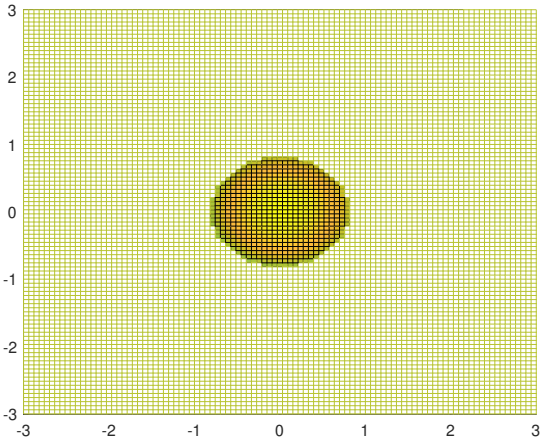

(b) Associated excursion set.

Figure 3.2.3: Appearance of a random field X around a local maxima above w for high w values and associated excursion set.

What we will need to keep in mind for the discussion below is that the Euler characteristic of a simple, ellipsoid-like set equals one in any dimension M.

To understand how the expected Euler characteristic of excursion sets relates to the P_{FA}, we need to study to the shape of sets for which X goes above w. Denoting $\mathbf{m}$ a local maxima of a realization of X above w, it can be proven that X is approximately parabolic around $\mathbf{m}$ so that the component centered around $\mathbf{m}$ in $A_w(X)$ has a simple, M-dimensional ellipsoïd form, as shown on Figure 3.2.3, of Euler characteristic 1. Formally, in the neighborhood of the origin, supposing $X(\mathbf{0}) = w$, when $w \to \infty$, then X can be expressed as [Adloo, Eq (4.2.1)], with probability one:

$$X(\boldsymbol{\xi}) = w - \frac{w}{2\sigma}\,\boldsymbol{\xi}^T \boldsymbol{\Lambda} \boldsymbol{\xi} + O(1)\,.$$

This result ensures that by computing the expected Euler characteristic of the excursion set $E[\varphi(A_w(X))]$, we are counting the number of components above w in multiple dimensions, as we were doing when computing the number of intervals of $A_w(X)$ in the case $M = 1$ (plus another term depending on how X behaves on the borders of the parameter space).

A rigorous mathematical formalization and proof of this informal discussion can be found in [ATW15, Chapter 5, 6], leading to Equation (3.5).

3.2.2 . Computing the expected Euler characteristic of excursion sets

Now that we understand intuitively why the expected Euler characteristic will provide an approximation of the P_{FA}, we will introduce some simple tools that can be used to compute it. First, we will give an alternative definition of the Euler characteristic of excursion sets that uses local quantities rather than the global shape of the manifold:

Theorem 3.2.1. *[Adloo, Theorem 3.1.3] Let $X : \mathbb{R}^M \to \mathbb{R}$ be C^2 over a compact $T \subset \mathbb{R}^M$ and assume that $X(t) < w$ for all $\mathbf{t}$ in the border ∂T of T. Then, if the χ_k, defined later, are all finite, the Euler characteristic of the excursion set $A_w(X)$ is given by:*

$$\varphi(A_w(X)) = (-1)^{M-1} \sum_{k=0}^{M-1} (-1)^k \chi_k\,, \tag{3.8}$$

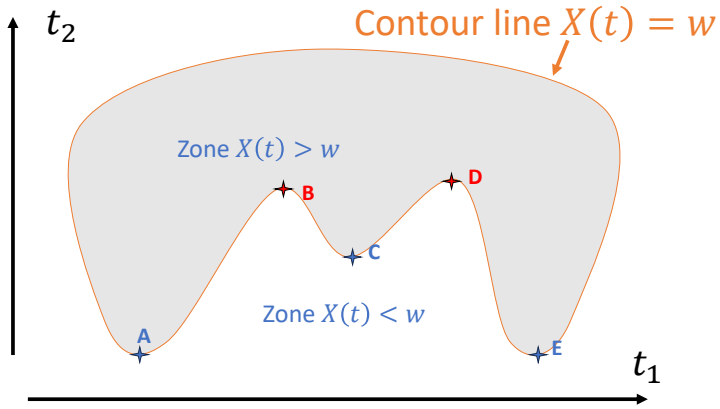

Figure 3.2.4: Example of a realization of a random field X on a 2D parameter space.

where χ_k is the number of points $\mathbf{t} \in T$ satisfying the following conditions:

- $X(\mathbf{t}) = w\,,$
- $\dfrac{\partial X}{\partial t_j} = 0\,, \quad \forall j \in [1, M-1]$
- $\dfrac{\partial X}{\partial t_M} > 0\,,$
- *the index of $\mathbf{D}(\mathbf{t})$ equals k*

where $\mathbf{D}(\mathbf{t})$ is the $(M-1)\times(M-1)$ matrix of second derivatives with elements $\dfrac{\partial^2 X}{\partial t_i \partial t_j}, i, j \in [1, M-1]^2$, and the index of $\mathbf{D}(\mathbf{t})$ is its number of negative eigenvalues (as a real symmetric matrix, $\mathbf{D}(\mathbf{t})$ is diagonalizable).

This characteristization is said to be point-like because we can compute the Euler characteristic of the excursion set by considering each point separately. Let us use the simple realization of X on Figure 3.2.4 in the $2D$ case to show how to use this characterization. The first condition requires that points in a set χ_k lie along the contour line $X(\mathbf{t}) = w$. The second condition states that those points should be critical points of the 1D function $h_{t_2}(t_1) = X(t_1, t_2)$ obtained for fixed t_2. The third condition implies that the 1D function $h'_{t_1}(t_2) = X(t_1, t_2)$ obtained for fixed t_1 increases. See that points A, B, C, D, and E are the only points that verify the first three conditions. $\mathbf{D}(\mathbf{t})$ is a scalar that is worth 1 if $\mathbf{t}$ is a local maximum of a function h_{t_2}, and 0 otherwise. A, C, and E are local maxima for the functions h_{t_2} with corresponding t_2 so that the index of $\mathbf{D}$ is 1 for those points and $\chi_1 = 3$. B and D being local minima, the index of $\mathbf{D}$ is 0, thus $\chi_0 = 2$. Injecting in (3.8) gives 1, which is the value given by the global characterization we mentioned earlier since this simple excursion set consists only of one connected set with no hole.

Let us then introduce the Kac-Rice "meta-theorem" (or counting theorem), which can be used to get the mean number of points in T verifying certain conditions.

Theorem 3.2.2. *[Adloo, Theorem 3.2.1] Let U and V be $\mathbb{R}^M$ and $\mathbb{R}^K$ valued N-parameter random fields on $T \subset \mathbb{R}^N$ and $B \subset \mathbb{R}^K$. We note $\nabla U(t)$ the $N \times N$ matrix of first-order partial derivatives of U at t. Under regularity conditions on $U, \nabla U$ and V detailed in [Adloo, p. 24], noting $E\left[N(U, V : N)\right]$ the expectation of the number of points in T such that $U(t) = u \in \mathbb{R}^N$ and $V(t) \in B$, $I_B(v)$ the characteristic function of B (worth 1 if $v \in B$ and 0 otherwise), and $p_t(u, \nabla u, v)$ the joint density of $(U(t), \nabla U(t), V(t))$, we have, noting $D = N(N-1)/2 + K$:*

$$E\left[N(U, V : N)\right] = \int_T \int_{\mathbb{R}^D} |\det \nabla u|\, I_B(v)\, p_t(u, \nabla u, v)\, d(\nabla u)\, dv\, dt\,.$$

Evaluating this theorem for $U = \left(X, \frac{\partial X}{\partial t_1}, \ldots, \frac{\partial X}{\partial t_{M-1}}\right)$, $u = (w, 0, \ldots, 0)$, V the vector composed of $\frac{\partial X}{\partial t_M}$ and then the elements of $\mathbf{D}$ arranged linearly, and finally $B = [0, +\infty[\times\mathbb{R}^{(N-1)(N-2)/2}$ yields the Euler characteristic. Indeed the choices of U and u ensure that the points we are counting follow the first two conditions of the point-like characterization of Theorem 3.2.1. Then, taking $\frac{\partial X}{\partial t_M}$ as the first component of V and restricting it to $[0, +\infty]$ ensures that the third condition is met. Finally, the choice of $\mathbb{R}^{(N-1)(N-2)/2}$ as the remaining element of B guarantees that the fourth condition is met (this last choice is less obvious, refer to [ATW15] for a detailed explanation). In the next subsections, we give the results that come from applying this theorem to 2D and 3D sets, which are the results we rely on for finding the P_{FA}-threshold relationships.

3.2.2.1 On $2D$ parameter space

When $M = 2$, the following theorem gives the expected Euler characteristic of the excursion set $A_w(X)$:

Theorem 3.2.3. *[Adloo, Theorem 3.3.1] Let X be a zero-mean, isotropic stationary Gaussian random field on the parameter space $T \subset \mathbb{R}^2$ with variance σ^2 and gradient covariance matrix $\mathbf{\Lambda} = \lambda\,\mathbf{I}$ and assume that ∂T, defined as the boundary of T, is continuously differentiable except at an at most finite number of points. Then*

$$E\left[\varphi(A_w(X))\right] = |T|\,\rho_2(w) + \frac{|\partial T|}{2}\rho_1(w) + \varphi(T)\Psi\left(\frac{w}{\sigma}\right), \tag{3.9}$$

where σ^2 is the variance of X (which does not depend on $\boldsymbol{\xi}$ since X is stationary),

$$\rho_k(w) = \frac{\exp\left(-w^2/2\sigma^2\right)\,\lambda^{k/2}}{(2\pi)^{(k+1)/2}\,\sigma^k} H_{k-1}\left(\frac{w}{\sigma}\right), \tag{3.10}$$

with H_k the k-th Hermite polynomial

$$H_k(x) = k! \sum_{j=0}^{\lfloor \frac{k}{2} \rfloor} \frac{(-1)^j x^{k-2j}}{j!\,(k-2j)!\,2^j}.$$

Note that $H_2(x) = x^2 - 1$, $H_1(x) = x$, and $H_0(x) = 1$. Ψ denotes the tail of the standard Gaussian distribution function. $|T|$ denotes the area measure of T, $|\partial T|$ denotes the line measure of ∂T.

The main idea of the proof is to apply the Kac-Rice Theorem 3.2.2 with the arguments discussed earlier on 2D parameter spaces, which make up the first term. Then, adjustments are made to take border effects into account, which leads to the next terms.

The hypothesis is made that X is isotropic, i.e. that the autocorrelation depends only on the norm of the difference of parameters: $f(\mathbf{t}, \mathbf{t}')$ can be rewritten $f(\|\mathbf{t} - \mathbf{t}'\|)$. This hypothesis is made so that X is stationary on the borders ∂T. In this case X restricted to $|\partial T|$ becomes uncorrelated with its derivatives, greatly simplifying the application of Kac-Rice Theorem 3.2.2 which yields the simple term $\frac{|\partial T|}{2}\rho_1(w)$ as the second term in (3.9). Additionally in this case $\mathbf{\Lambda}$, the covariance of the gradient matrix, is expressed as a scalar λ times $\mathbf{I}$.

3.2.2.2 Of $3D$ parameter space

Similarly to the case $M = 2$, for a random process defined on a 3D parameter space, we have the following theorem to compute the expected Euler characteristic:

Theorem 3.2.4. *[Adloo, Theorem 3.3.2] Let X meet the same conditions as in Theorem 3.2.3, except it is now defined on $T \subset \mathbb{R}^3$ and ∂T is twice continuously differentiable except at edges or creases of finite length and vertices where the edges meet. Then:*

$$E\left[\varphi(A_w(X))\right] = |T|\,\rho_3(w) + \frac{|\partial T|}{2}\rho_2(w) + \frac{H(\partial T)}{\pi}\rho_1(w) + \varphi(T)\Psi\left(\frac{w}{\sigma}\right), \tag{3.11}$$

where $H(\partial T)$ is given in Lemma 8 of [Wor95, p.655]:

$$H(\partial T) = \frac{1}{2}\int\int_{\partial T}(c_{max} + c_{min})\,d\mathbf{t}_T\,d\mathbf{t}_U + \frac{1}{2}\int_{\partial T_E}(\pi - \iota)\,d\mathbf{t}_E. \tag{3.12}$$

where $(\mathbf{t}_T, \mathbf{t}_U)$ is a set of unit orthogonal vectors in the tangent plane to the surface ∂T, c_{max} and c_{min} are respectively the maximum and minimum inside curvature at point $\mathbf{t}$. ∂T_E is the set of edges of ∂T (void if ∂T is smooth), $\mathbf{t}_E$ is the unit tangent vector to ∂T_E, and ι is the angular deficiency, i.e. the internal angle of ∂T at $\mathbf{t_E}$ between the two tangent planes to ∂T on either side of the edge. $|T|$ denotes the volume measure of T, $|\partial T|$ denotes the area measure of ∂T. The other terms are defined as in Theorem 3.2.3.

3.3 . Application to the off-grid Matched Filter for white noise $(\mathbf{\Gamma} = \mathbf{I})$

Now that we understand why the expected Euler characteristic approximation holds and know how to compute it, we will derive it for our random field X (3.2) to find the P_{FA} of the off-grid GLRT. Let us first treat the case of one unknown parameter.

3.3.1 . For one unknown parameter

When performing Doppler (or angle) detection using signal model (1.7) ($\boldsymbol{\xi} = \theta$), the random field X is defined on a 2D parameter space T. However, remember that condition (3.6) prevents us from directly using Theorem 3.2.3 to X by considering a rectangular parameter space $[0, 2\pi] \times [\theta_1, \theta_2]$, since when defined that way, X is periodic. Indeed, it is obvious that contradictions will arise in this case: for our random field $X(\alpha, \theta)$, we defined α as the phase belonging to $[0, 2\pi]$, but we could also have defined α as belonging in $[0, 4\pi]$, for example, so that the parameter space T is either $[0, 2\pi] \times \mathcal{D}$ or $[0, 4\pi] \times \mathcal{D}$. The excursion probability is of course no higher in the second case, but Theorem 3.2.3 will yield different answers in both instances. The answer to that issue is to consider that the process is borderless along the axis α, as mentioned informally in [Adloo, Section 5.2]. It is represented schematically as a cylinder in Figure 3.3.1a, but note that we treat it as a set of $\mathbb{R}^2$.

Another issue that appears is that X is not isotropic: indeed, in general, $E(X(\alpha, \theta)X(\alpha', \theta'))$ is not a function of the norm $\|(\alpha - \alpha', \theta - \theta')\|$. However, even though in our case X is not isotropic, there is no difficulty seeing that X is stationary along $|\partial T|$. Indeed, ∂T is defined as the set $\{(\alpha, \theta_1), (\alpha, \theta_2), \alpha \in [0, 2\pi]\}$. X restricted on ∂T can be decomposed in two random processes $\bar{X}_i(\alpha) = X(\alpha, \theta_i)$, $i \in [1, 2]$, and $E\left[\bar{X}_i(\alpha)\bar{X}_i(\alpha')\right] = E\left[X(\alpha, \theta_i)X(\alpha', \theta_i)\right]$ depends only on $\alpha - \alpha'$, as we saw in Section 3.1. Furthermore, as we noticed before when using the centrosymetric signal model (2.34) with X parametrized by (α, v), the matrix $\mathbf{\Lambda}$ becomes proportional to identity, and the necessary hypotheses of the theorems hold.

The application of Theorem 3.2.3 to this parameter space yields the following corollary:

Corollary 3.3.0.1. *The P_{FA}-threshold relationship of the off-grid MF tested on a cell $\mathcal{D} = [\theta_1, \theta_2]$ with steering vectors of size N for signal model (1.7) is:*

$$P_{FA} = \left(\sqrt{\frac{\pi(N^2 - 1)}{3}}(\theta_2 - \theta_1)\,w + 1\right)\exp\left(-w^2\right) + O\left(\exp\left(-c\,w^2\right)\right) \qquad \text{for some } c > 1\,. \tag{3.13}$$

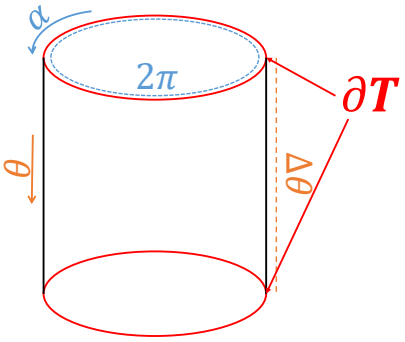

(a) T treated as an object in $\mathbb{R}^2$. It is schematized as a hollow cylinder.

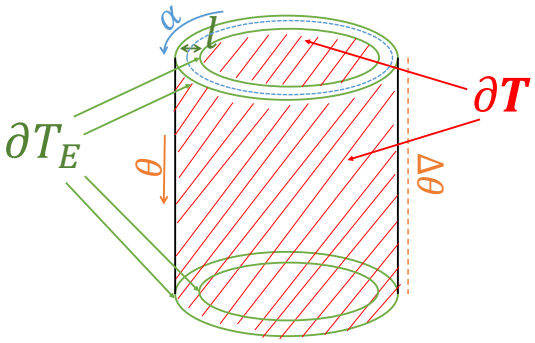

(b) T treated as an object in $\mathbb{R}^3$, with some thickness l.

Figure 3.3.1: Representations of the search domains T for one unknown parameter.

When $\mathcal{D} = [0, 1]$, only the first term in the parenthesis should remain: this special case was given in [Hay03] for Doppler detection based on earlier work from Rice [Ric44]. Note that the order of the approximation $O(.)$ is missing.

Remark 3.3.1. *Contrary to most asymptotic results in the detection literature, we stress that this relationship (like all the relationships of this chapter) is asymptotic in the threshold w^2 but not in N.*

Proof. Let us apply Theorem 3.2.3 to our process X for Doppler detection using the centrosymmetric signal model (2.34). σ^2 is equal to the variance of each component of $\underline{\mathbf{r}}$, i.e. $\sigma^2 = 1/2$. $\mathbf{\Lambda}$ is equal to $\frac{1}{2}\mathbf{I}$, so that $\lambda = \frac{1}{2}$ in theorem 3.2.3. The terms $\rho_2(w)$ and $\rho_1(w)$ are thus equal to $\frac{\exp(-w^2)}{(2\pi)^{3/2}}\sqrt{2}w$ and $\frac{\exp(-w^2)}{2\pi}$. As we mentioned earlier, for detection over a single cell, T is shaped akin to a hollow cylinder. After reparametrizing using, as usual, the centrosymmetric signal model from the proof of Lemma 2.3.1, v runs from $\pi\sqrt{\frac{N^2-1}{3}}\theta_1$ to $\pi\sqrt{\frac{N^2-1}{3}}\theta_2$, such that the cylinder is of radius 1 and height $\pi\sqrt{\frac{N^2-1}{3}}(\theta_2 - \theta_1)$. This gives the surface $|T| = 2\pi^2\sqrt{\frac{N^2-1}{3}}(\theta_2 - \theta_1)$, the length of the borders $|\partial T| = 4\pi$ and the Euler characteristic $\varphi(T) = 0$ since the Euler characteristic of a cylinder is zero [Ale98, p.99]. Injecting everything into (3.9) gives the expected result.

In the case of detection over the whole domain ($\theta \in [0, 1]$), T has no border along its Doppler axis either: $|\partial T| = 0$. T is shaped like a torus so that its Euler characteristic is still zero. □

Remark 3.3.2. *Alternatively, the same result could be obtained considering that the cylindric parameter space is a surface embedded in $\mathbb{R}^3$, applying Theorem 3.2.4 without relying on the argument that periodic processes can be considered borderless. Indeed, consider the related random field defined on $\mathbb{R}^3$:*

$$\tilde{X}(x, y, z) = (x\,\boldsymbol{\gamma}_1(z) + y\,\boldsymbol{\gamma}_2(z))^T\,\mathbf{r}\,.$$

When x, y are restricted to the trigonometric circle ($(x, y) = (\cos\alpha, \sin\alpha)$ for some $\alpha \in [0, 2\pi]$) and z is in the search domain $\mathcal{D}$ then

$$\tilde{X}(\cos\alpha, \sin\alpha, v) = X(\alpha, v).$$

This new process is not periodic anymore: $f(\mathbf{x}_1, \mathbf{x}_2) = 1 \implies \mathbf{x}_1 = \mathbf{x}_2$. Note how the covariance matrix of

the gradient $\tilde{\mathbf{\Lambda}}$ is still equal to $\mathbf{I}$ times $\frac{1}{2}$: indeed,

$$
\begin{aligned}
E\left[\frac{\partial\tilde{X}}{\partial x}^T\frac{\partial\tilde{X}}{\partial x}\right] &= E\left[\frac{\partial\tilde{X}}{\partial y}^T\frac{\partial\tilde{X}}{\partial y}\right] \\
&= \frac{1}{2}\boldsymbol{\gamma}_1(z)^T\boldsymbol{\gamma}_1(z) \\
&= \frac{1}{2}\,, \\
E\left[\frac{\partial\tilde{X}}{\partial x}^T\frac{\partial\tilde{X}}{\partial y}\right] &= \frac{1}{2}\boldsymbol{\gamma}_1(z)^T\boldsymbol{\gamma}_2(z) \\
&= 0\,, \\
E\left[\frac{\partial\tilde{X}}{\partial x}^T\frac{\partial\tilde{X}}{\partial z}\right] &= \frac{x}{2}\dot{\boldsymbol{\gamma}}_1(z)^T\boldsymbol{\gamma}_2(z) \\
&= 0 \quad \text{according to computations similar to that of (2.92)}\,, \\
E\left[\frac{\partial\tilde{X}}{\partial z}^T\frac{\partial\tilde{X}}{\partial z}\right] &= \frac{1}{2}\left(x^2\dot{\boldsymbol{\gamma}}_1(z)^T\dot{\boldsymbol{\gamma}}_1(z) + y^2\dot{\boldsymbol{\gamma}}_2(z)^T\dot{\boldsymbol{\gamma}}_2(z)\right) \\
&= \frac{1}{2} \quad \text{according to computations similar to that of (2.96)}\,.
\end{aligned}
$$

Since T is hollow, it has no volume: $|T| = 0$. Then, to help us characterize ∂T, consider the case where the cylinder has a non-zero thickness l, using the same idea as Worsley in [Wor95, Section 4.4] to find the expected Euler characteristic of the excursion sets of random fields defined on surfaces in $\mathbb{R}^3$. This thickened tube is represented in Figure 3.3.1b. The frontier ∂T is composed of the outer face of the cylinder, the inner face, plus some terms above and below, and there are 4 edges to the frontier, of angular deficiency $\iota = \pi/2$. In our case, the thickness l tends to 0, and the terms contributing in $|\partial T|$ are the inner and outer faces of the cylinder so that $|\partial T| = 4\pi^2\sqrt{\frac{N^2-1}{3}}(\theta_2 - \theta_1)$. For each point of the outer face, $c_{max} = 1$ and $c_{min} = 0$, while on the inner face, $c_{max} = 0$ and $c_{min} = -1$, so that the sum of the curvatures on the inner face cancels that of the outer face. Then, $H(\partial T)$ in (3.12) is determined by the length of the 4 edges 8π: $H(\partial T) = \frac{1}{2}8\pi(\pi - \iota) = 2\pi^2$. Injecting in (3.11), we fall back on the result given by formula (3.9).

As in the case of the off-grid NMF, the P_{FA} of the off-grid MF is expressed as the sum of a term proportional to the length of the cell plus another constant term e^{-w^2}, equal to the P_{FA} of the on-grid MF given in (1.27) plus a term of the order $O\left(\exp(-cw^2)\right)$. The first term corresponds to the probability of having a local maximum falling in the interior of the search domain. The on-grid term corresponds to the probability of having a local maximum falling outside the parameter space, but still close enough so that there is an excursion corresponding to it inside the parameter space.

3.3.2 . Application to the Matched Filter with two unknown parameters

Now let us turn to the problem of finding the P_{FA}-threshold relationship of the off-grid matched filter with two unknown parameters for STAP detection, using signal model (1.8). The search domain for $\boldsymbol{\xi}$ is a 2D cell $\mathcal{D} = [\theta_1, \theta_2] \times [\mu_1, \mu_2]$, so that X takes 3 parameters as arguments. As in the case of one unknown parameter, T should be borderless along axis α. T can then be viewed as a rectangular cuboid of dimensions 2π, $\Delta\theta$, $\Delta\mu$ where its faces along the phase axis are stuck together, as represented schematically in Figure 3.3.2 and which can only be properly represented in higher dimensions. X is still

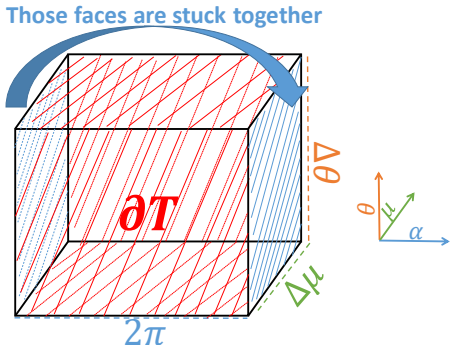

Figure 3.3.2: Two unknown parameters, with T treated as an object of $\mathbb{R}^3$. In this case, T can be viewed as a rectangular cuboid with two opposite faces stuck together.

not isotropic, but the necessary hypotheses are met for the same reasons as the $2D$ case when using the centrosymmetric signal model (2.34) using parametrization $\boldsymbol{\psi} = (\alpha, u, v)$. Let us apply Theorem 3.2.4 to this parameter space:

Heuristic 3.3.1. *The P_{FA}-threshold relationship of the off-grid MF with two unknown parameters is given, for STAP detection (signal model (1.10)) tested on a cell $\mathcal{D} = [\theta_1, \theta_2] \times [\mu_1, \mu_2]$ with steering vectors of size NP is:*

$$P_{FA} = \left[\frac{\pi}{6}\Delta\theta\Delta\mu\sqrt{(N^2-1)(P^2-1)}\left(2w^2-1\right) + \sqrt{\frac{\pi}{3}}\left(\Delta\theta\sqrt{N^2-1}+\Delta\mu\sqrt{P^2-1}\right)w + 1\right] e^{-w^2} + O\left(e^{-c\,w^2}\right) \qquad \text{for some } c > 1, \tag{3.14}$$

Remark 3.3.3. *The result is given as a heuristic because replicating the approach of remark 3.3.2 with this parameter space is much more involved, and we are not entirely satisfied with relying on Adler's informal argument that parameter spaces for periodic processes must be considered without boundaries [Adloo, section 5.2]. However, we have a very high degree of confidence that this holds, and simulations will strengthen this belief.*

As before, σ^2 equals the variance of the terms of $\underline{\mathbf{r}}$ so that $\sigma^2 = 1/2$, and $\boldsymbol{\Lambda} = \frac{1}{2}\mathbf{I}$ so that $\lambda = \frac{1}{2}$. We have $\rho_3(w) = \frac{\exp(-w^2)}{(2\pi)^2}\left(2w^2-1\right)$, $\rho_2(w) = \frac{\exp(-w^2)}{(2\pi)^{3/2}}\sqrt{2}w$, $\rho_1(w) = \frac{\exp(-w^2)}{2\pi}$. After reparametrizing using the usual centrosymmetric parametrization $\boldsymbol{\psi} = (\alpha, v, u)$ of the proof of Lemma 2.3.1, the cuboid has a volume $|T| = \frac{2}{3}\pi^3\sqrt{(N^2-1)(P^2-1)}\Delta\theta\Delta\mu$ and a surface $|\partial T| = 4\pi^2\left(\sqrt{\frac{N^2-1}{3}}\Delta\theta + \sqrt{\frac{P^2-1}{3}}\Delta\mu\right)$. The border $|\partial T|$ is composed of flat surfaces and the curvatures c_{min}, c_{max} equal zero. The angular deficiency between the surfaces that make up the ∂T is $\iota = \pi/2$. $H(\partial T)$ is thus the product of ι with half length of the edges 4π, thus $H(\partial T) = 2\pi^2$. Injecting in (3.11) gives the expected result.

Once again, when $\mathcal{D} = [0,1] \times [0,1]$, only the first term in the bracket remains.

Three terms appear in the developed formula: the first term accounts for the acceptance zone inside the surface of the 2D cell, while the second and third terms are the same as in (3.13). The second term translates what happens at the edge of the cells and is similar to what happens on a 1D cell. The corners of the cell explain the last term that is, once again, identical to the P_{FA} for the on-grid MF given in (1.27).

Note that we could derive the relationships of this section only because X is stationary under white noise. Unfortunately, the same methods cannot be applied to colored noise as is since X is not sta-

tionary anymore. In the next section, we investigate a less precise approximation of the P_{FA}-threshold relationship under contexts where X is not stationary.

3.4 . Leading term approximation for detection under colored noise $(\mathbf{\Gamma} \neq \mathbf{I})$ or using a chirp waveform

Unfortunately, in the case of colored noise or using a chirp waveform for range or range-Doppler detection (using signal models (1.5) or (1.8)), the random field X is not stationary anymore and the theorems that we applied in the previous section do not hold anymore, as the results given by the Kac-Rice counting Theorem are more involved (the Lipschitz-Killing curvatures [ATW07, Section 7.6] of the parameter space appear). However, it is easy to obtain the leading term of the Euler characteristic expansions so we will obtain an approximation of the order $O\left(w^{M-2}e^{-w^2}\right)$. Indeed, formula (4.3.6) of [ATW15, p.130] states that, for any real-valued process X with constant variance σ^2 defined on $\mathbb{R}^M$:

$$E\left[\varphi(A_{w(X)})\right] \approx \frac{\int_T |\det \mathbf{\Lambda}|^{1/2}\, dt}{\sigma^{2M-1}(2\pi)^{(M+1)/2}} w^{M-1}\, e^{-w^2/2\sigma^2}\,. \tag{3.15}$$

Remark 3.4.1. *This leading term approach was taken in [Lei+20] to compute the P_{FA} in the case of MIMO detection, neglecting border effects.*

Remark 3.4.2. *Let us check that under white noise case using signal models* (1.7) *or* (1.10) *for Doppler or STAP detection,* (3.15) *reduces to the terms in respectively w and w^2 in* (3.13) *and* (3.14)*. We use the centrosymmetric parametrization $\boldsymbol{\psi} = (\alpha, v)$ or $\boldsymbol{\psi} = (\alpha, v, u)$ of the proof of Lemma 2.3.1. In our cases, $\sigma^2 = \frac{1}{2}$. For one unknown parameter ($M = 2$), $\mathbf{\Lambda} = \frac{1}{2}\mathbf{I}$, so $|\det \mathbf{\Lambda}|^{1/2} = \frac{1}{2}$. $|T| = 2\pi^2\sqrt{\frac{N^2-1}{3}}(\theta_2 - \theta_1)$. Injecting in* (3.15)*, we can verify that the given approximation of the Euler characteristic reduces $\sqrt{\frac{\pi(N^2-1)}{3}}(\theta_2 - \theta_1)\, w$ (term in w in* (3.13)*. Similarly, for two unknown parameters ($M = 3$), $|T| = 2\frac{\pi^3}{3}\sqrt{(N^2-1)\,(P^2-1)}(\theta_2 - \theta_1)(\mu_2 - \mu_1)$, $|\det \mathbf{\Lambda}|^{1/2} = \left(\frac{1}{2}\right)^{1/2}$: by injecting in* (3.15)*, we verify that it reduces to the term $\frac{\pi}{3}\Delta\theta\Delta\mu\sqrt{(N^2-1)(P^2-1)}w^2$ (term in w^2 in* (3.14)*).*

As can be said earlier, what is interesting is that we can apply this corollary to find the P_{FA}-threshold relationship of the off-grid MF under colored Gaussian noise or using a chirp waveform, even though X is not stationary anymore:

- In the case of colored noise using signal models (1.7) or (1.10), $\mathbf{\Lambda}$ is equal to half the first fundamental form g_{ij} of $\boldsymbol{\gamma}$, and computing the integral in (3.15) is no different than computing the integrals in (2.32) or (2.40). It can be achieved easily thanks to the derivatives of $\boldsymbol{\gamma}$ that are given in Appendix 2.D.2, and can be employed whether $\mathcal{D} = [0, 1]$ or whether $\mathcal{D} \subsetneq [0, 1]$.
- It is interesting to see what this approximation reduces to when using a chirp waveform under white noise (signal model (1.5)). Note that
  - $\frac{\partial \boldsymbol{\gamma}}{\partial \alpha}^T \frac{\partial \boldsymbol{\gamma}}{\partial \alpha} = 1$,
  - $\frac{\partial \boldsymbol{\gamma}}{\partial \alpha}^T \frac{\partial \boldsymbol{\gamma}}{\partial \tau} = (-\sin\alpha\boldsymbol{\gamma}_1(\tau) + \cos\alpha\boldsymbol{\gamma}_2(\tau))^T \left(-\sin\alpha\dot{\boldsymbol{\gamma}_1}(\tau) + \cos\alpha\dot{\boldsymbol{\gamma}_2}(\tau)\right)$,
  - $\frac{\partial \boldsymbol{\gamma}}{\partial \tau}^T \frac{\partial \boldsymbol{\gamma}}{\partial \tau} = \left(-\sin\alpha\dot{\boldsymbol{\gamma}_1}(\tau) + \cos\alpha\dot{\boldsymbol{\gamma}_2}(\tau)\right)^T \left(-\sin\alpha\dot{\boldsymbol{\gamma}_1}(\tau) + \cos\alpha\dot{\boldsymbol{\gamma}_2}(\tau)\right)$.

Since $\dot{\boldsymbol{\gamma}_1}^T \boldsymbol{\gamma}_2 = 0$ and $\|\dot{\boldsymbol{\gamma}_1}\| = \|\dot{\boldsymbol{\gamma}_2}\|$,

$$\begin{aligned} |\det \boldsymbol{\Lambda}|^{1/2} &= \frac{1}{2}\left(\|\dot{\boldsymbol{\gamma}}_1(r)\|^2 - \left(\dot{\boldsymbol{\gamma}}_1(r)^T \boldsymbol{\gamma}_2(r)\right)^2\right)^{1/2}, \\ &= \frac{\pi h}{2B}\sqrt{\frac{K^2-1}{3}}, \end{aligned}$$

where the second equality comes from the computation we made in proof 2.B.2. In the end, the leading term corresponds to the first term in (3.13) for FMCW range detection.

It is, unfortunately, less easy to obtain the next terms of the expansion. Before moving on to the numerical tests of our P_{FA}-threshold relationships, in the next section we provide a small intermede to talk about how the tube method could be applied to the off-grid MF and how it relates to the Euler characteristic.

3.5 . Applying the volume of tubes method to the MF

While using the tube method to find the P_{FA}-threshold relationship of the MF does not appear as naturally as in the case of the NMF, it is still possible to use it to get an approximate of its P_{FA}-threshold relationship. There are deep links between the tube method and the Euler characteristic method [Sun93; Adl00; TK02], and the results given by both methods are equivalent under a lot of settings, even though the original approaches are quite different since the tube method is more focused on the geometry described by manifolds while the Euler characteristic approach consists in considering the parameter space on which the manifolds are defined. This was of course considerably hinted at by the fact that the P_{FA}-threshold relationships obtained in this chapter are very similar to the ones we found in the previous chapter, as an expansion with a leading term depending on the volume of the manifold times plus another term depending on the surface of the borders, plus a final on-grid term.

To begin with, let us see how to apply the tube formula to the matched filter. Consider the MF expression given in (3.2) as $\boldsymbol{\gamma}(\boldsymbol{\xi}, \alpha)^T \mathbf{r}$. When $\mathbf{r}$ follows a Gaussian distribution, there is a false alarm if $\boldsymbol{\gamma}(\boldsymbol{\xi}, \alpha)^T \mathbf{r} > w$. Let us note by $\mathbf{u} = \dfrac{\mathbf{r}}{\|\mathbf{r}\|}$ the normalized version of $\mathbf{r}$. The norm of $\mathbf{r}$ is a random variable that follows a χ squared distribution with two degrees of freedom, and $\mathbf{u}$ is uniformly distributed on the unit $2N$-sphere. The idea is to condition the MF output to the norm of $\mathbf{r}$. This gives, adapting from [Adl00, p.53]:

$$\begin{aligned} P_{FA} &= P\left(\max_{\mathcal{D}\times[0,2\pi]} \boldsymbol{\gamma}(\boldsymbol{\xi}, \alpha)^T \mathbf{r} > w\right) \\ &= \int_{\mathbb{R}^+} P\left(\max_{\mathcal{D}\times[0,2\pi]} \boldsymbol{\gamma}(\boldsymbol{\xi}, \alpha)^T \mathbf{r} > w \middle| \|\mathbf{r}\|\right) f_{\chi_2^2}(\|\mathbf{r}\|)\, d\|\mathbf{r}\| \\ &= \int_{\mathbb{R}^+} P\left(\max_{\mathcal{D}\times[0,2\pi]} \boldsymbol{\gamma}(\boldsymbol{\xi}, \alpha)^T \mathbf{u} > w\,\|\mathbf{r}\|\right) f_{\chi_2^2}(\|\mathbf{r}\|)\, d\|\mathbf{r}\| \\ &= \int_{\mathbb{R}^+} V_{w\|\mathbf{r}\|} f_{\chi_2^2}(\|\mathbf{r}\|)\, d\|\mathbf{r}\|, \end{aligned} \tag{3.16}$$

where $V_{w\|r\|}$ is the volume of the tube of geodesical radius $w\,\|r\|$ around the manifold $\boldsymbol{\gamma}$, defined in (2.8): we once again translated the statistical problem of comparing the maxima of the random field $X(\boldsymbol{\xi}, \alpha)$ to a threshold to a volume of tube geometrical problem. This problem can be solved using the results of Chapter 2, multiplying the relationships (2.32), (2.33), (2.36), (2.40), (2.37) or (2.41) (depending on the context) by the volume of $\mathbb{S}^{2N-1}$ to get the volume of the tube back (the last two relationships being heuristics). Remarkably, since the methods used in Chapter 2 provided relationships for colored noise distributions, it means that this volume of tube approach can be applied to find the P_{FA}-threshold

relationship of the MF for $\mathbf{\Gamma} \neq \mathbf{I}$. Unfortunately, the overlapping issue highlighted in Chapter 2 only enables us to provide an approximation of the P_{FA}, and this is unfortunately true for all thresholds. Indeed, noting w_{lim} the limit threshold for which there is no overlap, and decomposing (3.16) as

$$\int_{\mathbb{R}} V_{w\|\mathbf{r}\|} f_{\chi^2_2}\left(\|\mathbf{r}\|\right)\, d\|\mathbf{r}\| = \int_0^{\frac{w_{\text{lim}}}{w}} V_{w\|\mathbf{r}\|} f_{\chi^2_2}\left(\|\mathbf{r}\|\right)\, d\|\mathbf{r}\| + \int_{\frac{w_{\text{lim}}}{w}}^{\infty} V_{w\|\mathbf{r}\|} f_{\chi^2_2}\left(\|\mathbf{r}\|\right)\, d\|\mathbf{r}\|\,, \tag{3.17}$$

the volumes $V_{w\|\mathbf{r}\|}$ in the first term of the right-hand side of the equation are subject to overlap. The contribution of the overlap in the final result is a priori hard to characterize and is one of the reasons we used the Euler characteristics in this chapter. It reminds us of the terms $O\left(e^{-w^2/2\sigma^2}\right)$ found in our asymptotic relationships.

3.6 . Numerical validation

In order to verify (3.13) (resp. (3.14)), we computed an empirical P_{FA}-threshold relationship with 5×10^7 Monte Carlo draws in the Fourier resolution cell $[0, 1/N]$ (resp. $[0, 1/N] \times [0, 1/P]$), with steering vectors of fixed size $N = 10$ (resp. $N = 8$ and $P = 4$). The results are shown in Figure 3.6.1a (resp. 3.6.1b). In both cases, the relationship seems to be very accurate, except for P_{FA} close to one where there is a noticeable mismatch.

We also compared the relationship that we get from using the formula (3.13) , (3.14) in the case of FMCW range and range-Doppler detection with the empirical P_{FA}-threshold relationship obtained when using a chirp waveform (signal model (1.5)). Remember that we have a strong case for doing so in the case of range detection since Section 3.15 showed that the chirp leading term is the same as the leading term of the FMCW relationship. Results can be observed in Figures 3.6.2a and 3.6.2b. It can be seen that the FMCW relationships seem to be rather reasonable approximations of the chirp relationships.

Finally, in Figures 3.6.3a and 3.6.3b, the P_{FA}-threshold relationship obtained empirically for colored noise using model (1.17) with $\rho = 0.9$ for the covariance matrix $\mathbf{R}$ is compared with the leading term approximation given by formula (3.15) for signal models (1.7) and (1.10). Unfortunately, in this case, the approximation is less precise for the P_{FA}s that are commonly used in radar detection. Furthermore, it is lower than the empirical P_{FA}, while we would prefer upper bounds that limit the risk of false alarms. It is however still close enough to the true relationship, so that it may be good enough in some applications.

Remark 3.6.1. *Those relationships may perhaps be made better for low thresholds using the "non-rigorous" methodology used in [HTW00; HTW01], making use of order statistics.*

3.7 . Synthesis

In this chapter, we derived some asymptotic P_{FA}-threshold relationships for the Matched Filter using signal models (1.7) and (1.10) thanks to expected Euler characteristics of excursion sets. We achieved this by modeling the Matched Filter output as a stationary Gaussian Random Field. We showed that those relationships fit very well with empirical relationships obtained with Monte Carlo draws. For more involved cases where the random fields are not stationary anymore, i.e. when using signal models (1.5) or (1.8) for range or range-Doppler detection, or when the covariance matrix $\mathbf{R}$ is not proportional to identity anymore, we can easily compute the leading term of the approximations. The results obtained are less precise, giving this time a lower bound for the P_{FA}.

Table 3.7.1 sums up the results we have been able to derive on the P_{FA}-thresholds of the off-grid MF. Note that "leading term only" only refers to what we have found during this thesis, and it does not mean that a more precise relationship cannot possibly be found.

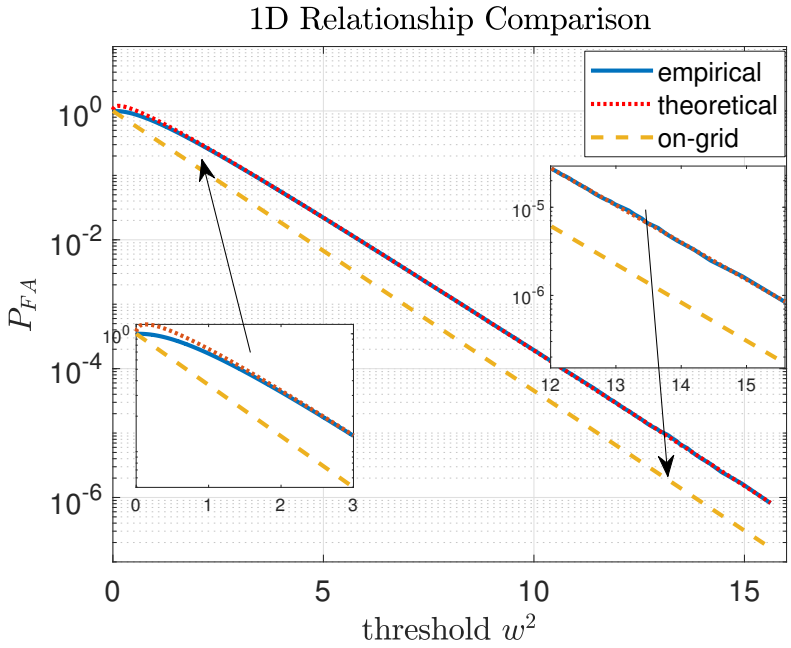

(a) One unknown parameter, signal model (1.7).

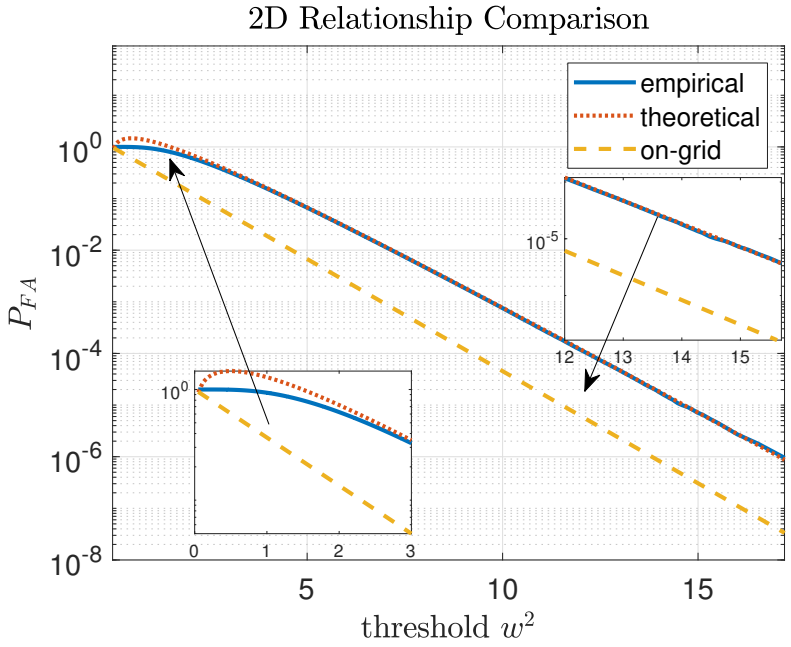

(b) Two unknown parameters, signal model (1.10).

Figure 3.6.1: Theoretical (3.13) (resp. (3.14)) (red) and empirical (blue) relationships obtained under white noise using 5×10^7 Monte Carlo draws with $N = 10$ (resp. $N = 8$ and $P = 4$) in Doppler and STAP contexts (signal models (1.7) and (1.10)). The on-grid relationship (1.21) (yellow) is shown for comparison purposes.

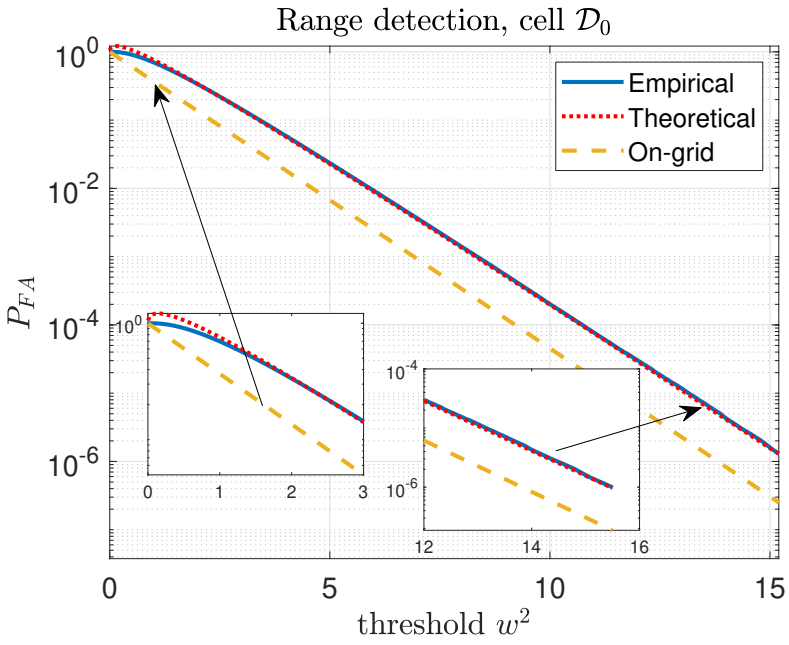

(a) One unknown parameter.

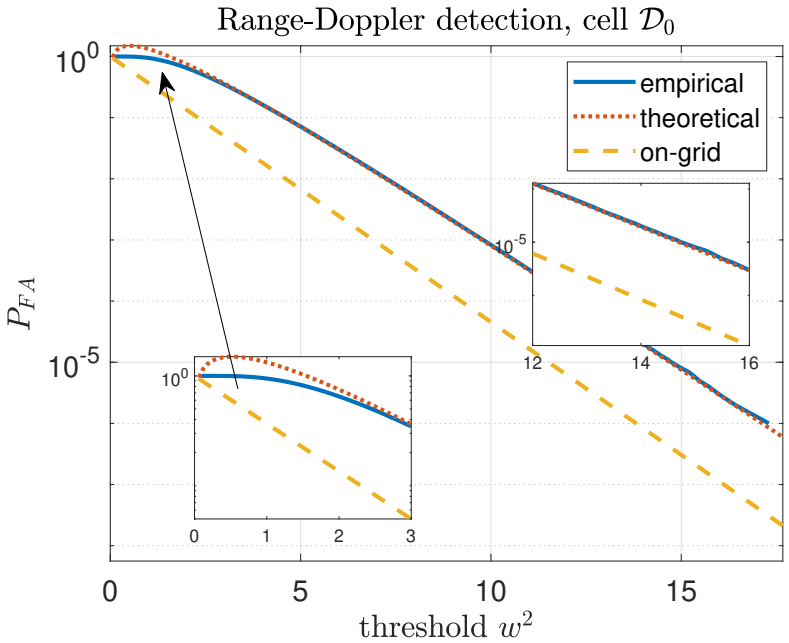

(b) Two unknown parameters.

Figure 3.6.2: Theoretical (3.13) (resp. (3.14)) (red) and empirical (blue) relationships obtained under white noise using 5×10^7 Monte Carlo draws with $K = 40$ (resp. $K = 40$ and $N = 10$) for range and range-Doppler detection using FMCW relationships obtained through (3.13) and (3.14) (signal models (1.7) and (1.10)), compared with empirical relationship obtained using a chirp waveform (signal models (1.5) and (1.8)). The on-grid relationship (1.21) is also drawn (yellow).

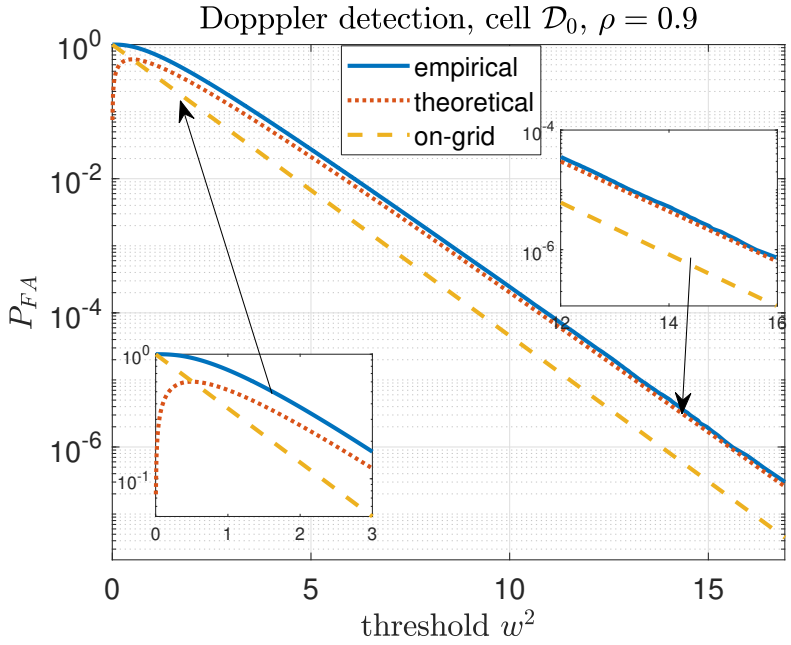

(a) One unknown parameter.

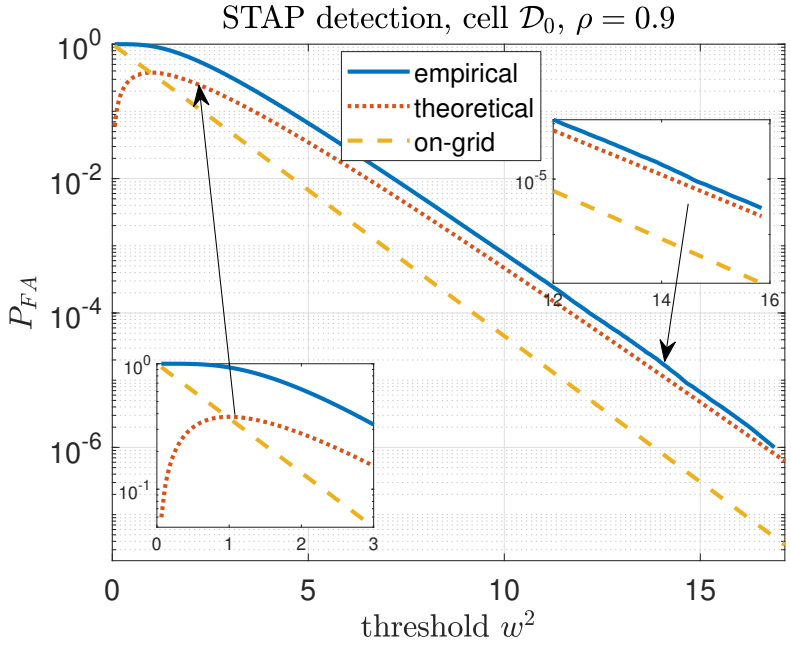

(b) Two unknown parameters.

Figure 3.6.3: Leading term approximations (3.15) (red) and empirical (blue) relationships obtained under colored noise with $\rho = 0.9$ in the covariance matrix model (1.17), using 5×10^7 Monte Carlo draws with $N = 10$ (resp. $N = 8$ and $P = 4$) in Doppler and STAP contexts (signal models (1.7) and (1.10)) The on-grid relationship (1.21) (yellow) is shown for comparison purposes.

	White noise	Colored noise
Doppler (Angle)	Yes (3.13)	Leading term only (3.15)
Range	Leading term only	Leading term only
STAP	Yes (3.14)	Leading term only
Doppler-Range	Leading term only	Leading term only

Table 3.7.1: Recap of the P_{FA}-threshold relationships obtained for the off-grid MF.

In the following chapter, we show how to capitalize on the P_{FA}-threshold relationships that we found in the two previous chapters by developing an efficient approximation of the off-grid GLRT.

4 - Practical aspects of the off-grid GLRT

In the first section, we presented the off-grid GLRTs as a solution to deal with off-grid targets, and in Chapters 2 and 3, we studied the statistics of the off-grid GLRT detectors under the null hypothesis, finding their P_{FA}-threshold relationships. This chapter has a more practical purpose and aims to answer the question of how to implement the GLRT in practice to cope with the presence of off-grid targets. This is done through the use of the tools of joint detection and estimation. The chosen methods are then going to be tested on experimental radar data: the idea will be to showcase the off-grid effects and correct them with an implementation of the GLRT.

Section 4.1 gives the motivation for finding efficient approximations of the GLRT. In Section 4.2, we investigate joint detection and estimation as a framework to approximate the GLRT. We test the detection performance of the chosen methods through simulations in Section 4.3. Finally, in Section 4.4, we implement those detectors on real data from the ONERA HYCAM radar.

Part of the work in Sections 4.2 and 4.3 was presented in the 2021 SSP Workshop [Dev+21].

4.1 . On the need for approximations of the off-grid GLRT

In Section 1.6, we presented the off-grid GLRT as a way to properly detect off-grid targets, but we highlighted the fact that these detectors are not straightforward to implement in practice. Indeed, while the off-grid detectors present the best-known performance for the detection of off-grid targets, in order to implement them perfectly, an infinite number of tests have to be run on a continuum of unknown parameters.

Remark 4.1.1. *In [De +10d], maximizing the test quantity in the off-grid GLRT is shown to be a semi-definite positive convex estimation problem, so that interior point methods can achieve the required precision in polynomial time in N.*

A simple approximation can be obtained with a simple oversampling of the grid with large factors. Formally, for one unknown parameter ξ the test oversampled by a factor of L is written:

$$\Lambda_{i,L}(\xi) = \max_{j\in[1,L]} \Lambda(\xi_j)\,, \quad i \in \{\text{MF,NMF}\}$$

where the L points ξ_j are evenly spaced in the cell centered around ξ. Oversampling the grid by a large factor is what we did, for example, in Section 2.5 and 3.6 to evaluate our P_{FA}-threshold relationships, where we simulated the GLRT detectors by finely oversampling the grid by factors of 30 to 100 (the main lobe can be thinner under colored noise as explained in Subsection 1.5.2 and shown in Figure 1.14a and 1.14b, so that the number of samples needed for a satisfying approximation of the off-grid GLRT varies according to the cell under test and the level of correlation of the noise). This is a valid method to approximate the behavior of the GLRT offline. However, in operational contexts, radars need to process data in real-time, and most of the time, such a costly approximation cannot be performed, and only a low number of samples will be used. Figure 4.1.1 compares the average detection probability (in the sense of (1.35)) of the oversampled MF and NMF for Doppler detection (signal model (1.7)) with $N = 10$ for different oversampling factors in the case of white noise with thresholds set according to Monte Carlo trials. It can be seen that in the case of the MF, even small oversampling factors (x2) are good estimates of the GLRT. However, in the case of the NMF, significant losses in P_D are observed for oversampling factors below 5. In Figure 4.1.2, the same simulations are run with highly correlated noise distribution. In the case of the MF, it can be observed that the oversampling by a factor of 2 is slightly worse than in the

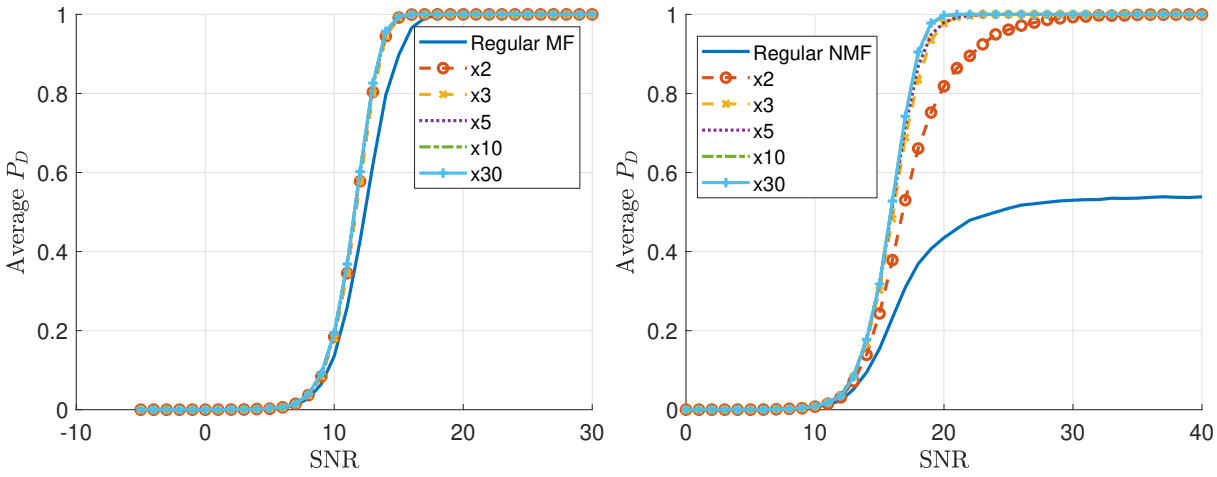

(a) MF (b) NMF

Figure 4.1.1: P_D versus SNR for oversampled MF and NMF, Doppler detection with $N = 10$, white noise, $P_{FA} = 10^{-6}$.

white noise case in order to approximate the off-grid MF, while still being satisfying for most applications. However, the average P_D of the oversampled NMF (factors x2 and x3) severely decreases. In particular, the asymptotic P_D for the NMF oversampled by a factor of 2 decreases below 0.6, and becomes lower than 1 for the x3 oversampling factor!

Remark 4.1.2. *Remember that, in accordance with the Remark 1.5.3, the asymptotic deficiency for the NMF will not be observed for N large enough.*

Remark 4.1.3. *Figure 4.1.4 compares the NMF noiseless response around various frequencies in $\mathcal{D}_0$ (which correspond to the frequencies tested by the NMF oversampled by a factor of 3) for ρ correlation factors of 0.9 and 0.999. As the noise keeps getting more correlated, the NMF response centered at 0 keeps getting thinner: this was shown in Figure 1.14a. As a result, the P_D of the NMF gets lower with the correlation of the noise. However, see that the response of the NMF gets wider at other frequencies in the cell, centered at $\theta_1 = -0.025$ and $\theta_2 = +0.025$. This makes the asymptotic average P_D over cell $\mathcal{D}_0$ of the oversampled detectors increase with ρ after decreasing for a while, as can be seen by comparing Figure 4.1.2 to Figure 4.1.3.*

The bad behavior of the oversampled NMF with a moderate number of samples for the detection of off-grid targets raises the following question: can we find a better approximation of the off-grid NMF running on the same low computational budget as an oversampling by a factor of 2? This is the goal of section 4.2, where we investigate joint detection and estimation to achieve better detection probability of off-grid targets.

Remark 4.1.4. *Since in the rest of this chapter, we will only investigate Doppler detection, the unknown parameter vector $\boldsymbol{\xi}$ is noted θ.*

4.2 . Joint detection and estimation for the approximation of the off-grid GLRT

4.2.1 . Proposed procedure

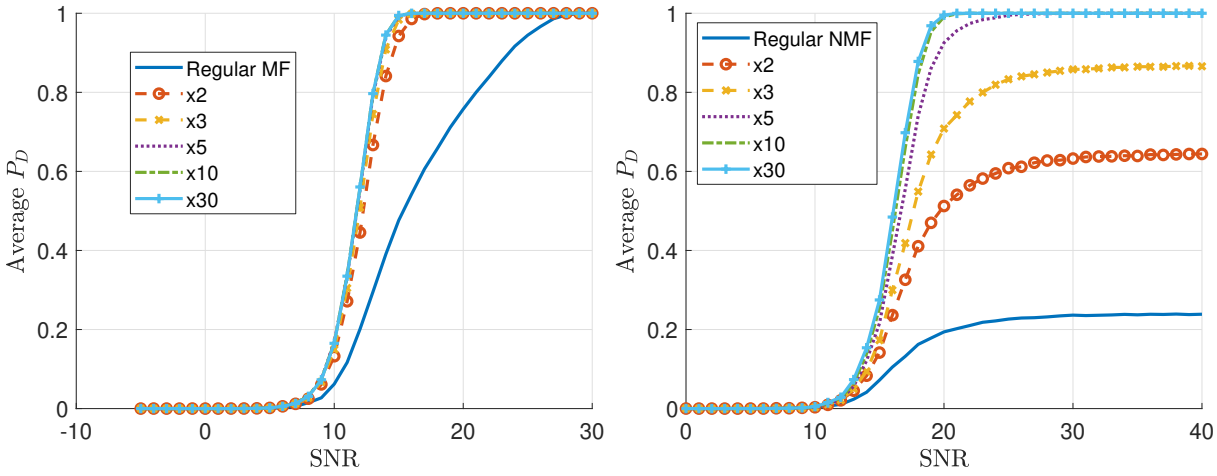

(a) MF (b) NMF

Figure 4.1.2: P_D versus SNR for oversampled MF and NMF, Doppler detection in cell $\mathcal{D}_0$ with $N = 10$, $\rho = 0.9$ in (1.17), $P_{FA} = 10^{-6}$.

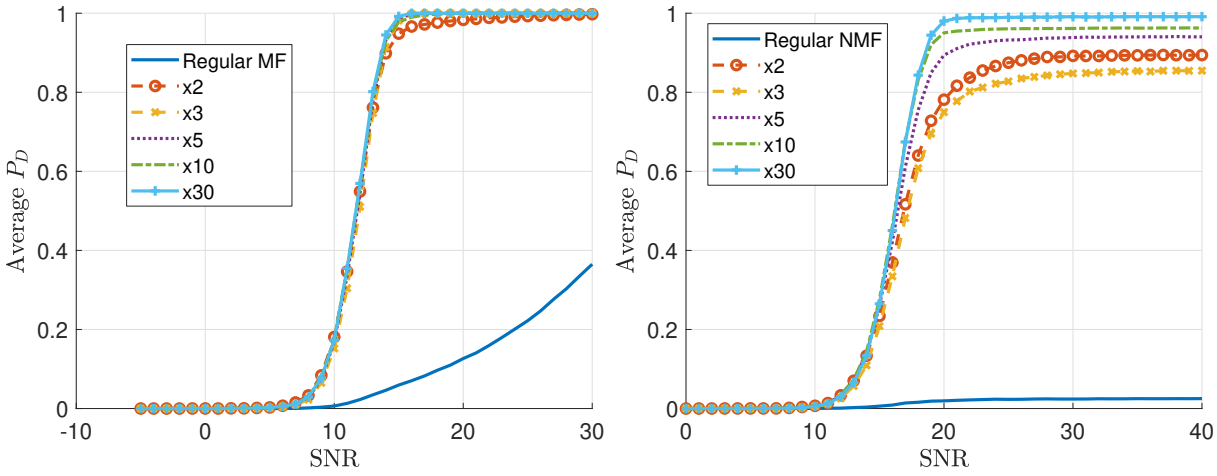

(a) MF (b) NMF

Figure 4.1.3: P_D versus SNR for oversampled MF and NMF, Doppler detection in cell $\mathcal{D}_0$ with $N = 10$, $\rho = 0.999$ in (1.17), $P_{FA} = 10^{-6}$.

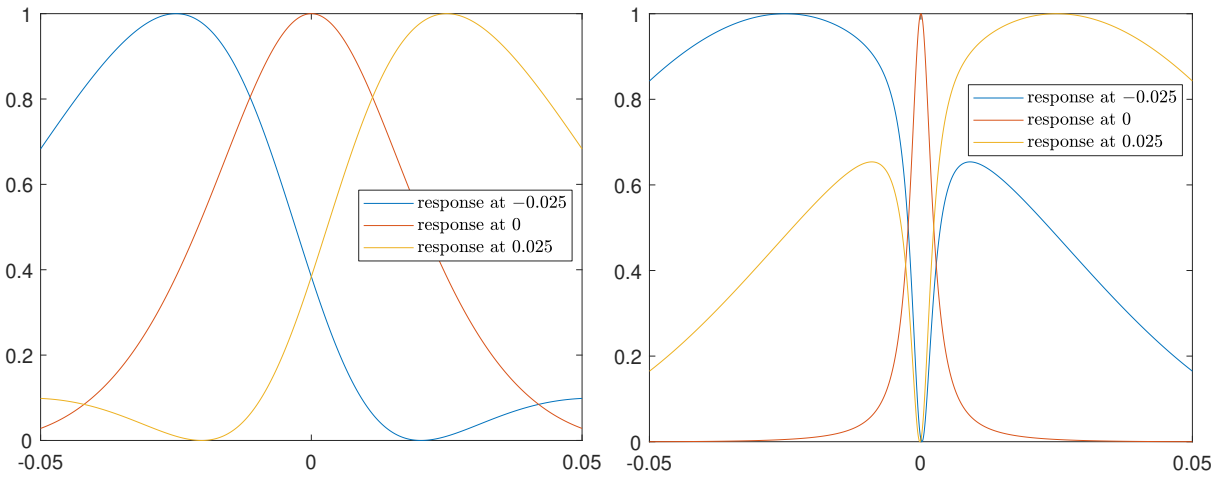

(a) $\rho = 0.9$ (b) $\rho = 0.999$

Figure 4.1.4: NMF response at frequencies $\theta = -0.025$, $\theta = 0$ and $\theta = 0.025$ for increasing noise correlation factors ρ using signal model (1.7) with $N = 10$.

As discussed in Section 1.1, classically, detection is the first step in the radar processing chain. It is then followed by a refined estimation of the target parameters to improve the tracking of the target during the next phase. In this section, we consider an alternative processing chain where the detection and estimation steps are merged into a joint detection and estimation procedure to benefit from the refined estimation of the parameter during the detection phase, in an attempt to reduce off-grid detection probability loss due to the presence of off-grid targets. We focus on the case of the signal model (1.7) so that only one parameter has to be estimated.

Remark 4.2.1. *Detecting on a grid is already a means to perform joint detection and estimation. Indeed, if a target is detected in cell k, with standard Fourier resolution cells of width $1/N$ using N pulses, then a rough estimate of its Doppler shift is the center of the cell i.e. $\hat{\theta} = k/N$.*

The new joint detection and estimation step consists of the following:

- Compute a set of tests on the grid as usual (or, equivalently when using signal model (1.7), compute the FFT of the signal).
- For each cell, compute a correction term $\hat{\delta}_i, i \in [1, N]$ for the possible positions of the target in the cell using this set of tests.
- Inject this correction into a new set of tests at positions $k/N + \hat{\delta}_k$ to try and detect the target.

Remark 4.2.2. *Once again, we stress that in this procedure, the target parameter θ is **systematically** estimated for each cell, regardless of whether a target has been detected before.*

The idea of performing joint detection and estimation to improve the detection performance has already been investigated in [GCL10; Aub+20; Xin+11] as a means to regain some of the SNR lost because of the target parameter uncertainty. In those works, the target power level σ^2 is supposed to be known, while we suppose it to be unknown.

4.2.2 . Estimation techniques for the target parameters

In this section, we investigate common estimation techniques for unknown target parameters. We retain two estimates:

- A collection of popular estimators based on interpolating the main FFT lobe is presented in [JK07], which can be applied for Doppler or angle correction. Their correction term for unwindowed data is given by:

$$\hat{\delta}_{\text{inter}} = -\text{Re}\left(\frac{X_{k+1} - X_{k-1}}{2X_k - X_{k-1} - X_{k+1}}\right), \tag{4.1}$$

where X_k is the output of the FFT tested at position k/N, expressed as:

$$X_k = \mathbf{s}\left(\frac{k}{N}\right)^H \mathbf{r}\,.$$

Interpolating the main FFT lobe to retrieve an estimate of the Doppler shift is mentioned in [Xin+11] to apply a robust detection scheme.

- Another popular estimation method for the steering error in radar systems is given by monopulse techniques [SB11a; Mos69]. Traditionally, those techniques have been developed to get a precise estimation of the target angular location by computing the ratio between the radar *sum* and *difference* channels, which correspond to the sum and the difference of the received signals at different angles. Indeed, without noise, this quantity is approximately proportional to the angle deviation around the mean of both tested positions. It was investigated in a joint detection and estimation scheme in [GCL10]. In this article, the authors compute the GLRT detector when the sum and difference channels are available for angle detection and estimation. Similarly, the authors of [ZWB09] applied an idea related to monopulse to improve the detection rate of multiple unresolved targets. This approach is extended in [OR11] where a GLRT is derived using the information of three adjacent matched filter returns.
The "monopulse-inspired" approximation that we consider thereafter that we presented in [Dev+21] is inspired by the monopulse estimate but is a far cry from it. We use it to estimate the Doppler or Angle deviation of a target. in a steering vector (1.7) by computing the ratio of the difference of two adjacent test points on their sum. We describe our methodology in the following. First, consider the ratio functions of the received signal (one per cell):

$$h_\theta(\mathbf{r}) = \frac{\Lambda_{NMF}(\theta - \frac{\Delta}{2}) - \Lambda_{NMF}(\theta + \frac{\Delta}{2})}{\Lambda_{NMF}(\theta - \frac{\Delta}{2}) + \Lambda_{NMF}(\theta + \frac{\Delta}{2})}\,, \tag{4.2}$$

and the associated functions g_θ (also one per cell):

$$g_\theta(\delta) = h_\theta(\mathbf{s}(\theta_0 + \delta))\,, \tag{4.3}$$

that is designed to give the value of h for a received signal $\mathbf{s}(\theta_0 + \delta)$ with a mismatch δ. If g is one-to-one for values of δ in $[-0.5/N, 0.5/N]$, then we can retrieve the mismatch information δ when injecting $\mathbf{s}(\theta + \delta)$ into the function h. It turns out that g is not always one-to-one for $\mathbf{\Gamma} \neq \mathbf{I}$, as shown in Figure 4.2.1. Hence in the following, we choose not to whiten the received signal in the function h: we simply take

$$h_\theta(\mathbf{r}) = \frac{|X_{\theta-\frac{\Delta}{2}}|^2 - |X_{\theta+\frac{\Delta}{2}}|^2}{|X_{\theta-\frac{\Delta}{2}}|^2 + |X_{\theta+\frac{\Delta}{2}}|^2}\,, \tag{4.4}$$

where $|X_k|$ is the absolute value of the FFT at position k/N. We retrieve the mismatch estimate with:

$$\hat{\delta}_{\text{mono}} = g_\theta^{-1}\left(h_\theta(\mathbf{r})\right)\,.$$

Remark 4.2.3. *Traditionally, the monopulse estimate is computed as*

$$\hat{\delta}_{mono} = C\frac{|X_{\theta-\frac{\Delta}{2}}| - |X_{\theta+\frac{\Delta}{2}}|}{|X_{\theta-\frac{\Delta}{2}}| + |X_{\theta+\frac{\Delta}{2}}|}\,, \tag{4.5}$$

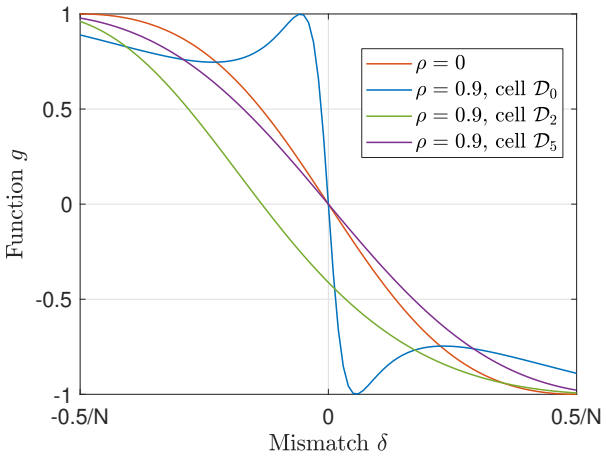

Figure 4.2.1: Functions g in $\mathcal{D}_0$ for matrices $\mathbf{\Gamma}$ generated for different values of ρ in (1.17) at different cells.

where C is a constant: this is based on the assumption that the ratio difference/sum varies linearly with the mismatch δ. From figure 4.2.1, our function g for $\rho = 0$ is also quite linear near 0, but not so much near the edges. We thus propose instead to take one more step and inverse g to get a more precise approximation of δ, with negligible computational cost once g has been tabulated.

Remark 4.2.4. *Those estimates are easily extensible to signal model* (1.10) *(STAP or FMCW detection). Two estimates are obtained for each cell and introduced in the final detection test.*

The two estimates $\hat{\delta}_{\text{inter}}$ and $\hat{\delta}_{\text{mono}}$ present the advantage of being very fast to compute once the FFT samples X_k have been obtained. When computing $\hat{\delta}_{\text{inter}}$ and $\hat{\delta}_{\text{mono}}$, the received signal is not whitened: this may not give the optimal estimation of δ in colored noise context for low SNR, but this is fine: our main goal is to correct the asymptotic P_D deficiency of the NMF, and for high SNR, the noise is going to be negligible compared to the useful component of the signal.

4.2.3 . Used detectors

Following our investigation of estimation techniques for the unknown target parameters, the detectors we consider in the sequel are of the form:

$$\Lambda_{\text{inter}}(\theta) = \frac{\left|\mathbf{s}(\theta+\hat{\delta}_{\text{inter}})^H \mathbf{\Gamma}^{-1}\,\mathbf{r}\right|^2}{\left(\mathbf{s}(\theta+\hat{\delta}_{\text{inter}})^H \mathbf{\Gamma}^{-1}\,\mathbf{s}(\theta+\hat{\delta}_{\text{inter}})\right)\,\left(\mathbf{r}^H \mathbf{\Gamma}^{-1}\,\mathbf{r}\right)} \underset{\text{H}_0}{\overset{\text{H}_1}{\gtrless}} w^2\,, \tag{4.6}$$

and

$$\Lambda_{\text{mono}}(\theta) = \frac{\left|\mathbf{s}(\theta+\hat{\delta}_{\text{mono}})^H \mathbf{\Gamma}^{-1}\,\mathbf{r}\right|^2}{\left(\mathbf{s}(\theta+\hat{\delta}_{\text{mono}})^H \mathbf{\Gamma}^{-1}\,\mathbf{s}(\theta+\hat{\delta}_{\text{mono}})\right)\,\left(\mathbf{r}^H \mathbf{\Gamma}^{-1}\,\mathbf{r}\right)} \underset{\text{H}_0}{\overset{\text{H}_1}{\gtrless}} w^2\,, \tag{4.7}$$

where $\hat{\delta}_{\text{inter}}$ and $\hat{\delta}_{\text{mono}}$ have been introduced in (4.1) and (4.4). They should be used in the context where the power level of the noise σ^2 is unknown (NMF assumption). While the first set of tests used in the estimators are simple FFTs (without whitening the signals), this set of tests should be computed as usual, i.e. whitening and normalizing the received signal.

The thresholds w^2 to be used should be modified compared to the NMF threshold given by (1.27) since the test parameters $\theta + \hat{\delta}_{\text{inter}}$ and $\theta + \hat{\delta}_{\text{mono}}$ depend on the received signal. However, those thresholds are hard to evaluate theoretically since they depend on the non-independent random variables $\mathbf{r}$, $\hat{\delta}_{\text{inter}}$

or $\hat{\delta}_{\text{mono}}$, which is why at first glance they need to be evaluated through Monte Carlo trials. However, we will show later that the P_{FA}-threshold relationships derived in Chapter 2 are good approximates of the P_{FA}-threshold relationships of those detectors.

Finally, let us describe some properties of this approach. First, see that when the SNR tends to infinity, $\mathbf{r}$ is equivalent to $\alpha\mathbf{s}(\theta)$ and our procedure yields the true parameter value i.e. $\hat{\theta} = \theta$. This ensures that the probability of detection tends to 1.

Remark 4.2.5. *In the classical monopulse context, when $\mathbf{\Gamma} = \mathbf{I}$, $\hat{\theta}$ is an approximate MLE [Mos69] and the test is an approximate GLRT. Simulations will show that our procedure is still close to the GLRT even when $\mathbf{\Gamma} \neq \mathbf{I}$.*

Our goal in introducing those detectors was to approximate the GLRT performance with a low computational cost. This objective is met, since:

- Computing the first set of on-grid tests has the same computational cost as a regular NMF test procedure.
- Then, computing the estimates $\hat{\delta}_{\text{inter}}$ or $\hat{\delta}_{\text{mono}}$ using the FFT samples obtained during the first step requires only additions and divisions of scalars and has a negligible computational cost compared with computing the NMF tests. The operation g_θ^{-1} reduces to a simple lookup table operation once the functions g_θ have been tabulated offline.
- Finally, computing the last set of tests that are performed in each cell has once again the same computational cost as a standard NMF test procedure.

In the end, we see that the joint detection and estimation scheme has the same computational cost as oversampling by a factor of 2. We will show in the next section that its detection performance in simulations is considerably better.

Remark 4.2.6. *It would be incorrect to claim that since the estimate $\hat{\delta}$ would be computed anyway during the estimation phase, this procedure does not increase the overall computational cost. Indeed, in the standard radar processing chain, the refined estimates are only computed when a target is detected, while we compute those estimates systematically for each resolution cell, leading to an increasing computational burden.*

4.3 . Numerical Evaluation

The goal of this section is to evaluate numerically the detectors proposed in Section 4.2 through simulations. Since the final objective that we fixed in Section 4.1 is to approximate the off-grid NMF detector for Doppler detection, the emphasis is made on the comparison with this detector. In Subsection 4.3.1, we check if the P_{FA}-threshold relationships of the obtained detectors approach the P_{FA}-threshold relationship computed in Chapter 2. In Subsection 4.3.2, we compare the P_D of the obtained detectors. Since the estimates in the detectors have been designed under the assumption of a white noise scenario, we test their robustness against colored noise distributions.

4.3.1 . Comparison of the P_{FA}-threshold relationships

As mentioned in Subsection 4.2.3, the derivation of the P_{FA}-threshold relationships of the detectors (4.6) and (4.7) are more involved to compute than the P_{FA}-threshold relationship of the NMF since the tested point $\theta_0 + \hat{\delta}$ is depends on the signal under test. See in Figure 4.3.1 that there is a significant gap between the P_{FA}-threshold relationship of the NMF and that of the considered detectors. It would, however, be nice if we could obtain an approximation of those relationships so that the threshold can be set without having to resort to Monte Carlo simulations. Let us thus compare the P_{FA}-threshold relationships of those detectors with the P_{FA}-threshold relationship of the off-grid NMF (2.33) obtained

in chapter 2 under white noise. The corrected test parameter $\theta + \hat{\delta}$ being covered in the $\max_{\theta \in \mathcal{D}}$ of the GLRT, we know that this is necessarily an upper bound so that it can be used without running the risk of increasing the false alarm rate. Furthermore, since the detectors are an approximation of the GLRT, there is a good chance that their P_{FA}-threshold relationship is close to that of the GLRT. This comparison can be seen in Figure 4.3.1 for the case of white noise and strongly colored noise ($\rho = 0.9$ in the model (1.17)). Under white noise, the P_{FA}-threshold relationships of the detectors seem to fit well with the P_{FA}-threshold relationship (2.33) for low enough P_{FA} (recall that for high P_{FA}, the P_{FA}-threshold relationships derived with the volume of tubes method suffer from overlap phenomena so a mismatch was to be expected), although a small difference can be noticed (which seems to be stronger for Λ_{mono}). Under colored noise, this difference increases a bit, especially for high P_{FA}s.

4.3.2 . Comparison of the P_D

In this section, we compare the detection performance of the chosen detectors with detectors of the same range of computational cost: the subspace-based DPSS NSMF mentioned in Subsection 1.5.3 with subspaces of size $M = 2$ (which was the dimension chosen in [RBO16]), and the NMF oversampled by a factor x2, described at the start of this chapter. Target parameters are drawn uniformly in given cells, and the signals are embedded in Gaussian Noise, with covariance matrices generated using the model (1.17). As usual in Radar detection, a given P_{FA} is fixed (here, the P_{FA} is fixed at the low value 10^{-6}). For a precise evaluation of the detectors, thresholds are fixed with Monte Carlo simulation. The mean detection rate is drawn for each SNR value. Results can be seen in Figure 4.3.2 for white noise (recall that in that case, the detection performance does not depend on the tested cell) and in Figure 4.3.3 for highly colored noise ($\rho = 0.9$) in cells $\mathcal{D}_0$ and $\mathcal{D}_5$.

First, let us note that the monopulse-based detector and the interpolation-based one offer very close P_D, with Λ_{mono} offering very slightly better performance across all tested contexts, which indicates more robustness to noise. The performance offered is very close to those of the off-grid NMF: the only significant gap seems to appear in cell $\mathcal{D}_0$ for $\rho = 0.9$, which may be explained by the fact that the covariance matrix $\mathbf{\Gamma}$ is not taken into account in the estimation of δ. As such, the P_D of those detectors tend to 1, which corrects the major flaw of the NMF detector that we were trying to correct, even in the cell $\mathcal{D}_0$ where its competitors, the oversampled NMF by a factor of 2 and the subspace-based DPSS NSMF do not reach an asymptotic P_D of 1. This brings up our third point: the joint detection and estimation strategy seems to always perform better than oversampling by a factor of 2 or approximating the cell structures as subspace. Along with the fact that we dispose of a convenient approximation of the P_{FA}-threshold relationships in the relationships computed in Chapter 2, those detectors look like good candidates to approximate the GLRT detection performance of off-grid targets. In the final part of this chapter, we will study the performance of those detectors when applied on real data.

4.4 . Implementation on real data

4.4.1 . The HYCAM radar dataset

HYCAM [Bro+13] is a demonstration Radar developed by ONERA, which can be seen in Figure 4.4.1. It is located in the Onera Palaiseau center, near Orly airport, as can be seen on the map displayed in Figure 4.4.2. Its main goal is to record raw signals to test novel concepts such as new waveforms or multifunction radar. Our dataset consists of 83 recordings of civil aircraft departing or arriving at Orly airport. Acquisitions have all been performed on the same day. The transmitted waveform is a train of simple chirp pulses (signal model (1.5)) of duration 2 μs, bandwidth $B = 2\,MHz$, with a PRI of $200\,\mu s$. The carrier frequency is $3\,Ghz$. The range resolution is thus 75 m, according to (1.6). The Doppler resolution depends on the number of pulses used: for $N = 10$ pulses, the Doppler resolution given by (1.9) is of

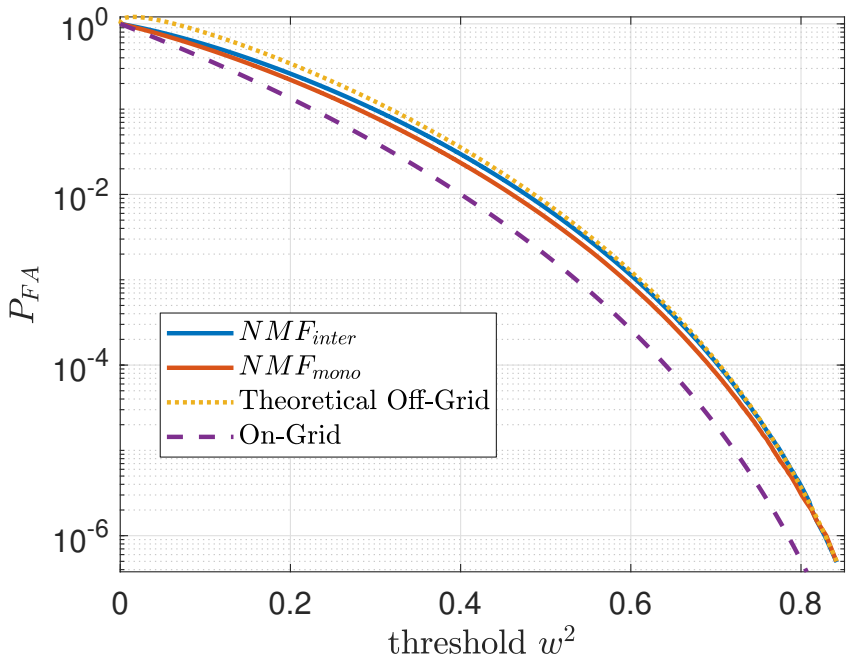

(a) $\rho = 0$

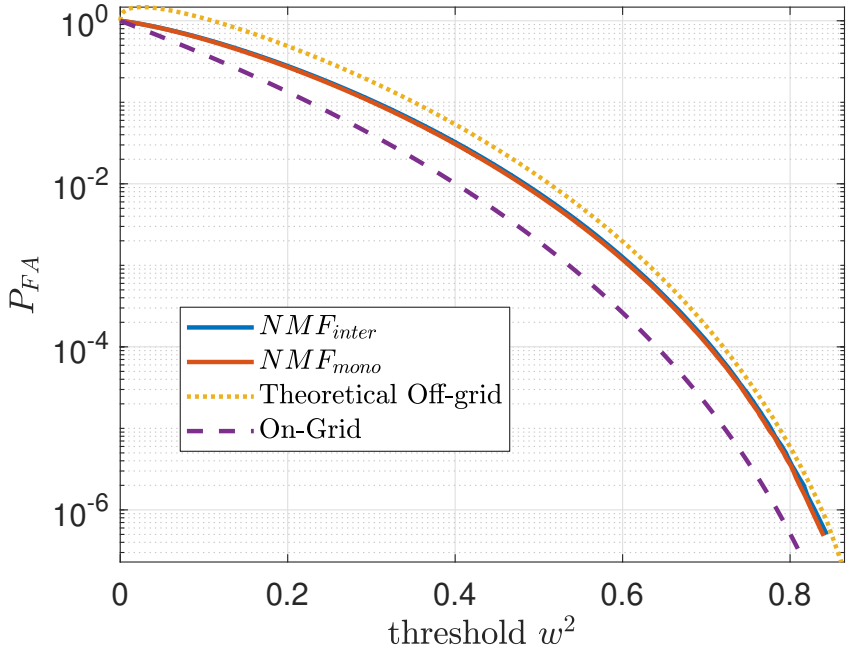

(b) $\rho = 0.9$, cell $\mathcal{D}_0$

Figure 4.3.1: Comparison of the P_{FA}-threshold relationships of (4.6) and (4.7) with the P_{FA} of the off-grid GLRT (2.33) and the P_{FA} of the NMF under Gaussian noise with $N = 10$, in one resolution cell.

$500\,Hz$, meaning the radar can differentiate targets that have at least a difference of $25\,m.s^{-1}$ in radial speed. Each of those recordings corresponds to a collection of bursts of 2500 pulses. For each recording, openly available flight path information enables access to the knowledge of the true target range, and after distance compression, only the 30 range bins closest to the target are kept in the recording.

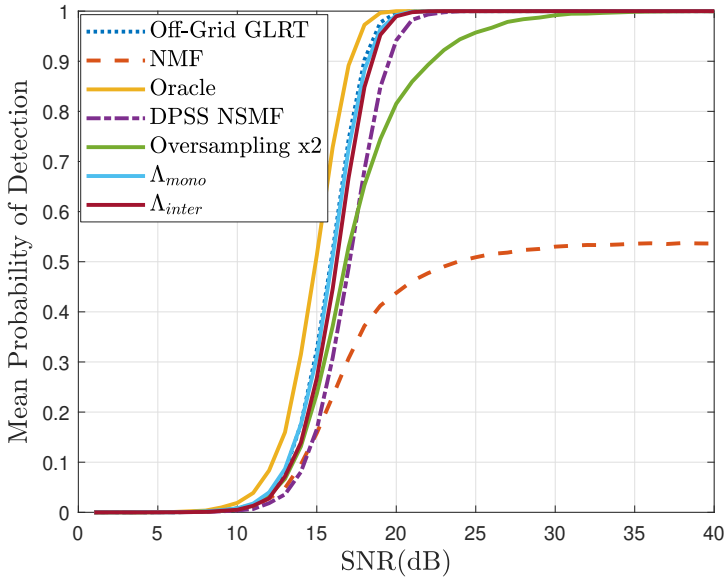

Figure 4.3.2: P_D versus SNR of the detectors Λ_{inter} (4.6), Λ_{mono} (4.7), the DPSS NSMF with subspace size $M = 2$ and the NMF oversampled by a factor of 2, the standard NMF (1.25), the off-grid NMF (1.37), and the oracle detector, with $N = 10$ under white noise and a fixed P_{FA} of 10^{-6}.

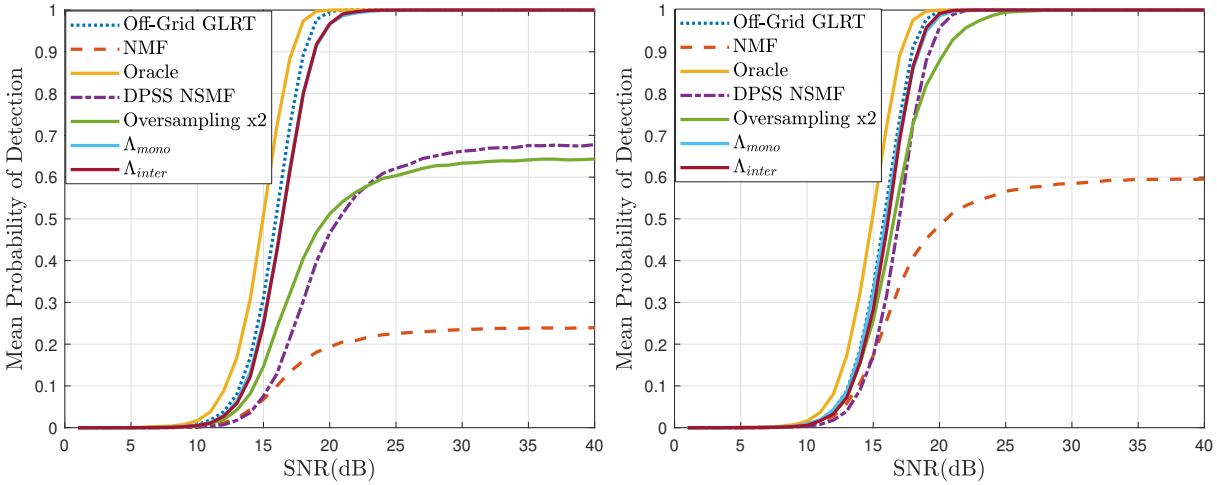

(a) At cell $\mathcal{D}_0$.

(b) At cell $\mathcal{D}_5$.

Figure 4.3.3: P_D versus SNR of the detectors Λ_{inter} (4.6), Λ_{mono} (4.7), the DPSS NSMF with subspace size $M = 2$ and the NMF oversampled by a factor of 2, the standard NMF (1.25), the off-grid NMF (1.37), and the oracle detector, with $N = 10$ with $\rho = 0.9$ (1.17) and a fixed P_{FA} of 10^{-6}.

Figure 4.4.1: Picture of the HYCAM Radar, taken from [Cat+13].

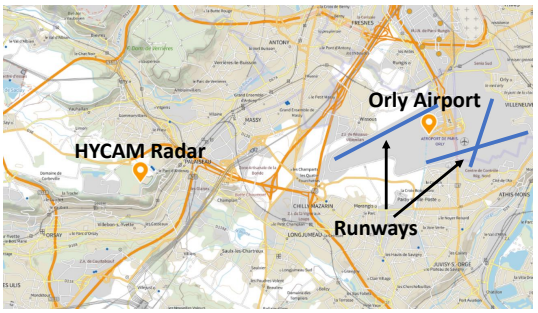

Figure 4.4.2: Position of HYCAM relative to Orly airport.

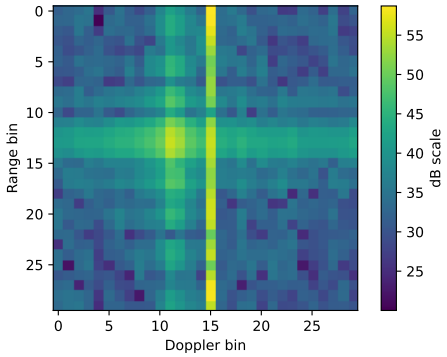

(a) With clutter.

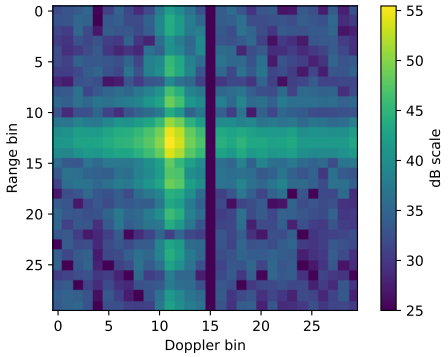

(b) With mean removed.

Figure 4.4.3: Doppler-Range map obtained by performing a Fast Fourier Transform on $N = 30$ pulses, keeping 30 range bins that are the closest to the target.

Remark 4.4.1. *Neglecting steering mistakes that can happen at the start and the end of an acquisition, a target should always be present in our data. However, for some recordings, there was a mistake in the target information so the direction in which the radar looked contained no target. For these recordings, data consists of noise and clutter only.*

Computing the Fast Fourier Transform along the Doppler axis yields a Doppler-Range map as can be observed in Figure 4.4.3a. In all the acquisitions, a ray can be seen at zero Doppler. This is due to stationary clutter returns, and it has to be filtered out by removing the mean of each range bin over each pulse. The resulting map can be seen in Figure 4.4.3b. After this operation, we can reasonably assume the noise to follow a white Gaussian distribution.

4.4.2 . Highlighting the off-grid effects on the probability of detection of the NMF

Before implementing the detector studied in this chapter, let us verify that the presence of off-grid targets degrades the probability of detection of the Normalized Matched Filter. Indeed, according to Subsection 1.5.2, the presence of off-grid targets should degrade the Normalized Matched Filter detection probability so that it does not converge to 1 with the SNR.

In order to showcase this effect, we will compare the NMF detection rate with that of the off-grid NMF. Indeed, the SNR of the target is the same in both cases, but the target should be detected more often by the off-grid NMF. To do this, we will need to implement the off-grid NMF. Since we do not have any

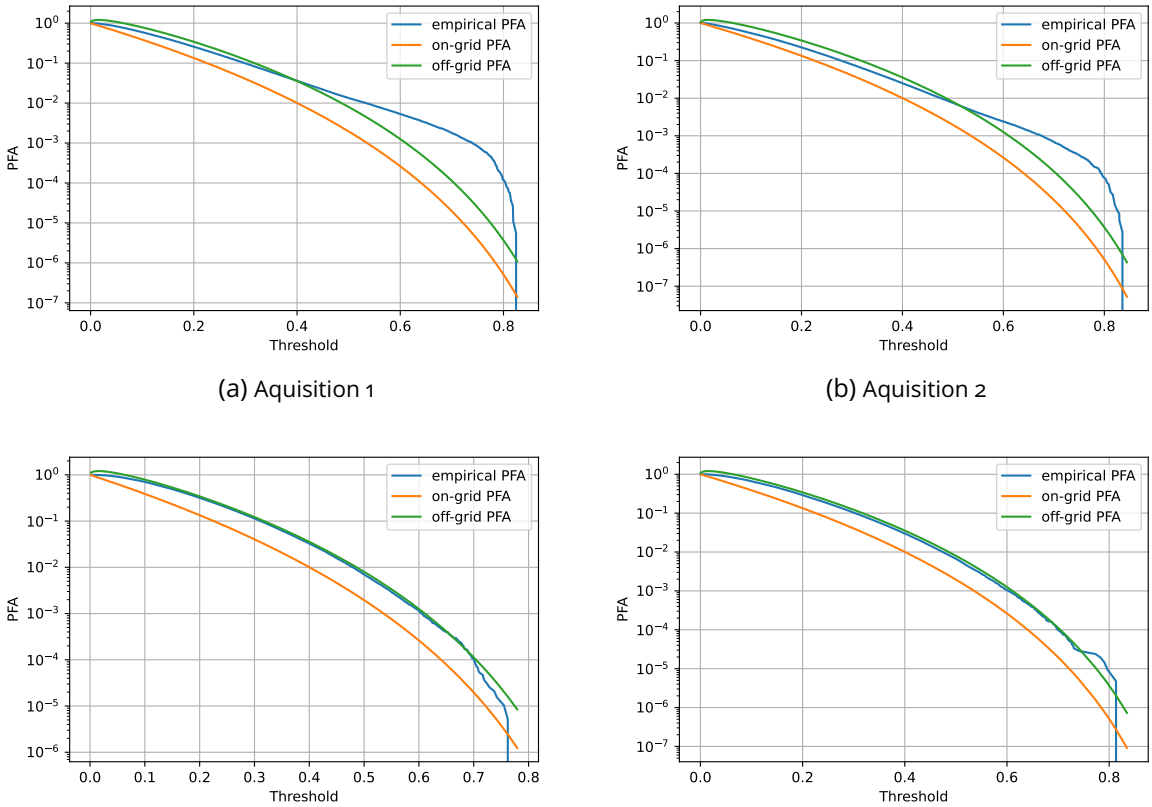

(a) Aquisition 1

(b) Aquisition 2

(c) Aquisition 3

(d) Aquisition 4

Figure 4.4.4: Comparison of the empirical P_{FA}-threshold relationships obtained empirically in the HYCAM recordings with the off-grid relationship computed in (2.33) and the on-grid relationship (1.27), using $N = 10$ pulses. In the selected data samples of both upper figures, the theoretical relationships do not fit well with the empirical P_{FA}s, while it does for the selected lower figures.

computational cost requirement, we will simply approximate it by zero-padding the FFT, oversampling by a factor of 30. We also need to set the threshold: for that purpose, we want to see if the P_{FA}-threshold relationship (2.33) for Doppler detection under white noise derived in Chapter 2 fits with the empirical distribution that can be observed on the real radar data. The results of this experiment can be seen in Figure 4.4.4, where each subfigure corresponds to the comparison of the P_{FA}-threshold relationship for a given target recording, processing the data 10 pulses per 10 pulses. To compute the empirical P_{FA}, we use off-grid NMF samples that are not in the Doppler cell where the target was detected nor in the adjacent cells, and we exclude the zero-Doppler cell where the clutter has been removed. Overall, the results are mixed: on the one hand, for part of the recordings (down), the relationship fits very well with what can be observed, but on the other hand, for some recordings (up), the relationship does not fit at all. In fact, the recordings for which the relationship fits well correspond to recordings where no target is present. We can presume that the noise plus clutter samples that are used for the data in which a target is present are contaminated by secondary lobes created by the target and thus do not follow a white Gaussian distribution. In any case, those results are still good enough for us to validate our results from Chapter 2 and prove the practical interest of the developed relationships. They can also be used to discriminate a scene where no target is present from a scene contaminated by a target, which is what we look to achieve here.

Now that we know how to fix the P_{FA}, we are interested in comparing the probability of detection of the NMF and the off-grid NMF. Figure 4.4.5 represents scatter plots of the detection rate of those detectors versus the SNR, which are computed over windows of $W = 15$ consecutive bursts of 10 pulses. When the target parameters are approximately constant over W consecutive scenes (this is the case for low values of W, including the value of 15 we chose), averaging the detection rate over W scenes enables us to get a reliable estimate of the P_D of the detectors for those target parameters and this SNR. The SNR is here empirically defined as the log of the average of the max of the oversampled Fourier transform (which most likely corresponds to the target) in each of the 15 scenes, divided by the average of the Fourier transform elsewhere in the scenes. Formally, noting FFT^i the oversampled Fourier transform in recording i, and $\boldsymbol{\xi}_M^i = \arg\max_{\boldsymbol{\xi}\in\mathcal{G}_O} FFT^i(\boldsymbol{\xi})$ the parameters where the maximum of the Fourier transform is attained for each recording, noting $\mathcal{G}_O$ the oversampled grid over which the FFT is computed and noting θ the Doppler component of $\boldsymbol{\xi}$:

$$SNR_{\text{empirical}} = 10\,\log_{10}\left(\frac{\displaystyle\sum_{i=1}^{W} FFT^i(\boldsymbol{\xi_M^i})}{\displaystyle\sum_{i=1}^{W}\sum_{\boldsymbol{\xi}\in\mathcal{G}_O,|\theta-\theta_M^i|>1/N,|\theta|>1/N} FFT^i(\boldsymbol{\xi})/N_i}\right),$$

where N_i is the number of points in the sum ranging on $\boldsymbol{\xi} \in \mathcal{G}_O, |\theta - \theta_M^i| > 1/N$. The off-grid phenomenon is highlighted by the fact that when the SNR is large enough, the detection rate of the off-grid GLRT is always 1, but this is not the case for the standard NMF: indeed, remark that in both plots there are points at high target SNR (> 25) for which the target is never detected by the NMF. Thus, for some target parameters, the NMF exhibits a probability of detection of 1 at high SNR , but for some parameters, its probability of detection is 0 or somewhere between 0 and 1. The off-grid deficiency of the NMF is further illustrated in Figure 4.4.6 which shows some NMF GLRT and NMF Doppler profiles separated by 0.5s each, computed at the true range of the target. The target starts off-grid, with a Doppler shift almost exactly between $\theta = 3/N$ and $\theta = 4/N$. The target is seen by the NMF GLRT, but not the NMF. Over time, the target Doppler gets closer to $\theta = 4/N$. At this point, it is detected both by the NMF GLRT and the NMF.

4.4.3 . Empirical performance of the detectors

In the previous section, we confirmed that the on-grid NMF used on the HYCAM radar dataset suffers from a loss in detection performance compared with the off-grid GLRT, as we predicted in Subsection 1.5.2. Our goal in this section is to implement the detectors Λ_{mono}, Λ_{inter} considered earlier in the chapter and confront them to the NMF oversampled by a factor of 2. Following the results of subsection 4.3.1 as well as our findings on the P_{FA}-threshold of the GLRT on empirical data in the previous section, the thresholds fixed for the Λ_{inter} and Λ_{mono} detectors are those found using (2.33), which may be considered as a precise upper bound. For full fairness of the comparison, the threshold for the NMF oversampled by a factor of 2 is fixed using Monte Carlo simulations, (we do not take the threshold for the off-grid GLRT, which is a bit higher). The detection performance of the detectors is evaluated in the same way as in the previous section, through SNR versus detection rate scatter plot. The results on selected acquisitions (the same as for Figure 4.4.5) can be seen in Figure 4.4.7. The results observed in Figure 4.3.2 corroborate what could be seen in simulations: for all tested SNR, both Λ_{inter} and Λ_{mono} perform considerably better than just oversampling the NMF tests by a factor of 2, consistently over all tested acquisitions. This suggests that those detectors are robust to practical conditions. Both tested detectors present similar performance on average.

To follow up this study, it would be interesting to extend the comparison of Λ_{inter}, Λ_{mono} and the

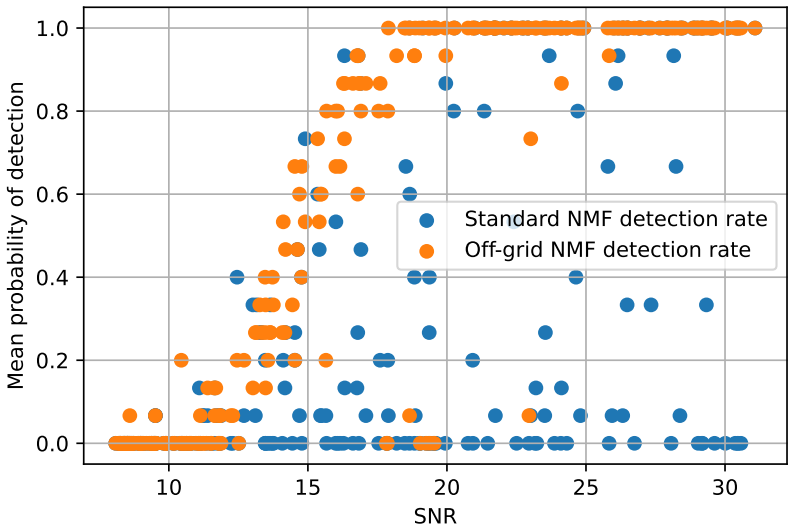

(a) Aquisition 1

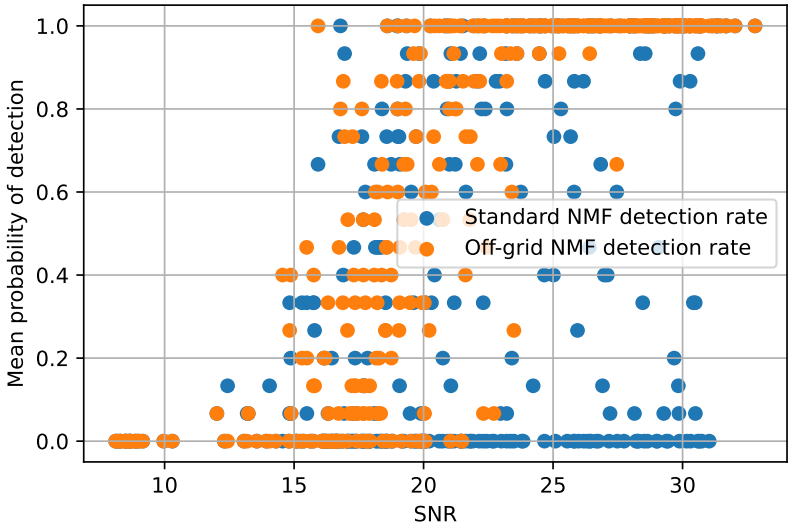

(b) Aquisition 2

Figure 4.4.5: P_D versus SNR of the standard NMF (1.25) and the off-grid NMF (1.37) computed on windows of 15 consecutive sets of bursts of $N = 10$ pulses, for a fixed P_{FA} of 10^{-6} on selected recordings from the HYCAM database.

oversampled NMF on real data in correlated noise contexts where the oversampled NMF detection rate does not converge to 1.

4.5 . Synthesis

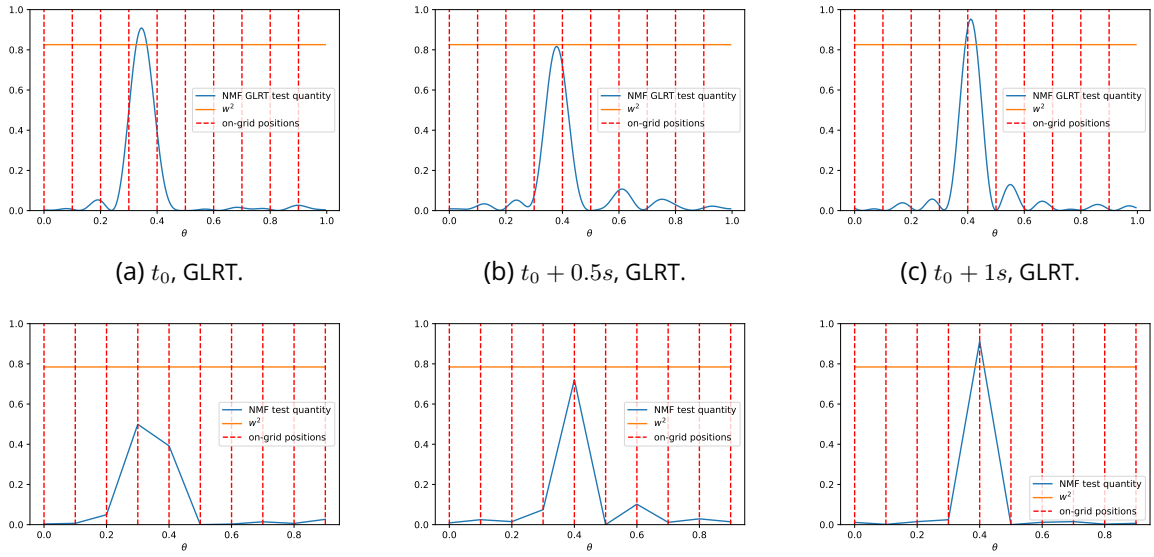

(a) t_0, GLRT. (b) $t_0 + 0.5s$, GLRT. (c) $t_0 + 1s$, GLRT.

(d) t_0, NMF. (e) $t_0 + 0.5s$, NMF. (f) $t_0 + 1s$, NMF.

Figure 4.4.6: Evolution of NMF GLRT (up) and NMF (down) test quantity over time. Doppler profiles are computed using $N = 10$ pulses, at the range bin of the target. The acquisitions are separated by 0.5s.

In this chapter, we have first been interested in investigating the joint detection and estimation literature as a way to approximate the off-grid GLRT. We proposed two estimates to inject in the NMF detection test, based on interpolation and a "monopulse-inspired" technique. Numerical simulations show that those detectors perform well against white noise, better than the simple solution based on oversampling the GLRT. Besides, the theoretical P_{FA}-threshold relationship of the NMF GLRT derived in Chapter 2 is a close upper bound for the P_{FA}-threshold relationships of those detectors.

In the second part of this chapter, we aim to test those detectors against real data from ONERA's HYCAM radar. We show, using noise-only acquisitions, that the P_{FA}-threshold relationships derived in Chapter 2 are verified for scenes without targets, and that, as predicted, the NMF does not perform well against real, off-grid targets: its P_D does not converge to 1 with the SNR. Then, we observe that both detectors introduced perform well in simulations, reaching a detection rate of 1 with SNR and performing considerably better than oversampling the NMF by a factor of 2.

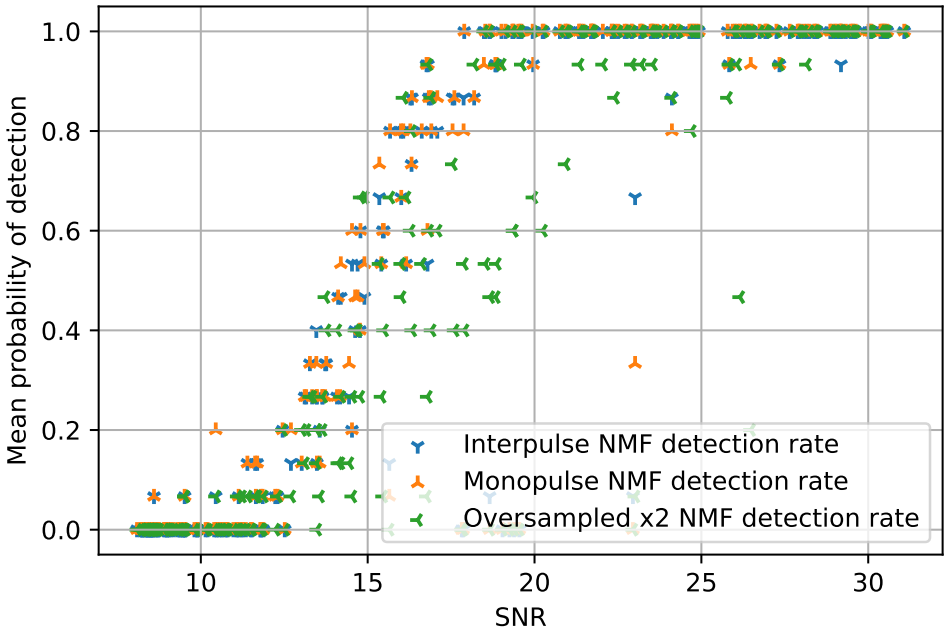

(a) Aquisition 1

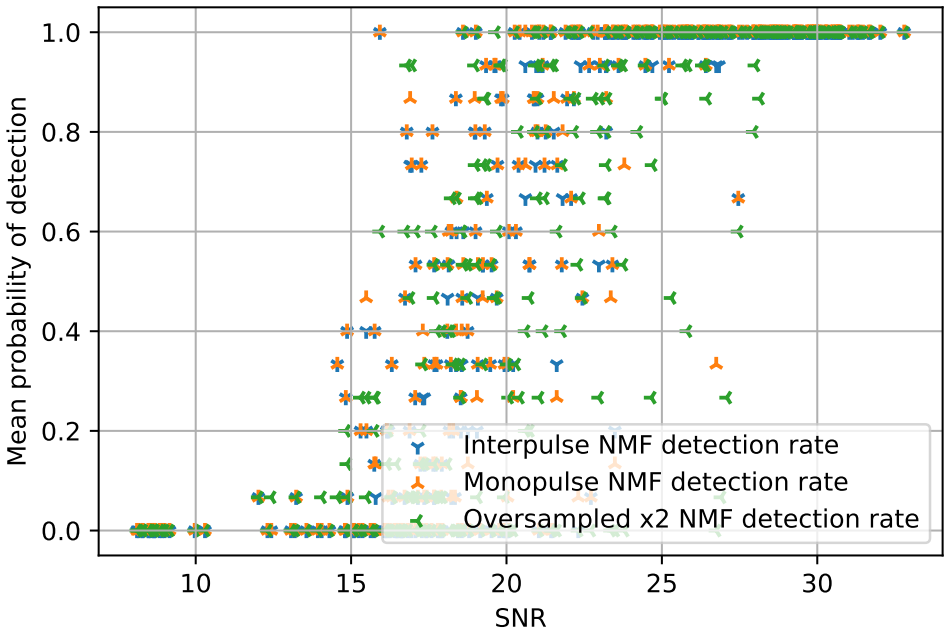

(b) Aquisition 2

Figure 4.4.7: P_D versus SNR of Λ_{inter} (4.6), (4.7) and the NMF oversampled by a factor of 2, computed on windows of 15 consecutive sets of bursts of $N = 10$ pulses, for a fixed P_{FA} of 10^{-6} on selected recordings from the HYCAM database.

5 - Conclusion and perspectives

Conclusion

During this thesis, we worked on the off-grid GLRTs, the standard GLRTs used in the detection literature but tested continuously over the whole parameter space. We focused on the off-grid Normalized Matched Filter and the off-grid Matched Filter. While conceptually simple, no analytical forms exist for those detectors, making their theoretical analysis and efficient implementation hard to achieve.

Our major focus was the search of P_{FA}-threshold relationships for those detectors. We achieved that goal thanks to the use of non-standard tools in the detection community, based on the volume of tubes and the expected Euler characteristic of excursion sets, two approaches that seem very different at first but are actually closely linked. We hope that our presentation of those tools gave the interested reader a glimpse of how powerful they are for dealing with continuous statistical problems. P_{FA}-threshold relationships are proposed for one or two unknown parameters for the off-grid NMF and the off-grid MF. They are only exact for low enough P_{FA} (or equivalently, high threshold w^2 values) in the case of the off-grid NMF, which is derived, and asymptotic in the threshold w in the case of the off-grid MF. Simulations validate our results as the found theoretical relationships fit perfectly with what is observed empirically through Monte Carlo simulations.

Noting that the performance offered by a simple oversampling of the signal was not always satisfying, our other contribution was to find how to approximate the off-grid NMF at a low computational cost, thanks to tools from the joint detection and estimation procedure. The obtained detectors are based on an interpolation of the main Fourier transform lobe and on a monopulse-inspired technique. They present theoretical performance close to that of the off-grid GLRT, and their P_{FA}-threshold relationships are well approximated by those found earlier in the manuscript. Tests on experimental data from HYCAM radar enable us to highlight the effects of off-grid targets on the P_D of the NMF and validate the P_{FA}-threshold relationships found in the manuscript. The proposed detectors are then tested against these experimental data, and they exhibit good detection performance, outperforming a simple oversampling of the NMF by a factor of 2.

Some avenues for future research are highlighted in the next section to expand the results of this thesis.

Perspectives

The case of adaptive detection

In this thesis, we focused on the non-adaptive case, i.e. we supposed that the covariance matrices of the noise plus clutter distribution we were dealing with were known, up to a scale factor in the case of the NMF. But in practice, the covariance matrix will have to be estimated from the data: this is the adaptive problem, explained in Subsection 1.3.3. The adaptive detectors also suffer from an off-grid mismatch of the target parameter, as can be seen in Figure 5.0.1a in the case of Kelly's detector (1.28) and in Figure 5.0.1b in the case of the ANMF (1.29) [BRO20].

To fight against this off-grid mismatch, the adaptive off-grid GLRT can naturally be defined as:

$$\Lambda_{\text{Kelly-GLRT}} = \max_{\boldsymbol{\xi}\in\mathcal{D}} \frac{\left|\mathbf{s}(\boldsymbol{\xi})^H \hat{\mathbf{R}}^{-1}\,\mathbf{r}\right|^2}{\left(\mathbf{s}(\boldsymbol{\xi})^H \hat{\mathbf{R}}^{-1}\,\mathbf{s}(\boldsymbol{\xi})\right)\left(1+\frac{1}{S}\mathbf{r}^H \hat{\mathbf{R}}^{-1}\,\mathbf{r}\right)} \underset{\mathrm{H}_0}{\overset{\mathrm{H}_1}{\gtrless}} w^2\,.$$

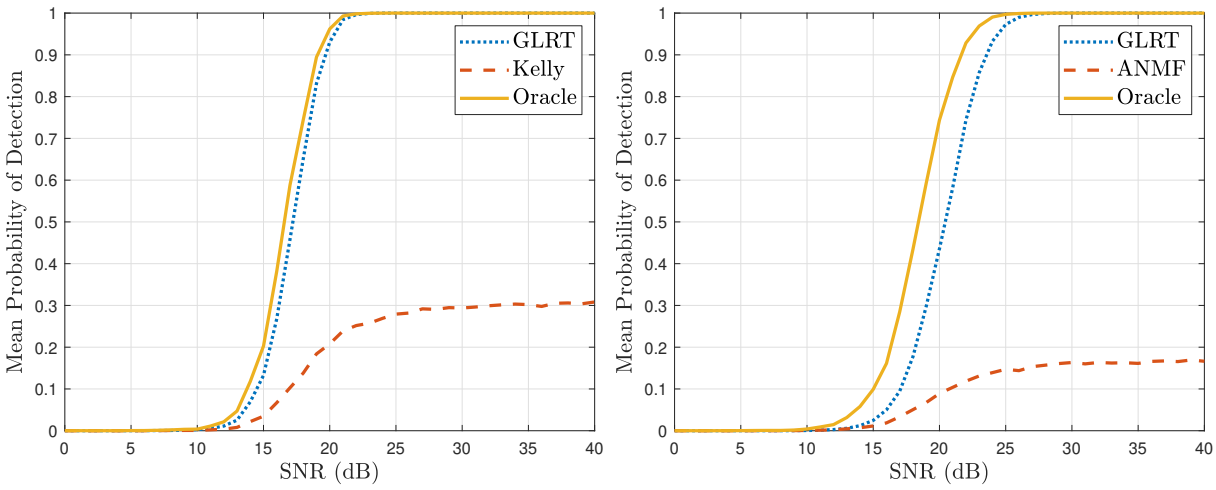

(a) Kelly's detector.

(b) ANMF.

Figure 5.0.1: Comparison of the average P_D over a cell of Kelly's detector and the ANMF for Doppler detection (signal model (1.7)). The oracle detector knows the true position of the target, but not the true covariance matrix. The SNR is again fixed as the maximum achievable SNR when $\mathbf{R}$ and the position of the target θ are known i.e. $SNR = |\alpha|^2 \mathbf{s}(\theta)\mathbf{R}^{-1}\mathbf{s}(\theta)$. $N = 10$ pulses, $S = 20$ training samples in cell $\mathcal{D}_0$, using covariance matrix model (1.17) with $\rho = 0.9$. $P_{FA} = 10^{-6}$, with thresholds set through Monte Carlo simulations.

in the case of homogeneous noise power level, and

$$\Lambda_{\text{ANMF-GLRT}} = \max_{\boldsymbol{\xi}\in\mathcal{D}} \frac{\left|\mathbf{s}(\boldsymbol{\xi})^H \hat{\mathbf{R}}^{-1}\,\mathbf{r}\right|^2}{\left(\mathbf{s}(\boldsymbol{\xi})^H \hat{\mathbf{R}}^{-1}\,\mathbf{s}(\boldsymbol{\xi})\right)\left(\mathbf{r}^H \hat{\mathbf{R}}^{-1}\,\mathbf{r}\right)} \underset{\text{H}_0}{\overset{\text{H}_1}{\gtrless}} w^2 .$$

in the case where the power level of the noise differs from the training data. As can be seen in Figure 5.0.1, the oracle P_D is largely recovered when using the GLRT tests, even when accounting for the increased threshold.

An interesting extension of the thesis work could be to extend the developed P_{FA}-threshold relationships to those detectors. However, this case seems much more involved. Consider the $\Lambda_{\text{ANMF-GLRT}}$ detector, for example. Since $\hat{\mathbf{R}}$ is mismatched w.r.t. $\mathbf{R}$, the vector $\hat{\mathbf{R}}^{-1/2}\mathbf{r}$ is not properly whitened and does not follow a white Gaussian distribution. As a result, it is not uniformly distributed over the unit sphere, making it impossible to replicate the geometrical tube approach taken in Chapter 2 without adjustments. An early intuition could be to look at the volume of inhomogeneous tubes [KTT22], whose radius depends on the tested point on the manifold: the radius of the tube could be expanded around areas where the noise is concentrated.

Remark 5.0.1. *Note that the search for the P_D of the off-grid GLRTs could also perhaps be achieved using those tools.*

P_{FA}-threshold relationships for the oversampled detectors

While we found satisfying P_{FA}-threshold relationships for the off-grid GLRTs, which are continuous maximums, the case of the oversampled detectors is surprisingly considerably harder to treat. Consider the case of one of the detectors (MF or NMF) oversampled on L points. Clearly enough, the P_{FA}-threshold relationships derived in this thesis give some upper bounds. Another bound that is easy to

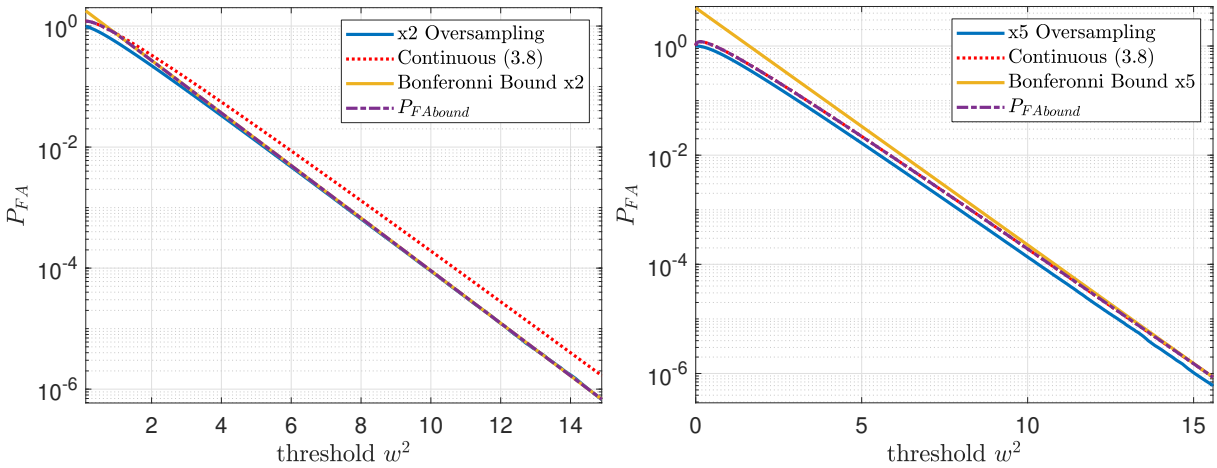

(a) Oversampling by a factor of 2.

(b) Oversampling by a factor of 5.

Figure 5.0.2: Comparison of the empirical P_{FA}-threshold relationships obtained empirically oversampling the MF test with the Bonferroni bounds (5.1), the continuous relationship (3.13) and the min of those two relationships, using signal model (1.7) with $N = 10$ under white noise.

derive is the Bonferonni bound, obtained as [TWG07]:

$$P_{FAbon} = LP_{FA}, \tag{5.1}$$

where the P_{FA} referred to is the on-grid P_{FA} ((1.21) or (1.27)). Which bound is better depends on the roughness of the underlying random field, the Bonferroni bound being better when the tested points are approximately independent. Taking the minimum of both P_{FA}-threshold relationships yields a better upper bound $P_{FAbound}$. A comparison between the Bonferonni bound, the continuous P_{FA}-threshold relationship (3.13) and the empirical P_{FA}-threshold relationship of the MF oversampled with factors 2 and 5 can be seen on Figure 5.0.2. While the Bonferonni bound is precise for $L = 2$, it gets worse for an oversampling factor $L = 5$. An idea for future research could be to improve this bound, possibly starting by investigating the methods given in [TWG07], which aim to combine both bounds to give a more precise relationship.

6 - Résumé en Français

Depuis le milieu du 20ème siècle, les systèmes radar sont largement utilisés dans des contextes civils et militaires pour la détection et le pistage de cibles. Leur principe est bien connu: ils émettent une onde vers une scène et, si une cible est présente dans la scène, le signal revient vers le radar par effet écho. La cible sera alors détectée par le radar, qui peut poursuivre par l'estimation des paramètres de la cible et son pistage.

L'utilisation de méthodes de traitement du signal est nécessaire pour convertir ce principe physique en un système utilisable en pratique. La théorie de la détection est utilisée dans la première étape de la chaîne de traitement radar. Elle vient fournir des tests de détection, qui sont utilisés pour séparer des échos d'un cible d'un bruit ambiant ou renvoyé par des éléments fixes de la scène, tout en limitant une probabilité de fausse alarme via le choix d'un seuil adapté. La procédure la plus courante, dite du Rapport de Vraisemblance généralisé (TRVG) consiste à remplacer les paramètres inconnus du signal attendu par leur maximum de vraisemblance (MV) dans le rapport de vraisemblance. Cependant, il n'existe pas toujours de forme analytique pour le MV de paramètres inconnus: c'est notamment le cas pour la distance des cibles au Radar, leur décalage Doppler, ainsi que l'angle qu'elles forment avec un réseau de capteur. Dans ce cas, la solution classique consiste à discrétiser l'espace de recherche des paramètre en une grille fixe, de telle manière à avoir des tests statistiquement indépendants, pour pouvoir ensuite tester la présence d'une cible pour chaque hypothèse sur la grille. Bien sûr, en pratique, les vrais paramètres de cible ne seront jamais parfaitement alignés avec les paramètres sur grille. Cette désadaptation, en retour, va avoir un impact négatif sur les performances de détection des détecteurs classiques. Il est bien connu, par exemple, que le Filtre Adapté (MF) présente l'équivalent d'une perte de 3dB en Rapport Signal à Bruit (RSB) par paramètre inconnu dans le pire des cas. Le cas du Filtre Adapté Normalisé (NMF), utilisé dans des contextes où le niveau de puissance du clutter est difficile à estimer, tel qu'en contexte marin, est plus spectaculaire. En effet, pour un nombre d'échantillon faibles à modérés, la probabilité de détection moyenne de ce détecteur ne tend plus vers 1 avec le RSB quand les paramètres de cibles sont uniformément répartis dans une cellule.

Pour pallier ce problème, plusieurs approches sont envisagées dans la littérature.

- Quand le problème de détection est envisagé comme un problème de reconstruction parcimonieuse (la parcimonie venant du faible nombre de cibles présente dans la scène), les performances de détection sont très fortement dégradée par la présence d'une désadaptation hors grille. Les solutions envisagées consistent en un raffinement du dictionnaire ou en l'introduction d'une perturbation linéaire.
- Les approches pratiques en radar consistent en l'utilisation d'une fenêtre d'apodisation pour aplatir le lobe principal en contrepartie d'une perte en RSB et d'une corrélation du bruit, ou à surréchantillonnage fin du signal reçu, qui permet d'améliorer les performances en détection au prix d'un coût en calcul plus élevé.
- En détection telle que classiquement envisagée dans la communauté traitement du signal, plusieurs études ont été menées pour réaliser une détection robuste à une désadaptation entre le modèle de signal attendu et le vrai signal reçu. Ces méthodes ne sont toutefois pas toujours adaptées pour le traitement de la désadaptation hors-grille. Supposons que le vrai signal reçu repose dans un cône autour du signal de référence, par exemple. Englober toute la variété des signaux hors-grille dans le cône impose une borne inférieure à la probabilité de fausse alarme (P_{FA}), hors en radar, on travaille couramment avec des P_{FA} très faibles, de l'ordre de 10^{-6}. Une autre approche consiste à fusionner les étapes de détection et d'estimation du paramètre de cible dans la chaîne de

détection radar. Le paramètre inconnu est estimé, pas forcément au sens du TV, souvent via une approximation au premier ordre du modèle de signal radar, puis injecté dans un test de détection.

Durant cette thèse, nous choisissons de nous focaliser sur ce que nous appellerons le TRVG "hors-grille", qui consiste simplement à effectuer le test de détection du TRVG en continu sur tout l'espace des paramètres de cible possibles. Cette solution semble proposer la meilleure probabilité de détection pour une probabilité de fausse alarme donnée. Bien que simple conceptuellement, elle présente toutefois plusieurs désavantages. D'une part, la statistique de ce test est plus difficile à évaluer théoriquement que la statistique des tests sur grille, car elle dépend de la distribution d'un continuum de variables non-indépendantes. En particulier, sa statistique sous l'hypothèse nulle, qui permet de fixer un seuil correspondant à une P_{FA} donnée, est inconnue. D'autre part, une implémentation naïve de ce test en pratique suppose la réalisation d'un grand nombre de tests en surréchantillonant finement la grille. Cependant, la puissance de calcul requise pour implémenter ce surréchantillonnage n'est pas toujours disponible dans des conditions opérationnelles réelles. Les contributions réalisées lors de cette thèse visent donc à étudier la statistique des TRVG hors-grille sous l'hypothèse nulle ainsi qu'à la recherche de méthode dans l'état de l'art offrant des performances de détection similaires à celle de ces détecteurs présentant un coût en calcul raisonnable.

Dans le chapitre 2, nous montrons que la recherche du seuil pour le NMF hors-grille revient à un calcul géométrique. Plus précisément, on montre que pour un seuil donné w et un signal complexe de N échantillons, la P_{FA} du NMF s'exprime comme le rapport du volume d'un tube de rayon $\phi = \cos^{-1} w$ autour de la variété des signaux normalisés sur la surface totale de la sphère $\mathbb{S}^{2N-1}$. Nous introduisons les outils nécessaires au calcul du volume de tube, et notamment la formule de Weyl, que l'on applique aux variétés définies par nos différents modèles de signaux. La formule de Weyl n'étant exacte que quand il n'y a pas de recouvrement du tube par lui-même, dans la suite chapitre nous calculons le seuil limite pour que cette condition ne soit pas vérifiée pour nos modèles de signaux. La validité de nos relations P_{FA}-seuil et du seuil limite sont confirmées par simulations numériques.

L'objectif du chapitre 3 est similaire à celui du chapitre 2 : nous y recherchons la relation P_{FA}-seuil du MF hors-grille. La méthode géométrique ne s'applique plus aussi naturellement. Pour parvenir à notre fin, nous modélisons la quantité à maximiser dans le MF hors-grille comme un champ aléatoire, puis nous approximons la P_{FA} comme l'espérance de la caractéristique d'Euler de l'ensemble d'excursion associé au champ aléatoire, ces concepts étant définis dans le chapitre. Les relations P_{FA}-seuils que nous obtenons sont une nouvelle fois validées par simulations numériques.

Enfin, après ces développements théoriques, le but du chapitre 4 est d'étudier les outils de la littérature permettant d'approximer les TRVG hors-grille en utilisant un faible coût de calcul, notamment dans le cas du NMF, dont la probabilité de détection ne converge par vers 1 assymptotiquement. Après avoir montré que des surréchantillonnages à faible cadence ne répondent pas totalement à notre problématique, car ils présentent toujours un défaut de probabilité de détection asymptotique dans des contextes de bruit coloré, notre intérêt se porte notamment pour la procédure de détection et d'estimation jointe, et nous identifions deux estimateurs du vrai paramètre de cible susceptibles d'être utilisés en pratique. L'un approxime le paramètre par interpolation de la transformée de Fourier, tandis que l'autre est inspiré par la méthode d'écartométrie. Nous montrons en simulations que les performances de détection approximent celle des TRVG hors-grille et que la relation P_{FA}-seuil des détecteurs ainsi créés s'approche fortement des relations calculées au chapitre 2. Dans une deuxième partie du chapitre, nous étudions les performances de ces détecteurs en conditions réelles en utilisant des données du radar de l'ONERA HYCAM. Après avoir mis en évidence la présence de cibles hors-grille, qui ne sont pas détectées par le NMF malgré un fort RSB, nous montrons que les détecteurs introduits plus tôt, basés sur une interpolation de la transformée de Fourier et une idée inspirée de l'écartométrie, présentent une meilleure probabilité de détection que celle d'un simple surréchantillonnage par un facteur 2.

La conclusion est l'occasion de rappeler les résultats trouvés lors de cette thèse et d'amener de nouvelles pistes de recherche, notamment l'étude des détecteurs adaptatifs hors-grille, pour lesquelles la matrice de covariance du bruit n'est pas connue, ainsi que la recherche de relation P_{FA}-seuil pour les TRVG surréchantillonnés.

Bibliography

[Adl00] R. J. Adler. "On excursion sets, tube formulas and maxima of random fields". In: *Annals of Applied Probability* (2000), pp. 1–74.

[Ale98] P. S. Aleksandrov. *Combinatorial topology*. Vol. 1. Courier Corporation, 1998.

[Ani+12] L. Anitori, A. Maleki, M. Otten, R. G. Baraniuk, and P. Hoogeboom. "Design and analysis of compressed sensing radar detectors". In: *IEEE Transactions on Signal Processing* 61.4 (2012), pp. 813–827.

[ASR88] M. Abramowitz, I. A. Stegun, and R. H. Romer. *Handbook of mathematical functions with formulas, graphs, and mathematical tables*. 1988.

[ATW07] R. J. Adler, J. E. Taylor, and K. J. Worsley. *Random fields and geometry*. Vol. 80. Springer, 2007.

[ATW15] R. J. Adler, J. E. Taylor, and K. J. Worsley. *Applications of Random Fields and Geometry: Foundations and Case Studies*. In preparation, 2015.

[Aub+20] A. Aubry, A. De Maio, S. Marano, and M. Rosamilia. "Single-pulse simultaneous target detection and angle estimation in a multichannel phased array radar". In: *Signal Processing, IEEE Transactions on* 68 (2020), pp. 6649–6664.

[BBR07] F. Bandiera, O. Besson, and G. Ricci. "An ABORT-like detector with improved mismatched signals rejection capabilities". In: *Signal Processing, IEEE Transactions on* 56.1 (2007), pp. 14–25.

[BDR07] F. Bandiera, A. De Maio, and G. Ricci. "Adaptive CFAR radar detection with conic rejection". In: *Signal Processing, IEEE Transactions on* 55.6 (2007), pp. 2533–2541.

[Bes06] O. Besson. "Detection of a signal in linear subspace with bounded mismatch". In: *Aerospace and Electronic Systems, IEEE Transactions on* 42.3 (2006), pp. 1131–1139. doi: 10.1109/TAES.2006.248195.

[Bes07] O. Besson. "Adaptive detection with bounded steering vectors mismatch angle". In: *Signal Processing, IEEE Transactions on* 55.4 (2007), pp. 1560–1564.

[Bes14] O. Besson. "On false alarm rate of matched filter under distribution mismatch". In: *IEEE Signal Processing Letters* 22.2 (2014), pp. 167–171.

[BOR09] F. Bandiera, D. Orlando, and G. Ricci. *Advanced Radar Detection Schemes Under Mismatched Signal Models*. Morgan & Claypool publishers, 2009.

[Bro+13] P. Brouard, L. Constancias, A. Brun, S. Attia, J. Peyret, and P. Dreuillet. "HYCAM: a new S-band surface radar testbed". In: *Radar Conference, IET International*. 2013. doi: 10.1049/cp.2013.0225.

[BRO20] J. Bosse, O. Rabaste, and J.-P. Ovarlez. "Adaptive subspace detectors for off-grid mismatched targets". In: *IEEE International Conference on Acoustics, Speech and Signal Processing (ICASSP)* (2020), pp. 4777–4780.

[BRS68] L. Brennan, I. Reed, and W. Sollfrey. "A comparison of average-likelihood and maximum-likelihood ratio tests for detecting radar targets of unknown Doppler frequency". In: *Information Theory, IEEE Transactions on* 14.1 (1968), pp. 104–110.

[BTR13] B. N. Bhaskar, G. Tang, and B. Recht. “Atomic norm denoising with applications to line spectral estimation”. In: *Signal Processing, IEEE Transactions on* 61.23 (2013), pp. 5987–5999.

[Can02] A. J. Cann. “Range gate straddling loss and joint probability with partial correlation”. In: *Aerospace and Electronic Systems, IEEE Transactions on* 38.3 (2002), pp. 1054–1058.

[Cat+13] M. Cattenoz, P. Brouard, A. Brun, L. Constancias, and L. Savy. “Coherent collocated MIMO radar: A study on real data”. In: *2013 14th International Radar Symposium (IRS)*. Vol. 1. IEEE. 2013, pp. 83–88.

[CLR95] E. Conte, M. Lops, and G. Ricci. “Asymptotically Optimum Radar Detection in Compound-Gaussian Clutter”. In: *Aerospace and Electronic Systems, IEEE Transactions on* 31.2 (Apr. 1995), pp. 617–625.

[Coc34] W. G. Cochran. “The distribution of quadratic forms in a normal system, with applications to the analysis of covariance”. In: *Mathematical Proceedings of the Cambridge Philosophical Society*. Vol. 30. 2. Cambridge University Press. 1934, pp. 178–191.

[CT65] J. W. Cooley and J. W. Tukey. “An algorithm for the machine calculation of complex Fourier series”. In: *Mathematics of computation* 19.90 (1965), pp. 297–301.

[De +08] A. De Maio, S. De Nicola, Y. Huang, S. Zhang, and A. Farina. “Adaptive detection and estimation in the presence of useful signal and interference mismatches”. In: *Signal Processing, IEEE Transactions on* 57.2 (2008), pp. 436–450.

[De +10a] A. De Maio, S. De Nicola, A. Farina, and S. Iommelli. “Adaptive detection of a signal with angle uncertainty”. In: *IET radar, sonar & navigation* 4.4 (2010), pp. 537–547.

[De +10b] A. De Maio, Y. Huang, D. P. Palomar, S. Zhang, and A. Farina. “Fractional QCQP with applications in ML steering direction estimation for radar detection”. In: *Signal Processing, IEEE Transactions on* 59.1 (2010), pp. 172–185.

[De 05] A. De Maio. “Robust adaptive radar detection in the presence of steering vector mismatches”. In: *Aerospace and Electronic Systems, IEEE Transactions on* 41.4 (2005), pp. 1322–1337.

[Dev+21] P. Develter, J. Bosse, O. Rabaste, P. Forster, and J.-P. Ovarlez. “Off-Grid Radar Target Detection with the Normalized Matched Filter: A Monopulse-Based Detection Scheme”. In: *IEEE Statistical Signal Processing Workshop (SSP)*. IEEE. 2021, pp. 226–230.

[Dev+22a] P. Develter, J. Bosse, O. Rabaste, P. Forster, and J.-P. Ovarlez. “On the False Alarm Probability of the Normalized Matched Filter for off-grid target detection”. In: *IEEE International Conference on Acoustics, Speech and Signal Processing (ICASSP)*. IEEE. 2022, pp. 5782–5786.

[Dev+22b] P. Develter, J. Bosse, O. Rabaste, P. Forster, and J.-P. Ovarlez. “Sur la probabilité de fausse alarme du Filtre Adapté Normalisé pour la détection de cibles hors-grille”. In: *GRETSI 2022*. 2022, pp. 1–5.

[Dev+23a] P. Develter, J. Bosse, O. Rabaste, P. Forster, and J.-P. Ovarlez. “False Alarm Regulation for Off-Grid Target Detection With The Matched Filter”. In: *IEEE International Conference on Acoustics, Speech and Signal Processing (ICASSP)*. IEEE. 2023, pp. 1–5.

[Dev+23b] P. Develter, J. Bosse, O. Rabaste, P. Forster, and J.-P. Ovarlez. “On the False Alarm Probability of the Normalized Matched Filter for off-grid targets: A geometrical approach and its validity conditions”. In: *Signal Processing, IEEE Transactions on* accepted for publication (2023).

[Dev+23c] P. Develter, J. Bosse, O. Rabaste, P. Forster, and J.-P. Ovarlez. “Sur la probabilité de fausse alarme du filtre adapté pour la détection distance-Doppler de cibles hors-grille”. In: *GRETSI 2023*. 2023, pp. 1–5.

[FL12] A. Fannjiang and W. Liao. “Coherence pattern–guided compressive sensing with unresolved grids”. In: *SIAM Journal on Imaging Sciences* 5.1 (2012), pp. 179–202.

[Fuh91] D. R. Fuhrmann. “Application of Toeplitz covariance estimation to adaptive beamforming and detection”. In: *IEEE Transactions on Signal Processing* 39.10 (1991), pp. 2194–2198.

[Gal22] Galloway, G. *Introduction to differential geometry*. https://www.math.miami.edu/~galloway/. Accessed: 2023-10-08. 2022.

[GCL10] J. Galy, E. Chaumette, and P. Larzabal. “Joint detection estimation problem of monopulse angle measurement”. In: *Aerospace and Electronic Systems, IEEE Transactions on* 46.1 (2010), pp. 397–413.

[GHL+90] Sylvestre Gallot, Dominique Hulin, Jacques Lafontaine, et al. *Riemannian geometry*. Vol. 2. Springer, 1990.

[Gra03] A. Gray. *Tubes*. Vol. 221. Springer Science & Business Media, 2003.

[Hay03] S. D. Hayward. “CFAR detection of targets with unknown Doppler shifts”. In: *Electronics Letters* 39.6 (2003), pp. 549–550.

[Hoh02] M. Hohenwarter. *GeoGebra - ein Softwaresystem für dynamische Geometrie und Algebra der Ebene*. Deutsch. Diplomarbeit, Universität Salzburg. 2002.

[Hot39] H. Hotelling. “Tubes and spheres in n-spaces, and a class of statistical problems”. In: *American Journal of Mathematics* 61.2 (1939), pp. 440–460.

[HTW00] RD Hill, RJA Tough, and KD Ward. “Distribution of the global maximum of a Gaussian random field and performance of matched filter detectors”. In: *IEE Proceedings-Vision, Image and Signal Processing* 147.4 (2000), pp. 297–303.

[HTW01] R. D. Hill, R. J. A. Tough, and K. D. Ward. “False alarm curve for envelope of Gaussian random field”. In: *Electronics Letters* 37.4 (2001), p. 1.

[Jay+03] E. Jay, J.-P. Ovarlez, D. Declercq, and P. Duvaut. “BORD: Bayesian optimum radar detector”. In: *Signal Processing* 83.6 (2003), pp. 1151–1162.

[Jay02] E. Jay. “Détection en environnement non gaussien”. PhD thesis. Université de Cergy Pontoise, 2002.

[JJ90] S. Johansen and I. M. Johnstone. “Hotelling’s theorem on the volume of tubes: some illustrations in simultaneous inference and data analysis”. In: *The Annals of Statistics* 18.2 (1990), pp. 652–684.

[JK07] E. Jacobsen and P. Kootsookos. “Fast, accurate frequency estimators [DSP Tips & Tricks]”. In: *IEEE Signal Processing Magazine* 24.3 (2007), pp. 123–125.

[JS89] I. Johnstone and D. Siegmund. “On Hotelling’s formula for the volume of tubes and Naiman’s inequality”. In: *The Annals of Statistics* (1989), pp. 184–194.

[Kal92] S. Z. Kalson. “An adaptive array detector with mismatched signal rejection”. In: *Aerospace and Electronic Systems, IEEE Transactions on* 28.1 (1992), pp. 195–207.

[Kay09] S. M. Kay. *Fundamentals of statistical processing, Volume 2: Detection theory*. Pearson Education India, 2009.

[Kel86] E. J. Kelly. “An Adaptive Detection Algorithm”. In: *Aerospace and Electronic Systems, IEEE Transactions on* AES-22.2 (1986), pp. 115–127. doi: 10.1109/TAES.1986.310745.

[KS89] M. Knowles and D. Siegmund. “On Hotelling’s approach to testing for a nonlinear parameter in regression”. In: *International Statistical Review/Revue Internationale de Statistique* (1989), pp. 205–220.

[KS95] D. E. Kreithen and A. O. Steinhardt. “Target detection in post-STAP undernulled clutter”. In: *Conference Record of The Twenty-Ninth Asilomar Conference on Signals, Systems and Computers*. Vol. 2. IEEE. 1995, pp. 1203–1207.

[KS99] S. Kraut and L. L. Scharf. “The CFAR adaptive subspace detector is a scale-invariant GLRT”. In: *Signal Processing, IEEE Transactions on* 47.9 (1999), pp. 2538–2541. doi: 10.1109/78.782198.

[KT01] S. Kuriki and A. Takemura. “Tail probabilities of the maxima of multilinear forms and their applications”. In: *Annals of statistics* (2001), pp. 328–371.

[KTT22] S. Kuriki, A. Takemura, and J. E. Taylor. “The volume-of-tube method for Gaussian random fields with inhomogeneous variance”. In: *Journal of Multivariate Analysis* 188 (2022), p. 104819.

[Las+15] M. Lasserre, S. Bidon, O. Besson, and F. Le Chevalier. “Bayesian sparse Fourier representation of off-grid targets with application to experimental radar data”. In: *Signal Processing* 111 (2015), pp. 261–273.

[Le 02] F. Le Chevalier. *Principles of radar and sonar signal processing*. Artech House, 2002.

[Lei+20] E. Leitinger, S. Grebien, B. Fleury, and K. Witrisal. “Detection and estimation of a spectral line in MIMO systems”. In: *2020 54th Asilomar Conference on Signals, Systems, and Computers*. IEEE. 2020, pp. 1090–1095.

[Mar60] J. Marcum. “A statistical theory of target detection by pulsed radar”. In: *IRE Transactions on Information Theory* 6.2 (1960), pp. 59–267.

[Mos69] E. Mosca. “Angle Estimation in Amplitude Comparison Monopulse Systems”. In: *Aerospace and Electronic Systems, IEEE Transactions on* AES-5.2 (1969), pp. 205–212. doi: 10.1109/TAES.1969.309906.

[NP33] J. Neyman and E. S. Pearson. “IX. On the problem of the most efficient tests of statistical hypotheses”. In: *Philosophical Transactions of the Royal Society of London. Series A, Containing Papers of a Mathematical or Physical Character* 231.694-706 (1933), pp. 289–337.

[Oll+12] E. Ollila, D. E. Tyler, V. Koivunen, and H. V. Poor. “Complex Elliptically Symmetric Distributions: Survey, New Results and Applications”. In: *Signal Processing, IEEE Transactions on* 60.11 (Nov. 2012), pp. 5597–5625. issn: 1053-587X. doi: 10.1109/TSP.2012.2212433.

[OPB15] J.-P. Ovarlez, F. Pascal, and A. Breloy. “Asymptotic detection performance analysis of the robust adaptive normalized matched filter”. In: *2015 IEEE 6th International Workshop on Computational Advances in Multi-Sensor Adaptive Processing (CAMSAP)*. IEEE. 2015, pp. 137–140.

[OR11] D. Orlando and G. Ricci. “Adaptive radar detection and localization of a point-like target”. In: *Signal Processing, IEEE Transactions on* 59.9 (2011), pp. 4086–4096.

[PP+08] K. B. Petersen, M. S. Pedersen, et al. “The matrix cookbook”. In: *Technical University of Denmark* 7.15 (2008), p. 510.

[RB18] C. D. Richmond and P. Basu. “Architectures for cooperative radar-communications: Average vs. generalized likelihood ratio tests”. In: *2018 IEEE Radar Conference (RadarConf18)*. IEEE. 2018, pp. 1584–1588.

[RBO16] O. Rabaste, J. Bosse, and J.-P. Ovarlez. “Off-grid target detection with Normalized Matched Subspace Filter”. In: *24th European Signal Processing Conference (EUSIPCO)*. Aug. 2016, pp. 1926–1930.

[RD16] F. Rouvière and A. Debreil. *Initiation à la géométrie de Riemann*. Calvage & Mounet, 2016.

[Ric+10] M. A Richards, J. Scheer, W. A. Holm, and W. L. Melvin. *Principles of modern radar*. Vol. 1. Citeseer, 2010.

[Ric44] S. O. Rice. “Mathematical analysis of random noise”. In: *The Bell System Technical Journal* 23.3 (1944), pp. 282–332.

[Rob+92] F. C. Robey, D. R. Fuhrmann, E. J. Kelly, and R. Nitzberg. “A CFAR adaptive matched filter detector”. In: *Aerospace and Electronic Systems, IEEE Transactions on* 28.1 (1992), pp. 208–216. doi: 10.1109/7.135446.

[SB11a] S. M. Sherman and D. K. Barton. *Monopulse principles and techniques*. Artech House, 2011.

[SB11b] P. Stoica and P. Babu. “Sparse estimation of spectral lines: Grid selection problems and their solutions”. In: *IEEE Transactions on Signal Processing* 60.2 (2011), pp. 962–967.

[SD91] L. L. Scharf and C. Demeure. *Statistical signal processing: detection, estimation, and time series analysis*. Prentice Hall, 1991.

[Sel65] I. Selin. “Detection of coherent radar returns of unknown Doppler shift”. In: *Information Theory, IEEE Transactions on* 11.3 (1965), pp. 396–400.

[SF94] L. L. Scharf and B. Friedlander. “Matched subspace detectors”. In: *Signal Processing, IEEE Transactions on* 42.8 (1994), pp. 2146–2157.

[SS78] J. L. Synge and A. Schild. *Tensor calculus*. Vol. 5. Courier Corporation, 1978.

[Str12] T. Strohmer. “Measure what should be measured: progress and challenges in compressive sensing”. In: *IEEE Signal Processing Letters* 19.12 (2012), pp. 887–893.

[Sun93] J. Sun. “Tail probabilities of the maxima of Gaussian random fields”. In: *The Annals of Probability* (1993), pp. 34–71.

[SW95] D. O. Siegmund and K. J. Worsley. “Testing for a signal with unknown location and scale in a stationary Gaussian random field”. In: *The Annals of Statistics* 23.2 (1995), pp. 608–639.

[Tan+13] G. Tang, B. N. Bhaskar, P. Shah, and B. Recht. “Compressed sensing off the grid”. In: *Information Theory, IEEE Transactions on* 59.11 (2013), pp. 7465–7490.

[Tan19] U. H. Tan. “Méthodologies de conception de formes d’onde pour radars sol. Application au cas du radar MIMO.” PhD thesis. Université Paris-Saclay (ComUE), 2019.

[TG07] J. A. Tropp and A. C. Gilbert. “Signal recovery from random measurements via orthogonal matching pursuit”. In: *Information Theory, IEEE Transactions on* 53.12 (2007), pp. 4655–4666.

[Tib96] R. Tibshirani. “Regression shrinkage and selection via the lasso”. In: *Journal of the Royal Statistical Society Series B: Statistical Methodology* 58.1 (1996), pp. 267–288.

[TK02] A. Takemura and S. Kuriki. “On the equivalence of the tube and Euler characteristic methods for the distribution of the maximum of Gaussian fields over piecewise smooth domains”. In: *Annals of Applied Probability* (2002), pp. 768–796.

[TWG07] J. E. Taylor, K. J. Worsley, and F. Gosselin. “Maxima of discretely sampled random fields, with an application to ‘bubbles’”. In: *Biometrika* 94.1 (2007), pp. 1–18.

[Wat13] S. Watts. “The effects of covariance matrix mismatch on adaptive CFAR performance”. In: *2013 International Conference on Radar*. IEEE. 2013, pp. 324–329.

[Wey39] H. Weyl. “On the volume of tubes”. In: *American Journal of Mathematics* 61.2 (1939), pp. 461–472.

[Wor01] K. J. Worsley. “Testing for signals with unknown location and scale in a χ^2 random field, with an application to fMRI”. In: *Advances in Applied Probability* 33.4 (2001), pp. 773–793.

[Wor94] K. J. Worsley. “Local maxima and the expected Euler characteristic of excursion sets of χ^2, F and t fields”. In: *Advances in Applied Probability* 26.1 (1994), pp. 13–42.

[Wor95] K. J. Worsley. “Estimating the number of peaks in a random field using the Hadwiger characteristic of excursion sets, with applications to medical images”. In: *The Annals of Statistics* (1995), pp. 640–669.

[WTW07] K. D. Ward, R. J. A. Tough, and S. Watts. “Sea clutter: scattering, the K distribution and radar performance”. In: *Waves in Random and Complex Media* 17.2 (2007), pp. 233–234.

[Xin+11] M. Xing, J. Su, G. Wang, and Z. Bao. “New parameter estimation and detection algorithm for high speed small target”. In: *Aerospace and Electronic Systems, IEEE Transactions on* 47.1 (2011), pp. 214–224.

[ZLG11] H. Zhu, G. Leus, and G. B. Giannakis. “Sparsity-cognizant total least-squares for perturbed compressive sampling”. In: *Signal Processing, IEEE Transactions on* 59.5 (2011), pp. 2002–2016.

[ZWB09] X. Zhang, P. Willett, and Y. Bar-Shalom. “Detection and localization of multiple unresolved extended targets via monopulse radar signal processing”. In: *Aerospace and Electronic Systems, IEEE Transactions on* 45.2 (2009), pp. 455–472.